BUBBLES, DROPLETS AND MICELLES FOR ACOUSTICALLY-MEDIATED DRUG/GENE DELIVERY

EDITED BY: Jean-Michel Escoffre, Marc Derieppe, Baudouin Denis De Senneville and Noboru Sasaki

PUBLISHED IN: Frontiers in Pharmacology

frontiers Research Topics

ISSN 1664-8714
ISBN 978-2-88963-936-6
DOI 10.3389/978-2-88963-936-6

About Frontiers

Frontiers is more than just an open-access publisher of scholarly articles: it is a pioneering approach to the world of academia, radically improving the way scholarly research is managed. The grand vision of Frontiers is a world where all people have an equal opportunity to seek, share and generate knowledge. Frontiers provides immediate and permanent online open access to all its publications, but this alone is not enough to realize our grand goals.

Frontiers Journal Series

The Frontiers Journal Series is a multi-tier and interdisciplinary set of open-access, online journals, promising a paradigm shift from the current review, selection and dissemination processes in academic publishing. All Frontiers journals are driven by researchers for researchers; therefore, they constitute a service to the scholarly community. At the same time, the Frontiers Journal Series operates on a revolutionary invention, the tiered publishing system, initially addressing specific communities of scholars, and gradually climbing up to broader public understanding, thus serving the interests of the lay society, too.

Dedication to Quality

Each Frontiers article is a landmark of the highest quality, thanks to genuinely collaborative interactions between authors and review editors, who include some of the world's best academicians. Research must be certified by peers before entering a stream of knowledge that may eventually reach the public - and shape society; therefore, Frontiers only applies the most rigorous and unbiased reviews.
Frontiers revolutionizes research publishing by freely delivering the most outstanding research, evaluated with no bias from both the academic and social point of view. By applying the most advanced information technologies, Frontiers is catapulting scholarly publishing into a new generation.

What are Frontiers Research Topics?

Frontiers Research Topics are very popular trademarks of the Frontiers Journals Series: they are collections of at least ten articles, all centered on a particular subject. With their unique mix of varied contributions from Original Research to Review Articles, Frontiers Research Topics unify the most influential researchers, the latest key findings and historical advances in a hot research area! Find out more on how to host your own Frontiers Research Topic or contribute to one as an author by contacting the Frontiers Editorial Office: researchtopics@frontiersin.org

BUBBLES, DROPLETS AND MICELLES FOR ACOUSTICALLY-MEDIATED DRUG/GENE DELIVERY

Topic Editors:
Jean-Michel Escoffre, INSERM U1253Imagerie et Cerveau (iBrain), France
Marc Derieppe, Princess Maxima Center for Pediatric Oncology, Netherlands
Baudouin Denis De Senneville, UMR5251 Institut de mathématiques de Bordeaux (IMB), France
Noboru Sasaki, Hokkaido University, Japan

Citation: Escoffre, J.-M., Derieppe, M., De Senneville, B. D., Sasaki, N., eds. (2020). Bubbles, Droplets and Micelles for Acoustically-Mediated Drug/Gene Delivery. Lausanne: Frontiers Media SA. doi: 10.3389/978-2-88963-936-6

Table of Contents

frontiers in Pharmacology

EDITORIAL
published: 26 June 2020
doi: 10.3389/fphar.2020.00954

Editorial: Bubbles, Droplets and Micelles for Acoustically-Mediated Drug/Gene Delivery

Jean-Michel Escoffre[1*], *Baudouin Denis de Senneville*[2], *Noboru Sasaki*[3] *and Marc Derieppe*[4]

[1] UMR 1253, iBrain, Université de Tours, Inserm, Tours, France, [2] Institut de Mathématiques de Bordeaux (IMB), UMR 5251 CNRS/Université de Bordeaux, Talence, France, [3] Laboratory of Veterinary Internal Medicine, Department of Clinical Sciences, Graduate School of Veterinary Medicine, Hokkaido University, Sapporo, Japan, [4] Department of Pediatric Neuro-oncology, Princess Maxima Center for Pediatric Oncology, Utrecht, Netherlands

Keywords: ultrasound, bubble, therapeutic ultrasound, drug delivery, gene delivery

Editorial on the Research Topic

Bubbles, Droplets and Micelles for Acoustically-Mediated Drug/Gene Delivery

This special issue presents novel contributions from 86 authors in a compilation of nine original articles and two review articles: four articles from Asia, three from America, and four from Europe. The issue presents findings in the fields of bactericidal therapy, cancer, inner-ear diseases, and underlying mechanisms of ultrasound-mediated drug/gene delivery, all of them with a clear goal: clinical translation. All findings reported in this issue had 8,517 views on April 10th 2020 (source of counting: Frontiers in Pharmacology).

Therapeutic ultrasound shows promising findings in ultrasound-mediated nitric oxide (NO) delivery using lipid-shelled nitric oxide-loaded microbubbles. NO is a potent bioactive gas that was evidenced to display biofilm dispersion and bactericide properties; its delivery in specific anatomical regions is increasingly investigated (Elnaggar et al., 2017), and paves the way for novel encapsulation formulations. In this issue, Lafond and colleagues report on an *in vitro* proof-of-concept demonstrating the relevance to co-encapsulate octafluoropropane in a microbubble formulation containing NO (Lafond et al.). The authors showed an increased payload loading, compatible acoustic properties using a clinical ultrasound scanner, and a significant increase in bacterial killing.

For cancer applications the interest in acoustic cluster therapy (ACT) for enhanced drug/drug carrier delivery is rising (Sontum et al., 2015). Here, two articles evidence enhanced therapeutic effect *in vivo*, 1) for the treatment of triple negative breast cancer using the stealth liposomal doxorubicin, Doxil® (Bush et al.), and 2) for human colon cancer treatment with combined irinotecan (Bush et al.).

An interesting article reports on promising data for future treatments of inner ear diseases (Lin et al.). The authors evidenced the possibility to perform drug delivery to the inner ear non-invasively by ultrasound- and microbubble-mediated permeabilization of the round window membrane. Preservation of the inner ear, this vulnerable and poorly-accessible sensory organ, was clearly documented by not only functional assessment, using auditory brainstem response recordings, but also a morphological evaluation with electron microscopy. To our knowledge, Lin and colleagues are the first to show ultrastructural changes of the round window membrane after its ultrasound- and microbubble-mediated permeabilization. Specifically, the ultrasound protocol applied in this

Edited and reviewed by:
Alastair George Stewart,
The University of Melbourne, Australia

****Correspondence:***
Jean-Michel Escoffre
jean-michel.escoffre@univ-tours.fr

Specialty section:
This article was submitted to Translational Pharmacology, a section of the journal Frontiers in Pharmacology

Received: *14 May 2020*
Accepted: *11 June 2020*
Published: *26 June 2020*

Citation:
Escoffre J-M, de Senneville BD, Sasaki N and Derieppe M (2020) Editorial: Bubbles, Droplets and Micelles for Acoustically-Mediated Drug/Gene Delivery. Front. Pharmacol. 11:954. doi: 10.3389/fphar.2020.00954

study evidenced that the observed damages did not affect the basement membrane, thus allowing epithelial regeneration. We look forward to consulting future results from this research line.

After around 15 years of fundamental findings and technical developments in focused ultrasound (FUS) for blood-brain barrier (BBB) opening (Hynynen et al., 2001), a few clinical studies using commercially-available FUS systems were published in the last 5 years (Carpentier et al., 2016) (Lipsman et al., 2018) (Idbaih et al., 2019) (Mainprize et al., 2019), thus confirming its potential to give a wealth of molecules and delivery systems, *e.g.,* nanomedicines and viral vectors, access to the parenchyma of the central nervous system (CNS). In this issue, Fisher and Price stress the relevance to combine FUS-mediated BBB opening and polymeric or lipid-based nanoparticles for drug and gene delivery to 1) make therapeutic advances in CNS disorders, 2) offer new opportunities in the detection of early biomarkers, for instance using FUS-mediated BBB opening for antibody delivery in the CNS, or 3) adopt novel approaches to uncover normal and diseased brain function, like targeted Propofol delivery to the thalamus to elicit and study functional changes in rat brain activity (Wang et al., 2018). The authors explain how specific delivery system formulations, *e.g.*, poly (aspartic acid)—polyethylene glycol (PAA-PEG) nanoparticles, can display favorable pharmacokinetic profiles and lead to increased therapeutic effect (Timbie et al., 2017).

Overall, this special issue brings a collection of research articles that seemingly contribute to the scientific advances in the different aspects of bubbles, droplets, and micelles for acoustically-mediated drug/gene delivery, from the formulation of acoustic-responsive agents to preclinical and clinical investigations. The rise of these therapeutic ultrasound applications is the result of longstanding collaborations between academic and private stakeholders of fundamental and applied research who join forces in a multidisciplinary landscape. To fulfill the medical needs is just a matter of time.

AUTHOR CONTRIBUTIONS

All four authors organized the Research Topic, invited authors, participated in the review process of the manuscripts, and wrote the editorial.

ACKNOWLEDGMENTS

The editors thank all authors for their contributions to this Research Topic, all the reviewers for their constructive feedbacks, and the editorial board of Frontiers in Pharmacology for the technical support throughout the publication process.

REFERENCES

Carpentier, A., Canney, M., Vignot, A., Reina, V., Beccaria, K., Horodyckid, C., et al. (2016). Clinical trial of blood-brain barrier disruption by pulsed ultrasound. *Sci. Trans. Med.* 8 (343re2), 1–9. doi: 10.1126/scitranslmed.aaf6086

Elnaggar, M. A., Subbiah, R., Han, D. K., and Joung, Y. K. (2017). Lipid-based carriers for controlled delivery of nitric oxide. *Expert Opin. Drug Deliv.* 14, 1341–1353. doi: 10.1080/17425247.2017.1285904

Hynynen, K., McDannold, N., Vykhodtseva, N., and Jolesz, F. A. (2001). Noninvasive MR Imaging–guided Focal Opening of the Blood-Brain Barrier in Rabbits. *Radiol.* 220, 640–646. doi: 10.1148/radiol.2202001804

Idbaih, A., Canney, M., Belin, L., Desseaux, C., Vignot, A., Bouchoux, G., et al. (2019). Safety and Feasibility of Repeated and Transient Blood-Brain Barrier Disruption by Pulsed Ultrasound in Patients with Recurrent Glioblastoma. *Clin. Cancer Res.* 25, 3793–3801. doi: 10.1158/1078-0432.CCR-18-3643

Lipsman, N., Meng, Y., Bethune, A., Huang, Y., Lam, B., Masellis, M., et al. (2018). Blood–brain barrier opening in Alzheimer's disease using MR-guided focused ultrasound. *Nat. Commun.* 9, 2336. doi: 10.1038/s41467-018-04529-6

Mainprize, T., Lipsman, N., Huang, Y., Meng, Y., Bethune, A., Ironside, S., et al. (2019). Blood-Brain Barrier Opening in Primary Brain Tumors with Non-invasive MR-Guided Focused Ultrasound: A Clinical Safety and Feasibility Study. *Sci. Rep.* 9, 1–7. doi: 10.1038/s41598-018-36340-0

Sontum, P., Kvåle, S., Healey, A. J., Skurtveit, R., Watanabe, R., Matsumura, M., et al. (2015). Acoustic Cluster Therapy (ACT)-a novel concept for ultrasound mediated, targeted drug delivery. *Int. J. Pharm.* 495, 1019–1027. doi: 10.1016/j.ijpharm.2015.09.047

Timbie, K. F., Afzal, U., Date, A., Zhang, C., Song, J., Wilson Miller, G., et al. (2017). MR image-guided delivery of cisplatin-loaded brain-penetrating nanoparticles to invasive glioma with focused ultrasound. *J. Control. Release* 263, 120–131. doi: 10.1016/j.jconrel.2017.03.017

Wang, J. B., Aryal, M., Zhong, Q., Vyas, D. B., and Airan, R. D. (2018). Noninvasive Ultrasonic Drug Uncaging Maps Whole-Brain Functional Networks. *Neuron* 100, 728–738. doi: 10.1016/j.neuron.2018.10.042

Conflict of Interest: The authors declare that the research was conducted in the absence of any commercial or financial relationships that could be construed as a potential conflict of interest.

frontiers in Pharmacology

REVIEW
published: 13 November 2019
doi: 10.3389/fphar.2019.01348

Recent Advances in the Use of Focused Ultrasound for Magnetic Resonance Image-Guided Therapeutic Nanoparticle Delivery to the Central Nervous System

*Delaney G. Fisher and Richard J. Price**

Department of Biomedical Engineering, University of Virginia, Charlottesville, VA, United States

Targeting systemically-administered drugs and genes to specific regions of the central nervous system (CNS) remains a challenge. With applications extending into numerous disorders and cancers, there is an obvious need for approaches that facilitate the delivery of therapeutics across the impervious blood-brain barrier (BBB). Focused ultrasound (FUS) is an emerging treatment method that leverages acoustic energy to oscillate simultaneously administered contrast agent microbubbles. This FUS-mediated technique temporarily disrupts the BBB, allowing ordinarily impenetrable agents to diffuse and/or convect into the CNS. Under magnetic resonance image guidance, FUS and microbubbles enable regional targeting—limiting the large, and potentially toxic, dosage that is often characteristic of systemically-administered therapies. Subsequent to delivery across the BBB, therapeutics face yet another challenge: penetrating the electrostatically-charged, mesh-like brain parenchyma. Non-bioadhesive, encapsulated nanoparticles can help overcome this additional barrier to promote widespread treatment in selected target areas. Furthermore, nanoparticles offer significant advantages over conventional systemically-administered therapeutics. Surface modifications of nanoparticles can be engineered to enhance targeted cellular uptake, and nanoparticle formulations can be tailored to control many pharmacokinetic properties such as rate of drug liberation, distribution, and excretion. For instance, nanoparticles loaded with gene plasmids foster relatively stable transfection, thus obviating the need for multiple, successive treatments. As the formulations and applications of these nanoparticles can vary greatly, this review article provides an overview of FUS coupled with polymeric or lipid-based nanoparticles currently utilized for drug delivery, diagnosis, and assessment of function in the CNS.

Keywords: focused ultrasound, nanoparticle, central nervous system, brain, drug and gene delivery

OPEN ACCESS

Edited by:
Jean-Michel Escoffre, INSERM U1253 Imagerie et Cerveau (iBrain), France

Reviewed by:
Shih-Ying Wu, Columbia University, United States
Tzu-Chen Yen, Linkou Chang Gung Memorial Hospital, Taiwan

****Correspondence:***
Richard J. Price
rprice@virginia.edu

Specialty section:
This article was submitted to Translational Pharmacology, a section of the journal Frontiers in Pharmacology

Received: *22 July 2019*
Accepted: *24 October 2019*
Published: *13 November 2019*

Citation:
Fisher DG and Price RJ (2019) Recent Advances in the Use of Focused Ultrasound for Magnetic Resonance Image-Guided Therapeutic Nanoparticle Delivery to the Central Nervous System. Front. Pharmacol. 10:1348. doi: 10.3389/fphar.2019.01348

INTRODUCTION

As advances in medicine continue to extend lifespans, the prevalence of diseases of the central nervous system (CNS) in the aging population also continues to grow. In turn, this rise in CNS diseases introduces more urgency to improve the delivery of therapeutics to the brain.

The brain is protected by the blood–brain barrier (BBB) which precludes most systemically-administered agents from entering its parenchymal space. This exclusion of therapeutic agents restricts treatment options and has greatly hindered successful therapeutic developments for CNS diseases. In addition to challenges associated with surpassing the BBB, the treatment of many CNS diseases also requires spatially targeted delivery of therapeutics to avoid altering normal tissue function. For example, many neuromodulatory drugs will stimulate differential effects depending on the brain region upon which they act. In such cases, non-specific delivery can induce overall dysregulation. In the case of brain tumors, toxic chemotherapeutics may be deleterious if administered to healthy brain tissue in high concentrations.

One emerging approach to opening the BBB in a spatially targeted brain region utilizes magnetic resonance image-guided focused ultrasound (FUS; **Figure 1**). Several clinical trials demonstrating the efficacy of this technique to safely open the BBB are underway with promising preliminary results (Carpentier et al., 2016; Lipsman et al., 2018; Idbaih et al., 2019; Mainprize et al., 2019). The underlying premise for BBB opening with focused ultrasound is provided in detail in other review articles (Timbie et al., 2015; Curley et al., 2017; Gorick et al., 2018), and we refer the reader to these reviews for a more in-depth report. Briefly, FUS transmits pressure waves that converge on a selected focal spot with millimeter precision. These pressure waves oscillate gas-encasing microbubbles that are administered systemically during FUS treatment (**Figure 2**; Timbie et al., 2015). This

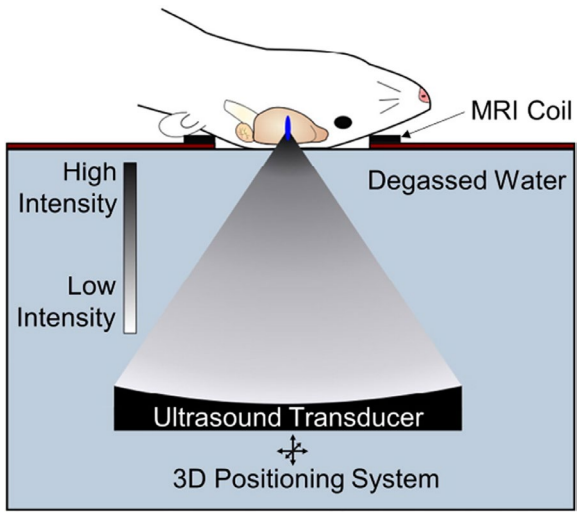

FIGURE 1 | Transcranial focused ultrasound (FUS) with microbubbles yields non-invasive, safe, repeated and targeted BBB disruption, leading to improved drug or gene delivery to the brain. Pre-clinical FUS studies in animals including mice and rats permit use of a single-element FUS transducer, due to favorable skull geometry. FUS can be guided with MR imaging and is capable of sub-millimeter resolution allowing precise targeting of structures in the CNS with minimal off-target effects. Adapted from Timbie et al. (2015). Reproduced with permission.

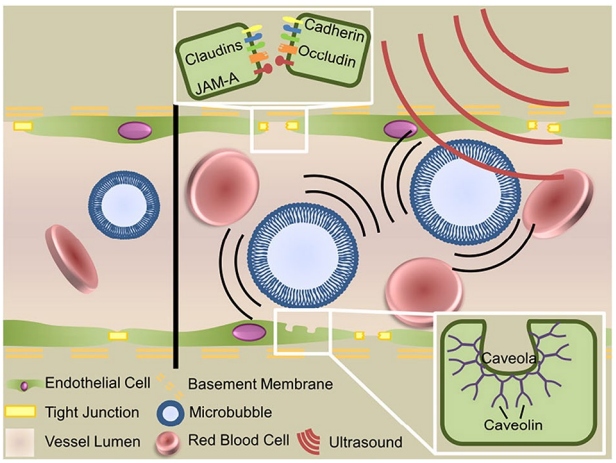

FIGURE 2 | Mechanisms of focused ultrasound mediated blood–brain barrier disruption. Circulating microbubbles oscillate in the ultrasonic field, producing forces that act on the vessel wall to generate three bioeffects that permit transport across the blood–brain barrier: disruption of tight junctions, sonoporation of the vascular endothelial cells and upregulation of transcytosis. Adapted from Timbie et al. (2015). Reproduced with permission.

mechanical effect leads to the disruption of tight junctions of endothelial cells in the focal region. This disruption then allows systemically-administered therapeutics that are normally obstructed by the BBB to enter the FUS-targeted brain region (Konofagou, 2012). Magnetic resonance image-guidance allows for confirmation of enhanced permeability of the BBB at the desired target as well as monitoring of heating *via* magnetic resonance thermometry (**Figure 3**; Mead et al., 2017). FUS also has the benefit of being minimally invasive in comparison to alternative technologies used to treat CNS disorders. Indeed, both convection-enhanced delivery and deep brain stimulation require invasive interventions. While intranasal administration can noninvasively bypass the BBB, it has limited capacity to selectively target brain regions, is limited by the dosage volume that can be administered, and is difficult to obtain proper alignment in the nasal cavity for effective delivery (Agrawal et al., 2018; Gänger and Schindowski, 2018). Chemical agents (e.g. Cereport and Regadenoson) that modulate tight junctions between endothelial cells have also been proposed. However, these drugs do not provide selective BBB opening and have not yet proven to be highly effective in clinical trials (Prados et al., 2003; Jackson et al., 2017; Jackson et al., 2018).

Transpassing the blood–brain barrier alone, however, may not always be sufficient for efficacious therapeutic treatment. The brain parenchyma contains extracellular matrix components that form a dense, mesh-like structure which further hinders dissemination of therapeutic agents within a target brain tissue (Mastorakos et al., 2015). To overcome this additional hurdle, nanoparticles with strategic surface modifications can allow a therapeutic agent to diffuse throughout the desired brain region (Kenny et al., 2013; Saraiva et al., 2016). There are countless nanoparticle formulations,

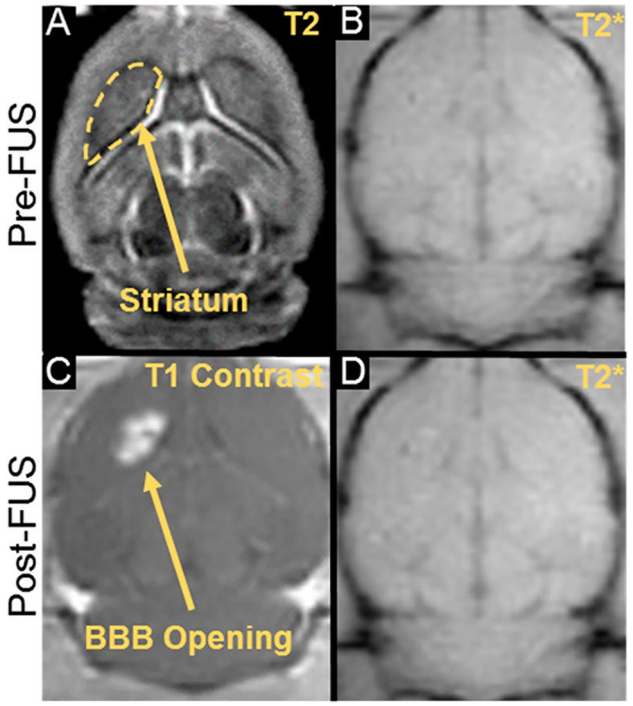

FIGURE 3 | MR imaging for guidance, confirmation, and safety evaluation of FUS treatments. **(A)** Pre- treatment planning using T2 pre-FUS images. **(C)** BBB opening in the striatum as confirmed by post-FUS contrast-enhanced T1 imaging. **(B, D)** Treatment safety may be assessed by comparing pre- and post-FUS T2* images. Adapted from Mead et al. (2017). Reproduced with permission.

but in general they consist of a core region wherein a polymer or lipid material encapsulates or presents on its surface the therapeutic agent. The core region is then typically coated with a non-adhesive molecule (commonly polyethylene glycol) and/or molecules intended to bind to specific molecular targets. Such nanoparticle coatings may allow them to more effectively diffuse through a larger volume of brain parenchyma and/or enable them to more precisely bind to specific molecular targets (Suk et al., 2016). Moreover, nanoparticles may be designed to tailor the pharmacokinetics of the loaded drug by improving the therapeutic window, increasing selectivity of dispensation, and/or improving temporal control (Kolhar et al., 2013; Timbie et al., 2017; Zhong et al., 2019).

In this review, recent advances in the use of FUS and nanoparticle design for delivery to the brain are discussed. We begin by reviewing polymers and lipid-based compositions that are commonly used in fabricating non-viral nanoparticles and then follow with discussions of how such nanoparticles are being used in combination with focused ultrasound for therapy, diagnosis, and assessments of function. Emerging developments and prospective areas for research are also explored. We affirm that the combination of FUS and nanoparticles offers promising treatment and detection options for a host of CNS disorders as well as functional study of the brain.

POLYMER AND LIPID-BASED NANOPARTICLES FOR DELIVERY TO THE CNS WITH FUS

Polymer Components of Nanoparticles for Delivery to the CNS With FUS

Polyethylene Glycol (PEG)

The ability of a nanoparticle to escape detection by immune cells increases its ability to reach the intended target tissue and accumulate there. Nanoparticles may be extracted from the circulation after intravenous administration *via* the reticuloendothelial system. Several proteins are known to bind to nanoparticles (e.g. albumin, immunoglobulin G, apolipoproteins, fibrinogen), which can further hinder the ability of a nanoparticle to reach its target tissue (Soppimath et al., 2001; Aggarwal et al., 2009). To decrease protein adsorption, and thus avoid recognition by the immune system, polyethylene glycol (PEG) is often conjugated to the surface of nanoparticles. Dense coatings of this hydrophilic and flexible molecule can sterically hinder proteins from adsorbing to the surface (Vasir and Labhasetwar, 2007; De Jong, 2008; Aggarwal et al., 2009; Spicer et al., 2018). PEGylation can mask the underlying properties of the nanoparticle core surface, effectively increasing its biocompatibility and half-life (Owens and Peppas, 2006). This being said, there have also been indications that repeated injection of PEGylated nanoparticles can elicit an immune response that leads to accelerated blood clearance of these nanoparticles (Dams et al., 2000). Nevertheless, applying a dense PEG coat to nanoparticles has shown to be effective in producing biocompatible brain-penetrating nanoparticles upon FUS application without producing any significant signs of toxicity (Mastorakos et al., 2015; Mead et al., 2016; Suk et al., 2016; Mead et al., 2017) (**Figure 4**). Further, increased PEGylation yields increased distribution within the target tissue (Mastorakos et al., 2015; Suk et al., 2016; Negron et al., 2019). For example, increasing the PEG density beyond conventional PEGylation ratios when designing PEGylated polyethylenimine (PEI) nanoparticles (i.e. PEG : PEI molar ratio of 26 rather than 8) showed higher brain distribution and gene transfection after injection of reporter gene-loaded PEG-PEI nanoparticles into the striatum of healthy rat brains (Mastorakos et al., 2015). Incorporating PEGylated nanoparticles with FUS allows widespread drug delivery within target brain regions (Nance et al., 2014; Mead et al., 2016; Suk et al., 2016).

Poly(Lactic-co-Glycolic Acid) (PLGA)

Poly(lactic-co-glycolic acid) (PLGA) is one of the more widely used core materials for generating biodegradable nanoparticles (Danhier et al., 2012; Panyam et al., 2002). Its constituents—lactic acid and glycolic acid—are readily metabolized, and PLGA has approval for several medical applications by both the Food and Drug Administration and the European Medicine Agency (Danhier et al., 2012). PLGA nanoparticles infiltrate cells within minutes of exposure *in vitro* and are capable of being both phagocytosed and inducing endolysosomal release (Panyam et al., 2002). If introduced to the circulation alone, the

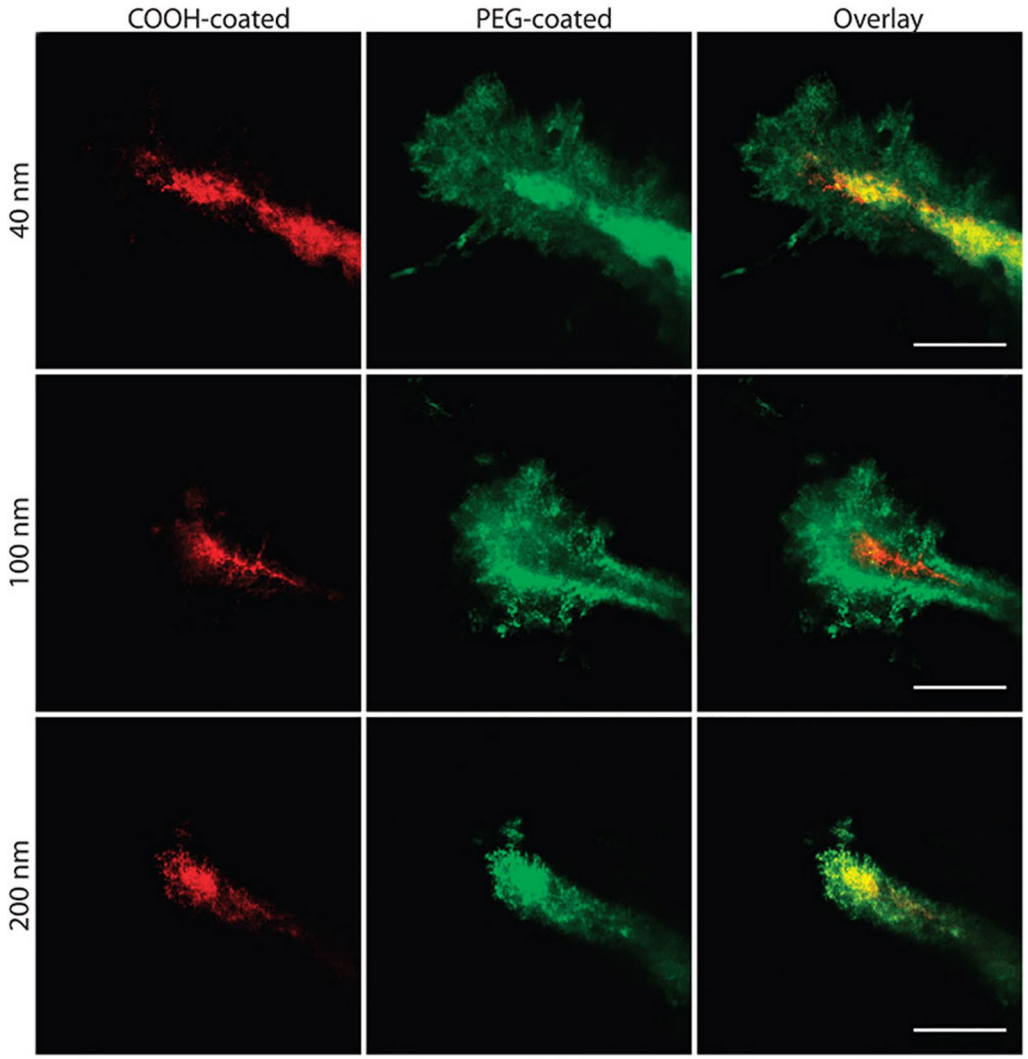

FIGURE 4 | Nanoparticle penetration into mouse brain tissue *in vivo*. Direct comparison of the distribution of fluorescent nanoparticles of similar sizes with different surface coatings after intracranial co-injection into mice. Images were acquired 60 min after injection. Scale bars = 50 μm. Adapted from Nance et al. (2012). Reproduced with permission.

hydrophobicity of PLGA triggers the reticuloendothelial system to clear these particles from the blood stream (Owens and Peppas, 2006). Commonly, PEG is conjugated to PLGA nanoparticles to mask their hydrophobicity and prevent plasma protein binding, as described above. PEGylation also helps conceal the natural negative charge of PLGA particles for enhanced uptake of the nanoparticles in *in vivo* conditions wherein a negative charge can cause undesirable protein interactions (Danhier et al., 2012). PLGA nanoparticles are conducive to various surface modifications and drug-loadings allowing successful implementation in a host of applications. These include cancers, inflammation, and CNS diseases (Danhier et al., 2012). Despite successful implementation, PLGA nanoparticles suffer from low drug loading and high drug burst release, which can greatly limit the amount of drug reaching the target tissue in an already difficult treatment site like the brain (Danhier et al., 2012). Nance et al. demonstrated that FUS-mediated BBB opening allowed delivery of PLGA-PEG particles to the brain within the focal region (Nance et al., 2014), indicating that FUS-mediated BBB opening may be leveraged to increase the probability that efficacious dosage levels of PLGA nanoparticles are met.

Poly(Aspartic Acid) (PAA)

Though less commonly used, poly(aspartic acid) (PAA) nanoparticles are biodegradable nanocomplexes that offer higher drug-loading capacity. These nanoparticles have displayed the capacity to act as safe and efficient carriers for gene delivery (Nie et al., 2015; Song et al., 2015), as well as for drug delivery (Zhang et al., 2017). For example, using convection enhanced-delivery, an administration method which directly injects a substance into the brain, it has been demonstrated that PAA-PEG nanoparticles loaded with the

chemotherapeutic cisplatin were able to diffuse through the brain parenchyma and increase survival time of rats with glioblastoma (Zhang et al., 2017). In another study, FUS administration drastically augmented delivery of polymer nanoparticles with a comparable PEG coating in two glioma models (Timbie et al., 2017) (**Figure 5**). After validating the ability of FUS to enhance nanoparticle delivery to brain tumors, the drug-loaded PAA-PEG nanoparticles were combined with FUS-mediated BBB opening to yield a markedly enhanced distribution of these PAA-PEG nanoparticles and a decrease in tumor growth (Timbie et al., 2017). Additionally, in this study Timbie et al. found that tumors treated with the cisplatin-loaded PAA-PEG nanoparticles and FUS displayed reduced invasiveness into surrounding tissue, suggesting this treatment may also inhibit glioma recurrence. These studies highlight the capability of PAA nanoparticles to be used in conjunction with FUS to deliver drugs and gene therapies to the brain, and this remains a rich avenue for therapeutic development in the future.

Polyethylenimine (PEI)

Developing nanoparticles for effective gene therapy as an alternative to viral vectors is an expanding area of research. Polyethylenimine (PEI) is a nanoparticle material commonly used for gene delivery (Lungwitz et al., 2005; Pandey and Sawant, 2016). Composed of many amine groups, PEI can bind compactly with DNA, and its free nitrogens are able to absorb protons within the acidic endosomal environment upon nanoparticle uptake (Behr, 1994; Kircheis et al., 2001). This proton absorption both mediates the disruption of the endosome and delays lysosomal fusion to the endosome (Godbey et al., 1999; Jere et al., 2009). Additionally, PEI facilitates transport

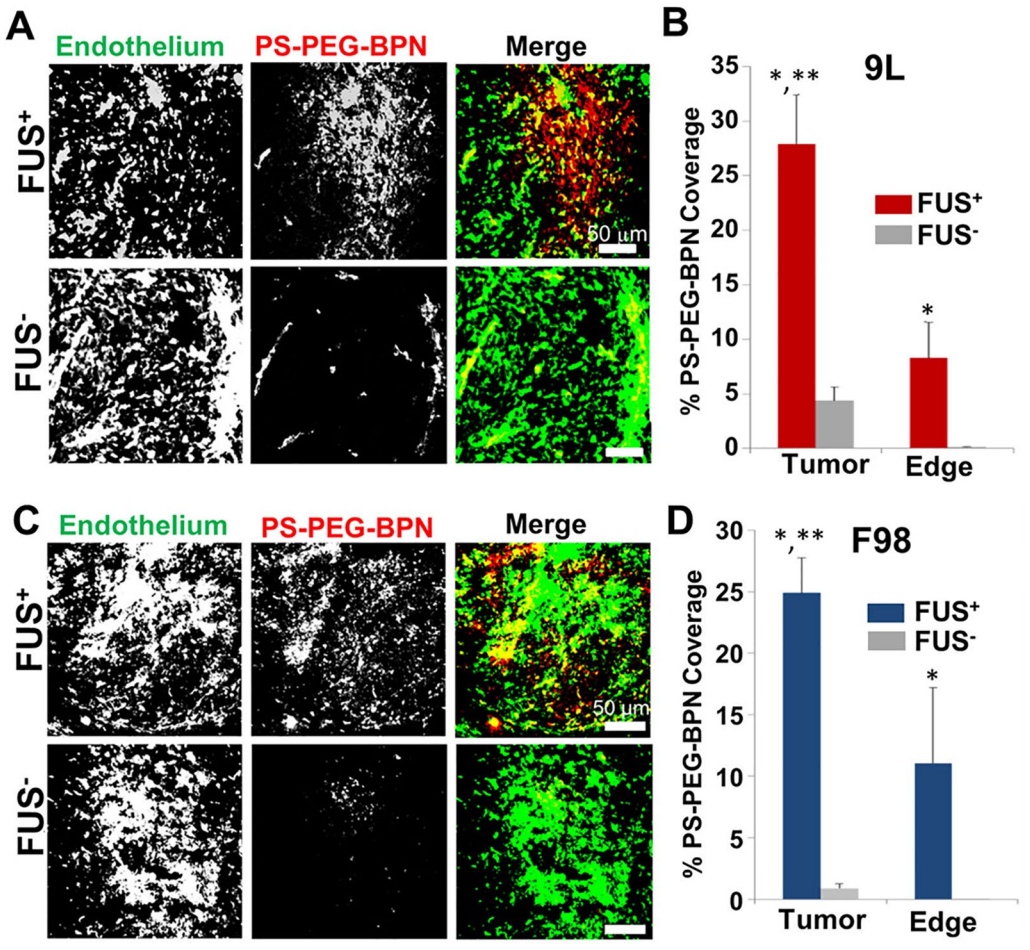

FIGURE 5 | MR image-guided FUS markedly enhances the delivery of 60 nm fluorescent tracer nnaoparticles (PS-PEG-BPN) across the blood-tumor (BTB) and blood–brain barriers (BBB) in 9L and F98 tumors in rats. **(A)** Representative confocal microscopic images of 9L tumor cross-sections from FUS treated (FUS+) and untreated (FUS–) rats. PS-PEG-BPN (red) are shown in relation to tumor endothelium (green). **(B)** Bar graph of PS-PEG-BPN delivery to 9L tumors and tumor edge regions. N = 6 per group. *P < 0.05 vs. FUS– in same region. **P < 0.05 vs. FUS+ in Edge region. **(C)** Representative confocal microscopic images of F98 tumor cross-sections from FUS treated (FUS+) and untreated (FUS–) rats. PS-PEG-BPN (red) are shown in relation to tumor endothelium (green). **(D)** Bar graph of PS-PEG-BPN delivery to F98 tumors and tumor edge regions. N = 4 per group. *P < 0.05 vs. FUS– in same region. **P < 0.05 vs. FUS+ in Edge region. Adapted from Timbie et al. (2017). Reproduced with permission.

into cell nuclei, mediating expression of the encapsulated gene (Godbey et al., 1999; Huang et al., 2010). Though often considered the gold standard of nanoparticle materials for gene transfection, PEI can demonstrate cytotoxicity (Godbey et al., 2001; Ira et al., 2003; Moghimi et al., 2005). However, when densely coated with PEG, PEI nanoparticles do not exhibit significant toxic effects to cells (Huang et al., 2010; Mastorakos et al., 2015; Mead et al., 2017). When administered *in vivo via* convection enhanced delivery, PEGylated PEI nanovectors carrying a reporter gene were able to transfect both healthy rat brain tissue and gliomas (Negron et al., 2019). Increased PEGylation resulted in a larger volume of transgene expression and greater percentage of the tumor volume. These PEGylated PEI nanoparticles also proved efficient for gene transfection when used with FUS to deliver a neurotrophic factor to the striatum of Parkinsonian rats (Mead et al., 2017). These studies bolster PEGylated PEI nanoparticles as a promising tool for FUS-mediated gene therapy in the CNS.

Poly(B-Amino Ester) (PBAE)

One biodegradable polymer that has received considerable recent interest as a nanoparticle component is poly(β-amino esters) (PBAE). Indeed, PBAE-based nanocomplexes have shown effective drug delivery in *in vitro* systems and are beginning to show promise *in vivo* (Green and Kim, 2019; Guerrero-Cázares et al., 2014; Mangraviti et al., 2015; Mastorakos et al., 2017). The potential for this nanoparticle was highlighted when its pH-sensitive solubility properties were utilized to release chemotherapeutics once in the decreased-pH endolysosomal environment (Shenoy et al., 2005). PBAE nanoparticles have now been used in the targeting of *in vivo* glioblastoma primary brain tumors. Using convection-enhanced delivery, it has been shown that DNA-loaded PBAE nanoparticles provide effective gene transfection of brain tumors in rats (Mastorakos et al., 2017). We affirm that the ability to combine PBAE nanoparticles with FUS delivery will greatly improve their ability to be used in more therapeutic applications and reduce the invasiveness of their administration. Moreover, PBAE particles have been shown to be robust. They have the capacity to be lyophilized and stored for up to two years and still display effective delivery to glioblastoma cells (Guerrero-Cázares et al., 2014). Going forward, one challenge in the design for FUS-compatible PBAE nanoparticles is making formulations that are stable in the bloodstream.

Lipid-Based Nanoparticles for Delivery to the CNS With FUS

Liposomes

Liposomes have also been explored for brain-targeted drug delivery in conjunction with FUS-induced BBB opening (Treat et al., 2012; Yang et al., 2012). The main constituents of liposomes are amphiphilic phospholipids that form concentric bilayers (Puri et al., 2009). The aqueous core of the liposome can be loaded with hydrophilic or polar molecules, whereas the fatty acyl chains of the liposome bilayer can store hydrophobic molecules. The phospholipids that compose the liposome determines stability, loading efficiency, and physical phase. Commonly, chemically modified phosphatidylcholines are the primary phospholipid within a liposome. Frequently used modifications include dipalmitoylphosphatidylcholine (DPPC), hydrogenated soybean phosphatidylcholine (HSPC), dimyristoylglycerophosphatidylcholine (DGPC), distearoylglycerophosphatidylcholine (DSPC), and dioleoylglycerophosphatidylcholine (DOPC) (Chang and Yeh, 2012). Similar to nanoparticles, liposomes benefit from PEGylation to evade the reticuloendothelial system and absorption of blood proteins. PEG is typically introduced into liposomes *via* PEGylated lipopolymers like PEG-distearoylglycerophosphoethanolamine (DSPE) (Schroeder et al., 2009). Additionally, cholesterol is often utilized in the liposome composition to stimulate dense packing of the surrounding phospholipids, which enhances the liposome's stability and decreases its permeability (Bozzuto and Molinari, 2015).

Liposome encapsulated drugs for brain delivery with FUS have been used with many drugs and for various applications (Treat et al., 2012; Yang et al., 2012; Lin et al., 2015; Lin et al., 2016; Zhao et al., 2018; Lin et al., 2019). In 2012, liposomal doxorubicin delivery to rat gliosarcoma following FUS-mediated BBB opening was investigated (Treat et al., 2012). Weekly examination of tumor growth *via* magnetic resonance imaging indicated that the combination therapy group of liposomal doxorubicin with FUS-mediated BBB opening slowed tumor growth compared to liposomal doxorubicin or FUS only groups. Further, the combination group also had a 24% increase in survival time over the nontreated group. More recently, liposomal glial-derived neurotrophic factor (GDNF) and FUS-induced BBB opening were used for treatment in a mouse model of Huntington's disease (Lin et al., 2019). Mice were treated with either liposomal GDNF, BBB opening *via* FUS, or the combination of the two on a weekly basis for a total of 9 weeks and motor function was assessed during this time. Six weeks following the last treatment, mice were sacrificed, and brains were assessed for GDNF expression, protein aggregates, apoptosis, and downstream targets of GDNF. The combination of FUS-induced BBB opening and liposomal GDNF resulted in improved motor function compared to either treatment alone. Mice receiving the combination therapy had higher levels of GDNF expression, decreased protein aggregates and cell death, and increased neuron growth. These studies indicate the utility of FUS for greatly improving the therapeutic effects of drugs for brain-based delivery when encapsulated in liposomes.

Nanoemulsions/Nanodroplets

Phase-changing nanoemulsions or nanodroplets have recently gained interest for use with FUS to control spatial and temporal delivery of therapeutics within the brain (Chen et al., 2013; Wu et al., 2018; Yildirim et al., 2019). While these nanoparticles can be comprised of lipids or polymer shells, they have historically been encased *via* lipid-based bilayers (Yildirim et al., 2019). When administered, these nanoemulsions are composed of a lipid or polymer surface that encapsulates a liquid core and the therapeutic agent. Upon exposure to the FUS pressure waves, the liquid core transitions to gas. This expansion can eject and release the drug from the nanoemulsion at the focal site as well as be utilized to produce on-demand microbubbles. Nanoemulsions can be tricky to design, however, as instability for storage purposes and liquid-to-gas transition upon injection

are common challenges for these particles (Rapoport et al., 2011). Careful considerations for boiling point of the nanoemulsion core, emulsifying agent, and needle gauge can help overcome some of these issues (Airan et al., 2017; Gorick et al., 2019).

One group indicated the feasibility of these particles for use with FUS to deliver molecules to the brain by targeting mouse hippocampus with dextran-loaded nanodroplets (Chen et al., 2013). Delivery with nanodroplets resulted in a more uniform delivery of dextran throughout the hippocampus when compared to microbubbles of the same lipid composition. This group later examined different liquid cores to optimize the delivery of molecules to the brain with FUS (Wu et al., 2018). Octafluoropropane and decafluorobutane-based nanodroplets were assessed for their vaporization efficiency and their ability to deliver dextran to mouse hippocampus. Octafluoropropane was found to have a greater vaporization efficiency, which lead to increased delivery of dextran to the brain under FUS application. Nanoemulsions offer an exciting new method to encapsulate molecules for brain-targeted delivery that can aid in temporal control in addition to the spatial control of FUS-mediated BBB opening.

Conjugated NP and Microbubbles

Up to this point, the nanoparticles discussed have been assumed to be injected separately from the microbubbles (i.e. nanoparticles unbound to microbubbles) upon application for drug delivery with FUS. Conjugating nanoparticles onto microbubbles has been explored as an option to increase delivery efficiency of the encapsulated agent. Nanoparticles can be bound to microbubbles *via* biotin/avidin interactions or—more commonly for *in vivo* studies—maleimide/thiol linkage (Mullin et al., 2013). Attachment of nanoparticles to microbubbles allows validation of nanoparticles' presence at the site of BBB opening. Further, conjugation of nanoparticles to microbubbles enhances drug delivery by increasing cavitation near the nanoparticle (Schroeder et al., 2009). For the treatment of rat glioma, one group loaded liposomes with shRNA for targeting neovascular cells and conjugated these nanoparticles onto lipid-shelled microbubbles (Zhao et al., 2018). Rats receiving treatment of FUS and nanoparticle-microbubble complexes displayed decreased tumor growth and increased survival time than controls or individual (i.e. FUS or nanoparticle-microbubble complex only) treatment groups. Conjugated nanoparticle-microbubble complexes when combined with FUS-mediated BBB opening is a promising strategy for further increasing delivery efficiency in the CNS.

APPLICATIONS OF NANOPARTICLES IN COMBINATION WITH FOCUSED ULTRASOUND FOR THE TREATMENT OF CNS PATHOLOGIES

The use of nanoparticles for treating diseases has been investigated at the pre-clinical level for many years now. Recent developments in the use of FUS for safely opening the BBB have exposed new opportunities for nanoparticles in the treatment of neurological disorders. The following section discusses emerging developments of FUS-mediated nanoparticle delivery to the brain that have centered on designs allowing gene transfer, molecular targeting, and temporal control.

Gene Therapy to the CNS With FUS

Gene therapy has gained considerable traction as a treatment option for many disorders, those of the CNS being no exception (Ojala et al., 2015; Keeler et al., 2017; Piguet et al., 2017; Price et al., 2019). Design for gene delivery vectors must balance between lowering cytotoxicity and increasing transfection efficiency. While viral vectors have often been the choice gene carrier, concerns remain about their loading capacity, safety, and production scalability (Thomas et al., 2003; Xu and Anchordoquy, 2011). Thus, non-viral vectors represent attractive alternatives for many applications, though they are not lacking in limitations of their own: decreased transfection efficiency, electrostatic interactions, and aggregation (Thomas et al., 2003; Mansouri et al., 2004; David and Doherty, 2017). Nanoparticles, many derived from formulations described above, have been coupled with FUS to deliver genes as a therapeutic treatment for neurological disorders (Suzuki et al., 2011; Timbie et al., 2015).

In 2014, Nance et al. were amongst the first to characterize the ability of FUS to deliver systemically-administered polymer nanoparticles to magnetic resonance image-targeted brain regions (Nance et al., 2014). Using simple fluorescent polystyrene (PS)-PEG tracer nanoparticles, the authors characterized the effect of nanoparticle size on diffusion within *ex vivo* and *in vivo* rat brains. Compared to 110 nm and 240 nm particles sizes, 60 nm particles had the least hindered transport rate. When systemically injected and delivered across the BBB with FUS, these 60 nm PS-PEG nanoparticles penetrated the brain parenchyma, and their coverage increased with increasing FUS pressures. Additionally, they validated that this FUS-mediated delivery to targeted brain regions could be extended to a 75 nm, biodegradable PLGA-PEG nanoparticle.

Moving this work into gene therapy, Mead et al. used highly compacted (56 nm) PEI-PEG nanoparticles to transport a luciferase reporter gene under a β-actin promoter to rat striatum (Mead et al., 2016). After FUS-mediated BBB disruption and systemic injection of the gene-loaded nanoparticles, bioluminescence—indicating transfection of the luciferase reporter gene—was visible only within the focal region targets and persisted for at least 28 days as detected by *ex vivo* bioluminescence (**Figure 6**). Of note, bioluminescent signal could be detected within a day with these non-viral vectors in contrast to longer delays that may be seen with some viral vectors (Miao et al., 1998).

Implementing these findings to CNS disorders, the same group successfully used this FUS-mediated gene therapy delivery system to reverse Parkinsonian behavioral and molecular deficits in a neurotoxin-induced, rat model of Parkinson's disease (Mead et al., 2017). PEI-PEG nanoparticles carrying a plasmid for GDNF were intravenously injected, and

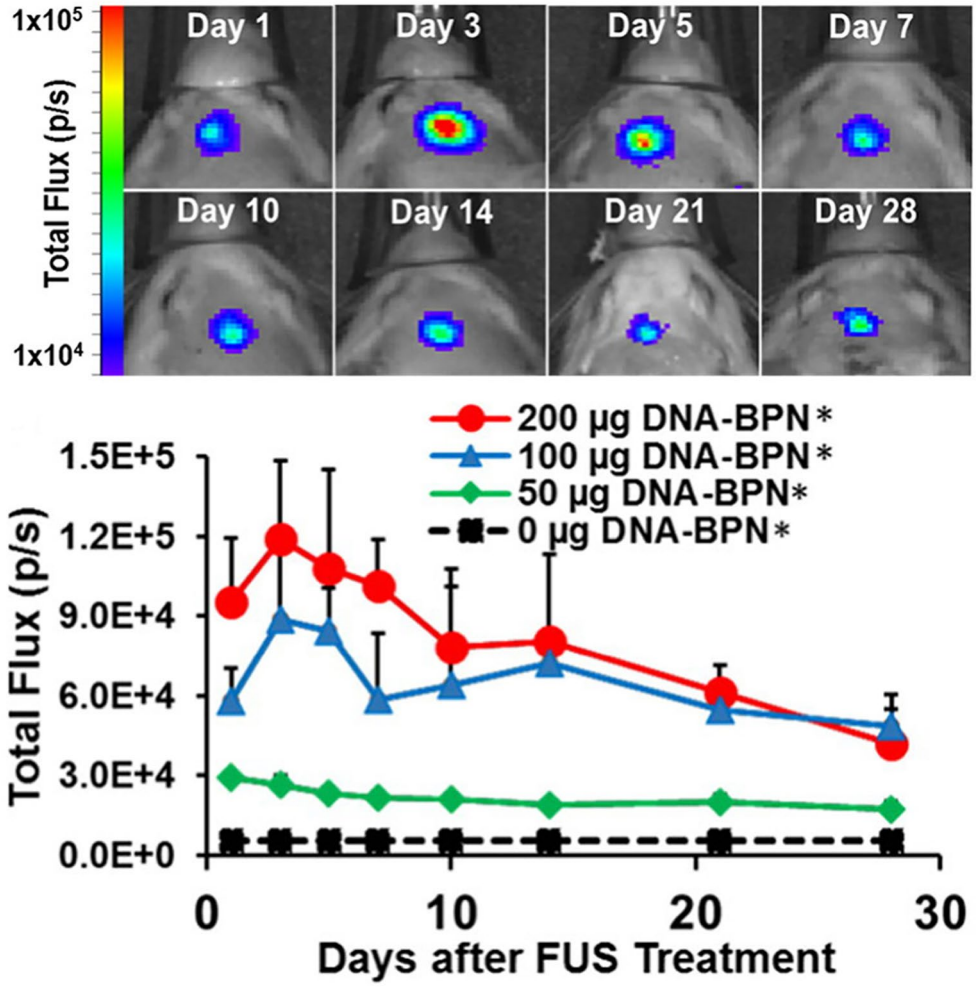

FIGURE 6 | FUS-mediated delivery of reporter gene-bearing non-vial nanoparticles (DNA-BPN) across the BBB leads to robust and localized transgene expression in the rat brain. Top: Representative IVIS bioluminescence images after DNA-BPN delivery to rat brain using FUS and MBs. Bottom: Line graph of bioluminescence total flux over the 28-day test period. n = 5 at each dose. *Significantly different than all other doses tested ($p < 0.05$). Adapted from Mead et al. (2016). Reproduced with permission.

FUS was applied to the neurotoxin-induced lesion of the left striatum. Twelve weeks following GDNF delivery, both striatal GDNF and dopamine levels were significantly elevated in the treated striatum compared to those of the neurotoxin-only control rats. Beginning at week 4 and extending until at least week 12, behavioral deficits were also rescued in the FUS and GDNF-treated rats as measured by the apomorphine-induced rotational bias and forepaw use bias behavioral tests (**Figure 7**). These results indicate that FUS-mediated BBB opening is an auspicious method in the application of gene therapy for the treatment of neurological disorders.

Similarly, another group demonstrated the ability to use a PEGylated liposome of DPPC/cholesterol composition to encapsulate either luciferase reporter gene or GDNF. They then used FUS to deliver this therapeutic liposome into the right hemispheres of healthy mice (Lin et al., 2015). Luciferase expression was maintained for at least 4 days following FUS treatment and was significantly higher than non-encapsulated luciferase. Additionally, the authors found that gene expression was dose dependent; however, the day of peak expression differed for the different doses. FUS-induced BBB opening and delivery of liposomal GDNF plasmid was able to increase GDNF expression over control group, whereas liposomal GDNF plasmid administration did not. These studies indicate the promise of gene delivery through a variety of nanoparticle formulations in CNS disorders, further potentiated by the ability to overcome the BBB noninvasively with FUS-mediated delivery (Price et al., 2019).

Molecular Control of Drug Delivery to the CNS With FUS

The capacity to use FUS to selectively administer a therapeutic agent to a specified brain region in itself creates promising

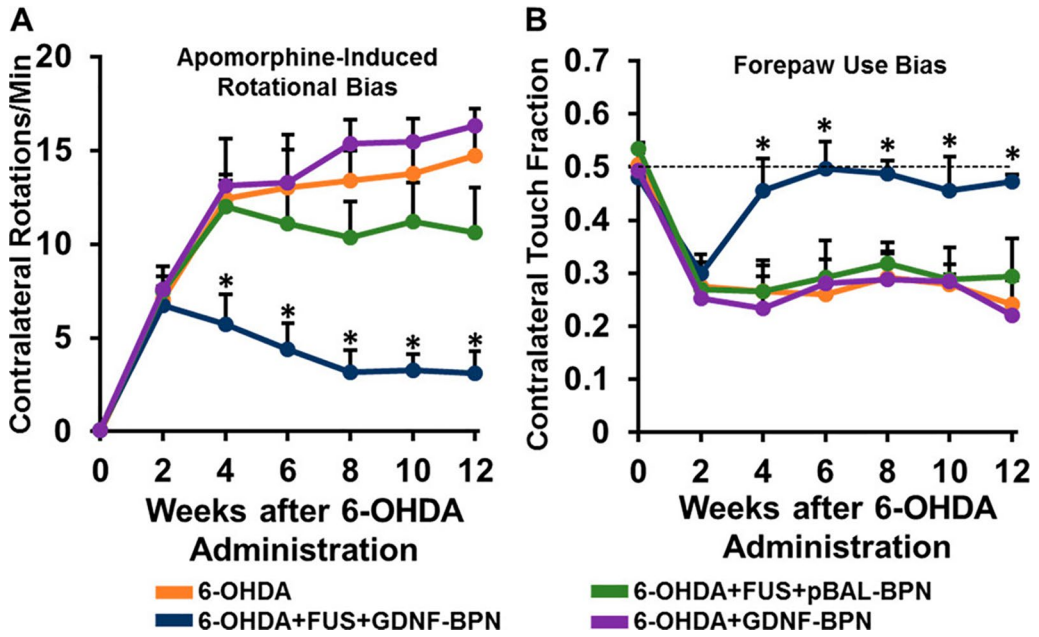

FIGURE 7 | Delivery of glial cell-derived neurotrophic factor gene-bearing nanoparticles (GDNF-BPN) with FUS restores locomotor function in PD rats. **(A)** Line graph of average contralateral rotations per minute after apomorphine administration. **(B)** Line graph of contralateral touch fraction in the forepaw use bias test. n > 14 in each group at weeks 0 through 6; n > 7 in each group at weeks 8 through 12. *Significantly different than all other groups at the same time point ($p < 0.01$).Adapted from Mead et al. (2017). Reproduced with permission.

therapeutic opportunities never before available. To go beyond the spatial targeting that FUS allows, applying this system with nanoparticles that have receptor-specific ligands conjugated to their surface can allow molecular targeting within a defined region. This combination opens the door for treatments that require targeting of particular receptors but only in a specific brain region.

Luo et al. took advantage of the fusion of FUS-mediated BBB opening and molecular-targeting nanoparticles to treat glioblastoma. Both the endothelial cells lining the BBB and glioblastoma cells are abundant in lipoprotein receptor-related protein, which binds the ligand angiopep-2 (Luo et al., 2017). Angiopep-2-conjugated PLGA nanoparticles were designed to release encapsulated doxorubicin and perfluorooctyl bromide upon FUS exposure. PLGA nanoparticles with angiopep-2 surface modifications specifically accumulated in glioblastoma cells at more than 13-fold higher than the same nanoparticle without angiopep-2 conjugation. Another group compared the ability of liposomal doxorubicin and angiopep-1-conjugated liposomal doxorubicin to target and accumulate in murine glioblastoma when combined with FUS-mediated BBB opening (Yang et al., 2012). They found that FUS+peptide-conjugated liposomes had a significantly higher uptake in the brain tumors than FUS+non-targeted liposomes, and both groups had a higher uptake than either liposome without FUS-induced BBB disruption. These results of increased targeting of glioblastoma cells highlights the utility of combining FUS with molecular-targeting nanoparticles in the CNS. Moreover, in many diseases of the brain there are molecular targets unique to the disease that could be utilized in nanoparticle fabrication. For Alzheimer's disease, nanoparticles have already been designed to target amyloid beta aggregates (Song et al., 2016). Combining molecular delivery of molecular-targeting nanoparticles following FUS-mediated BBB opening could hold potential for greatly improving drug delivery to CNS disease targets.

Temporal Control of Drug Delivery to the CNS With FUS

In addition to molecular targeting, nanoparticles can also be designed to be responsive to pressure or temperature changes. Using FUS to "trigger" the release of drugs from these nanoparticles adds a new mechanism of temporal control to this drug delivery system. As discussed previously, one unique category of pressure-sensitive nanoparticles that have been used with FUS for brain-targeted delivery are nanoemulsions. In application, these nanoemulsions provide a temporal mechanism for drug delivery with release only occurring throughout the duration of FUS. FUS-activated nanoemulsions loaded with Propofol are a noteworthy example (Airan et al., 2017) (**Figure 8**). While the drug Propofol is already capable of bypassing the BBB, normal systemic administration of the anesthetic does not allow for spatial targeting within a certain region of the brain, leading to a dysregulated, anesthetic effect. FUS in this application was not used to open the BBB but rather to trigger drug release at the desired brain region. After inducing convulsions in a rat seizure model, FUS was applied to release Propofol to a select brain region in both hemispheres. As validated *via* electroencephalogram, FUS-mediated, targeted Propofol release suppressed seizures in these rats. This application is particularly promising in the case of neuromodulation. While repeated BBB opening with FUS will be clinically acceptable in the setting of

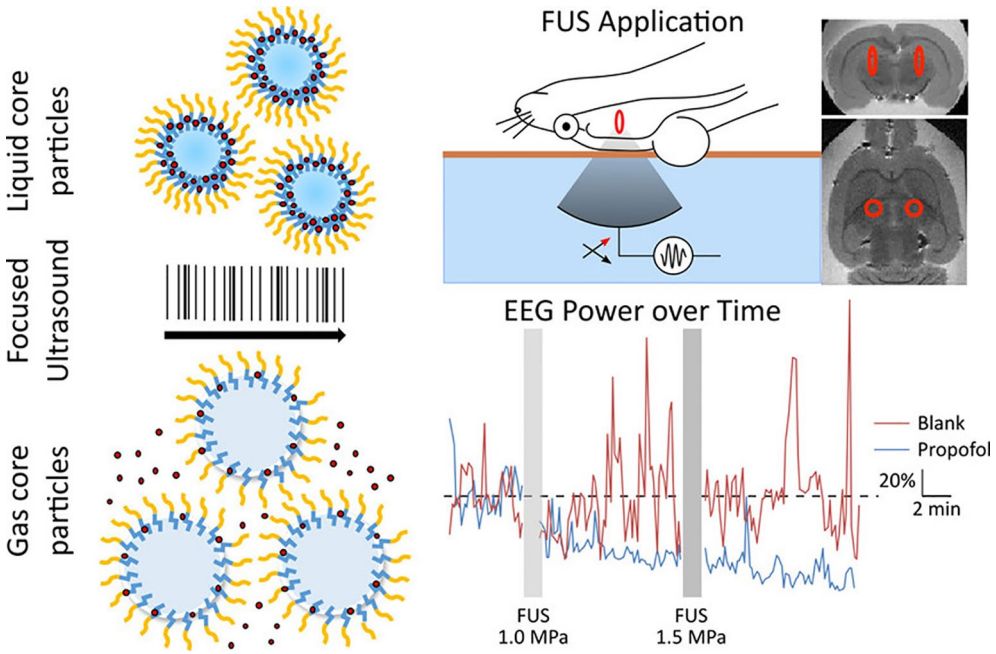

FIGURE 8 | Liquid nanoparticles composed of biodegradable and biocompatible components and containing propofol release the drug upon exposure to focused ultrasound. The uncaged propofol was shown to silence seizures in an acute rat seizure model. Adapted from Airan et al. (2017). https://pubs.acs.org/doi/abs/10.1021/acs.nanolett.6b03517. Reproduced with permission. Further permissions related to this figure should be directed to the American Chemical Society (ACS).

many debilitating CNS diseases, it will likely be contraindicated for others. These low-intensity, nanoemulsion activation approaches may be especially useful in such applications. Further, in the case of psychiatric disorders, many drugs have already been developed that are capable of bypassing the BBB but require localized administration to increase their efficacy and reduce side effects. These FUS-activated nanoemulsions have demonstrated the capability of encapsulating other hydrophobic drugs which gives promise to the extension of this application with other psychiatric medications (Zhong et al., 2019).

Another emerging, pressure-sensitive nanoparticle is gas vesicles. Gas vesicles are derived from photosynthetic microbes that produce these gas-filled nanostructures to change their buoyancy for optimal light exposure (Lu et al., 2018). By responding to magnetic fields dissimilarly than water, these gas vesicles can act as magnetic resonance image contrast agents. Using FUS, gas vesicles can then be collapsed to produce background images that can be subtracted from the intact gas vesicle images. This background image subtraction enhances the signal-to-noise ratio, which is especially helpful in scenarios with confounding background signals, such as is the case with some tumors. Because these are biologically produced nanostructures, gas vesicles can be genetically modified to respond to different pressures. This feature allows for the construction of multiplexed magnetic resonance images. In bacterial hosts, gas vesicles can be expressed under inducible promoters. Extension of this inducible expression into mammalian hosts holds exciting promise for capturing changes in molecular states or cellular responses *via* non-invasive magnetic resonance imaging.

The ability of FUS to be applied and specifically heat tissue allows another application of nanoparticle design: thermosensitive nanocomplexes. Magnetic resonance image-guidance, in addition to providing precise targeting, lends access to monitoring changes in temperature to the tissue—a technique known as magnetic resonance-thermometry. Nanoparticles that are sensitive to these heat changes allow drug release to occur once the target temperature is reached. In the case of tumor treatments, thermosensitive nanoparticles are particularly desirable as tumor ablation can be paired with drug release. In one study, treatment with thermosensitive liposomes that encapsulated the chemotherapeutic doxorubicin prior to tumor ablation delayed tumor growth to a greater extent than either treatment alone (Hijnen et al., 2017). Another study indicated that PEG-coated liposomal encapsulation of doxorubicin combined with FUS-induced hyperthermia successfully constrained tumor growth in a murine brain metastasis model following just a single treatment (Wu et al., 2014).

DIAGNOSTIC AND FUNCTIONAL TESTING APPLICATIONS OF NANOPARTICLES AND FUS

The use of FUS with nanoparticles for the treatment of CNS disorders is exciting and propitious for the development of new therapeutic options in this challenging field. Nevertheless, the noninvasive nature of this technology also holds great potential

for its applications where only minimal perturbation of a subject is warranted. Aside from therapeutic applications of FUS and nanoparticles, this combination can also be implemented for disease screenings and functional studies of the brain.

Detection and Diagnosis

With few standard screening processes in place currently, detection of neurodegenerative diseases is sorely needed (Visser et al., 2008; Panegyres et al., 2016). Reliant on the onset of their symptoms for diagnoses, these CNS diseases are often too far progressed to have effective treatment options. Similar to imposing surface modifications for specific drug release, molecular-targeting nanoparticles can also be leveraged to detect or enhance imaging of disease markers. The capability to fabricate nanoparticles that target disease markers and to utilize FUS to deliver them to the CNS is emergent. Using FUS to deliver antibodies across the BBB has been demonstrated several times, indicating the possibility to allow antibody-conjugated nanoparticles to bypass the BBB for detection of CNS disease markers (Sheikov et al., 2004; Kinoshita et al., 2006; Aryal et al., 2014). In the case of Parkinson's disease, Alzheimer's disease, and Huntington's disease, the ability to detect early aggregation of their molecular signatures (alpha-synuclein, amyloid beta, and mutant huntingtin, respectively) could be a promising detection method (Manoutcharian et al., 2016).

Functional Studies

Our ability to develop novel and more effective treatments for CNS disorders relies upon a continued commitment of understanding normal brain function. To this end, the ability to use FUS and nanoparticles to noninvasively perturb brain activity is a promising, unmatched method to investigate the functional connectivity of the brain. Using FUS-activated nanoemulsions carrying Propofol, select rat brain regions were targeted for local Propofol release, and then positron emission tomography (PET) imaging was used to assess global changes in brain activity (Wang et al., 2018). As optogenetic modulation of the frontal cortex has been shown to modulate activity in the thalamus, researchers investigated if targeted release of Propofol to the thalamus could thus elicit functional changes to the frontal cortex. Indeed, frontal cortical activity changes were seen upon uncaging of Propofol in the thalamus. As the thalamus regulates many brain regions, unsurprisingly, many other brain regions also showed altered function after thalamus targeting. This study is particularly exciting for functional studies of the brain in alive, minimally-perturbed animal models. Additionally, the ability to use FUS for neuromodulation comes with the advantage of being able to target deep brain regions which is not possible with optogenetic techniques that require transmission of light for activation.

CONCLUSION

Despite many positive developments and significant pre-clinical progress, many debilitating CNS disorders still do not have cures. Further, in many cases, even symptomatic treatment options are limited. Combining non-viral nanoparticles that are capable of controlling pharmacokinetic mechanisms with FUS to spatially and noninvasively deliver therapeutics to the brain creates potentially powerful drug and gene delivery systems. Such combinations offer therapeutic options that are not possible with other technologies used for bypassing the BBB. Additionally, FDA-approved FUS systems for targeting of the brain already exist and are showing promising initial results for inducing BBB opening in clinical trials (Carpentier et al., 2016; Lipsman et al., 2018; Idbaih et al., 2019; Mainprize et al., 2019). Looking ahead, the capacity to administer biocompatible nanoparticles to mitigate otherwise toxic or adverse delivery of therapeutic agents with the additional advantage of controlling spatial, molecular, and temporal delivery of therapeutics to the brain noninvasively with FUS affirms the advantage of this combined approach for neurological treatments, detection, and functional studies.

AUTHOR CONTRIBUTIONS

Writing—Original Draft Preparation: DF. Writing—Review and Editing: DF and RP. Supervision: RP. Funding Acquisition: RP.

FUNDING

This work was supported by NIH R01NS111102, R01CA197111, and R01EB020147.

REFERENCES

Aggarwal, P., Hall, J. B., Mcleland, C. B., Dobrovolskaia, M. A., and Mcneil, S. E. (2009). Nanoparticle interaction with plasma proteins as it relates to particle biodistribution, biocompatibility and therapeutic efficacy. *Adv. Drug Deliv. Rev.* 61, 428–437. doi: 10.1016/j.addr.2009.03.009

Agrawal, M., Saraf, S., Saraf, S., Antimisiaris, S. G., Chougule, M. B., and Shoyele, S. A. (2018). Nose-to-brain drug delivery: an update on clinical challenges and progress towards approval of anti-Alzheimer drugs. *J. Control. Release* 281, 139–177. doi: 10.1016/j.jconrel.2018.05.011

Airan, R. D., Meyer, R. A., Ellens, N. P. K., Rhodes, K. R., Farahani, K., and Pomper, M. G. (2017). Noninvasive targeted transcranial neuromodulation via focused ultrasound gated drug release from nanoemulsions. *Nano Lett.* 17, 652–659. doi: 10.1021/acs.nanolett.6b03517

Aryal, M., Arvanitis, C. D., Alexander, P. M., and McDannold, N. (2014). Ultrasound-mediated blood-brain barrier disruption for targeted drug delivery in the central nervous system. *Adv. Drug Deliv. Rev.* 72, 94–109. doi: 10.1016/j.addr.2014.01.008

Behr, J. P. (1994). Gene transfer with synthetic cationic amphiphiles: prospects for gene therapy. *Bioconjug. Chem.* 5, 382–389. doi: 10.1021/bc00029a002

Bozzuto, G., and Molinari, A. (2015). Liposomes as nanomedical devices. *Int. J. Nanomedicine* 10, 975–999. doi: 10.2147/IJN.S68861

Carpentier, A., Canney, M., Vignot, A., Reina, V., Beccaria, K., and Horodyckid, C. (2016). Clinical trial of blood-brain barrier disruption by pulsed ultrasound. *Sci. Transl. Med.* 8, 343re2–343re2. doi: 10.1126/SCITRANSLMED.AAF6086

Chang, H.-I., and Yeh, M.-K. (2012). Clinical development of liposome-based drugs: formulation, characterization, and therapeutic efficacy. *Int. J. Nanomed.* 7, 49–60. doi: 10.2147/IJN.S26766

Chen, C. C., Sheeran, P. S., Wu, S. Y., Olumolade, O., Dayton, P. A., and Konofagou, E. E. (2013). Targeted drug delivery with focus ultrasound-induced blood-brain barrier opening Using acoustically-activated nanodroplets. *IEEE Int. Ultrason. Symp. IUS* 172, 615–618. doi: 10.1109/ULTSYM.2013.0159

Curley, C. T., Sheybani, N. D., Bullock, T. N., and Price, R. J. (2017). Focused ultrasound immunotherapy for central nervous system pathologies: challenges and opportunities. *Theranostics* 7, 3608–3623. doi: 10.7150/thno.21225

Dams, E. T. M., Laverman, P., Oyen, W. J. G., Storm, G., Scherphof, G. L., and Van Der Meer, J. W. M. (2000). Accelerated blood clearance and altered biodistribution of repeated injections of sterically stabilized liposomes. *J. Pharmacol. Exp. Ther.* 292, 1071–1079.

Danhier, F., Ansorena, E., Silva, J. M., Coco, R., Le Breton, A., and Préat, V. (2012). PLGA-based nanoparticles: an overview of biomedical applications. *J. Control. Release* 161, 505–522. doi: 10.1016/j.jconrel.2012.01.043

David, R. M., and Doherty, A. T. (2017). Viral vectors: the road to reducing genotoxicity. *Toxicol. Sci.* 155, 315–325. doi: 10.1093/toxsci/kfw220

De Jong, W. H. (2008). Drug delivery and nanoparticles : Applications and hazards. *Int. J. Nanomedicine* 3, 133–149. doi: 10.2147/IJN.S596

Gänger, S., and Schindowski, K. (2018). Tailoring formulations for intranasal nose-to-brain delivery: a review on architecture, physico-chemical characteristics and mucociliary clearance of the nasal olfactory mucosa. *Pharmaceutics* 10, 116. doi: 10.3390/pharmaceutics10030116

Godbey, W. T., Wu, K. K., and Mikos, A. G. (2001). Poly(ethylenimine)-mediated gene delivery affects endothelial cell function and viability. *Biomaterials* 22, 471–480.

Gorick, C. M., Chappell, J. C., and Price, R. J. (2019). Applications of ultrasound to stimulate therapeutic revascularization. *Int. J. Mol. Sci.* 20, 3081. doi: 10.3390/ijms20123081

Gorick, C. M., Sheybani, N. D., Curley, C. T., and Price, R. J. (2018). Listening in on the microbubble crowd: advanced acoustic monitoring for improved control of blood-brain barrier opening with focused ultrasound. *Theranostics* 8, 2988–2991. doi: 10.7150/thno.26025

Green, J. J., and Kim, Y. J. (2019). Biodegradable STING agonist nanoparticles for enhanced cancer immunotherapy. *Nanomedicine* 14, 237–246. doi: 10.1016/j.nano.2017.10.013.Biodegradable

Guerrero-Cázares, H., Tzeng, S. Y., Young, N. P., Abutaleb, A. O., Quiñones-Hinojosa, A., and Green, J. J. (2014). Biodegradable polymeric nanoparticles show high efficacy and specificity at DNA delivery to human glioblastoma in vitro and invivo. *ACS Nano* 8, 5141–5153. doi: 10.1021/nn501197v

Hijnen, N., Kneepkens, E., de Smet, M., Langereis, S., Heijman, E., and Grüll, H. (2017). Thermal combination therapies for local drug delivery by magnetic resonance-guided high-intensity focused ultrasound. *Proc. Natl. Acad. Sci.* 114, E4802–E4811. doi: 10.1073/pnas.1700790114

Idbaih, A., Canney, M., Belin, L., Desseaux, C., Vignot, A., and Bouchoux, G. (2019). Safety and feasibility of repeated and transient blood-brain barrier disruption by pulsed ultrasound in patients with recurrent glioblastoma. *Clin. Cancer Res.* 25, 3793–3801. doi: 10.1158/1078-0432.CCR-18-3643

Ira, Mély, Y., and Krishnamoorthy, G. (2003). DNA Vector polyethyleneimine affects cell pH and membrane potential: a time-resolved fluorescence microscopy study. *J. Fluoresc.* 13, 339–347. doi: 10.1023/A:1025381812568

Jackson, S., George, R. T., Lodge, M. A., Piotrowski, A., Wahl, R. L., and Gujar, S. K. (2017). The effect of regadenoson on the integrity of the human blood–brain barrier, a pilot study. *J. Neurooncol.* 132, 513–519. doi: 10.1007/s11060-017-2404-1

Jackson, S., Weingart, J., Nduom, E. K., Harfi, T. T., George, R. T., and McAreavey, D. (2018). The effect of an adenosine A2A agonist on intra-tumoral concentrations of temozolomide in patients with recurrent glioblastoma. *Fluids Barriers CNS* 15, 1–9. doi: 10.1186/s12987-017-0088-8

Jere, D., Jiang, H., Arote, R., Kim, Y., Choi, Y., Cho, M., et al. (2009). Degradable polyethylenimines as DNA and small interfering RNA carriers. *Expert Opin. Drug Deliv.* 6, 827–834. doi: 10.1517/17425240903029183

Keeler, A., ElMallah, M., and Flotte, T. (2017). Gene Therapy 2017: progress and future directions. *Clin. Transl. Sci.* 10, 242–248. doi: 10.1111/cts.12466

Kenny, G. D., Bienemann, A. S., Tagalakis, A. D., Pugh, J. A., Welser, K., and Campbell, F. (2013). Multifunctional receptor-targeted nanocomplexes for the delivery of therapeutic nucleic acids to the brain. *Biomaterials* 34, 9190–9200. doi: 10.1016/j.biomaterials.2013.07.081

Kinoshita, M., McDannold, N., Jolesz, F. A., and Hynynen, K. (2006). Noninvasive localized delivery of Herceptin to the mouse brain by MRI-guided focused ultrasound-induced blood-brain barrier disruption. *Proc. Natl. Acad. Sci.* 103, 11719–11723. doi: 10.1073/pnas.0604318103

Kircheis, R., Wightman, L., Schreiber, A., Robitza, B., Rossler, V., Kursa, M., et al. (2001). Polyethylenimine/DNA complexes shielded by transferrin target gene expression to tumors after systemic application. *Gene Ther.* 8, 28–40. doi: 10.1038/sj.gt.3301351

Kolhar, P., Anselmo, A. C., Gupta, V., Pant, K., Prabhakarpandian, B., and Ruoslahti, E. (2013). Using shape effects to target antibody-coated nanoparticles to lung and brain endothelium. *Proc. Natl. Acad. Sci.* 110, 10753–10758. doi: 10.1073/pnas.1308345110

Konofagou, E. E. (2012). Optimization of the ultrasound-induced blood-brain barrier opening. *Theranostics* 2, 1223–1237. doi: 10.7150/thno.5576

Lin, C. Y., Hsieh, H. Y., Chen, C. M., Wu, S. R., Tsai, C. H., and Huang, C. Y. (2016). Non-invasive, neuron-specific gene therapy by focused ultrasound-induced blood-brain barrier opening in Parkinson's disease mouse model. *J. Control. Release* 235, 72–81. doi: 10.1016/j.jconrel.2016.05.052

Lin, C. Y., Hsieh, H. Y., Pitt, W. G., Huang, C. Y., Tseng, I. C., and Yeh, C. K. (2015). Focused ultrasound-induced blood-brain barrier opening for non-viral, non-invasive, and targeted gene delivery. *J. Control. Release* 212, 1–9. doi: 10.1016/j.jconrel.2015.06.010

Lin, C. Y., Tsai, C. H., Feng, L. Y., Chai, W. Y., Lin, C. J., and Huang, C. Y. (2019). Focused ultrasound-induced blood brain-barrier opening enhanced vascular permeability for GDNF delivery in Huntington's disease mouse model. *Brain Stimul.* 12, 1143–1150. doi: 10.1016/j.brs.2019.04.011

Lipsman, N., Meng, Y., Bethune, A. J., Huang, Y., Lam, B., and Masellis, M. (2018). Blood-brain barrier opening in Alzheimer's disease using MR-guided focused ultrasound. *Nat. Commun.* 9, 2336. doi: 10.1038/s41467-018-04529-6

Lu, G. J., Farhadi, A., Szablowski, J. O., Lee-Gosselin, A., Barnes, S. R., and Lakshmanan, A. (2018). Acoustically modulated magnetic resonance imaging of gas-filled protein nanostructures. *Nat. Mater.* 17, 456–463. doi: 10.1038/s41563-018-0023-7

Lungwitz, U., Breunig, M., Blunk, T., and Göpferich, A. (2005). Polyethylenimine-based non-viral gene delivery systems. *Eur. J. Pharm. Biopharm.* 60, 247–266. doi: 10.1016/j.ejpb.2004.11.011

Luo, Z., Jin, K., Pang, Q., Shen, S., Yan, Z., and Jiang, T.Luo, Z., Jin, K., Pang, Q., Shen, S., Yan, Z., and Jiang, T. , et al. (2017). On-demand drug release from dual-targeting small nanoparticles triggered by high-intensity focused ultrasound enhanced glioblastoma-targeting therapy. *ACS Appl. Mater. Interfaces* 9, 31612–31625. doi: 10.1021/acsami.7b10866

Mainprize, T., Lipsman, N., Huang, Y., Meng, Y., Bethune, A., and Ironside, S. (2019). Blood-brain barrier opening in primary brain tumors with non-invasive MR-guided focused ultrasound: a clinical safety and feasibility study. *Sci. Rep.* 9, 1–7. doi: 10.1038/s41598-018-36340-0

Mangraviti, A., Tzeng, Â. S. Y., Kozielski, Â. K. L., Wang, Â. Y., Jin, Â. Y., Gullotti, D., et al. (2015). Polymeric nanoparticles for nonviral gene therapy extend brain tumor survival in Vivo. *ACS Nano*. 1236–1249. doi: 10.1021/nn504905q

Manoutcharian, K., Perez-Garmendia, R., and Gevorkian, G. (2016). Recombinant antibody fragments for neurodegenerative diseases. *Curr. Neuropharmacol.* 15, 779–788. doi: 10.2174/1570159x01666160930121647

Mansouri, S., Lavigne, P., Corsi, K., Benderdour, M., Beaumont, E., and Fernandes, J. C. (2004). Chitosan-DNA nanoparticles as non-viral vectors in gene therapy: Strategies to improve transfection efficacy. *Eur. J. Pharm. Biopharm.* 57, 1–8. doi: 10.1016/S0939-6411(03)00155-3

Mastorakos, P., Zhang, C., Berry, S., Oh, Y., Lee, S., and Eberhart, C. G. (2015). Highly PEGylated DNA nanoparticles provide uniform and widespread gene transfer in the brain. *Adv. Healthc. Mater.* 4, 1023–1033. doi: 10.1002/adhm.201400800

Mastorakos, P., Zhang, C., Song, E., Kim, Y. E., Park, H. W., Berry, S., et al. (2017). Biodegradable brain-penetrating DNA nanocomplexes and their use to treat malignant brain tumors. *J. Control. Release* 262, 37–46. doi: 10.1016/j.jconrel.2017.07.009

Mead, B. P., Kim, N., Miller, G. W., Hodges, D., Mastorakos, P., and Klibanov, A. L. (2017). Novel focused ultrasound gene therapy approach noninvasively restores dopaminergic neuron function in a rat Parkinson's disease model. *Nano Lett.* 17, 3533–3542. doi: 10.1021/acs.nanolett.7b00616

Mead, B. P., Mastorakos, P., Soo, J., Klibanov, A. L., Hanes, J., and Price, R. J. (2016). Targeted gene transfer to the brain via the delivery of brain-penetrating DNA nanoparticles with focused ultrasound. *J. Control. Release* 223, 109–117. doi: 10.1016/j.jconrel.2015.12.034

Miao, C. H., Snyder, R. O., Schowalter, D. B., Patijn, G. A., Donahue, B., and Winther, B. (1998). The kinetics of rAAV integration in the liver. *Nat. Genet.* 19, 13–15. doi: 10.1038/ng0598-13

Mullin, L. B., Phillips, L. C., and Dayton, P. A. (2013). Nanoparticle delivery enhancement with acoustically activated microbubbles. *IEEE Trans. Ultrason. Ferroelectr. Freq. Control* 60, 65–77. doi: 10.1109/TUFFC.2013.2538

Nance, E., Woodworth, G. F., Sailor, K., Shih, T.-Y., Xu, Q., Swaminathan, G., et al. (2012). A dense poly(ethylene glycol) coating improves penetration of large polymeric nanoparticles within brain tissue. *Sci. Transl. Med.* 4, 149ra119. doi: 10.1126/scitranslmed.3003594

Nance, E., Timbie, K., Miller, G. W., Song, J., Louttit, C., and Klibanov, A. L. (2014). Non-invasive delivery of stealth, brain-penetrating nanoparticles across the blood–brain barrier using MRI-guided focused ultrasound. *J. Control. Release* 189, 123–132. doi: 10.1016/j.jconrel.2014.06.031

Negron, K., Khalasawi, N., Lu, B., Ho, C. Y., Lee, J., and Shenoy, S. (2019). Widespread gene transfer to malignant gliomas with In vitro-to-In vivo correlation. *J. Control. Release* 303, 1–11. doi: 10.1016/j.jconrel.2019.04.010

Nie, J. J., Dou, X. B., Hu, H., Yu, B., Chen, D. F., and Wang, R. X. (2015). Poly(aspartic acid)-based degradable assemblies for highly efficient gene delivery. *ACS Appl. Mater. Interfaces* 7, 553–562. doi: 10.1021/am506730t

Ojala, D. S., Amara, D. P., and Schaffer, D. V. (2015). Adeno-associated virus vectors and neurological gene therapy. *Neurosci.* 21, 84–98. doi: 10.1177/1073858414521870

Owens, D. E., and Peppas, N. A. (2006). Opsonization, biodistribution, and pharmacokinetics of polymeric nanoparticles. *Int. J. Pharm.* 307, 93–102. doi: 10.1016/j.ijpharm.2005.10.010

Pandey, A. P., and Sawant, K. K. (2016). Polyethylenimine: a versatile, multifunctional non-viral vector for nucleic acid delivery. *Mater. Sci. Eng. C.* 68, 904–918. doi: 10.1016/j.msec.2016.07.066

Panegyres, P. K., Berry, R., and Burchell, J. (2016). Early dementia screening. *Diagnostics* 6, 1–13. doi: 10.3390/diagnostics6010006

Panyam, J., Zhou, W.-Z., Prabha, S., Sahoo, S. K., and Labhasetwar, V. (2002). Rapid endo-lysosomal escape of poly(dl -lactide- co -glycolide) nanoparticles: implications for drug and gene delivery. *FASEB J.* 16, 1217–1226. doi: 10.1096/fj.02-0088com

Piguet, F., Alves, S., and Cartier, N. (2017). Clinical gene therapy for neurodegenerative diseases: past, present, and future. *Hum. Gene Ther.* 28, 988–1003. doi: 10.1089/hum.2017.160

Prados, M. D., Schold, S. C., Fine, H. A., Jaeckle, K., Mechtler, L., and Fetell, M. R. (2003). A randomized, double-blind, placebo-controlled, phase 2 study of RMP-7 in combination with carboplatin administered intravenously for the treatment of recurrent malignant glioma. *Neuro Oncol.* 5, 96–103. doi: 10.1093/neuonc/5.2.96

Price, R. J., Fisher, D. G., Suk, J. S., Hanes, J., Ko, H. S., and Kordower, J. H. (2019). Parkinson's disease gene therapy: will focused ultrasound and nanovectors be the next frontier? *Mov. Disord.* 34,1279–1282. doi: 10.1002/mds.27675

Puri, A., Loomis, K., Smith, B., Lee, J. H., Yavlovich, A., and Heldman, E. (2009). Lipid-based nanoparticles as pharmaceutical drug carriers: from concepts to clinic. *Crit. Rev. Ther. Drug Carrier Syst.* 26, 523–580. doi: 10.1615/CritRevTherDrugCarrierSyst.v26.i6.10

Rapoport, N., Nam, K. H., Gupta, R., Gao, Z., Mohan, P., and Payne, A. (2011). Ultrasound-mediated tumor imaging and nanotherapy using drug loaded, block copolymer stabilized perfluorocarbon nanoemulsions. *J. Control. Release* 153, 4–15. doi: 10.1016/j.jconrel.2011.01.022

Saraiva, C., Praça, C., Ferreira, R., Santos, T., Ferreira, L., and Bernardino, L. (2016). Nanoparticle-mediated brain drug delivery: overcoming blood – brain barrier to treat neurodegenerative diseases. *J. Control. Release* 235, 34–47. doi: 10.1016/j.jconrel.2016.05.044

Schroeder, A., Kost, J., and Barenholz, Y. (2009). Ultrasound, liposomes, and drug delivery: principles for using ultrasound to control the release of drugs from liposomes. *Chem. Phys. Lipids* 162, 1–16. doi: 10.1016/j.chemphyslip.2009.08.003

Sheikov, N., McDannold, N., Vykhodtseva, N., Jolesz, F., and Hynynen, K. (2004). Cellular mechanisms of the blood-brain barrier opening induced by ultrasound in presence of microbubbles. *Ultrasound Med. Biol.* 30, 979–989. doi: 10.1016/j.ultrasmedbio.2004.04.010

Shenoy, D., Little, S., Langer, R., and Amiji, M. (2005). Poly(ethylene oxide)-modified poly(β-amino ester) nanoparticles as a pH-sensitive system for tumor-targeted delivery of hydrophobic drugs. 1. In vitro evaluations. *Mol. Pharm.* 2, 357–366. doi: 10.1021/mp0500420

Song, H. Q., Dou, X. B., Li, R. Q., Yu, B. R., Zhao, N. N., and Xu, F. J. (2015). A general strategy to prepare different types of polysaccharide-graft-poly(aspartic acid) as degradable gene carriers. *Acta Biomater.* 12, 156–165. doi: 10.1016/j.actbio.2014.10.041

Song, Q., Song, H., Xu, J., Huang, J., Hu, M., and Gu, X. (2016). Biomimetic ApoE-reconstituted high density lipoprotein nanocarrier for blood-brain barrier penetration and amyloid beta-targeting drug delivery. *Mol. Pharm.* 13, 3976–3987. doi: 10.1021/acs.molpharmaceut.6b00781

Soppimath, K. S., Aminabhavi, T. M., and Kulkarni, A. R. (2001). Biodegradable polymeric nanoparticles as drug delivery devices. *J. Control. Release* 70, 1–20. doi: 10.1016/s0168-3659(00)00339-4

Spicer, C. D., Jumeaux, C., and Stevens, M. M. (2018). Peptide and protein nanoparticle conjugates: versatile platforms for biomedical applications. *Chem. Soc Rev.* 47, 3574–3620. doi: 10.1039/c7cs00877e

Suk, J. S., Xu, Q., Kim, N., Hanes, J., and Ensign, L. M. (2016). PEGylation as a strategy for improving nanoparticle-based drug and gene delivery. *Adv. Drug Deliv. Rev.* 99, 28–51. doi: 10.1016/j.addr.2015.09.012

Suzuki, R., Oda, Y., Utoguchi, N., and Maruyama, K. (2011). Progress in the development of ultrasound-mediated gene delivery systems utilizing nano- and microbubbles. *J. Control. Release* 149, 36–41. doi: 10.1016/J.JCONREL.2010.05.009

Thomas, C. E., Ehrhardt, A., and Kay, M. A. (2003). Progress and problems with the use of viral vectors for gene therapy. *Nat. Rev. Genet.* 4, 346–358. doi: 10.1038/nrg1066

Timbie, K. F., Afzal, U., Date, A., Zhang, C., Song, J., and Wilson Miller, G. (2017). MR image-guided delivery of cisplatin-loaded brain-penetrating nanoparticles to invasive glioma with focused ultrasound. *J. Control. Release* 263, 120–131. doi: 10.1016/j.jconrel.2017.03.017

Timbie, K. F., Mead, B. P., and Price, R. J. (2015). Drug and gene delivery across the blood-brain barrier with focused ultrasound. *J. Control. Release* 219, 61–75. doi: 10.1016/j.jconrel.2015.08.059

Treat, L. H., McDannold, N., Zhang, Y., Vykhodtseva, N., and Hynynen, K. (2012). Improved anti-tumor effect of liposomal doxorubicin after targeted blood-brain barrier disruption by MRI-guided focused ultrasound in rat glioma. *Ultrasound Med. Biol.* 38, 1716–1725. doi: 10.1016/j.ultrasmedbio.2012.04.015

Vasir, J. K., and Labhasetwar, V. (2007). Biodegradable nanoparticles for cytosolic delivery of therapeutics. *Adv. Drug Deliv. Rev.* 59, 718. doi: 10.1016/J.ADDR.2007.06.003

Visser, P. J., Verhey, F. R. J., Boada, M., Bullock, R., De Deyn, P. P., and Frisoni, G. B. (2008). Development of screening guidelines and clinical criteria for predementia Alzheimer's disease. *Neuroepidemiology* 30, 254–265. doi: 10.1159/000135644

Wang, J. B., Aryal, M., Zhong, Q., Vyas, D. B., and Airan, R. D. (2018). Noninvasive ultrasonic drug uncaging maps whole-brain functional networks. *Neuron*. 100, 728–738. doi: 10.1016/j.neuron.2018.10.042

Wu, S.-K., Chiang, C.-F., Hsu, Y.-H., Lin, T.-H., Liou, H.-C., and Fu, W.-M. (2014). Short-time focused ultrasound hyperthermia enhances liposomal doxorubicin delivery and antitumor efficacy for brain metastasis of breast cancer. *Int. J. Nanomedicine*, 4485. doi: 10.2147/ijn.s68347

Wu, S. Y., Fix, S. M., Arena, C. B., Chen, C. C., Zheng, W., and Olumolade, O. O. (2018). Focused ultrasound-facilitated brain drug delivery using optimized nanodroplets: vaporization efficiency dictates large molecular delivery. *Phys. Med. Biol.* 63, 035002. doi: 10.1088/1361-6560/aaa30d

Xu, L., and Anchordoquy, T. (2011). Drug delivery trends in clinical trials and translational medicine: challenges and opportunities in the delivery of nucleic acid-based therapeutics. *J. Pharm. Sci.* 100, 38–52. doi: 10.1002/jps.22243

Yang, F. Y., Wang, H. E., Liu, R. S., Teng, M. C., Li, J. J., and Lu, M. (2012). Pharmacokinetic analysis of 111In-labeled liposomal doxorubicin in murine glioblastoma after blood-brain barrier disruption by focused ultrasound. *PloS One* 7, 1–7. doi: 10.1371/journal.pone.0045468

Yildirim, A., Blum, N. T., and Goodwin, A. P. (2019). Colloids, nanoparticles, and materials for imaging, delivery, ablation, and theranostics by focused ultrasound (FUS). *Theranostics* 9, 2572–2594. doi: 10.7150/thno.32424

Zhang, C., Nance, E. A., Mastorakos, P., Chisholm, J., Berry, S., and Eberhart, C. (2017). Convection enhanced delivery of cisplatin-loaded brain penetrating nanoparticles cures malignant glioma in rats. *J. Control. Release* 263, 112–119. doi: 10.1016/j.jconrel.2017.03.007

Zhao, G., Huang, Q., Wang, F., Zhang, X., Hu, J., and Tan, Y. (2018). Targeted shRNA-loaded liposome complex combined with focused ultrasound for blood brain barrier disruption and suppressing glioma growth. *Cancer Lett.* 418, 147–158. doi: 10.1016/j.canlet.2018.01.035

Zhong, Q., Yoon, B. C., Aryal, M., Wang, J. B., Ilovitsh, T., and Baikoghli, M. A. (2019). Polymeric perfluorocarbon nanoemulsions are ultrasound-activated wireless drug infusion catheters. *Biomaterials*. 206, 73–86. doi: 10.1016/j.biomaterials.2019.03.021

Conflict of Interest: The authors declare that the research was conducted in the absence of any commercial or financial relationships that could be construed as a potential conflict of interest.

frontiers in Pharmacology

ORIGINAL RESEARCH
published: 19 November 2019
doi: 10.3389/fphar.2019.01299

Therapeutic Dose Response of Acoustic Cluster Therapy in Combination With Irinotecan for the Treatment of Human Colon Cancer in Mice

Nigel Bush[1], Andrew Healey[2], Anant Shah[1], Gary Box[2], Vladimir Kirkin[2], Spiros Kotopoulis[3], Svein Kvåle[3], Per Christian Sontum[3] and Jeffrey Bamber[1]*

[1] Joint Department of Physics, Institute of Cancer Research, London, United Kingdom, [2] CRUK Cancer Therapeutics Unit, The Institute of Cancer Research, London, United Kingdom, [3] Phoenix Solutions AS, Oslo, Norway

OPEN ACCESS

Edited by:
Jean-Michel Escoffre, INSERM U1253 Imagerie et Cerveau (iBrain), France

Reviewed by:
Kazuo Maruyama, Teikyo University, Japan
Alban Girault, University of Picardie Jules Verne, France

***Correspondence:**
Nigel Bush
Nigel.Bush@icr.ac.uk

Specialty section:
This article was submitted to Translational Pharmacology, a section of the journal Frontiers in Pharmacology

Received: *26 July 2019*
Accepted: *10 October 2019*
Published: *19 November 2019*

Citation:
Bush N, Healey A, Shah A, Box G, Kirkin V, Kotopoulis S, Kvåle S, Sontum PC and Bamber J (2019) Therapeutic Dose Response of Acoustic Cluster Therapy in Combination With Irinotecan for the Treatment of Human Colon Cancer in Mice. Front. Pharmacol. 10:1299. doi: 10.3389/fphar.2019.01299

Introduction: Acoustic Cluster Therapy (ACT) comprises coadministration of a formulation containing microbubble-microdroplet clusters (PS101) together with a regular medicinal drug and local ultrasound (US) insonation of the targeted pathological tissue. PS101 is confined to the vascular compartment and when the clusters are exposed to regular diagnostic imaging US fields, the microdroplets undergo a phase shift to produce bubbles with a median diameter of 22 μm. Low frequency, low mechanical index US is then applied to drive oscillations of the deposited ACT bubbles to induce biomechanical effects that locally enhance extravasation, distribution, and uptake of the coadministered drug, significantly increasing its therapeutic efficacy.

Methods: The therapeutic efficacy of ACT with irinotecan (60 mg/kg i.p.) was investigated using three treatment sessions given on day 0, 7, and 14 on subcutaneous human colorectal adenocarcinoma xenografts in mice. Treatment was performed with three back-to-back PS101+US administrations per session with PS101 doses ranging from 0.40–2.00 ml PS101/kg body weight (n = 8–15). To induce the phase shift, 45 s of US at 8 MHz at an MI of 0.30 was applied using a diagnostic US system; low frequency exposure consisted of 1 or 5 min at 500 kHz with an MI of 0.20.

Results: ACT with irinotecan induced a strong, dose dependent increase in the therapeutic effect (R^2 = 0.95). When compared to irinotecan alone, at the highest dose investigated, combination treatment induced a reduction in average normalized tumour volume from 14.6 (irinotecan), to 5.4 (ACT with irinotecan, p = 0.002) on day 27. Median survival increased from 34 days (irinotecan) to 54 (ACT with irinotecan, p = 0.002). Additionally, ACT with irinotecan induced an increase in the fraction of complete responders; from 7% to 26%. There was no significant difference in the therapeutic efficacy whether the low frequency US lasted 1 or 5 min. Furthermore, there was no significant difference between the enhancement observed in the efficacy of ACT with irinotecan when PS101+US was

administered before or after irinotecan. An increase in early dropouts was observed at higher PS101 doses. Both mean tumour volume (on day 27) and median survival indicate that the PS101 dose response was linear in the range investigated.

Keywords: acoustic cluster therapy, microbubbles, ultrasound, drug delivery, dose/response, irinotecan, colorectal cancer

INTRODUCTION

A prerequisite for successful therapy with a medicinal drug is that the active substance reaches its target pathology and that toxicity to healthy tissue and nontargeted organs is limited. However, once a drug is administrated systemically, the mononuclear phagocyte system, the vascular endothelium, the disrupted tumour blood flow, the interstitial and osmotic pressure, the tumour stroma, endosomal escape, and drug efflux pumps are a few amongst a multitude of other biological barriers that severely restrict its effective delivery from the vascular compartment into the tissue of the targeted pathology (Nizzero et al., 2018). In effect, for a number of drugs, the current, passive transvascular delivery paradigm is inefficient, and insufficient tumour penetration of therapeutic agents to reach effective local concentrations is often the outcome. In combination with low therapeutic indexes, increasing the dosages is not a viable strategy due to serious and widespread adverse effects, generally severely limiting the clinical utility of a range of potent drugs.

Whereas lack of sufficient extravasation of drug to the targeted pathology is an issue over a range of medicinal therapeutic segments, this is predominant in the field of chemotherapy for cancer treatment. Regular chemotherapeutics and a range of more novel immune therapies induce severe side effects at partially effective doses and typically, these medicinal regimes are not completed because the cancer is eradicated but because the body cannot tolerate more treatment. The outcome is then only palliative benefit or life prolongation instead of a cure (Hui and Bruera, 2016). For hepatic metastases from colon and pancreatic cancer, primary pancreatic cancer and triple negative breast cancer treated with standard of care chemotherapy, this is unfortunately often the case.

In order to resolve this fundamental problem, over the past decades, a wide range of concepts to improve on pathology-specific uptake (targeted drug delivery) have been explored (Devarajan and Jain, 2015). Within oncology, numerous drug carrier concepts, e.g., liposomes, micelles, dendrimers, and nanoparticles, have been employed either to passively make use of the passive enhanced permeability and retention effect (Maeda et al., 2000) or in combination with surface ligands to actively promote accumulation in tumour tissue through biochemical affinity to specifically expressed target groups. While huge resources have been spent on finding functional concepts for targeted drug delivery over the last two decades, and despite promising preclinical results for several of these, there has been very limited transition to drug products and clinical practice. In truth, the objective remains essentially unresolved in current standard of care medicinal therapy.

In recent years, several concepts for ultrasound (US) mediated drug delivery have been investigated, some with quite encouraging results (Tsutsui et al., 2004; Martin and Dayton, 2013; Unga and Hashida, 2014). Most of these concepts explore the use of commercially available US contrast microbubbles injected intravenously. Insonation of the target pathology leads to a variety of biomechanical effects that enhance extravasation and distribution of drug molecules to target tissue (Kooiman et al., 2014; Lentacker et al., 2014). Coinjection of Gemcitabine and Sonovue®, with localized US insonation for a hypothesized-enhanced drug uptake and therapeutic effect during treatment of pancreatic cancer (PDAC), has been explored in clinical trials with encouraging results (Dimcevski et al., 2016). A similar approach is being investigated for treatment of Glioblastoma in humans (Carpentier et al., 2016). While these studies have shown great promise, there are still several limitations (van Wamel et al., 2016b) and Acoustic Cluster Therapy (ACT) has been developed as a new therapeutic bubble concept specifically designed to improve on the shortcomings of contrast microbubbles for US-targeted drug delivery (Sontum et al., 2015; Healey et al., 2016). ACT exploits different mechanisms to those induced by contrast microbubbles and addresses important deficiencies of the latter. In brief, ACT comprises of an intravenous injection of microbubble-microdroplet cluster dispersion (PS101) coadministration with a drug, followed by a two-step, local US insonification for (i) activation and (ii) delivery enhancement procedure. US activation (at diagnostic US frequencies and MI > 0.10) induces a liquid-to-gas phase shift of the microdroplet component and the formation of large (~22 μm median diameter) bubbles, referred to as ACT bubbles. The ACT bubbles are designed to have a size distribution that causes them to lodge in the microvasculature of the tissue in which the activation occurred, forming transient occlusions in these capillaries. The subsequent US enhancement step induces controlled volume oscillations of the ACT bubbles that lead to enhanced local permeability of the vasculature and other localized mechanical effects, allowing for improved extravasation of a coinjected drug and its improved distribution into the tumour tissue extracellular matrix. The ACT bubbles, being 1,000 times larger (by volume) than contrast microbubbles, will induce orders of magnitude greater biomechanical work. Furthermore, being lodged in the vascular compartment until they dissolve, the ACT bubbles are in direct contact with a substantial portion of the endothelial wall (Sontum et al., 2015) over 5–10 min. This also allows for prolonged insonation to induce biomechanical effects using low frequency (e.g., 0.5 MHz) low amplitude (MI < 0.30) US. The concept represents an unprecedented approach to US-targeted drug delivery that may improve greatly the efficacy of, for example, current chemotherapy regimen.

ACT has been explored in combination with a range of drugs for enhancing their efficacy in the treatment of several cancer xenograft models in mice, including Abraxane® (nab-paclitaxel) and paclitaxel for treatment of human prostate cancer (Park, 2016; van Wamel et al., 2016b), paclitaxel for treatment of human pancreatic ductal carcinoma (PDAC) (Kotopoulis et al., 2017) and Doxil™ for treatment of triple negative breast cancer (companion paper in this journal issue). In these studies, an impressive increase in the therapeutic efficacy over drug alone is observed when combined with the ACT procedure. To date, however, no study using ACT has explored anything other than a fixed dose of PS101, the effect of the timing and duration of the PS101+US procedure, nor the treatment of colon cancer. In the current paper, we evaluate whether PS101+US is able to enhance the efficacy of a clinically relevant drug, irinotecan, for treatment of human colorectal cancer (CRC) in mice. Furthermore, in order to investigate the relationship between PS101 dose and therapeutic response, we examine the effect level of a wide range of PS101 doses. Finally, the effect of varying the timing and duration of the ACT procedure is investigated.

Colorectal cancer is the third most common cancer worldwide and approximately 30% of patients with CRC will develop liver metastases during the course of their disease. Only about 25% of these are amenable to curative-intent treatment through metastatectomyand have a 10-year survival rate of 26% (Minagawa et al., 2000). For this disease, US-targeted treatment of hepatic metastases with ACT has a range of potential applications including: as a part of a neo-adjuvant regime prior to resection to improve survival outcome, to downstage and increase the fraction of patients amenable for curative resection and, finally, to improve on survival outcome and palliation for nonresectable conditions.

MATERIALS AND METHODS

Mice and Tumours

SW620 human colon carcinoma cells (American Type Culture Collection, Manassas, VA, USA, lot no. 8924081) were grown in DMEM containing 10% foetal bovine serum in a humidified atmosphere of 5% CO_2 at 37°C and passaged before renewal from frozen. Cells were regularly screened for mycoplasma by PCR using in-house primers.

Human tumour SW620 xenografts were established in 6-week-old female athymic nude mice, ICR : Ncr-Foxn1 (nu), bred in-house. Mice were housed in groups of five in individually ventilated cages (IVCs) and allowed access to food and water ad libitum. All mice were treated in accordance with local and national animal welfare guidelines (Workman et al., 2010). The studies were performed under a UK Home Office project license and approved by the Local Animal Welfare & Ethical Review Body.

Before tumour implantation, mice were anaesthetised with isoflurane; a 100µl tumour cell suspension containing $3x10^6$ cells was then slowly injected subcutaneously into the left flank of the recipient mice. Tumours were allowed to grow for 7–14 days and treatment started when the tumours were palpable and had attained an average volume of 90 ± $3mm^3$. Prior to each treatment anaesthesia was induced by subcutaneous (s.c.) injection of Fentanyl citrate: Fluanisone (HypnormVetaPharma Ltd, Leeds, UK) and Midazolam (Hypnovel®, Roche Products Ltd, Welwyn Garden City, UK) (0.28:10:4.5mg/kg). During treatments, the mice were maintained on a mouse handling table (Vevo™, Fujifilm Visualsonics Inc., Toronto), and the body temperature was controlled thermostatically, with vital signs carefully monitored. Following treatments, mice were kept in a temperature-controlled recovery chamber until fully recovered.

Therapeutics

Clinical grade irinotecan (CPT-11, Seacross Pharmaceuticals Ltd, UK) was resuspended in 0.9% saline and administered intraperitoneally (i.p.) on days 0, 7, and 14 at a single dose of 60 mg/kg. The first injection of three PS101 doses was injected intravenously (i.v.) approximately 11 min after the irinotecan injection, or irinotecan was injected immediately after the last of three PS101 injections and US insonation.

As ACT treatments employ an anaesthesia step and such are expected to increase animal physical stress (Gargiulo et al., 2012) resulting in a higher systemic sensitivity to irinotecan, an irinotecan doses of 60 mg/kg were chosen; equivalent to 60% of the maximum tolerated dose in literature (Motwani et al., 2001). Literature values show that irinotecan has a maximum blood plasma concentration (C_{max}) between 0.5 and 1 h after i.p. injection, at which time, it is in the range of 6–10µg/ml (Araki et al., 1993; Guichard et al., 1998). The irinotecan was cleared to less than 1% of C_{max} within 24 h.

PS101 (Sontum et al., 2015) was provided by Phoenix Solutions AS, (Oslo, Norway). PS101 was prepared by reconstituting commercially available microbubbles, Sonazoid™ (GE Healthcare), with a microdroplet emulsion of perfluoromethylcylopentane (F2 Chemicals Ltd., UK) microdroplets. The reconstituted PS101 formulation consists of a suspension of small microbubble-microdroplet conjugates ("clusters") 6×10^7 clusters/ml, with a median cluster diameter of 5 µm. The content of perfluoromethylcylopentane in PS101 is 6.8 mg/ml. For administration of low doses, to allow for acceptable injection volumes, PS101 was diluted in 0.9% saline prior to administration.

Apparatus for *in Vivo* US Activation and Delivery Enhancement

The experimental setup (**Figure 1**) consists of a mouse table covered with a 5-mm thick layer of acoustic absorber (Aptflex F48™, Precision Acoustics, Dorchester, UK) which reduces acoustic reflections from the far side of the animal. An open polyethylene water bath mounted above the animal and two US transducers for separate agent activation and delivery. US activation of PS101 and simultaneous imaging confirmation of activation was achieved with a clinical, diagnostic Aplio XG US scanner (Toshiba Medical Systems Corporation, Tochigi, Japan) combined with a 1204BT linear array to provide simultaneous interleaved, nonlinear contrast mode, and fundamental mode imaging at 8 MHz (van Wamel et al., 2016a). ACT delivery

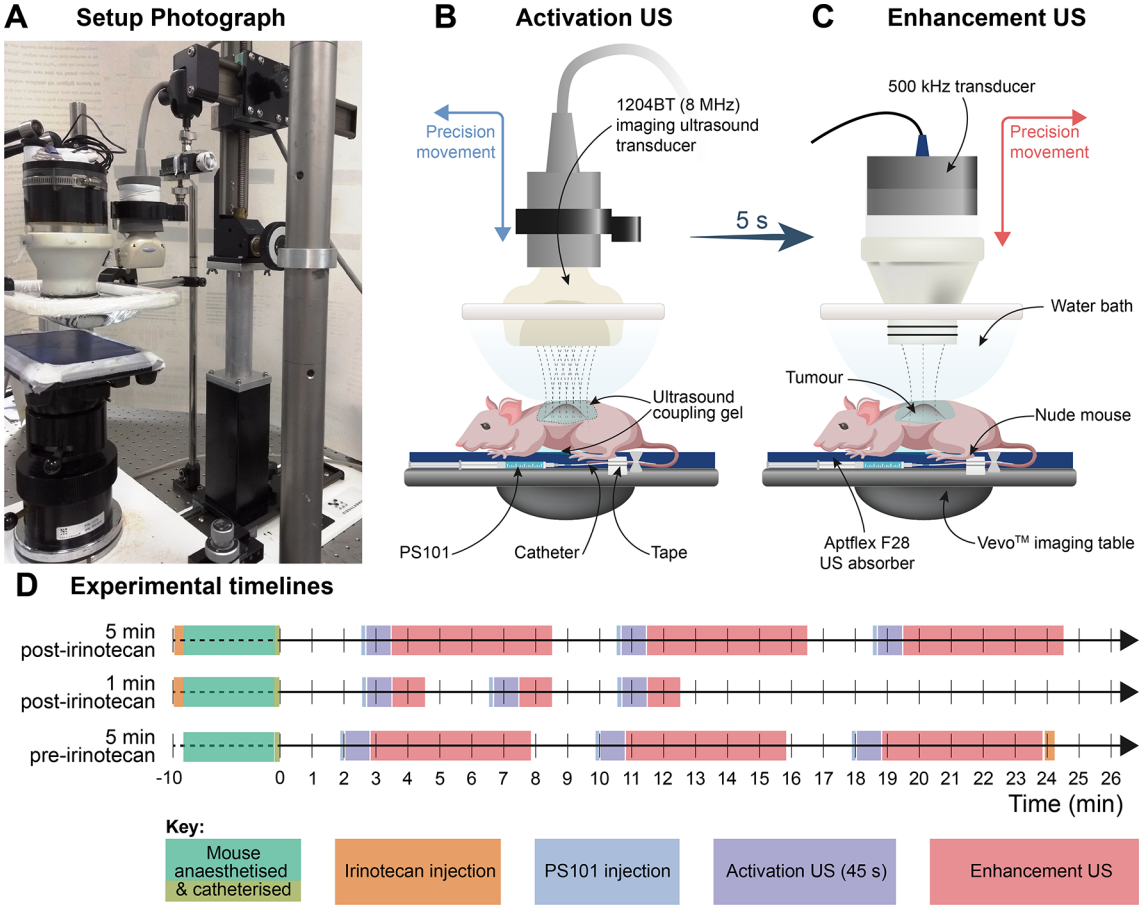

FIGURE 1 | Ultrasound (US) administration apparatus and experimental timelines. (Panel **A**) is a photograph of the activation and delivery enhancement setup showing the animal bed with the low frequency transducer in position for delivery enhancement and the clinical transducer to one side which had been transposed with the other transducer after the activation step; (Panels **B** and **C**) are schematics illustrating the positioning of the activation and delivery enhancement transducers, respectively. The water bath and acoustic transmission gel interface permit easy US transducer-to-tumour depth setting and transducer interposition. The tail vein catheter and tail are tapped to the imaging table. (Panel **D**) shows the timelines for the procedures.

enhancement was achieved separately using a custom made 500 kHz, 55 mm active diameter, single element spherically focused transducer which had a radius of curvature of 90 mm (Imasonic SAS, Voray-sur-l'Ognon, France).

The two transducers were arranged to be interposable on a precision sliding arm (**Figure 1**) mounted above the animal, directed at the subcutaneous tumour, insonating through an open polyethylene water bag above the animal, with acoustic coupling gel between the water bath and the mouse. The tumour centre was positioned to sit at the (single) transmit focus of the activation transducer and beyond the focus of the enhancement transducer (14 cm from its front face). For calculation of delivery enhancement MI values, the enhancement field was characterised by measuring the spatial and temporal peak-negative pressure *a priori in situ* at the equivalent tumour location in the therapy rig, using a calibrated Onda HGL-0200 hydrophone (Onda Corp., Sunnyvale, CA). The activation MI values were given as the output displayed on the Toshiba Aplio US activation scanner.

The anaesthetised mice were positioned prone on the treatment table with their left flank and tumour uppermost. For PS101 delivery, a new catheter was made up prior to each treatment by combining a winged infusion set, Surflo®, 27G butterfly needle (Terumo Europe, Leuven, Belgium), 70-mm polyethylene tubing, 0.4-mm internal diameter (Biochrom Ltd, Cambridge,UK), and a 27G, 0.5" needle. The catheter primed with a 0.9% saline solution was inserted into the lateral tail vein of the mouse and patency checked by injecting a small volume (<5 µl) of saline solution. The hub of the cannula was then filled with 0.9% saline and closed with a cap and taped to the animal's tail with surgical tape, which gave a dead space of 10 µl to be accounted for in subsequent injection. PS101 was drawn into a 1-ml syringe and 60 µl (50 µl effective dose, plus 10 µl to allow for dead space) was injected intravenously into the animal's lateral tail vein *via* the preplaced catheter. Following the PS101 injection, the tumour was insonated using the 1204BT transducer for 45 s at 8 MHz at an MI of 0.30 for activation, then the US transducers were transposed and the tumour was further insonated for 1 or 5 min (c.f. treatment groups, **Table 1**) at 500 kHz (2 cycle excitation, 125 ms burst period) at an MI of 0.20 for delivery enhancement by excitation of ACT bubble oscillations.

TABLE 1 | Summary of the treatment groups; number of mice, PS101 dose, PS101+US/irinotecan order, and enhancement ultrasound duration.

Group	Number of animals	Treatment		PS101+US procedure	
		Drug [i.p.](60 mg/kg)	PS101 Dose [i.v.] 3 x (ml/kg)	Pre-irinotecan or Post-irinotecan	Enhancement US duration (min)
1	8	Saline	–	–	–
2	15	Irinotecan	–	–	–
3	8	Irinotecan	0.40	Post	5
4	10	Irinotecan	1.03	Post	5
5	8	Irinotecan	1.53	Post	1
6	8	Irinotecan	2.00	Post	5
7	9	Irinotecan	2.00	Post	1
8	9	Irinotecan	2.00	Pre	5

PS101 dosing followed by US activation and enhancement was then repeated two more times with the shortest possible time (~2 min) between the end of an enhancement step and the beginning of the next PS101 injection.

Tumour Treatment Regimes

Animals were randomized into eight treatment cohorts of 8 to 15 mice per group. Two control groups, saline only and irinotecan only, received sham US exposure to mimic additional procedure induced stress on the animals. The six remaining groups received US exposure as described in Apparatus for *in-vivo* ultrasound activation and delivery enhancement section and PS101 at doses from 0.4 to 2.0 ml PS101/kg at various timepoints relative to the irinotecan injection and with various US enhancement durations (**Table 1**).

Groups 2–7 provided results for the condensed dose-response study.

Liver Toxicity

A liver toxicity study was performed to determine if ACT with or without irinotecan induced any sustained liver damage over a 24-h period. **Table 2** summarizes the treatment groups evaluated. Each group consisted of four mice. All mice were healthy and tumour free. All groups except the irinotecan groups (Groups 3 and 4 **Table 2**) underwent 3 × 45 s activation and 5-min enhancement US directed to treat the entire liver. In Groups 7 and 8 (**Table 2**), the irinotecan was injected i.p. a minimum of 10 min before PS101 injection and US exposure, i.e., mimicking Group 6 from **Table 1**.

TABLE 2 | Summary of the liver toxicity study groups.

Group	Number of animals	Treatment (dose)	Blood collection time (h)
1	4	Sonazoid (2.00 ml/kg) + US	1.5
2			24.5
3		Irinotecan (60 mg/kg)	1.5
4			24.5
5		PS101 (2.00 ml/kg) + US	1.5
6			24.5
7		PS101 (2.00 ml/kg) + Irinotecan + US	1.5
8			24.5

Blood Collection and Processing

Blood samples were collected 1.5 or 24.5 h after the first treatment and were collected by terminally anaesthetising the mice using isofluraneand performing a cardiac puncture with a 21G needle (Becton Dickinson, Franklin Lakes, NJ, USA) and a heparinised syringe. A volume of approximately 600 µl was collected from each mouse into a 1-ml microcentrifuge tube which had been washed with heparin (Eppendorf, Hamburg, Germany). To separate the serum, the samples were centrifuged at 3,000 rpm at 4°C for 15 min and 300 µl of the supernatant was subsequently transferred to a 1-ml microcentrifuge tube (Eppendorf). Sampled were stored at -20°C until analyzed.

Two liver enzymes, alanine aminotransferase (ALT) and aspartate aminotransferase (AST), were quantified using a UniCelDxC 600 Synchron Clinical System (Beckman Coulter, Brea, CA, USA) following the manufactures recommend procedures and reagents.

Literature values for the normal range in mice were used to minimize the number of animals used. Specifically, the normal range for AST and ALT in mice are reported to be in the range of 300 ± 100 units/L and 100 ± 50 units/L (Oršolić et al., 2010; Gao et al., 2014).

Monitoring Therapeutic Response

Animals were monitored daily for body weight and tumour size *via* calliper measurement for 120 days after study start. Tumour volumes were calculated using the ellipsoid equation: $\frac{4}{3}\pi\left(\frac{a}{4}+\frac{b}{4}\right)^3$. Tumour size is reported as fold-increase relative to the size on the day of the first treatment. Body weight was used as a proxy for toxicity. Tumour growth inhibition (TGI) percentage was calculated using the equation: $\frac{\left(V_c - V_t\right)}{\left(V_c - V_0\right)} \times 100$, where V_c and V_t are the mean fold increase of the control and treated tumour respectively, on day 27. V_0 is the control tumour fold growth at the start of the treatment, which is always equal to 1.

Following the 3Rs of ethical research and current EU directives (Directive 2010/63/EU, 2010), a drug + US-only group was not included in the study as the US exposure levels are well below that which might cause bioeffects (Miller et al., 2008; Nelson et al., 2009). Similarly, groups where the treatment was not expected

to affect tumour growth, based on previous publications and literature, were not included and considered outside the scope of this study such as PS101 alone and US alone.

As all animals were sacrificed after 120 days to minimize the unnecessary burden. Mice that survived 120 days with no palpable evidence of tumours and were able to go the three weeks of therapy plus 2-week recovery period were considered complete responders.

Statistical Analysis

Results for average tumour normalized volume are expressed as mean ± standard error. Statistical comparisons of mouse weights, tumour normalized volume, and liver enzymes were performed using an ordinary one-way ANOVA with multiple comparisons and a two-stage setup method for controlling the false discovery rate, or a student's t-test where only two groups were compared. Survival was compared using a log-rank (Mantel-Cox) test between two groups. Mice that were unable to complete the 3-week treatment plus 2-week recovery period, are reported as censored subjects as tick marks in the survival curves. All mice are reported in the tumour normalized volume data. Correlation was evaluated using a one tailed, nonparametric, Spearman test. Complete responders were evaluated using a contingency table and a two-sided Fisher's exact test. A p-value less than or equal to 0.05 was considered statistically significant. All statistical analyses were performed in Prism 8.1.2 (GraphPad Software Inc, San Diego, CA, USA).

RESULTS

Toxicity

Mean body weight changes as a function of time are shown in **Figure 2**. Irinotecan itself was associated with a body weight drop of 5% observed one to two days after each treatment cycle. The mice were able to recover to normal body weight by the day of each subsequent treatment. In contrast, mice treated with the highest PS101 dose (2.00 ml/kg) showed an increase in toxicity observed as a 15% drop in body weight one to two days after

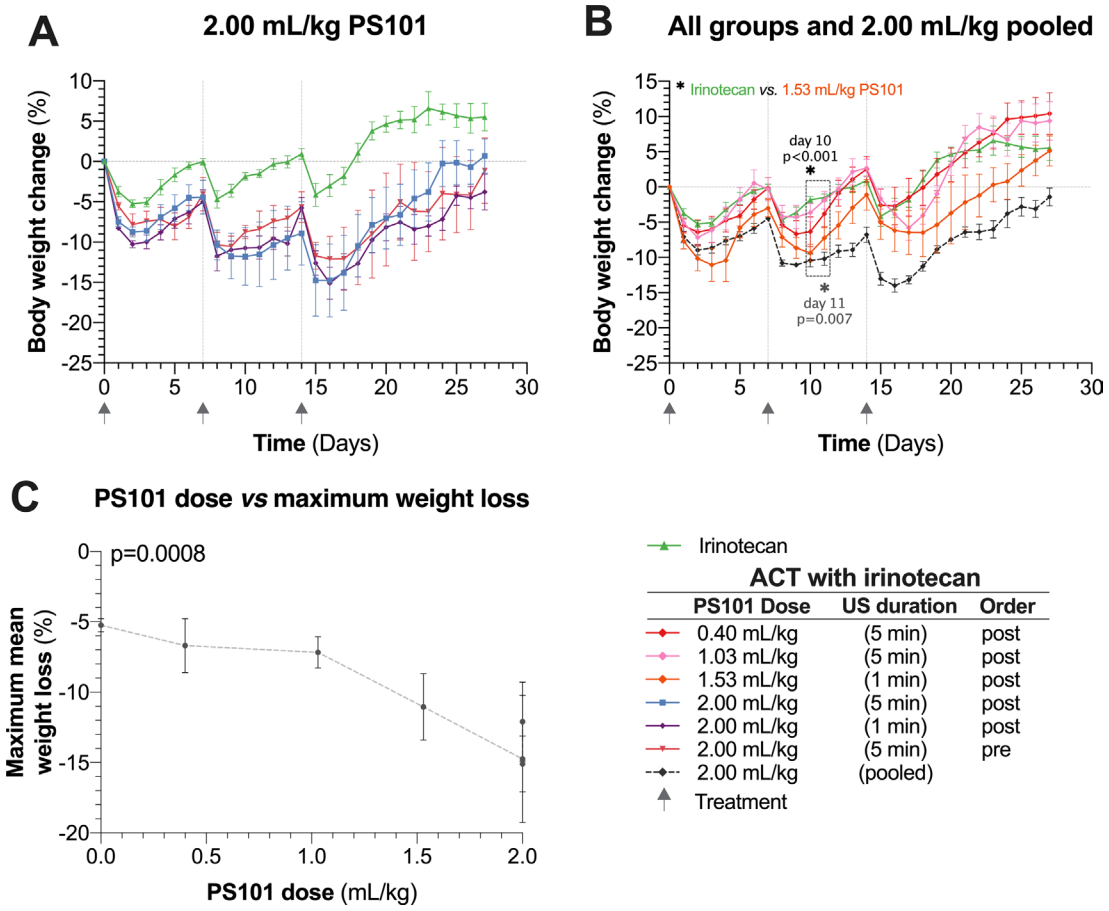

FIGURE 2 | Normalized mouse body weight as a function of time. (Panel **A**) shows the results for irinotecan alone and ACT with irinotecan for the highest dose of PS101 (2.00 ml/kg). Mouse body weight was significantly lower in all the 2.00 ml/kg PS101 groups for the entire 27 days (p = 0.035, ANOVA). (Panel **B**) pools the 2.00 ml/kg groups and compares the weight change against all other ACT with irinotecan groups. Increasing the PS101 dose increased the loss in body weight. The three grey arrows on the time axis indicate the treatment days. (Panel **C**) compares the maximum body weight loss to the PS101 dose. The correlation was significant (p = 0.0008).

treatment. When comparing to the irinotecan group alone, this weight loss was statistically significant for the entire measured period of 27 days ($p = 0.035$).

The mice treated using ACT with irinotecan (PS101 dose of 2.00 ml/kg) was not able to return to their normal body weight prior to the next treatment cycle. After the three treatment cycles, all mice treated using ACT with irinotecan showed progressive recovery of body weight and the majority of mice reached their starting weight two weeks (the recovery period) after the last treatment. The mean body weight of any 2.00 ml/kg PS101 group never fell below 20% of the starting weight (**Figure 2A**).

This transient increased weight loss following ACT treatment was observed for all PS101 doses (**Figure 2B**). At the lowest PS101 dose (0.4 and 1.03 ml/kg), the difference between ACT with irinotecan vs. irinotecan alone was not significant ($p > 0.27$ and 0.18 respectively). Overall, increasing the PS101 dose increased the mean normalized body weight loss ($p < 0.001$) (**Figure 2C**).

Tumour Volumes

Figure 3 shows tumour relative volume as a function of time. Irinotecan alone was associated with significant tumour inhibition compared to the saline controls, clearly observable in **Figure 3A** ($p < 0.0001$, day 19, unpaired t-test). Overall, at day 27, all ACT with irinotecan groups, except for the lower dose of 0.40 ml/kg PS101 ($p = 0.641$) showed significantly inhibited tumour growth when compared to irinotecan alone ($p = 0.002–0.034$).

Figure 3B compares the groups treated using ACT with irinotecan at a dose of 2.00 ml/kg PS101. There was no difference between the growth curves for 5 and 1 min enhancement-US duration ($p = 0.904$), in the groups where PS101 and US were administered post-irinotecan. While there was an observable difference between the 5-min enhancement-US duration pre-irinotecan group compared to both post-irinotecan groups, this difference was not significant ($p = 0.495$ vs. 5 min and 0.555 vs. 1 min). The slight separation between the pre-irinotecan and post-irinotecan groups was observable approximately 2 days after the second treatment (day 9) where the mean tumour volume of the post-groups was approximately 0.5-fold larger than the pre-groups. Two days after the third treatment (day 16) a slight mean tumour volume regression was observed in the pre-irinotecan group only. The separation continued throughout the 27-day period. A violin plot of all the mice that survived to the end of the treatment can be seen in **Supplemental Figure 2A**.

The normalized tumour volumes of the dose-response study in **Figure 3C** shows the groups that received PS101 and enhancement US for 5 min post-irinotecan with various PS101 doses. In general, increasing the dose of PS101 improved the treatment efficacy observed as increased tumour inhibition. As previously stated, the 0.4 ml/kg PS101 group showed no difference to irinotecan alone. At 1.03 ml/kg PS101, the mean tumour volume was 6.1-fold smaller than the irinotecan-alone group at day 27 but the difference was barely significant ($p = 0.050$). Increasing the PS101 dose to 2.00 ml/kg resulted in a tumour inhibition of 8.5-fold vs. irinotecan alone at day 27, i.e., less than half the tumour volume, and was statistically significant ($p = 0.023$).

The effect of different PS101 doses when applying enhancement US for 1 min can be seen in **Figure 3D**. In general, there was no difference observed between the two doses of 1.53 ml/kg vs. 2.00 mg/kg PS101. At day 25, a small separation was observed between these two groups, but this is a result of a single mouse with rapid tumour growth 10 days after the last treatment cycle. Hence, only the 2.00 ml/kg group was significantly different from irinotecan alone ($p = 0.018$).

As no significant difference was observed between the 2.00 ml/kg PS101 groups, independent of the enhancement US duration or order of administration in relation to the irinotecan, all the mice in these groups were pooled and compared to the other PS101 doses in **Figure 3E**. Here, a clear trend can be seen that increasing the PS101 dose resulted in an extended period of tumour inhibition post treatment that monotonically increased with PS101 dose.

Median Overall Survival

Figure 4 shows the effect of ACT with irinotecan in terms of the overall survival. Mice not treated with any therapeutic, i.e., just saline, had a median survival of 19 days. Treating with irinotecan increased median survival to 34 days and was significant ($p < 0.0001$). All groups treated using ACT with irinotecan showed an increased median survival (**Figure 4A**).

Figure 4B compares the groups treated using ACT with irinotecan at 2.00 ml/kg dose of PS101. There was no significant difference between any of the ACT with irinotecan treated groups. Comparing to irinotecan alone, only the 1 and 5 min post-irinotecan groups were significant, increasing median survival from 34 days to 58 and 54 days ($p = 0.016$ and 0.050), respectively.

The survival results from the "dose response" study (**Figure 4C**) showed that performing ACT with irinotecan using a PS101 dose of 0.40 ml/kg did not significantly improve survival ($p = 0.295$) over irinotecan alone due to early dropouts but did increase the median overall survival by 8 days (from 34 to 42 days). Increasing the PS101 dose to 1.03 ml/kg further increased survival rendering it significantly different from that with irinotecan alone ($p = 0.027$) with a median of 41 days. Further increasing the PS101 dose to 2.00 ml/kg further improved the efficacy of irinotecan resulting in a median survival of 54 days ($p = 0.050$).

Figure 4D compares the survival of the groups that underwent enhancement US for one min at two PS101 doses. One minute of US enhancement post-irinotecan at a PS101 dose of 1.53 ml/kg resulted in a survival increase of 13 days over irinotecan alone, from 34 to 47 days. Nevertheless, this result was not significant ($p = 0.115$). Increasing the PS101 dose to 2.00 ml/kg resulted in a further improvement in survival to 58 days, rendering it significantly better than irinotecan alone ($p = 0.016$). This was the longest survival of all the groups in this study.

Once again, as observed in the tumour volume analysis, there was no significant difference in overall survival between all the groups treated using ACT with irinotecan at a PS101 dose of 2.00

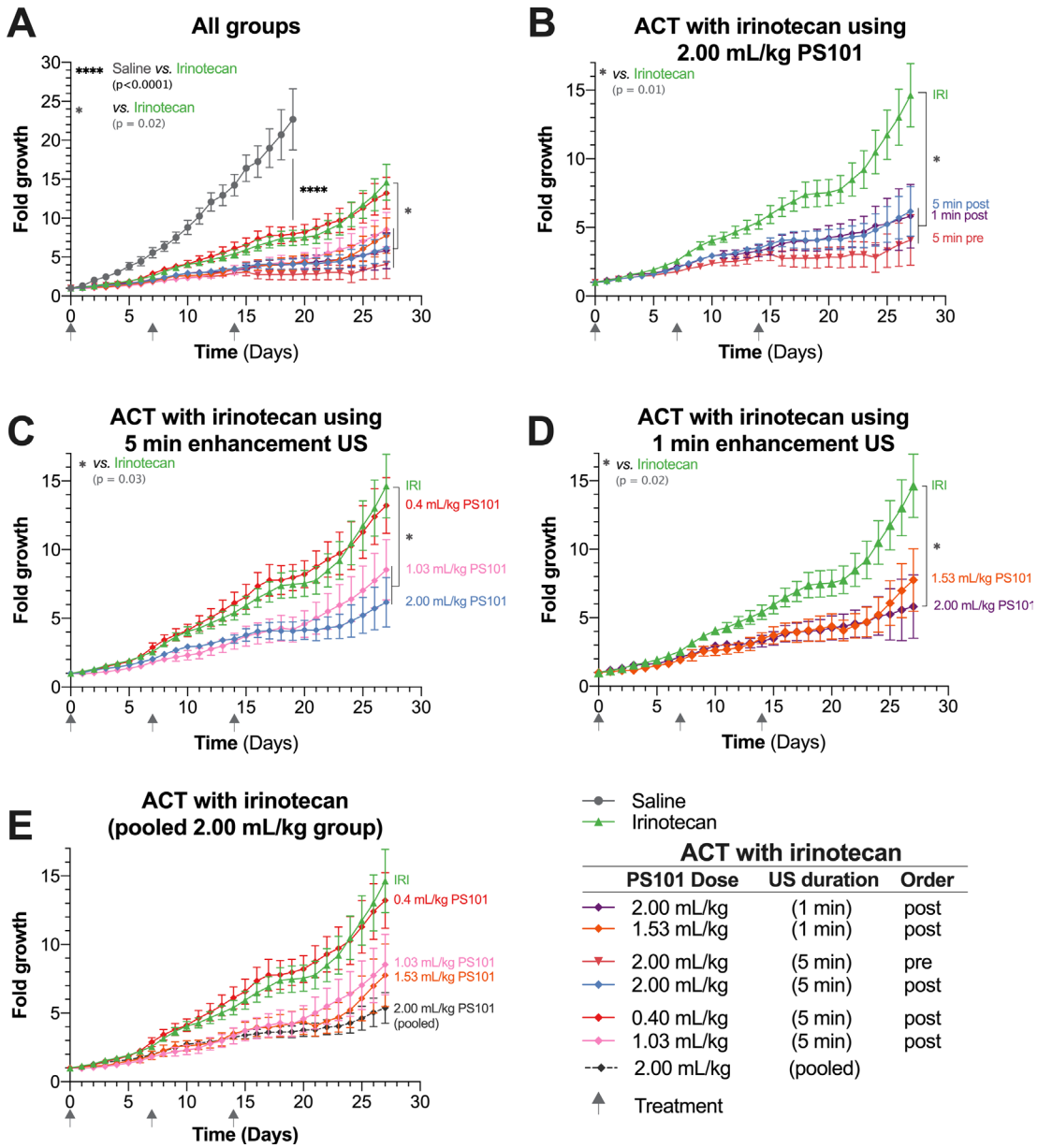

FIGURE 3 | Tumour growth as a function of time. Each panel shows a subset of the data to aid comparisons. (Panel **A**) shows all the groups within this study in a single graph. (Panel **B)** focuses on the groups treated using Acoustic Cluster Therapy (ACT) with irinotecan at 2.00 ml/kg PS101. (Panel **C**) is a "dose response" study and shows the groups treated using ACT with irinotecan where PS101 is administered post irinotecan, with 5 min duration ultrasound (US) at three different doses of PS101. (Panel **D**) compares the efficacy of irinotecan alone vs. ACT with irinotecan where PS101 is administered after irinotecan, with one-minute enhancement US at two different PS101 doses. (Panel **E**) pools all the mice that received 2.00 ml/kg PS101 and compares the data to those for the irinotecan alone and other ACT with irinotecan.

ml/kg, independent of the enhancement-US duration and whether PS101+US was administered before or after irinotecan. Hence, the data from these groups were pooled and compared with those for the other PS101 doses (**Figure 4E**). Pooling the data resulted in a median overall survival of 54 days. There was no significant difference between the pooled group and any 2.00 ml/kg group ($p = 0.980$). Comparing the pooled data to irinotecan alone improves the significance over irinotecan alone ($p = 0.002$ vs. $p = 0.016$).

Complete Responders

All groups except for the saline group showed complete responders (**Table 3**). In the irinotecan-alone group, while all

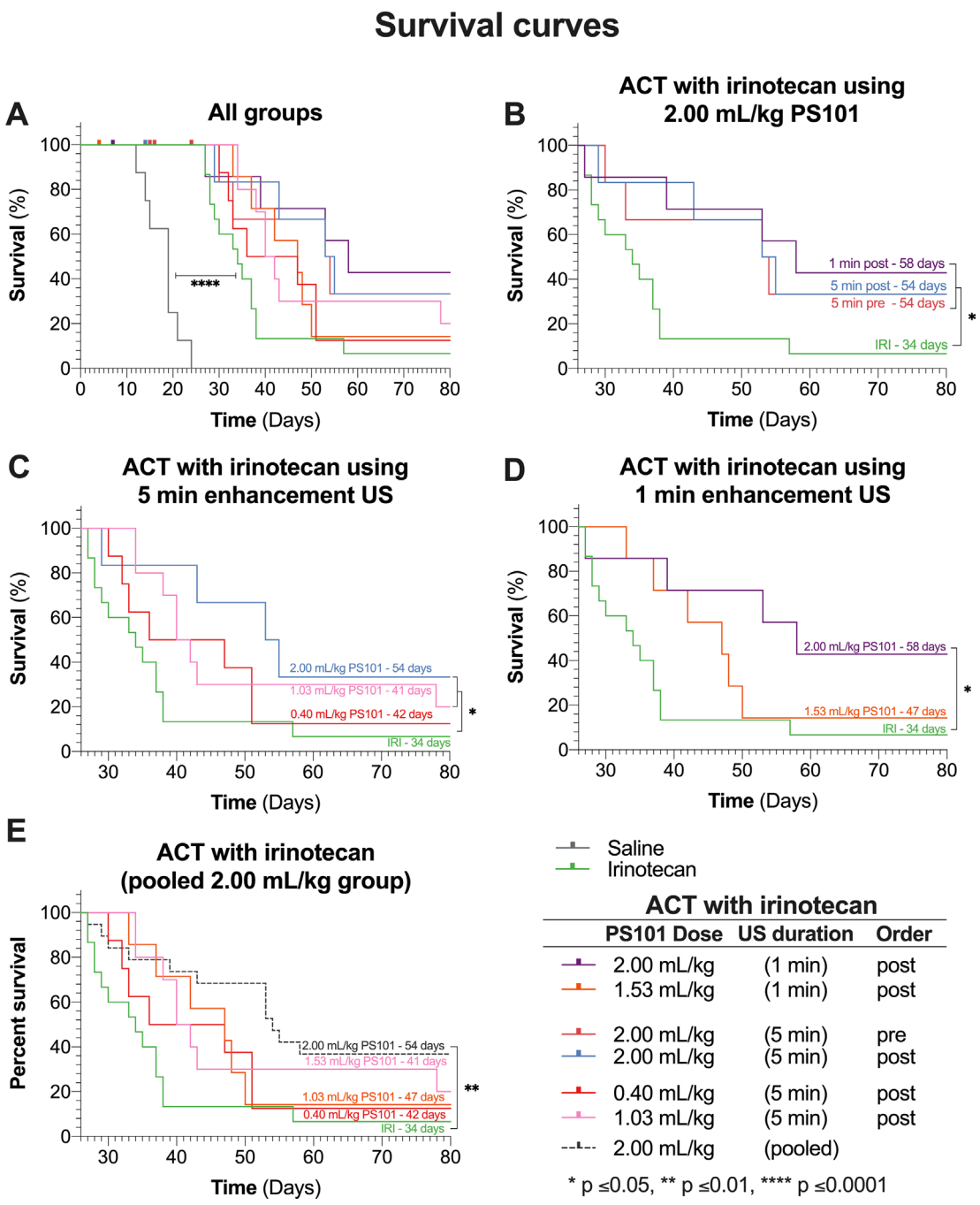

FIGURE 4 | Survival curves of all groups in the study. Each panel shows a subset of the data, each for chosen to allow specific comparisons. The labels on the survival curves indicate the groups and the median survival. (Panel **A**) shows the survival curves of all the groups in the study. Mice that did not complete the full 28 days of treatment are marked as censored subjects. (Panel **B**) compares results for various enhancement-US durations and whether PS101+US was administered pre-irinotecan or post-irinotecan, for mice that received 2.00 ml/kg PS101. (Panel **C**) shows the survival curves of the dose response study for groups that received ACT with irinotecan with 5-min enhancement US at three doses. (Panel **D**) shows the survival curves of mice that received PS101 and US post-irinotecan with one min of US enhancement at two different PS101doses. (Panel **E**) pools all the mice that received 2.00 ml/kg PS101 and compares the survival curve to those for the other ACT with irinotecan groups and irinotecan alone.

TABLE 3 | Summary of the number of mice that were able to complete the treatment plus recovery period, and the number of complete responders for each group.

Group	Description	Number completed treatment and recovery period	Number of complete responders
1	Saline	0 out of 8 (0%)	0 out of 8 (0%)
2	Irinotecan only	15 out of 15 (100%)	1 out of 15 (7%)
3	0.40 ml/kg PS101, 5 min, post	8 out of 8 (100%)	1 out of 8 (13%)
4	1.03 ml/kg PS101, 5 min, post	10 out of 10 (100%)	2 out of 10 (20%)
5	1.53 ml/kg PS101, 1 min, post	7 out of 8 (88%)	1 out of 8 (13%)
6	2.00 ml/kg PS101, 5 min, post	6 out of 8 (75%)	1 out of 8 (13%)
7	2.00 ml/kg PS101, 1 min, post	7 out of 9 (78%)	2 out of 9(22%)
8	2.00 ml/kg PS101, 5 min, pre	6 out of 9 (67%)	2 out of 9(22%)
	2.00 ml/kg (pooled)	19 out of 26 (73%)	5 out of 26 (19%)

mice were able to complete the treatment and recovery period, there was only 1 out of 15 mice (7%) that showed complete response. In contrast, all groups treated using ACT with irinotecan showed a higher percentage of responders than the irinotecan alone group (13%–22% vs. 7%). When pooling the 2.00 ml/kg PS101 groups 5 out of 26 mice (19%) showed complete response; i.e., more than a tripling of complete response. However, the increase in complete responders was not significant ($p = 0.388$).

Dose Response

Figure 5 shows the correlation between ACT with irinotecan at various doses vs. median overall survival and tumour volume at day 27. In general, an increasing PS101 dose is associated with an increased overall survival and a decreased tumour volume at day 27. The linear regression of PS101 dose on overall survival indicated a slope of 1.46 days/ml/kg of PS101 with a highly significant correlation (95% CI = 0.90 to 2.02, $R^2 = 0.90$, $p = 0.005$) in addition to the 34 days of survival when treated with irinotecan alone (**Figure 5A**).

A similar beneficial trend was observed for tumour volume (**Figure 5B**). The linear regression of PS101 dose on mean normalized tumour volume indicated a slope of -0.68-fold/ml/kg PS101 with a highly significant correlation (95% CI = -0.86 to -0.51, $R^2 = 0.95$, $p = 0.001$). Furthermore, the same trend was observed for the TGI percentage where the slope indicated an inhibition of 32.27%/ml/kg PS101 (95% CI = 20.19 to 44.36, $R^2 = 0.93$, $p = 0.008$, **Supplemental Figure 2B)**.

Liver Toxicity

Figure 6 shows the results from the liver toxicity study. In general, 1.5 h after the treatment start all groups exhibited elevated AST and ALT levels when compared to literature normal values. Only the group treated using ACT with irinotecan showed a significant difference, indicating there is a compounding effect when combining ACT with irinotecan ($p = 0.0152 – 0.0263$ for AST at 1.5 h, $p = 0.0004 – < 0.0001$ for ALT at 1.5 h). After 24.5 h the mean levels of both enzymes decreased, reaching levels that were not significantly different from normal. At this timepoint, the was no significant difference between any of the groups.

DISCUSSION

The use of ACT with irinotecan for the treatment of CRC showed a significant improvement in both TGI and overall survival when compare to irinotecan alone. The number of complete responders more than doubled when performing ACT with irinotecan vs. irinotecan alone. Performing the PS101+US before or after the irinotecan injection had no significant effect on the improved

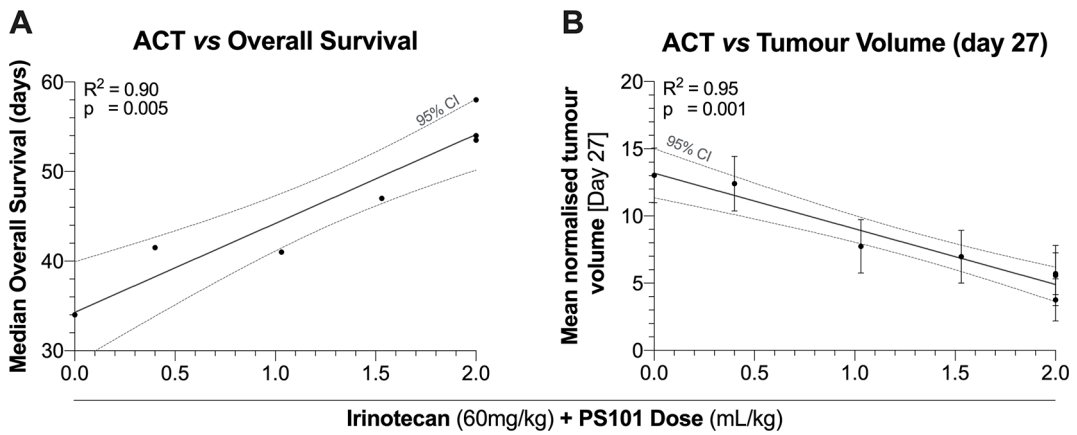

FIGURE 5 | Median overall survival (Panel **A**) and tumour volume (Panel **B**) as a function of the PS101 dose employed when ACT was used to enhance treatment with irinotecan. Increasing the PS101 dose was related to both an increased survival and a reduced tumour volume at day 27.

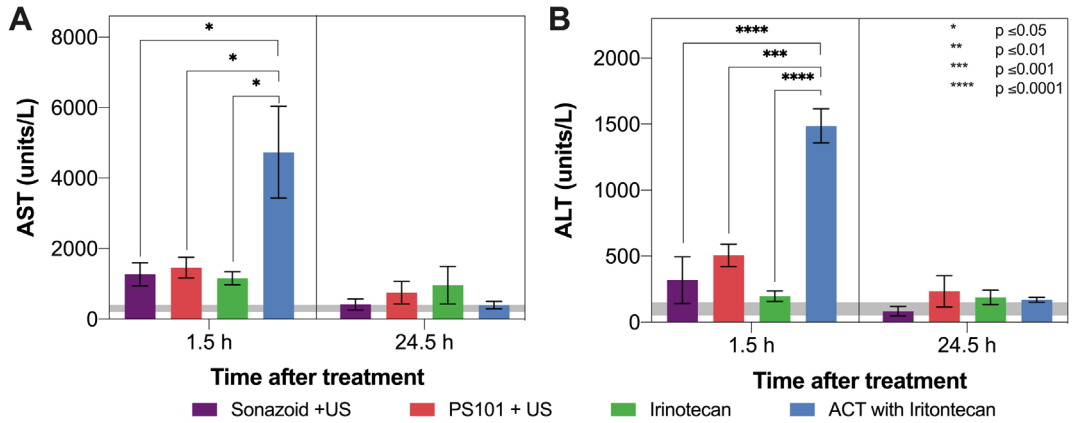

FIGURE 6 | Aspartate aminotransferase (AST) (Panel **A**) and alanine aminotransferase (ALT) (Panel **B**) levels 1.5 and 24.5 h after treatment start. The grey horizontal bar shows normal values reported in literature. Only ACT with irinotecan 1.5 h after treatment start shows a significant difference to any other groups. Decreased levels were observed for all groups after 24.5 h.

efficacy. In addition, applying US for 1 vs. 5 min also resulted in no significant difference. The dose-response study showed that in the doses evaluated there was a linear correlation with therapeutic efficacy.

Toxicity

On the observed increased level of toxicity (c.f. **Figure 2**), several studies have shown that the gastrointestinal toxicity of irinotecan is influenced by the intestinal microbiota and inflammation conditions (Brandi et al., 2006; Chityala et al., 2017). In addition, treatment with microbubbles has been shown to induce caecal lesions in murine models (Rasmussen et al., 2003) and the development of such is likely to enhance the gastrointestinal toxicity of irinotecan. Furthermore, in the current study, with tumours inoculated on the flank of the animals, collateral US insonation of the intestine was inevitable due to the small size of the animal. It is hypothesised that the increase in irinotecan toxicity observed in this study is due to an increase in inflammatory conditions from the development of caecal lesions and/or to an increased concentration of irinotecan in the intestine, due to collateral insonation. Hence, it is regarded appropriate to have excluded from the survival analysis mice that were unable to complete the treatment and recovery period. While commercial microbubbles and PS101 do have different physical properties, and this may influence the formation of caecal lesions, it is important to note that a large portion of PS101 is indeed a commercial US contrast agent; Sonazoid.

In previous studies, which used ACT at similar PS101 doses to those employed here but with an experimental configuration that shielded the abdomen from the US exposure, no weight loss was observed in any of the groups, including an ACT alone (i.e., PS101+US) group (van Wamel et al., 2016b). Furthermore, extensive toxicity studies have been performed on other species and this phenomenon was not observed (Myhre et al., 2016). This strongly supports the theory that the weight loss observed in this study is due to development of caecal lesions and/or collateral insonation of the intestines resulting in enhanced off-site delivery of irinotecan, and that this was not a systemic toxicity issue.

It should be noted that such effects are very unlikely to translate to the clinical application of ACT for enhancing the efficacy of irinotecan in the treatment of CRC in humans; collateral insonation of the intestine is unlikely in the larger species and the development of caecal lesions upon treatment with microbubbles is specific to murine species (Dirven et al., 2003).

The liver toxicity study showed that PS101+US did not induce any additional toxicity when compared to using the clinical US contrast agent Sonazoid™+US. This indicates that there is no acute or transient liver toxicity due to the positively charged particles in the PS101 formulation. As both the elevated AST and ALT levels were transient and dropped close to normal levels after 24.5 h, this suggests that the mechanism behind ACT may also be transient.

Growth Inhibition and Survival

As noted from **Figures 3** and **4**, all groups treated using ACT with irinotecan showed a decreased tumour growth rate and an increased median survival compared to irinotecan alone. At the highest PS101 dose investigated a more than 70% reduction in tumour volume was observed vs. drug alone at day 27. Also, a more than 70% increase in median survival vs. drug alone was observed. Even though not statistically significant, the fraction of complete responders in the highest PS101 dose groups was 26% vs. 7% for drug alone. The level of this enhancement effect is comparable to other studies on other disease models treated with different drugs (van Wamel et al., 2016b) further indicating the drug- and disease-agnostic nature of the ACT concept.

Under the assumptions that the generated ACT bubbles have a lifetime of approximately 5 min (van Wamel et al., 2016a) and that the drug-delivery enhancement provided by

the biomechanical effects of ACT would be optimal if applied when the drug is actually in the vascular compartment, the procedures applied in the previous studies have all performed the PS101 injection + US procedures after administration of drug, at a time that is close to the drug's maximum plasma concentration. Surprisingly, in this study, we observed no significant difference between 1 or 5 min of enhancement-US insonation, nor between performing the PS101 injection + US administration before vs. after administration of drug. With regards to the length of US insonation, this finding could indicate that the lifetime of the ACT bubbles in the present work was shorter than that observed in other studies (van Wamel et al., 2016a). Previously, the 5-min lifetime observation was made in the absence of low frequency enhancement-US insonation, which could be postulated to decrease the lifetime. Alternatively, the observation that insonating with enhancement US for longer than 1 min conveys no additional benefit could mean that all of the beneficial effects are induced within the first minute, i.e., they saturate after a short period of US insonation and may occur partly as a consequence of activation-US insonation as well as enhancement-US insonation. This possibility is partially consistent with the observations made in van Wamel et al. (van Wamel et al., 2016a), which reported a significant and substantial improvement of tumour dye-uptake by using ACT with 800CW-PEG dye, vs. dye alone, even when insonating for 45 s with only high-frequency activation-US. Nevertheless, it is important to note that the addition of 5 min of enhancement-US insonation roughly doubled the enhancement of dye delivery in the tumour.

With regards to the sequencing of the procedure, the lack of significant difference between the results for the predrug vs. postdrug application of PS101+ US procedures demonstrated that the drug does not need to be present in the vascular compartment at time of PS101+US administration. This observation would seem to indicate that PS101+US induces an effect on the tumour vasculature and/or interstitial structures that persists and allows for enhanced uptake/distribution of drug even some time after the procedure. This is also consistent with observations made in van Wamel et al (van Wamel et al., 2016a) which reports an increase in uptake of a drug surrogate 1 to 2 h after the PS101+US procedure. This is further corroborated by Åslund et al. (Åslund et al., 2017), which investigated opening of the blood brain barrier with ACT and found that its effect on uptake of gadodiamide in the brain tissue slowly decreased over a period of 72 h, indicating that the microvascular fenestrations that the PS101+US procedure may have opened or induced, close rather slowly. Both these observations indicate the need for further work to fully understand the mechanisms involved but importantly also indicate the noncritical nature of sequencing and timing, which allows for suitable flexibility in clinical applications.

Dose/Response

As indicated from **Figure 5**, the dose response relation for PS101, evaluated both as a function of tumour size at day 27 and median survival, seems linear over the range investigated, with no sign of saturation effects. This would indicate that PS101 doses higher than 2.00 ml/kg could lead to even stronger enhancement of a drug's therapeutic benefit. Nevertheless, it should be considered whether such high doses would be feasible in a clinical regime and how a preclinical murine dose would relate to the clinical counterpart.

As the ACT concept is currently in early clinical trials at Royal Marsden Hospital (UK), where it is explored for treatment of hepatic metastases from CRC and PDAC cancers in combination with standard of care chemotherapy (FOLFOX/FOLFIRI for CRC origin and nab-paclitaxel plus gemcitabine for PDAC origin; ClinicalTrials.gov Identifier: NCT04021277), this research provides an important step into understanding the importance of both administration order and dose.

Limitations and Future Work

While this study has shown that ACT with irinotecan can improve the therapeutic efficacy when compared to irinotecan alone, the mechanism behind this improvement was not investigated. While it may be speculated that this improved efficacy may be due to increased delivery of the drug to the target tissue, this remains to be verified. There are numerous other mechanisms that may affect tumour growth which may be induced by ACT and may be synergistic with the action of the chemotherapeutic agents, such as, changes in intracellular signalling (Furusawa et al., 2012; Haugse et al., 2019), vasculature (Keravnou et al., 2016; Kotopoulis et al., 2017), increased immune response and metabolic activity (Casey et al., 2010). These, and other potential mechanisms, should be investigated in future work to fully understand the biological response to ACT.

CONCLUSION

ACT can significantly enhance the inhibition of tumour growth and increase the overall survival benefit provided by irinotecan in a subcutaneous human CRC xenograft. The improved efficacy of ACT with irinotecan was shown to increase linearly with the dose of PS101 in the range investigated (0.40–2.00 ml/kg) for both tumour inhibition and overall survival. There was no significant difference in performing ACT before or after the irinotecan injection. Furthermore, there was no significant difference performing the US enhancement process for 1 or 5 min.

The results from this study indicate the flexibility of ACT, which may have implications for its application in the clinic.

DATA AVAILABILITY STATEMENT

The datasets generated from this study can be found in the public repository hosted by "LabArchives". Full URL: https://mynotebook.labarchives.com/share_attachment/My%

2520Notebook/MjAuOHw0OTA0MTEvMTYtNC9UcmVlTm9kZS8zNjcxNzgxNjAwfDUyLjg=.

ETHICS STATEMENT

The animal study was reviewed and approved by The ICR Animal Welfare & Ethical Review Body.

AUTHOR CONTRIBUTIONS

NB, AH, AS, GB, VK, SKv, PS, and JB contributed to the conception and design of the study. NB, AS, and GB performed the experiments. NB, AH, SKo, SKv, PS, and JB all cowrote the manuscript. All authors contributed to the manuscript revision, read, and approved the submitted manuscript.

FUNDING

This research was funded by Phoenix Solutions AS, partially through Research Council of Norway grant no. 228604.

SUPPLEMENTARY MATERIAL

The Supplementary Material for this article can be found online at: https://www.frontiersin.org/articles/10.3389/fphar.2019.01299/full#supplementary-material

REFERENCES

Araki, E., Ishikawa, M., Iigo, M., Koide, T., Itabashi, M., and Hoshi, A. (1993). Relationship between development of diarrhea and the concentration of SN-38, an active metabolite of CPT-11, in the intestine and the blood plasma of athymic mice following intraperitoneal administration of CPT-11. *Japanese J. Cancer Res.* 84 (6), 697–702. doi: 10.1111/j.1349-7006.1993.tb02031.x

Åslund, A. K. O., Snipstad, S., Healey, A., Kvåle, S., Torp, S. H., Sontum, P. C., et al. (2017). Efficient enhancement of blood-brain barrier permeability using Acoustic Cluster Therapy (ACT). *Theranostics*. 7(1), 23–30. doi: 10.7150/thno.16577

Brandi, G., Dabard, J., Raibaud, P., Di Battista, M., Bridonneau, C., Pisi, A. M., et al. (2006). Intestinal microflora and digestive toxicity of irinotecan in mice. *Clin. Cancer Res.* 12 (4), 1299–1307. doi: 10.1158/1078-0432.CCR-05-0750

Carpentier, A., Canney, M., Vignot, A., Reina, V., Beccaria, K., Horodyckid, C., et al. (2016). Clinical trial of blood-brain barrier disruption by pulsed ultrasound. *Sci. Transl. Med.* 8 (343), 343re2. doi: 10.1126/scitranslmed.aaf6086

Casey, G., Cashman, J. P., Morrissey, D., Whelan, M. C., Larkin, J. O., Soden, D. M., et al. (2010). Sonoporation mediated immunogene therapy of solid tumors. *Ultrasound Med. Biol.* 36 (3), 430–440. doi: 10.1016/j.ultrasmedbio.2009.11.005

Chityala, P. K., Gao, S., Hu, M., and Ghose, R. (2017). Altered irinotecan pharmacokinetics during inflammation in mice. *FASEB J.* 31 (1), 822.11. doi: 10.1096/fasebj.31.1_supplement.822.11

Devarajan, PV, and Jain, S, editors. (2015). *Targeted Drug Delivery: Concepts and Design*. Cham: Springer International Publishing. doi: 10.1007/978-3-319-11355-5

Dimcevski, G., Kotopoulis, S., Bjånes, T., Hoem, D., Schjøt, J., Gjertsen, B. T., et al. (2016). A human clinical trial using ultrasound and microbubbles to enhance gemcitabine treatment of inoperable pancreatic cancer. *J. Control Release* 243, 172–181. doi: 10.1016/j.jconrel.2016.10.007

Directive 2010/63/EU (2010). Directive 2010/63/EU of the European Parliament and of the Council of 22 September 2010 on the protection of animals used for scientific purposes. *Off. J. Eur. Union*. L276, 33–79.

Dirven, H. A. A. M., Rasmussen, H., Johnsen, H., Videm, S., Walday, P., and Grant, D. (2003). Intestinal and hepatic lesions in mice, rats, and other laboratory animals after intravenous administration of gas-carrier contrast agents used in ultrasound imaging. *Toxicol. Appl. Pharmacol.* 188 (3), 165–175. doi: 10.1016/S0041-008X(03)00100-5

Furusawa, Y., Fujiwara, Y., Campbell, P., Zhao, Q. L., Ogawa, R., Hassan, M. A., et al. (2012). DNA double-strand breaks induced by cavitational mechanical effects of ultrasound in cancer cell lines. *PLoS One* 7, e29012. doi: 10.1371/journal.pone.0029012 PONE-D-11-18985 [pii]

Gao, F., Yuan, Q., Gao, L., Cai, P., Zhu, H., Liu, R., et al. (2014). Cytotoxicity and therapeutic effect of irinotecan combined with selenium nanoparticles. *Biomaterials*. 35 (31), 8854–8866. doi: 10.1016/j.biomaterials.2014.07.004

Gargiulo, S., Greco, A., Gramanzini, M., Esposito, S., Affuso, A., Brunetti, A., et al. (2012). Mice anesthesia, analgesia, and care, part I: anesthetic considerations in preclinical research. *ILAR J.* 53 (1), E55–E69. doi: 10.1093/ilar.53.1.55

Guichard, S., Chatelut, E., Lochon, I., Bugat, R., Mahjoubi, M., and Canal, P. (1998). Comparison of the pharmacokinetics and efficacy of irinotecan after administration by the intravenous versus intraperitoneal route in mice. *Cancer Chemother. Pharmacol.* 42 (2),165–170. doi: 10.1007/s002800050801

Haugse, R., Langer, A., Gullaksen, S.-E., Sundøy, S., Gjertsen, B., Kotopoulis, S., et al. (2019). Intracellular signaling in key pathways is induced by treatment with ultrasound and microbubbles in a leukemia cell line, but not in healthy peripheral blood mononuclear cells. *Pharmaceutics* 7. doi: 10.3390/pharmaceutics11070319

Healey, A. J., Sontum, P. C., Kvåle, S., Eriksen, M., Bendiksen, R., Tornes, A., et al. (2016). Acoustic cluster therapy: *in vitro* and *ex vivo* measurement of activated bubble size distribution and temporal dynamics. *Ultrasound Med. Biol.* 42 (5), 1145–1166. doi: 10.1016/j.ultrasmedbio.2015.12.011

Hui, D., and Bruera, E. (2016). Integrating palliative care into the trajectory of cancer care. *Nat. Rev. Clin. Oncol.* 31 (1), 822.11. doi: 10.1038/nrclinonc.2015.201

Keravnou, C. P., De Cock, I., Lentacker, I., Izamis, M. L., and Averkiou, M. A. (2016). Microvascular injury and perfusion changes induced by ultrasound and microbubbles in a machine-perfused pig liver. *Ultrasound Med. Biol.* 13, 159–171. doi: 10.1016/j.ultrasmedbio.2016.06.025

Kooiman, K., Vos, H. J. H. H. J., Versluis, M., De Jong, N., Jong, N. de, and De Jong, N. (2014). Acoustic behavior of microbubbles and implications for drug delivery. *Adv. Drug Deliv. Rev.* 72, 28–48. doi: 10.1016/j.addr.2014.03.003

Kotopoulis, S., Stigen, E., Popa, M., Safont, M. M., Healey, A., Kvåle, S., et al. (2017). Sonoporation with Acoustic Cluster Therapy (ACT®) induces transient tumour volume reduction in a subcutaneous xenograft model of pancreatic ductal adenocarcinoma. *J. Control Release* 245, 70–80. doi: 10.1016/j.jconrel.2016.11.019

Lentacker, I., De Cock, I., Deckers, R., De Smedt, S. C., and Moonen, C. T. W. (2014). Understanding ultrasound induced sonoporation: definitions and underlying mechanisms. *Adv. Drug Deliv. Rev.* 72 (15), 49–64. doi: 10.1016/j.addr.2013.11.008

Maeda, H., Wu, J., Sawa, T., Matsumura, Y., and Hori, K. (2000). Tumor vascular permeability and the EPR effect in macromolecular therapeutics: a review. *J. Control Release*. 1–2 (1), 271–284. doi: 10.1016/S0168-3659(99)00248-5

Martin, K. H., and Dayton, P. A. (2013). Current status and prospects for microbubbles in ultrasound theranostics. *Wiley Interdiscip. Rev. Nanomed. Nanobiotechnol.* 5 (4), 329–345. doi: 10.1002/wnan.1219

Miller, D. L., Averkiou, M. A., Brayman, A. A., Everbach, E. C., Holland, C. K., Wible, J. H., et al. (2008). Bioeffects considerations for diagnostic ultrasound contrast agents. *J. Ultrasound Med.* 27 (4), 611–632. doi: 10.7863/jum.2008.27.4.611

Minagawa, M., Makuuchi, M., Torzilli, G., Takayama, T., Kawasaki, S., Kosuge, T., et al. (2000). Extension of the frontiers of surgical indications in the treatment of liver metastases from colorectal cancer: long-term results. *Ann. Surg.* 231 (4), 487–499. doi: 10.1097/00000658-200004000-00006

Motwani, M., Jung, C., Shah, M. A., Schwartz, G. K., Sirotnak, F. M., She, Y., et al. (2001). Augmentation of apoptosis and tumor regression by flavopiridol in the presence of CPT-11 in Hct116 colon cancer monolayers and xenografts. *Clin. Cancer Res.* 7 (12), 4209–4219.

Myhre, O., Bjørgan, M., Grant, D., Hustvedt, S. O., Sontum, P. C., and Dirven, H. (2016). Safety assessment in rats and dogs of Acoustic Cluster Therapy, a novel concept for ultrasound mediated, targeted drug delivery. *Pharmacol. Res. Perspect*. 4 (6), e00274. doi: 10.1002/prp2.274

Nelson, T. R., Fowlkes, J. B., Abramowicz, J. S., and Church, C. C. (2009). Ultrasound biosafety considerations for the practicing sonographer and sonologist. *J. Ultrasound Med.* 28 (2), 139–150. doi: 10.7863/jum.2009.28.2.139

Nizzero, S., Ziemys, A., and Ferrari, M. (2018). Transport Barriers and Oncophysics in Cancer Treatment. *Trends Cancer*. 4 (4), 277–280. doi: 10.1016/j.trecan.2018.02.008

Oršolić, N., Benković, V., Lisičić, D., Đikić, D., Erhardt, J., and Horvat Knežević, A. (2010). Protective effects of propolis and related polyphenolic/flavonoid compounds against toxicity induced by irinotecan. *Med. Oncol.* 27, 1346–1358. doi: 10.1007/s12032-009-9387-5

Park, K. (2016). Acoustic cluster therapy for better treatment of solid tumors. *J. Control Release*. 236, 117. doi: 10.1016/j.jconrel.2016.07.010

Rasmussen, H., Dirven, H. A. A. M., Grant, D., Johnsen, H., and Midtvedt, T. (2003). Etiology of cecal and hepatic lesions in mice after administration of gas-carrier contrast agents used in ultrasound imaging. *Toxicol. Appl. Pharmacol.* 118 (3), 176–184. doi: 10.1016/S0041-008X(03)00101-7

Sontum, P., Kvåle, S., Healey, A. J., Skurtveit, R., Watanabe, R., Matsumura, M., et al. (2015). Acoustic Cluster Therapy (ACT)-A novel concept for ultrasound mediated, targeted drug delivery. *Int. J. Pharm.* 495, 1019–1027. doi: 10.1016/j.ijpharm.2015.09.047

Tsutsui, J. M., Xie, F., and Porter, R. T. (2004). The use of microbubbles to target drug delivery. *Cardiovasc. Ultrasound*. 2 (23) doi: 10.1186/1476-7120-2-23

Unga, J., and Hashida, M. (2014). Ultrasound induced cancer immunotherapy. *Adv. Drug Deliv. Rev.* 72 (15), 144–153. doi: 10.1016/j.addr.2014.03.004

van Wamel, A., Healey, A., Sontum, P. C., Kvåle, S., Bush, N., Bamber, J., et al. (2016a). Acoustic cluster therapy (ACT) — pre-clinical proof of principle for local drug delivery and enhanced uptake. *J. Control Release* 224, 158–164. doi: 10.1016/j.jconrel.2016.01.023

van Wamel, A., Sontum, P. C., Healey, A., Kvåle, S., Bush, N., Bamber, J., et al. (2016b). Acoustic Cluster Therapy (ACT) enhances the therapeutic efficacy of paclitaxel and Abraxane® for treatment of human prostate adenocarcinoma in mice. *J. Control Release* 236, 15–21. doi: 10.1016/j.jconrel.2016.06.018

Workman, P., Aboagye, E. O., Balkwill, F., Balmain, A., Bruder, G., Chaplin, D. J., et al. (2010). Guidelines for the welfare and use of animals in cancer research. *Br. J. Cancer*. 102, 1555–1577. doi: 10.1038/sj.bjc.6605642

Conflict of Interest: Authors AH, SKo, SKv, and PS were employed by the company Phoenix Solutions AS at the time of manuscript submission. Authors NB, AH, SKv, and PS are shareholders of Phoenix Solutions AS at the time of submission.

The remaining authors declare that the research was conducted in the absence of any commercial or financial relationships that could be construed as a potential conflict of interest.

The authors declare that this study received funding from Phoenix Solutions AS. The funder had the following involvement with the study: study design, data analysis, decision to publish, and preparation of the manuscript.

frontiers in Pharmacology

ORIGINAL RESEARCH
published: 05 December 2019
doi: 10.3389/fphar.2019.01463

Ultrasound-Sensitive Liposomes for Triggered Macromolecular Drug Delivery: Formulation and *In Vitro* Characterization

Maria B. C. de Matos[1], Roel Deckers[2], Benjamin van Elburg[3], Guillaume Lajoinie[4], Bárbara S. de Miranda[4], Michel Versluis[3], Raymond Schiffelers[5] and Robbert J. Kok[1]*

[1] Department of Pharmaceutics, Utrecht Institute for Pharmaceutical Sciences (UIPS), Utrecht University, Utrecht, Netherlands, [2] Imaging Division, University Medical Center Utrecht, Utrecht, Netherlands, [3] Physics of Fluids Group, MESA+ Institute for Nanotechnology and Technical Medical (TechMed) Center, University of Twente, Enschede, Netherlands, [4] R&D, ABNOBA GmbH, Pforzheim, Germany, [5] Laboratory Clinical Chemistry & Hematology, University Medical Center Utrecht, Utrecht, Netherlands

OPEN ACCESS

Edited by:
Jean-Michel Escoffre, INSERM U1253Imagerie et Cerveau (iBrain), France

Reviewed by:
Anthony Novell, UMR8081 Imagerie par Résonance Magnétique Médicale et Multi-Modalités (IR4M), France
Nicolas Tsapis, UMR8612 Institut Galien Paris Sud (IGPS), France

***Correspondence:**
Roel Deckers
R.Deckers-2@umcutrecht.nl

Specialty section:
This article was submitted to Translational Pharmacology, a section of the journal Frontiers in Pharmacology

Received: *04 July 2019*
Accepted: *13 November 2019*
Published: *05 December 2019*

Citation:
de Matos MBC, Deckers R, van Elburg B, Lajoinie G, de Miranda BS, Versluis M, Schiffelers R and Kok RJ (2019) Ultrasound-Sensitive Liposomes for Triggered Macromolecular Drug Delivery: Formulation and In Vitro Characterization. Front. Pharmacol. 10:1463. doi: 10.3389/fphar.2019.01463

Mistletoe lectin-1 (ML1) is a nature-derived macromolecular cytotoxin that potently induces apoptosis in target cells. Non-specific cytotoxicity to normal cells is one of the major risks in its clinical application, and we therefore propose to encapsulate ML1 in a nanocarrier that can specifically release its cargo intratumorally, thus improving the efficacy to toxicity ratio of the cytotoxin. We investigated the encapsulation of ML1 in ultrasound-sensitive liposomes (USL) and studied its release by high-intensity focused ultrasound (HIFU). USL were prepared by entrapment of perfluorocarbon nanodroplets in pegylated liposomes. The liposomes were prepared with different DPPC/cholesterol/DSPE-PEG2000 lipid molar ratios (60/20/20 for USL20; 60/30/10 for USL10; 65/30/5 for USL5) before combination with perfluorocarbon (PFC) nanoemulsions (composed of DPPC and perfluoropentane). When triggered with HIFU (peak negative pressure, 2–24 MPa; frequency, 1.3 MHz), PFC nanodroplets can undergo phase transition from liquid to gas thus rupturing the lipid bilayer of usl. Small unilamellar liposomes were obtained with appropriate polydispersity and stability. ML1 and the model protein horseradish peroxidase (HRP) were co-encapsulated with the PFC nanodroplets in USL, with 3% and 7% encapsulation efficiency for USL20 and USL10/USL5, respectively. Acoustic characterization experiments indicated that release is induced by cavitation. HIFU-triggered release of HRP from USL was investigated for optimization of liposomal composition and resulted in 80% triggered release for USL with USL10 (60/30/10) lipid composition. ML1 release from the final USL10 composition was also 80%. Given its high stability, suitable release, and ultrasound sensitivity, USL10 encapsulating ML1 was further used to study released ML1 bioactivity against murine CT26 colon carcinoma cells. Confocal live-cell imaging demonstrated its functional activity regarding the interaction with the target cells. We furthermore demonstrated the cytotoxicity of the released ML1 (I.E., After USL were treated with HIFU). The potent cytotoxicity (IC_{50} 400 ng/ml; free ML1 IC_{50} 345 ng/ml)

was compared to non-triggered USL loaded with ML1. Our study shows that USL in combination with HIFU hold promise as trigger-sensitive nanomedicines for local delivery of macromolecular cytotoxins.

Keywords: ultrasound-sensitive liposomes, high-intensity focused ultrasound, triggered drug release, macromolecule encapsulation and release, live-cell imaging, perfluorpentane

INTRODUCTION

Cytotoxins, like diphtheria, shiga, ricin, and mistletoe lectin-1 (ML1), are good examples of nature-derived macromolecules that display outstanding toxicity and, therefore, great potential for cancer treatment. They come from different natural sources but present a common bifunctional A–B structure and belong to the same class of ribosome inactivating proteins (type 2, RIP-II) (Cummings and Schnaar, 2017). Although these proteins vary in the specific mode of action, their cytotoxic effect on target cells follows three common steps: 1) B-chain mediated cell internalization, 2) translocation of the A-chain into the cytosol and 3) irreversible inhibition of the protein synthesis by the toxic polypeptide (Roberts and Lord, 1992). In particular, ML1 is the major active component of mistletoe extracts which are being used in adjuvant cancer treatment (Fritz et al., 2004; Horneber et al., 2008; Kim et al., 2012; Marvibaigi et al., 2014). The intravenous administration of crude extracts or purified lectins is not suitable owing to the severe risks created by their non-specific cytotoxicity for normal cells. Thus, the ability to exploit the potential of ML1 entirely depends on finding nanocarriers that can direct and localize its anti-cancer activity to tumors, while preserving healthy tissues.

Nanomedicine-based targeting approaches can increase the therapeutic index of drugs in two ways. First, they improve treatment localization and increase efficacy, while reducing toxicity to normal tissues. Second, the encapsulated drug compounds are protected from the degradation or elimination processes that naturally occur in a physiological environment. A good example of nanomedicines are liposomes, which can encapsulate both hydrophilic and hydrophobic drugs and be prepared using well-established techniques such as lipid-film hydration or remote loading (Allen and Cullis, 2013). The main drawback of these long circulating stealth formulations, like Doxil®, is the inadequate release of the drug within the tumor microenvironment: although there is high tumor accumulation of encapsulated drug, levels of free drug are only moderate, which limits the therapeutic efficacy. Thus, it is important to focus novel nanocarrier formulations that enable an active release mechanism rather than passive, spontaneous release of the loaded drug. If adequate release can be achieved intratumorally, the therapeutic availability can be restored once the nanomedicine has reached its intended target tissue (van Elk et al., 2016; Hua et al., 2018). Triggerable nanocarriers make use of endogenous or exogenous stimuli to release their cargo. Endogenous stimuli-responsive nanocarriers exploit factors associated with the tumor microenvironment such as low pH, redox gradients or the presence of specific enzymes. Exogenous-responsive nanocarriers respond to external stimuli such as temperature, light or ultrasound (Stylianopoulos and Jain, 2015; Wicki et al., 2015; Al-Ahmady and Kostarelos, 2016). In addition to small molecule delivery, recent reports have shown temperature-triggered drug delivery systems of macromolecules, including ML1 (Yuyama et al., 2000; Saxena et al., 2015; Huang et al., 2017; Matos et al., 2018). Such temperature-sensitive liposomes, however, showed only partial release of the macromolecular cargo: ca. 40% release of FITC-dextran 4 kDa and 10% release of ML1 (Matos et al., 2018). The current thermosensitive release hypothesis postulates that lysolipids form nanopores in the bilayer during the phase transition (~42°C) through which the entrapped drugs can be released (Ta and Porter, 2013) in a size-dependent manner (Matos et al., 2018).

In view of the low release efficiency of temperature-sensitive liposomes, we aimed to develop an alternative nanocarrier system that releases macromolecular payloads more efficiently. We combine liposomes with perfluorocarbon (PFC) nanoemulsions thus creating ultrasound-sensitive liposomes (USL). Upon ultrasound-mediated activation the liposome-encapsulated PFC nanodroplet will vaporize and expand to produce a gas bubble, which will disrupt the liposomal bilayer and trigger drug release, as demonstrated in previous reports using small molecular weight drugs and aiming for intracellular delivery (Javadi et al., 2012; Pitt et al., 2014; Husseini et al., 2015). In the current manuscript, we first optimized the protocol for creating USL using the HRP as macromolecular payload model. Next, USL formulations of ML1 were prepared and evaluated for their encapsulation efficiency, acoustic response, and release by high-intensity focused ultrasound (HIFU). Lastly, we investigated whether ML1 released from ML1-USL is functionally active, by demonstrating its uptake in cancer cells and cytotoxic activity after HIFU triggered release.

MATERIALS AND METHODS

Chemicals

The phospholipids 1,2-dipalmitoyl-sn-glycero-3-phosphocholine (DPPC), and 1,2-distearoyl-sn-glycero-3-phosphoethanolamine-N-PEG_{2000} ($DSPE\text{-}PEG_{2000}$) were purchased from Lipoid (Ludwigshafen, Germany). Cholesterol, 3,3',5,5'-Tetramethylbenzinide (1-Step™ Ultra TMB-ELISA Substrate Solution) and HRP were purchased from Sigma-Aldrich. Perfluoropentane, tech. 90%, was purchased from Alpha Aesar (Germany). ML1 reference standard for ELISA (4.5 µg/ml) was provided by ABNOBA GmbH (Germany).

Anti-ML1 monoclonal antibodies with specificity to ML1 A-chain anti-ML-A-5F5, and anti-ML-A-5H8-HRP (POD) were obtained from SIFIN (Berlin, Germany). CellTiter 96® AQueous One Solution Cell Proliferation Assay (MTS) was provided by Promega. The lipophilic fluorescent dyes 3,3′-dioctadecyloxacarbocyanine perchlorate ($DiOC_{18}(3)$; DIO') and Alexa Fluor® 647 were purchased from Invitrogen.

Methods

Mistletoe Lectin-1 Isolation and Characterization

ML1 was isolated from mistletoe plant material as described before (Matos et al., 2018). In brief, ML1 was isolated by affinity chromatography from mistletoe plant material that was harvested in June from ash tree (*Fraxinus excelsior* L.). After purification, ML1 was characterized by FPLC using a Mono S cation exchange column (Pharmacia/GE Healthcare, Uppsala, Sweden) and a 0.6 M NaCl salt gradient in 0.015 M citrate buffer (pH 4.0) at a detection wavelength of 280 nm. For chromatograms, see (Beztsinna et al., 2018). ML1 concentrations were quantified by UV/Vis at 280 nm (NanoDrop ND-1000; Thermo Fisher Scientific) using an extinction coefficient of 104850 $M^{-1}cm^{-1}$. ML1 concentrations were also quantified by sandwich ELISA, as describe elsewhere (Eifler et al., 1993). Anti-ML-A-5F5 was used as trapping antibody while anti-ML-A-5H8-POD was used as detection antibody.

ML1 was fluorescently labeled with Alexa Fluor 647 (AF647) succinimidyl ester according to the manufacturer's protocol. In brief, 250 µL of 0.02 M bicarbonate buffer pH 8.3 was added to 2 ml of ML1 5.6 mg/ml (12 mg, 0.2 µmol). The diluted protein was reacted with AF647 dye (1:5 protein/dye mol/mol ratio) under stirring at room temperature for 1 h and purified by dialysis (Slide-A-Lyzer 0.5 to 3 ml, MWCO 10000 Da). Purified AF647-ML1 was characterized by analytical size-exclusion chromatography on a Bio Sep 3000 column (20 min, PBS 1 ml/min) and NanoDrop (AlexaFluor extinction coefficient 239,000 M^{-1} cm^{-1}). The typical final ML1:dye ratio was 2:1 (mol/mol). Labelled ML1 was kept protected from the light at 4°C until further use.

Preparation of Nanocarrier Formulations

The preparation of USL involves several steps as depicted in the scheme below (**Figure 1**). Each of the steps is described in detail in the following sections.

Preparation of PFC Nanoemulsions

PFC nanoemulsions were prepared by thin film-hydration method (Javadi et al., 2012; Lattin et al., 2015). A lipid film containing 10 mg (15 µmol) of DPPC was prepared by evaporating the solvents from a 0.5-ml DPPC solution (20 mg/ml in chloroform) using a rotavapor at 60°C. The film was kept for 1 h in a nitrogen stream at room temperature before it was hydrated with 2 ml HBS (10 mM HEPES buffer pH 7.4 containing 150 mM NaCl)

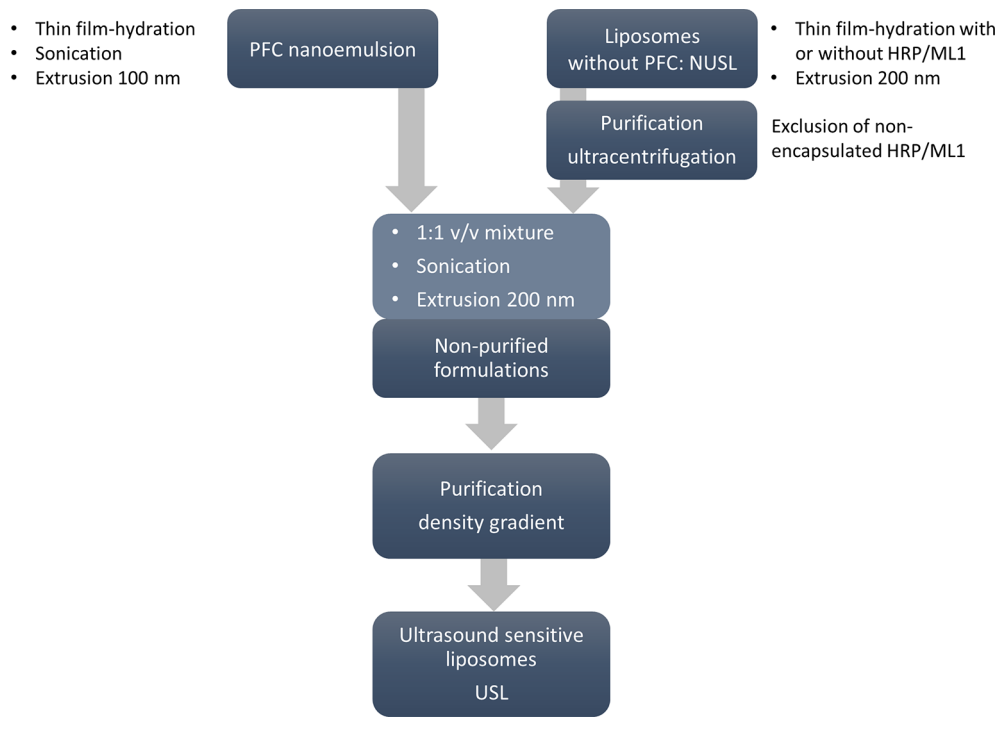

FIGURE 1 | Workflow for the preparation of USL. First PFC/DPPC were prepared by thin film-hydration method and the resulting emulsion was downsized by sonication and extrusion through 100-nm pore size membrane. In parallel, the non-ultrasound sensitive liposomal formulations (NUSL; with and without cargo) were prepared by thin film-hydration and extrusion through 200-nm extrusion membranes and purified to remove the non-encapsulated cargo. Finally, PFC nanoemulsion and NUSL were mixed in the same volume ratio using sonication and one last step of extrusion through 200-nm pore size membrane. The formulations were purified by sucrose gradient to separate non-encapsulated drug, nanoemulsions, and empty liposomes from the final USL.

thus yielding DPPC vesicles with a final concentration of 7.5 mM; the resulting DPPC dispersion was cooled to 4°C on an ice bath. Perfluoropentane (0.6 ml; 3.5 mmol; density 1.6 g/ml) was added to the DPPC dispersion, and the mixture was sonicated (Branson Sonifier 20 kHz 13 mm) 3 times for 30 sec on the lowest energy input (10% duty cycle), with 1 min interval between each sonication. The resulting emulsion was extruded ten times over 100 nm polycarbonate extrusion membranes (Whatman) to reduce the size and narrow the polydispersity of the nanodroplets, as was confirmed by dynamic light scattering (DLS) using a Zetasizer Nano-S (Malvern Instruments).

Preparation of Liposomes

Liposomes with different lipid compositions were also prepared by the lipid film and extrusion method. DPPC/Cholesterol/DSPE-PEG_{2000} lipid molar ratios before combination with PFC nanoemulsions (named NUSL, non-ultrasound sensitive liposomes) were 60/20/20 for NUSL20; 60/30/10 for NUSL10; 65/30/5 for NUSL5; control liposomes were prepared with DPPC/Cholesterol/DSPE-PEG_{2000} 65/30/5 mol ratio only. For fluorescently labeled liposomes, 0.5 mol% of DIO' was added when applicable. In brief, 80 μmol total lipid (TL) was dissolved in 4 ml 1:1 chloroform/methanol. Solvents were evaporated in a rotavapor for 20 min at 60 °C. The formed lipid films were kept for 1 h in a nitrogen stream and hydrated at 50°C with 1 ml HBS (in case of control liposomes) or HBS solutions of ML1 (1.5 mg/ml) or HRP (0.2 mg/ml). After reconstitution of liposomes, the final lipid concentration was 80 mM. Liposomes were extruded ten times over 400 and 200 nm pore-size polycarbonate filters at 45°C. Non-encapsulated ML1 and HRP were removed by ultracentrifugation of the liposomes (Beckmann ultracentrifuge, 2 cycles, 55000 rpm, 1 h, 4 °C) and resuspension in 1 ml HBS.

Combination of PFC Nanoemulsion and Liposomes into USL

USL were formed by mixing the DPPC-PCF5 nanoemulsion and the NUSL liposomes in a 1:1 volume ratio. The resulting solutions were sonicated (Branson Sonifier 20 kHz 13 mm) 3 times for 30 sec on the lowest energy input (10% duty cycle), with 1 min interval between each sonication, on ice bath. Finally, USL were extruded over 200 nm pore size polycarbonate membranes. The theoretical DPPC/Cholesterol/DSPE-PEG_{2000} lipid compositions of the final formulations (named USL, ultrasound sensitive liposomes) were USL20: 65/17/17; USL10: 63/30/7; USL5: 70/26/4. All USL formulations were purified by sucrose density gradient centrifugation to remove un-encapsulated drugs, nanoemulsions, and empty liposomes. In brief, sucrose solutions (10, 15, 20, 25, 40 and 50 w/w%) were prepared by dissolving pure sucrose in deionized water. The sucrose solutions with different mass fractions were carefully added to 15-ml ultracentrifuge tubes (Beckmann) in different volumes (2, 2, 2, 1, 1, 1 ml, respectively). Unpurified USL dispersion (1 ml) was carefully added to the top of the gradient and centrifuged at 35000 rpm for 16 h and 4°C (Beckmann ultracentrifuge). Non-encapsulated PFC nanoemulsion droplets have the highest density (1.6 g/ml) and settled at the bottom of the tube; free ML1 and emulsion-free NUSL had the lowest density and were collected in the upper sucrose layers. USL were recovered from the 20% sucrose layer. Isolated fractions were dialyzed against 2 L of HBS buffer for 24 h. USL and other fractions stored at 4°C until further studies.

Characterization of PFC Nanoemulsions and Liposomes

Size and Polydispersity Index

The hydrodynamic diameter and polydispersity index of all lipid formulations were measured by dynamic light scattering using a Zetasizer Nano-S (Malvern Instruments). Appropriate dilutions were made in HBS buffer.

Lipid Recovery

The lipid recovery (TL) was determined by measuring the amount of phospholipids in 160 liposomal aliquots according to the method of Rouser et al. (1970). Sodium biphosphate was used as a reference. The blue colored reaction product was detected at 797 nm spectrophotometrically (SPECTROstar plate reader, BMG Labtech, Ortenberg, Germany).

Recovery of Payloads—HRP and ML1

An aliquot of 20 L of liposome dispersion was diluted in 1000 μL of HBS, to which TritonX-100 0.1% v/v was added to destroy the liposomal bilayer. HRP was determined enzymatically by eHRP–TMB reaction. In brief, 100 μL of HRP was added to the wells of a 96-well plate. The substrate (TMB, 25 μL/well) was added, and the mixture was allowed to react for 2 min 30 sec, after which the reaction was stopped by addition of 25 μL/well 1 M sulfuric acid. The yellow colored reaction product was detected at 450 nm with the spectrometric plate reader. ML1 was determined by sandwich ELISA as described above. Loading contents (LC%) and encapsulation efficiencies (EE%) were calculated as follows:

$$LC\% = \frac{nmol\ payload}{nmol\ total\ lipid} \times 100 \quad (1)$$

$$EE\% = \frac{payload_{end}}{payload_{start}} \times 100 \quad (2)$$

where, $payload_{end}$ is payload of HRP or ML1 determined experimentally after formulation and purification, and $payload_{start}$ is the starting amount of payload. Concentrations are expressed in μg/ml.

Transmission Electron Microscopy

The inclusion of the nanoemulsion in the liposomes was confirmed by negative staining transmission electron microscopy (TEM). In brief, NUSL or USL samples were placed on a carbon-coated copper grid (300 mesh; Plano GmbH, Wetzlar, Germany) and allowed to settle for 2 min before being blotted away by filter paper. An ammonium molybdate solution (1%) was added to the grid for 2 min, after which the solution was blotted away, and the grid was allowed to dry. Images were recorded at 120 kV on a Philips CM12 transmission electron microscope coupled to a GATAN Multiscan 400HP camera.

Stability Studies and Release Experiments

Storage Stability

Storage stability of liposomes was assessed at 4°C and included colloidal stability (i.e., nanoparticle size and polydispersity) and drug retention capacity over a time period of 4 weeks. At each time point, small aliquots were diluted and analyzed by DLS or analyzed for released cargo (i.e., HRP) by enzymatic analysis. Drug retention capacity was calculated as follows:

$$\text{Drug retention } \% = \frac{\text{payload}_0 - \text{leaked}_t}{\text{payload}_0} \times 100 \quad (3)$$

where $payload_{(0)}$ is the amount of encapsulated HRP at the initial timepoint of the stability study and leaked $_{(t)}$ is the amount of HRP detected in the supernatant of the liposomes.

Ultrasound Triggered Release Experiments

Ultrasound-triggered release experiments were performed using an in-house developed HIFU setup (Oerlemans et al., 2013) consisting of a single-element US transducer (Imasonic, Besançon, France) placed inside a water bath containing a sample holder for a PCR tube. The PCR tube is positioned at the focal point of the single-element focused US transducer. The HIFU transducer had a focal length of 80 mm and a diameter of 120 mm. The pulsed (pulse repetition period = 50 ms, duty cycle = 1%) sinusoidal signal (1.3 MHz) was generated using a RF generator and amplifier (AG1021). The dimensions of the focal point were 1 × 1 × 3 mm (at −3 dB). Liposomal stock solutions (USL, NUSL), ML1 and HRP reference solutions and 1:1 v/v mixtures of PFC nanoemulsion plus NUSL were diluted 50-fold in HBS; 170 µl was transferred into the reaction vessel (170 µL PCR tubes; BioRad) and positioned in the HIFU setup. Samples were exposed to ultrasound (see exposure conditions below) and immediately thereafter transferred to an ice bath (4°C). Reference samples that had not been treated with ultrasound were kept at 4°C and were used as background levels of ML1 and HRP. In all cases, not more than 2% of background release was observed. Samples treated with TritonX-100 (0.1% v/v) were used as reference in which full release had occurred. Release of HRP was analyzed without further processing of the sampled aliquots. In the case of ML1, samples were processed by Vivaspin ultrafiltration (300 kDa MWCO; Sartorius) after which the ultrafiltrate was analyzed for released ML1 by ELISA as described above. In all release experiments, the percent release of the compounds was quantified by using the equation:

$$\text{Release } \% = \frac{\text{amount released}}{\text{total release by TritonX100}} \times 100 \quad (4)$$

where amount released is the amount of HRP or ML1 at a certain time point or fixed temperature, and total release by TritonX100 is the total mass found after liposomes were treated with Triton X-100.

HIFU Exposure Conditions

HIFU exposure conditions were optimized by (1) varying the peak negative pressure (2–24 MPa) conditions at constant exposure duration (1 min at room temperature), and (2) by varying the exposure time at constant peak negative pressures (5 or 24 MPa at room temperature). The samples were immediately transferred to the ice bath until further analysis as described above. Peak negative pressures in the focal point were calibrated as a function of input voltage using a fiber-optic hydrophone (Precision Acoustics) in a tank filled with water. The thermal effect of the HIFU exposure conditions were measured inside the PCR tube immediately after ultrasound exposure using a calibrated fiber optic thermometer (Neoptix, Canada).

Acoustic Characterization

Transducers

Three single-element transducers were used to characterize the acoustic behavior of nanoemulsions and liposomes: one for sonication, one for cavitation detection and one for attenuation measurement. The sonication transducer was calibrated using a fiber-optic hydrophone (Precision Acoustics). An arbitrary/function generator (WW1281A; Tabor Electronics) was utilized to generate twenty sinusoidal pulses of 100 cycles of 1.3 MHz at a pulse repetition frequency (PRF) of 100 Hz. This signal was then amplified using a 56-dB power amplifier (VBA100-200; Vectawave) and used to excite the transmitting C302 transducer (90% bandwidth, panametrics).

A passive receiving transducer (Vermon, SR 885C1001, Tours, France, 3 MHz, −6 dB relative bandwidth = 200%) was placed at 90° to the axis of the active sonicating transducer and detected acoustic emissions produced by the sonicated nanoemulsions and liposomes. Furthermore, a passive V304 (panametrics) receiving transducer was placed in line with active sonicating transducer to measure the attenuation of the transmitted signal due to scattering and/or absorption by nanoemulsions and liposomes. The signals collected from receiving transducers were acquired with a sampling frequency of 12.5 MS/s using a digital oscilloscope (TDS5034B; Tektronix, Beaverton, OR) and sent to a PC for analysis. Triggering was ensured by a pulse delay generator (Berkeley Nucleonics, model 575) controlled directly *via* a computer.

The experimental setup consisted of an acrylic tank filled with degassed water at room temperature, three transducers and an exposure chamber. The exposure chamber was aligned in the focal zone of the three transducers. The exposure chamber was designed using Solidworks, and printed with a 3D printer (RapidShape S30L). The front, back, and side of the sample chamber were covered with mylar with a thickness of less than 175 µm. The fourth side of the chamber contains a stirrer to avoid buoyancy affects or stagnation.

The exposure chamber was slowly filled with the nanoemulsions or liposome emulsions using a syringe. Subsequently, the sample was sonicated at 1.5 or 3.0 MPa with a twenty 100-cycle ultrasound pulses. After each measurement, the sample was removed from the exposure chamber, and the chamber was flushed with degassed, deionized water. All the experiments were performed at room temperature (20°C).

Cavitation and Attenuation Detection

To analyze the acoustic emissions, the recorded data were processed using fast Fourier transform (FFT) analysis in

MATLAB (MathWorks, Natlick, MA, USA) to create frequency spectra (see also **Figure 2**). The harmonics were defined as the maxima within ± 250 kHz around the harmonic frequency (n*f, f: excitation frequency, n = 1, 2, 3, or 4) in the frequency spectrum. The ultraharmonics were defined as the maxima within ± 100 kHz around the ultraharmonic frequency (m/2*f, f: excitation frequency, m = 3, 5, or 7) in the frequency spectrum. The subharmonics were defined as the maxima within ± 100 kHz around the subharmonic frequency (f/2, f: excitation frequency) in the frequency spectrum. Broadband noise was defined as the root-mean squared amplitude of the frequency spectrum after excluding the harmonics, ultraharmonics, and subharmonics as defined above. Attenuation, measured in dB, was calculated using the equation:

$$L_{\mathrm{dB}} = -20 \cdot log10 \frac{A}{\mathrm{A}_{\mathrm{ref}}} \tag{5}$$

with A the amplitude of the first harmonic of the transmitted signal with nanoemulsion, USL or NUSL in the exposure chamber and A_{ref} the amplitude of the first harmonic of the transmitted signal with water in the exposure chamber.

Bioactivity of Free and Formulated ML1

Bioactivity of ML1 that had been encapsulated in liposomes and released by HIFU was studied in two experimental settings that reflect either the uptake of ML1 in target cells (functionality of the A-chain of ML1) or that represent the biological activity of ML1 (cytotoxin activity). All experiments were conducted with murine CT26 colon carcinoma cells that has been obtained from American Type Culture Collection (ATCC). RPMI cell culture media, PBS, and FBS were purchased from Sigma-Aldrich, and OptiMem was obtained from Gibco. CT26 cells were cultured in RPMI supplemented with 10% FBS, at 37°C in a 5% CO_2 and humidified atmosphere. For all cell experiments, CT26 colon carcinoma cells were first seeded in 96-well plates (10000 cells/well) and allowed to adhere for 24 h prior to the experiment.

Uptake of Released ML1

Uptake studies were conducted with HIFU-treated DiO'-labeled liposomes (NUSL, USL, DiO' at 0.5% mol of total lipid) that had been loaded with AF647-labeled ML1. Liposomes were diluted 1:10 in OptiMEM (final concentrations 2 g/ml AF647-ML1 and 7 mM total lipid) and treated with HIFU as described above with the following acoustic settings: 5 MPa for 1 min exposure and 24 MPa for 1 min exposure. Samples were transferred to the ice bath and

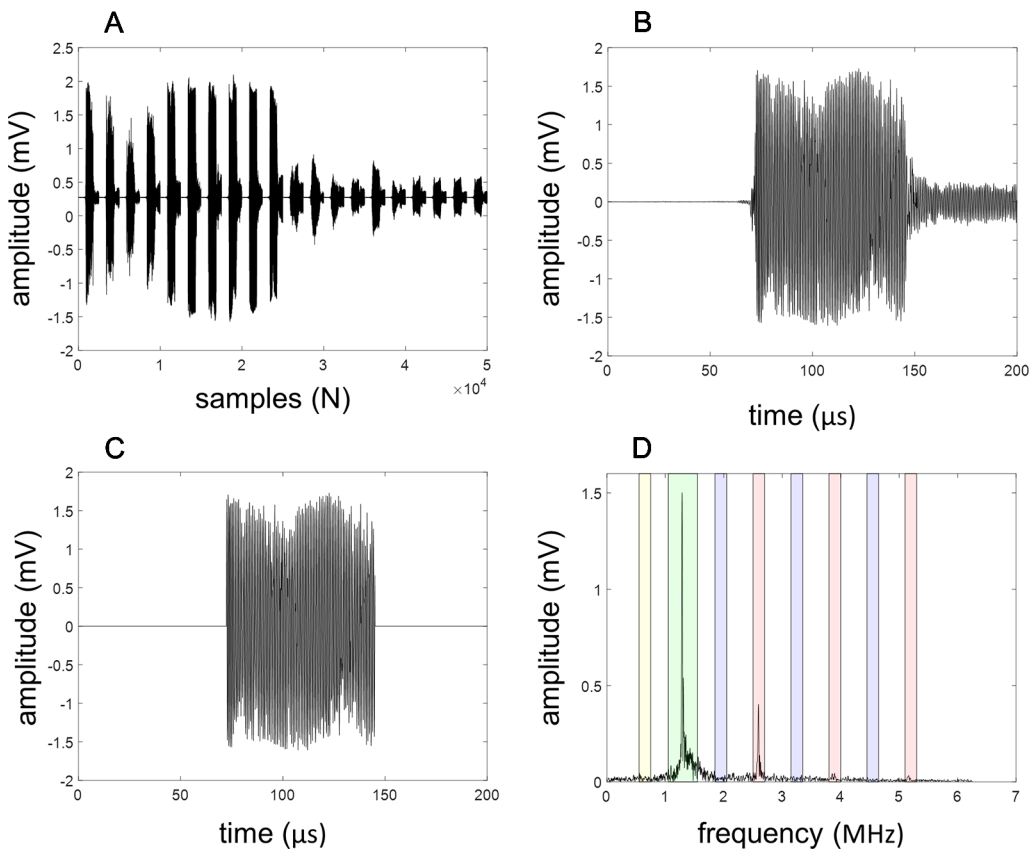

FIGURE 2 | Illustration of acoustic characterization. A total of 20 pulses existing of 100 cycles were collected **(A)**. The detected signal from each pulse **(B)** is first trimmed **(C)** and subsequently converted to its frequency spectrum using a fast Fourier transformation **(D)**. The amplitude within the selected regions (red = harmonics, green subharmonic, blue = ultraharmonics) are calculated for each pulse and plotted as a function of number of pulses.

used for uptake studies without further processing. Before adding the samples, nuclei of CT26 cells were pre-stained with Hoechst 33342. After replacement of the culture medium with the HIFU-treated samples, 96-well µClear® black plates (Greiner) were transferred into a Yokogawa Cell Voyager CV7000s microscope (Tokyo, Japan). Live-cell confocal microscopy images were taken for 4 h at 37°C and analyzed for uptake of liposomes (red), uptake of ML1 (green), and nuclei (blue). Uptake was semi-quantified with Columbus® image analysis software (PerkinElmer) using automated protocols for nuclei and cytoplasm detection and build-in functionalities for fluorescence intensity determination.

Cytotoxic Activity of ML1

Cytotoxic activity of ML1 was indirectly measured by a mitochondrial activity assay that quantified the number of surviving cells. For these experiments, non-labeled ML1 and non-labeled liposomes were used. ML1 containing liposomes (NUSL, USL, control liposomes) were diluted in RPMI+10%FBS (20 µl in 1000 µl) and 170 µl of the diluted sample was then exposed to HIFU as described above with the following acoustic setting: 5 MPa for 1 min exposure and 24 MPa for 1 min exposure. Samples were transferred to the ice bath and analyzed for cytotoxic activity after dilution of 50 µl of the samples with 80 µl of culture medium. The obtained samples were transferred onto the cells and incubated under culture conditions for 4 h.

Final concentrations incubated with the cells were 80 to 800 ng/ml for ML1 and 0.4 to 8 mM TL. After refreshing the media with drug-free culture medium, cells were cultured for an additional 44 h in the incubator before determining the number of surviving cells according to the supplier's instruction (CellTiter 96®; AQueous One Solution Cell Proliferation Assay). Bioactivity IC_{50} values of each treatment were calculated by non-linear dose-response curve fitting using GraphPad Prism software. Appropriate reference samples included free ML1, blank liposomes, and samples not treated with HIFU ultrasound.

Data Analysis

Data are presented as the average and standard deviation of three independent experiments with triplicate samples unless stated otherwise. Data were statistically tested in GraphPad Prism 7 (Graph-Pad Software, Inc, San Diego, CA) by comparison of groups with different tests (see figure captions for details of performed tests). Differences between groups with $p < 0.05$ were considered statistically significant.

RESULTS AND DISCUSSION

Characterization of PFC Nanoemulsions and Liposomes

The final size of PFC nanoemulsion was 118 ± 11 nm (PDI, 0.26 ± 0.01) which is the expected size range after extrusion over 100 nm filters. Although PFC nanoemulsions were relatively stable. The size and PDI of PFC nanodroplets doubled upon storage at 4°C in 48 h, and after 4 days the size had increased drastically (1120 nm; PDI, 1.0). We therefore systematically used freshly prepared PFC nanoemulsions for the experiments.

The characteristics of NUSL and the corresponding USL are shown in **Table 1**. Before their loading with PFC nanodroplets NUSL10 and NUSL5 displayed sizes and PDI within the expected range (size 156–191 nm, PDI 0.11-0.09). NUSL20 showed sizes two times smaller than expected (i.e., 95 nm instead of ~200 nm), which may be related to the formation of DSPE-PEG_{2000} micelles due to very high concentrations of this lipid in the formulation (Johnsson and Edwards, 2003; Johansson et al., 2005; Sandström et al., 2008; Evjen et al., 2010; Vainikka et al., 2011). Although one would expect an increase in PDI for such a mixture of two subsets of nanoparticles, the DLS-algorithm based single population analysis is unable to resolve this accurately (van Gaal et al., 2010). Considering the standard deviations, similar encapsulation efficiencies for HRP and ML1 were found for all NUSL formulations, i.e. no specific trend was observed towards the lipid composition.

After mixing the PFC nanoemulsion with the NUSL by sonication to enable the inclusion of PFC nanodroplets, the now-formed USL were extruded again to reassure a monodispersed size distribution. The average size remained unchanged but we observed an increase in PDI by ca. 2-fold (not shown), as anticipated by the fact that it is a mixture of two populations with different sizes.

TABLE 1 | Physicochemical characteristics and loading results of NUSL and USL.

Formulation		Size, nm	PDI	TL, %	EE%	LC µg drug: µmol lipid
NUSL HRP	NUSL20	95 ± 1	0.12 ± 0.02	58 ± 1	29 ± 1	3.7 ± 0.2
	NUSL10	156 ± 2	0.11 ± 0.01	63 ± 2	40 ± 1	4.6 ± 0.3
	NUSL5	191 ± 4	0.09 ± 0.03	62 ± 2	25 ± 3	3.6 ± 0.1
USL HRP	USL 20	98 ± 2	0.17 ± 0.02	12 ± 1	3 ± 1	1.1 ± 0.3
	USL10	209 ± 13	0.15 ± 0.02	17 ± 1	7 ± 1	2.0 ± 0.1
	USL5	181 ± 1	0.06 ± 0.05	11 ± 1	7 ± 1	3.2 ± 0.2
NUSL ML1	NUSL20	97 ± 2	0.11 ± 0.03	66 ± 2	21 ± 1	4.1 ± 0.1
	NUSL10	186 ± 4	0.12 ± 0.01	72 ± 1	23 ± 1	4.5 ± 0.1
	NUSL5	179 ± 5	0.07 ± 0.04	59 ± 2	21 ± 1	4.7 ± 0.2
USL ML1	USL 20	88 ± 8	0.16 ± 0.01	18 ± 1	2 ± 1	2.9 ± 0.4
	USL10	179 ± 1	0.15 ± 0.01	14 ± 2	4 ± 1	6.7 ± 0.6
	USL5	201 ± 8	0.07 ± 0.03	15 ± 1	4 ± 1	6.5 ± 0.4

Lipid molar ratio of DPPC/Cholesterol/DSPE-PEG2000 for (N)USL20: 60/20/20; for (N)USL10: 60/30/10; for (N)USL5: 65/30/5. TL%, total lipid yield; EE%, encapsulation efficiency; LC, loading content expressed as µg drug to µmol lipid ratio. Average ± standard deviation of 2 independent samples.

USL were separated from non-encapsulated nanoemulsion and non-encapsulated HRP or ML1 by sugar density gradients. The top layer contained mainly non-encapsulated proteins, fraction 1 (10% sucrose) contained purified NUSL, fraction 2 (20% sucrose) contained purified USL and the bottom fraction (50% sucrose) contained the nanoemulsion. Fraction 2 or USL was dialyzed to replace the external sugar solution by fresh HBS. The sizes and PDI of the final preparations were comparable to their corresponding NUSL formulation. When comparing the PDI of purified USL with the PDI of the USL before sucrose gradient purification, the decrease in PDI suggests that we have removed the non-encapsulated PFC nanodroplets and that we obtained a monodisperse sample. The encapsulation of the nanoemulsion was further confirmed by TEM (**Figure 3**). The recovery of lipids (TL%) and encapsulated cargo (EE%) decreased substantially when NUSL were converted into USL, but the LC remained constant. We attribute the numerical decrease to the USL formation process: to prepare USL, that is, to incorporate the PFC nanoemulsion in the liposomes, it is necessary to apply sonication to the NUSL already encapsulating the drug. This step includes not only transient opening of the NUSL bilayer and thus loss of some of the encapsulated cargo, but also partial replacement of the internal volume by PFC nanoemulsion. Moreover, the purification over sugar density gradients also removed liposomal vesicles that had not been loaded with PFC, which was responsible for ~80% loss in recovery of both phospholipid and loaded drugs. Since LC% were not affected largely, it can be inferred that the loss of drugs was primarily related to low inclusion of PFC and removal of NUSL, rather than leakage of HRP or ML1 during sonication and extrusion.

Stability Studies and Release Experiments

Storage Stability

Formulations containing 5 and 10 mol% DSPE-PEG$_{2000}$ with and without PFC nanoemulsion, i.e. (N)USL5 and (N)USL10, were stable with respect to particle size (**Figure 4A**) as well as drug retention (**Figure 4B**) when stored at 4°C for 1 month. On the contrary, (N)USL20 leaked 50% of the loaded HRP in the first week of storage, and also showed decreases in size revealing

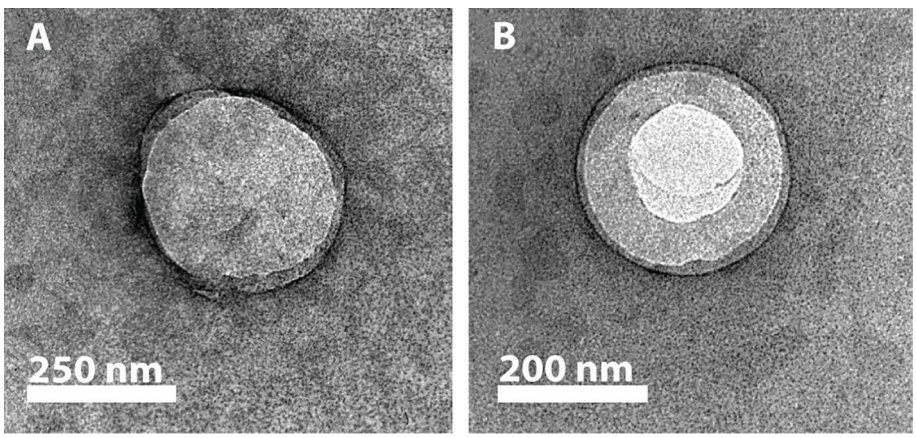

FIGURE 3 | Representative TEM images of negatively stained NUSL10 **(A)** and USL10 **(B)** after purification. The images show the absence (NUSL) and the presence (USL) of nanoemulsion in the core of the resulting liposomes.

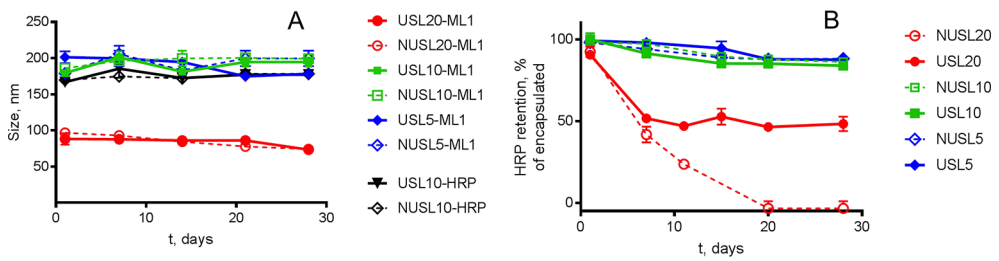

FIGURE 4 | Storage stability of USL at 4°C in HBS buffer. Panel **(A)** shows size measurements, obtained by DLS over a period of 30 days, of nanoparticles (NUSL and USL) loaded with HRP and ML1. Panel **(B)** shows HRP retention. In both graphs, the colors of the lines and the symbols correspond to the same lipid composition: the red line corresponds to liposomal formulations composed of initial 20 mol% DSPE-PEG$_{2000}$ and containing (full line and circle, USL20) or not (dashed line and empty circle, NUSL20) PFC nanoemulsion; the green line corresponds to liposomal formulations composed of initial 10 mol% DSPE-PEG$_{2000}$ and containing (full line and square, USL10) or not (dashed line and empty square, NUSL10) PFC nanoemulsion; the blue line corresponds to liposomal formulations composed of initial 5 mol% DSPE-PEG$_{2000}$ and containing (full line and diamond, USL5) or not (dashed line and empty diamond, NUSL5) PFC nanoemulsion. Data are the average ± standard deviation of three independent samples.

colloidal instability. This can be related to the amounts of 15% to 20% DSPE-PEG_{2000} in the (N)USL formulation. DSPE-PEG_{2000} amounts above 12 mol% are known for the formation of micelles and increased instability of liposomal bilayers (Johnsson and Edwards, 2003; Johansson et al., 2005; Sandström et al., 2008; Evjen et al., 2010; Vainikka et al., 2011). Since both NUSL20 and USL20 showed similar leakage in the first week of storage, PFC nanoemulsion does not seem to play a role in the instability.

Acoustic Characterization

Figures 5 A–D depict the first harmonic (H1, 1.3 MHz), second harmonic (H2, 2.6 MHz), subharmonic (0.65 MHz) and broad band noise responses, respectively, from the PFC nanoemulsion, USL10, NUSL10, and water. The second harmonic, subharmonic, and broadband noise signals emitted by USL were clearly stronger as compared to signals emitted by PFC nanoemulsions, NUSL, and water. The presence of broadband emission is characteristic for inertial cavitation and therefore indicates that cavitating microbubbles were formed within the USL10 sample. The harmonic, subharmonic, and broadband noise signals of USL were pressure dependent and gradually decreased in time. As the peak negative pressure was increased from 1.5 MPa to 3.0 MPa the non-linear acoustic emission signals of USL increased in amplitude and remained elevated over a longer duration, i.e. more pulses. The gradual decrease of acoustic emission with increasing number of pulses sent is likely related to the depletion of the sample by disrupting particles that were activated by preceding pulses and activating new particles that are less responsive. The PFC nanoemulsions also showed some non-linear acoustic emission signals during the first pulses, whereas the non-linear acoustic emission signals of water were absent, as expected. Exposure of NUSL10 to elevated peak negative pressure (3.0 MPa) also causes inertial cavitation, but the activity did not decrease in time, by opposition to all other emulsions. **Figure 5E** shows the attenuation, measured in dB, of the transmitted signal for the PFC nanoemulsion, USL10, NUSL10, and water. For the USL the attenuation declined with increasing number of pulses, mirroring the acoustic scattering, i.e. the sample is depleted by

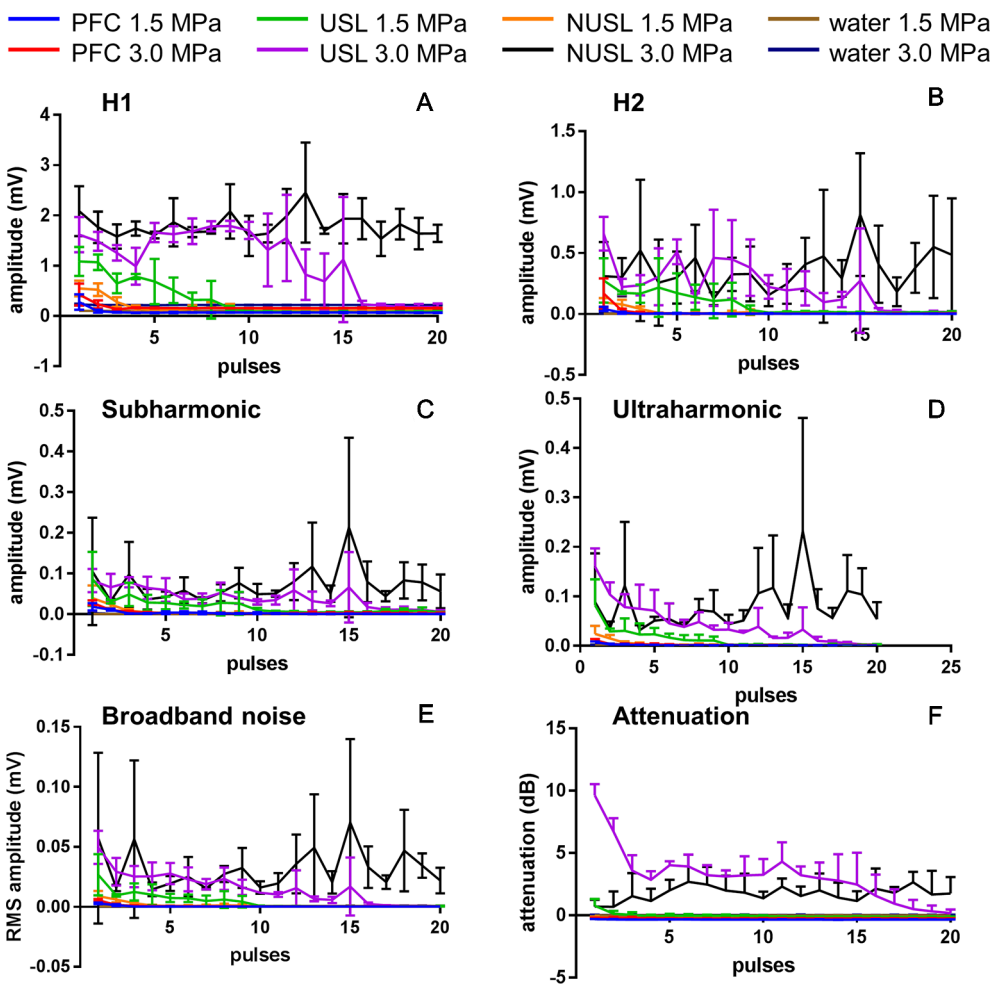

FIGURE 5 | Acoustic characterization of PFC nanoemulsion, USL10 and NUSL10 at 2 acoustic pressures (1.5 and 3.0 MPa). The amplitude of the first **(A)** and second **(B)** harmonic frequency and of the subharmonic frequency **(C)** and ultraharmonic frequency **(D)**, the RMS value of the broadband noise **(E)** of the scattered signal as well as the attenuation **(F)** of the transmitted signal were measured. N = 3.

the disruption of the particles. PFC and NUSL samples did not cause significant attenuation of the ultrasound pulses, except for NUSL10 at 3.0 MPa. The origin of this increased and sustained attenuation and scattering will deserve further investigation in the future. Beyond the acoustic characteristics, these measurements provide proof regarding the formation of cavitation bubbles from the emulsion. These microbubbles, in all likelihood, play a major role in the observed drug release.

HIFU-Triggered Release Experiments

To investigate HIFU-triggered release of macromolecular drugs from USL, we assessed acoustic time- and pressure-dependent release of HRP and ML1 (**Figures 6** and **7**, respectively). **Figure 6** shows the release of HRP (panel A) and ML1 (panel B) from USL10 over time at fixed peak negative pressure (24 MPa). With both macromolecules as cargo, we obtained highest release for 1 to 2 min HIFU exposure time. At higher acoustic pressures or longer exposure times, the percentage of HRP and of ML1 recovered decreased, and we speculate that it is due to the cargo damage (not shown).

Remarkably, NUSLs also showed HIFU triggered release, although the released amounts were considerably lower than observed for USL. It has been previously observed that normal liposomes can respond to ultrasound fields (Evjen et al., 2010; Oerlemans et al., 2013). Doxorubicin was released from such so-called sonosensitive liposomes (DSPE/DSPE-PEG_{2000}/Chol 62:8:30 mol%) 7-fold more than from reference doxorubicin-loaded liposomes (HSPC/DSPE-PEG_{2000}/Chol 57:5:38 mol%) (Evjen et al., 2010). For USL, however, bubble nucleation is promoted directly within the liposomes by the low stability perfluorocarbon, which explains a much more important release. As a result, larger macromolecules like HRP and ML1 can be released from DSPE-PEG_{2000}-containing liposomes but the release extent can be significantly improved by incorporating the PFC nanoemulsion.

To investigate whether the HIFU-triggered release of USL really depends on the inclusion of PFC nanodroplets inside the liposomes, we evaluated the release of HRP from mixtures of NUSL and PFC nanoemulsions. Since we did not further treat the mixture of PFC and NUSL to promote encapsulation of the PFC nanodroplets, this formulation represented the physical mixture of two different nanoparticles, rather than a combined nanoparticle. HRP release after different peak negative pressures (2–24 MPa) and fixed exposure time (1 min) is shown in **Figures 7A–C**. The USL formulations showed superior release, when compared to the NUSL formulations or the NUSL mixed with nanoemulsion. The formulations containing emulsion only on the outside (NUSL*x*+PFC) showed an intermediate release performance. This confirms the importance of the presence of cavitation-promoting PCF directly inside the liposomes. Intermediate response resulting from the presence of the nanoemulsion near the liposomes is influencing drug release, possibly by enhanced energy transfer to the lipid bilayer that can deform or disrupt the bilayer. The phase transition of PFC from liquid to gas, which is in the range of 1 to 10 MPa (Aliabouzar et al., 2018), and the resulting expansion seems a plausible mechanism for the more efficient payload release. Thermal effects can be excluded since the maximum temperature increase upon HIFU exposure did not exceed 2 degrees (data not shown). USL20 and USL10 released the highest amounts of HRP while USL 5 released the least of the three formulations. However, USL20 showed the least storage stability, as was previously noticed. Overall, USL10 stands out as the best formulation and emphasizes the need to have the nanoemulsion inside the liposomes to maximize ultrasound-triggered release. The lower pressures (i.e. 2 and 5 MPa) cause already a significant macromolecular drug release (>50%) and can most likely be used *in vivo* without causing adverse events. In contrast, care has to be taken when the higher pressures are used *in vivo* since these pressures may cause undesired tissue damage (Health Protection Agency, 2010).

USL5 and USL20 containing ML1 were additionally tested for HIFU-triggered release at the lowest range of acoustic pressures and the results for ML1 release are summarized in **Figures 7D**, **E**. Similar to HRP-loaded USL formulations, USL5 released less ML1 than its counterparts USL20 and USL10 and we believe this can be attributed to the higher stability provided by a smaller amount of DSPE-PEG_{2000}, as discussed previously. In conclusion, the formulations can be ordered according to their overall performance: USL20 < USL5< USL10. We chose USL10 carry on the *in vitro* bioactivity and continued our experiments using 1 min exposure time and 5 and 24 MPa peak negative pressures. Both pressures are significantly above the cavitation threshold, see section 3.2.2.

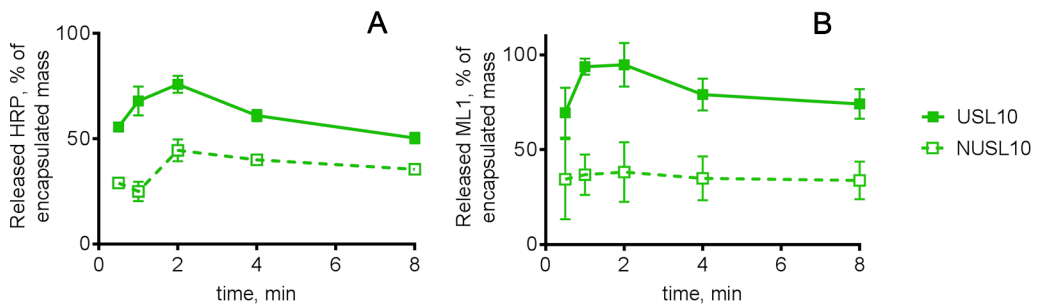

FIGURE 6 | HRP and ML1 release from USL10 and NUSL10 as function of exposure time at fixed negative pressure (24 MPa), n = 4. In both graphs, the full line and full squares correspond to USL10, and the dashed line and empty squares correspond to NUSL10. For each exposure time the difference in HRP **(A)** or ML1 **(B)** release between USL10 and NUSL10 samples was significant (multiple t-test for all time points with Holm-Sidak correction).

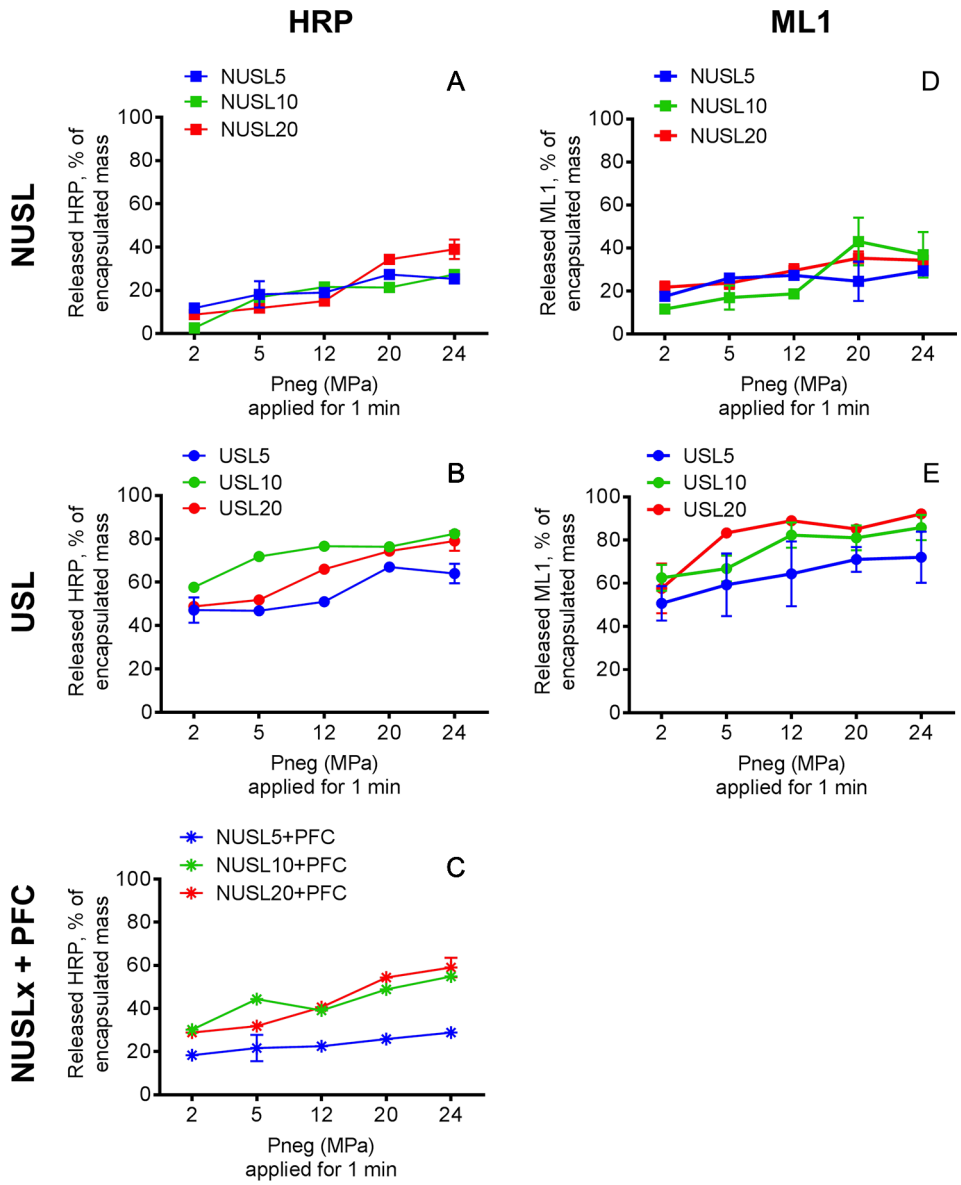

FIGURE 7 | HRP release profiles from **(A)** NUSL (squares), **(B)** USL (circles) and **(C)** NUSL (stars) spiked with nanoemulsion, and ML1 release profiles from **(D)** NUSL formulations (squares) and **(E)** USL. All samples were exposure to HIFU for 1 min and variable negative pressure (2–24 MPa) and subsequently analyzed. In all graphs, the colors of the lines correspond to the same lipid composition: the red line corresponds to liposomal formulations composed of initial 20% mol DSPE-PEG2000; the green line corresponds to liposomal formulations composed of initial 10% mol DSPE-PEG2000; the blue line corresponds to liposomal formulations composed of initial 5% mol DSPE-PEG2000. Background release (i.e., without HIFU) was insignificant (<2%) for the tested conditions. Data are the average ± standard deviation of three independent samples. A 2-way ANOVA with Tukey's multiple comparisons test showed that at each pressure and for each lipid composition the HRP release from USL was significantly higher compared to NUSL and NUSLx + PFC. Similarly, a 2-way ANOVA with Sidak's multiple comparisons test showed that at each pressure and for each lipid composition the ML1 release from USL was significantly higher compared to NUSL.

Bioactivity of Formulated ML1

To investigate the overall bioactivity of the formulated ML1 we studied two phenomena related to the functionality of the protein. ML1 is composed of a cytotoxic A-chain linked to the lectin B-chain responsible for cellular binding and for mediating the protein uptake (Pizzo and Maro, 2016). It is therefore imperative to ensure that the structure of the protein is conserved to maintain its cytotoxic capacity. Taking this in mind, we studied both uptake of ML1 in CT26 cells and its cytotoxic activity. Uptake of ML1 was visualized by live-cell confocal fluorescence microscopy, using fluorescently labeled ML1 loaded in fluorescently labeled liposomes. CT26 cells were incubated for 4 h with HIFU-treated formulations, and the released ML1 induced cytotoxicity was measured 48 h later, as described before (Beztsinna et al., 2018; Matos et al., 2018).

Uptake of Released ML1

Figure 8 shows the live-cell confocal fluorescence microscopy pictures and semi-quantitative analysis of the uptake study. We detected cell-associated AF647-ML1 signal when the protein had been released from liposomes, or (in control experiments) added free AF647-ML1 to the cells. Although ML1 was released from NUSL10 after HIFU treatment (see **Figure 6**), the fluorophore amount (in AF647-ML1) was probably too low to be detected by the live cell imager. USL10 showed some spontaneous release without HIFU treatment which was only detected by the image analysis software. After HIFU treatment and at both acoustic conditions, ML1 released from USL10 was internalized by CT26, resulting in a punctuated red pattern in the cells cytoplasm. In the latest timepoint, ML1 was also found co-localized with the cell nucleus.

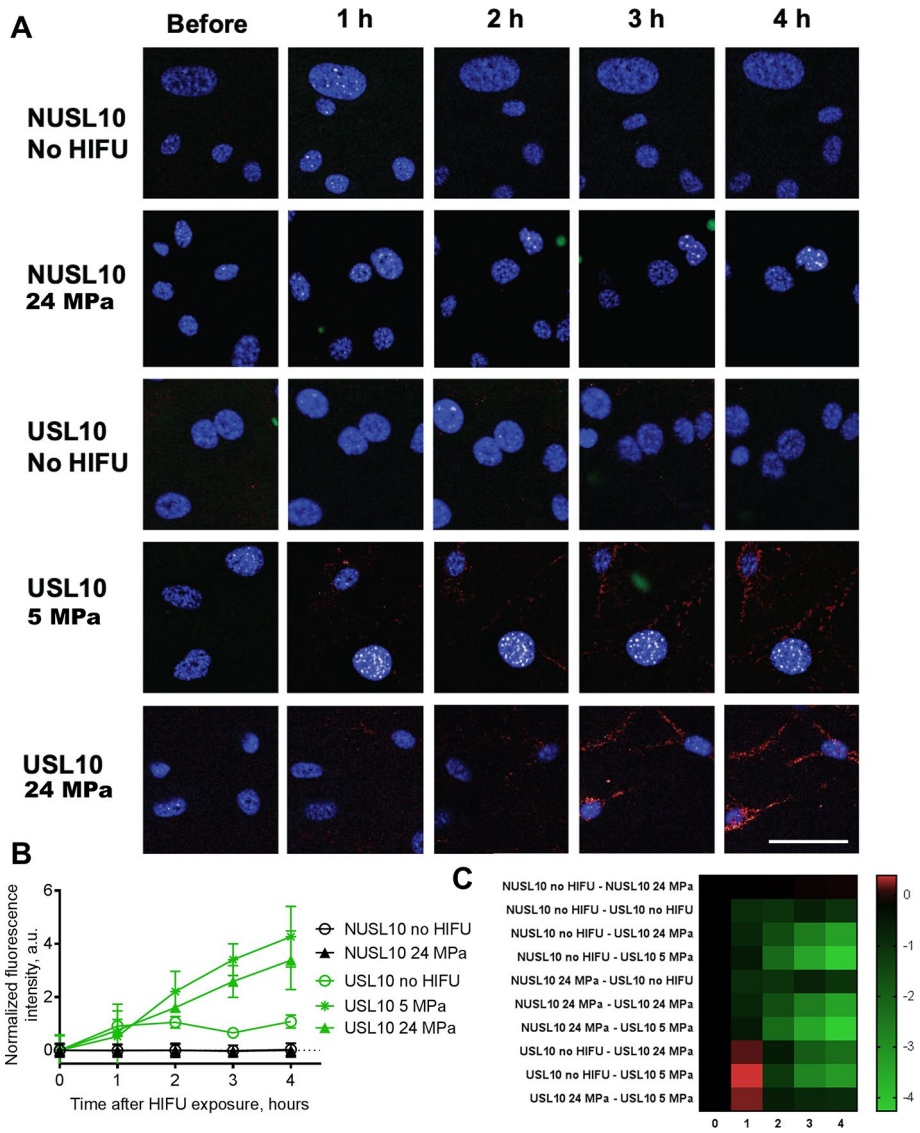

FIGURE 8 | Uptake of ML1 released from NUSL10 and USL10 after HIFU treatment. Liposomal formulations were diluted in cell culture media and transferred without further processing onto CT26 and cells were evaluated for 4-h uptake of ML1 by live cell imaging **(A)**. For the uptake studies, liposomes were labeled with DiO' (green) while ML1 was labeled with AF647 (red). Nuclei of CT26 were stained with Hoechst 33342 (blue) prior to addition of the preconditioned culture media. Scale bar is 50 micron and is applicable to all images. Timepoint "Before" correspond to the point immediately before adding the liposomes, thus cells negative control. Semi-quantitative analysis of co-localization of the cell cytoplasm and AF647ML1 released from NUSL10 and USL10 is shown in the graph. In the graph **(B)**, the black lines correspond to NUSL10 with no HIFU treatment (empty circle symbol) and after 24 MPa 1 min HIFU (full triangle symbol). The green lines correspond to USL10 with no treatment (empty circle symbol), USL10 after 5 MPa 1 min HIFU (full square symbol) and USL10 after 24 MPa 1 min HIFU (full triangle symbol). The results of NUSL10 exposed to 5 MPa 1 min were comparable to those of NUSL10 exposed to 24 MPa 1 min and therefore omitted for clarity. Data are the average ± standard deviation of triplicate samples. The result of a 2-way ANOVA with Tukey's multiple comparison test is presented as a heat map of the 95% confident intervals of the mean difference for all groups (i.e. 10) at all exposure times (i.e. 0, 1, 2, 3, and 4 h) **(C)**. Green indicates a significant difference between 2 groups.

Cytotoxic Activity of ML1

CT26 cells are sensitive to ML1 in the low ng/ml range as shown before by us using similar assays (Beztsinna et al., 2018; Matos et al., 2018). Since we planned to refresh the media after 4 h of incubation with liposomes, we now evaluated cell death induced by ML1 after the 4-h exposure to liposomes followed by incubation with fresh culture medium for 44 h. We also investigated whether the treatment with HIFU would affect its cytotoxicity, in view of reports that ultrasound can lead to local heating (>40°C) (Ng and Liu, 2002), which may possibly inactivate ML1. We exposed free ML1 to two different peak negative pressures (5 and 24 MPa) for 1 min and tested different concentrations of the treated ML1 on CT26 cells. The cytotoxic profile is presented in **Figure 9** and resulted in quite similar dose-response curves and IC_{50} values of 280 to 350 ng/ml. We concluded that ML1 cytotoxicity is not influenced by the HIFU exposure at these experimental conditions, remaining constant around 300 ng/ml.

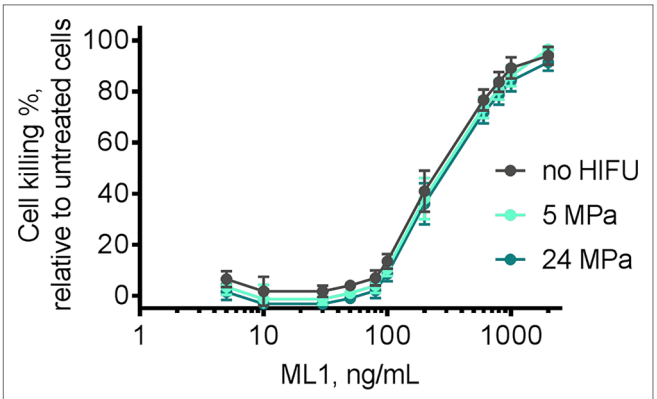

FIGURE 9 | Cytotoxicity of free ML1 after exposure to HIFU 1 min negative pressures 5 MPa (light blue line) and 24 MPa (dark blue line). After HIFU treatment, ML1 was incubated with CT26 cells for 4 h, following which the medium was replaced by toxin-free medium. The IC_{50} was measured indirectly by MTS after 48 h. Free ML1 without any HIFU treatment was used as reference (grey line) and incubated with cells using the same protocol. Untreated cells were used as 0% killing control (n = 2). Untreated ML1 had an IC_{50} of 281 ng/ml, 5 MPa treated ML1 an IC_{50} of 316 ng/ml and 24 MPa ML1 an IC_{50} of 345 ng/ml.

As we demonstrated in the previous sections, only ML1-USL formulations were able to release ML1 when exposed to HIFU, while ML1-NUSL released the cytotoxic cargo to a much lower extent. This result was confirmed by the cytotoxicity evaluation of ML1 containing liposomes. Viability of CT26 after treatment with ML1-NUSL10 was only affected minimally, as only 10% cell killing was observed irrespective of HIFU had been applied (**Figure 10A**). These results are in good agreement with the live-cell imaging studies in which no uptake was visualized from ML1-NUSL10 (see **Figure 7**). Since ML1 is such a potent cytotoxin, the cell viability assay can detect the minor amount of release while the confocal fluorescence microscope was not sensitive enough to detect such low amounts of AF647ML1 (in the ng/ml range). When no HIFU was applied to ML1-USL10 (**Figure 10B**), there was 30% cell killing for the highest tested concentration. Extrapolation of the cell killing curve, indicates that it would require ca. 950 ng/ml of released ML1 to reach 50% cell killing. This is in line with the uptake quantification results (**Figure 8**) where the uptake difference was 4-fold different between the HIFU-exposed formulations and the non-treated formulation. Regarding ML1-USL10 after exposure to HIFU, potent cytotoxic activity was observed (**Figure 10B**), corresponding to IC_{50} values of 471 and 408 ng/ml for 5 MPa and for 24 MPa, respectively.

CONCLUSION

We have demonstrated the potential of ultrasound sensitive liposomes as nanocarriers for high-molecular weight toxins like ML1. We tested three distinct formulations in terms of stability,

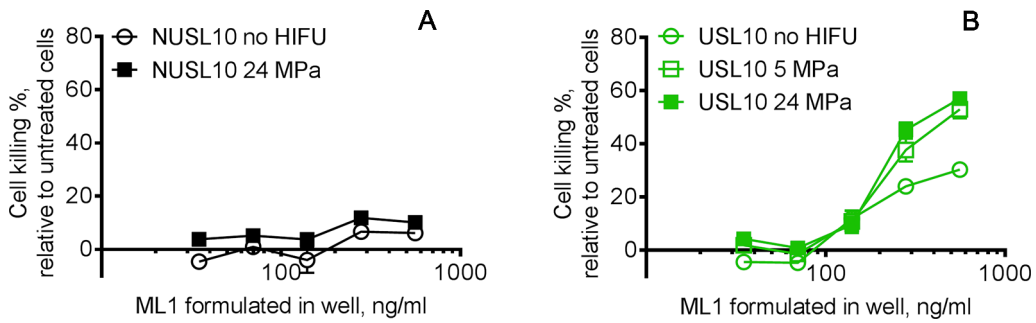

FIGURE 10 | Bioactivity of released ML1 after USL10 and NUSL10 were exposed to HIFU. The released ML1 was in contact with cells for 4 h, then the medium was replaced by fresh medium and the cytotoxicity was measured 44 h later. **(A)** The black lines correspond to NUSL10 with no HIFU treatment (empty circle symbol) and after 24 MPa 1 min HIFU (full square symbol). **(B)** The green lines correspond to USL10 with no treatment (empty circle symbol), USL10 after 5 MPa 1 min HIFU (empty square symbol) and USL10 after 24 MPa 1 min HIFU (full square symbol). The cytotoxicity results of NUSL10 exposed to 5 MPa 1 min were comparable to those of NUSL10 exposed to 24 MPa 1 min and therefore omitted for clarity. For NUSL no significant differences were found between no HIFU and 24 MPa. For USL 5 and 24 MPa HIFU exposure leads to significant more cell killing compared to no HIFU at all ML1 concentrations, except for 139.6 ng/ml. Data are the average ± standard deviation of three independent experiments. A Wilcoxon matched-pairs signed rank test **(A)** and a 2-way ANOVA with Tukey's multiple comparisons test **(B)** were performed.

release, and *in vitro* bioactivity. Overall, and as expected, the formulation containing the highest amount of PEG (i.e., USL20) is the most unstable in storage conditions and did not perform better than the two other counterparts with HIFU. The other two USLs, USL10 and USL5, complied with all requirements, i.e., a homogeneous size, stability, HIFU release, and *in vitro* tests. USL10 stood out as the one releasing higher amounts of ML1. Our experiments with CT26 cells confirmed that USL10-ML1 potently inhibited tumor cell viability after HIFU treatment. These promising results secure further investigation of these ultrasound sensitive formulations of ribosome-inactivating cytotoxins.

DATA AVAILABILITY STATEMENT

The datasets generated for this study are available on request to the corresponding author.

AUTHOR CONTRIBUTIONS

MM, RK, RD and GL designed the study and wrote the manuscript. MM performed all the formulation optimization studies, mistletoe lectin labeling, release, cell viability, and live-cell confocal imaging experiments, and analyzed the results. BM performed the transmission electron microscopy experiments. RD, BE and GL performed the acoustic experiment and results analysis. All authors discussed the results and commented on the manuscript.

ACKNOWLEDGMENTS

The authors acknowledge Phospholipid Research Center (Heidelberg) for funding and Lipoid GmbH for the generous supplying of lipids. Christoph Heyder and Gero Leneweit are kindly acknowledged for supply of ML1. We thank Dr. Tim Segers for substantial contribution to the ultrasound setup.

REFERENCES

Al-Ahmady, Z., and Kostarelos, K. (2016). Chemical Components for the Design of Temperature-Responsive Vesicles as Cancer Therapeutics. *Chem. Rev.* 116 (6), 3883–3918. doi: 10.1021/acs.chemrev.5b00578

Aliabouzar, M., Kumar, K. N., and Sarkar, K. (2018). Acoustic Vaporization Threshold of Lipid-Coated Perfluoropentane Droplets. *J. Acoust. Soc. Am.* 143, 2001–2012. doi: 10.1121/1.5027817

Allen, T. M., and Cullis, P. R. (2013). Liposomal Drug Delivery Systems: From Concept to Clinical Applications. *Adv. Drug Deliv. Rev.* 65 (1), 36–48. doi: 10.1016/j.addr.2012.09.037

Beztsinna, N., de Matos, M. B. C., Walther, J., Heyder, C., Hildebrandt, E., Leneweit, G., et al. (2018). Quantitative Analysis of Receptor-Mediated Uptake and pro-Apoptotic Activity of Mistletoe Lectin-1 by High Content Imaging. *Sci. Rep.* 8 (1), 2768. doi: 10.1038/s41598-018-20915-y

Cummings, R. D., and Schnaar, R. L. (2017). Chapter 31: R-Type Lectins. Eds. A. Varki, R. D. Cummings, J. D. Esko, et al. (Cold Spring Harbor (NY): Cold Spring Harbor Laboratory Press).

Eifler, R., Pfuller, K., Gockeritz, W., and Pfuller, U. (1993). "Improved Procedures for Isolation of Mistletoe Lectins and Their Subunits: Lectin Pattern of the European Mistletoe," in *Lectins 9: Biology, Biochemistry, Clinical Biochemistry*, 9th ed.,. Eds. J. Basu, M. Kundu, P. Chakrabari, and T. C. Bog-Hansen (New Delhi: Wiley Eastern Limited), 1–5.

Evjen, T. J., Nilssen, E. A., Rögnvaldsson, S., Brandl, M., and Fossheim, S. L. (2010). Distearoylphosphatidylethanolamine-Based Liposomes for Ultrasound-Mediated Drug Delivery. *Eur. J. Pharmaceutics Biopharm.* 75 (3), 327–333. doi: 10.1016/j.ejpb.2010.04.012

Fritz, P., Dippon, J., Kierschke, T., Siegle, I., Möhring, A., Moisa, A., et al. (2004). Impact of Mistletoe Lectin Binding in Breast Cancer. *Anticancer Res.* 242 C, 1187–1192.

Health Protection Agency. (2010). *"Health Effects of Exposure to Ultrasound and Infrasound: Report of the Independent Advisory Group on Non-Ionising Radiation." Edited by Advisory Group on Non-ionising Radiation* (England: London). https://assets.publishing.service.gov.uk/government/uploads/system/uploads/attachment_data/file/335014/RCE-14_for_web_with_security.pdf.

Horneber, M. A., Bueschel, G., Huber, R., Linde, K., and Rostock, M. (2008). Mistletoe therapy in oncology. *Cochrane Database Syst. Rev.* 2, CD003297. doi: 10.1002/14651858.CD003297.pub2

Hua, S., de Matos, M. B. C., Metselaar, J. M., and Storm, G. (2018). Current Trends and challenges in the clinical translation of nanoparticulate nanomedicines: pathways for translational development and commercialization. *Front. Pharmacol.* 9, 790. doi: 10.3389/fphar.2018.00790

Huang, X., Li, M., Bruni, R., Messa, P., and Cellesi, F. (2017). The effect of thermosensitive liposomal formulations on loading and release of high molecular weight biomolecules. *Int. J. Pharmaceutics* 524 (1–2), 279–289. doi: 10.1016/j.ijpharm.2017.03.090

Husseini, G. A., Pitt, W. G., and Javadi, M. (2015). Investigating the stability of eliposomes at elevated temperatures. *Technol. Cancer Res. Treat* 14 (4), 379–382. doi: 10.1177/1533034614551480

Javadi, M., Pitt, W. G., Belnap, D. M., Tsosie, N. H., and Hartley, J. M. (2012). Encapsulating nanoemulsions inside eliposomes for ultrasonic drug delivery. *Langmuir* 28 (41), 14720–14729. doi: 10.1021/la303464v

Johansson, E., Engvall, C., Arfvidsson, M., Lundahl, P., and Edwards, K. (2005). Development and initial evaluation of PEG-Stabilized bilayer disks as novel model membranes. *Biophys. Chem.* 113 (2), 183–192. doi: 10.1016/j.bpc.2004.09.006

Johnsson, M., and Edwards, K. (2003). Liposomes, disks, and spherical micelles: aggregate structure in mixtures of gel phase Phosphatidylcholines and Poly(Ethylene Glycol)-Phospholipids. *Biophys. J.* 85 (6), 3839–3847. doi: 10.1016/S0006-3495(03)74798-5

Kim, K. C., Yook, J. H., Eisenbraun, J., Kim, B. S., and Huber, R. (2012). Quality of life, immunomodulation and safety of adjuvant mistletoe treatment in patients with gastric carcinoma – a randomized, controlled pilot study. *BMC Complement. Altern. Med.* 12 (1), 172. doi: 10.1186/1472-6882-12-172

Lattin, J. R., Javadi, M., McRae, M., and Pitt, W. G. (2015). Cytosolic Delivery via Escape from the Endosome Using Emulsion Droplets and Ultrasound. *J. Drug Targeting* 2330, 1–11. doi: 10.3109/1061186X.2015.1009074

Marvibaigi, M., Supriyanto, E., Amini, N., Abdul Majid, F. A., and Jaganathan, S. K. (2014). Preclinical and clinical effects of mistletoe against breast cancer. *BioMed. Res. Int.* 2014, 785479. doi: 10.1155/2014/785479

Matos, M B.C. de, Beztsinna, N., Heyder, C., Fens, M. H. A. M., Mastrobattista, E., Schiffelers, R. M., et al. (2018). Thermosensitive Liposomes for Triggered Release of Cytotoxic Proteins. *Eur. J. Pharmaceutics Biopharm.* 132, 211–221. doi: 10.1016/j.ejpb.2018.09.010

Ng, K. Y., and Liu, Y. (2002). Therapeutic Ultrasound: Its Application in Drug Delivery. *Med. Res. Rev.* 22 (2), 204–223. doi: 10.1002/med.10004

Oerlemans, C., Deckers, R., Storm, G., Hennink, W. E., and Nijsen, J. F. W. (2013). Evidence for a New Mechanism behind HIFU-Triggered Release from Liposomes. *J. Controlled Release* 168 (3), 327–333. doi: 10.1016/j.jconrel.2013.03.019

Pitt, W. G., Singh, R. N., Perez, K. X., Husseini, G. A., and Jack, D. R. (2014). Phase transitions of perfluorocarbon nanoemulsion induced with ultrasound: a mathematical model. *Ultrasonics Sonochemistry* 21 (2), 879–891. doi: 10.1016/j.ultsonch.2013.08.005

Pizzo, E., and Maro, A. D. (2016). A New Age for Biomedical Applications of Ribosome Inactivating Proteins (RIPs): From Bioconjugate to Nanoconstructs. *J. Biomed. Sci.* 23 (1), 54. doi: 10.1186/s12929-016-0272-1

Roberts, L. M., and Lord, J. (1992). Cytotoxic Proteins. *Curr. Opin. In Biotechnol.* 3 (4), 422–429. doi: 10.1016/0958-1669(92)90171-E

Rouser, G., Fleischer, S., and Yamamoto, A. (1970). Two Dimensional Thin Layer Chromatographic Separation of Polar Lipids and Determination of Phospholipids by Phosphorus Analysis of Spots. *Lipids* 5 (5), 494–496. doi: 10.1007/BF02531316

Sandström, M. C., Johansson, E., and Edwards, K. (2008). Influence of Preparation Path on the Formation of Discs and Threadlike Micelles in DSPE-PEG2000/ Lipid Systems. *Biophys. Chem.* 132 (2–3), 97–103. doi: 10.1016/j.bpc.2007.10.011

Saxena, V., Gacchina, J. C., Negussie, A. H., Sharma, K. V., Dreher, M. R., and Wood, B. J. (2015). Temperature-Sensitive Liposome-Mediated Delivery of Thrombolytic Agents. *Int. J. Hyperthermia* 31 (1), 67–73. doi: 10.3109/02656736.2014.991428

Stylianopoulos, T., and Jain, R. K. (2015). Design Considerations for Nanotherapeutics in Oncology. *Nanomed.: Nanotechnol. Biol. Med.* 11 (8), 1893–1907. doi: 10.1016/j.nano.2015.07.015

Ta, T., and Porter, T. M. (2013). Thermosensitive Liposomes for Localized Delivery and Triggered Release of Chemotherapy. *J. Controlled Release* 169 (1–2), 112–125. doi: 10.1016/j.jconrel.2013.03.036

Vainikka, K., Reijmar, K., Yohannes, G., Samuelsson, J., Edwards, K., Jussila, M., et al. (2011). Polyethylene Glycol-Stabilized Lipid Disks as Model Membranes in Interaction Studies Based on Electrokinetic Capillary Chromatography and Quartz Crystal Microbalance. *Anal. Biochem.* 414 (1), 117–124. doi: 10.1016/j.ab.2011.03.016

van Elk, M., Murphy, B. P., Eufrásio-da-Silva, T., O'Reilly, D. P., Vermonden, T., Hennink, W. E., et al. (2016). Nanomedicines for Advanced Cancer Treatments: Transitioning towards Responsive Systems. *Int. J. Pharmaceutics* 515 (1–2), 132–164. doi: 10.1016/j.ijpharm.2016.10.013

van Gaal, E. V., Spierenburg, G., Hennink, W. E., Crommelin, D. J. A., and Mastrobattista, E. (2010). Flow cytometry for rapid size determination and sorting of nucleic acid containing nanoparticles in biological fluids. *J. Controlled Release* 141 (3), 328–338. doi: 10.1016/j.jconrel.2009.09.009

Wicki, A., Witzigmann, D., Balasubramanian, V., and Huwyler, J. (2015). Nanomedicine in Cancer Therapy: Challenges, Opportunities, and Clinical Applications. *J. Controlled Release* 200, 138–157. doi: 10.1016/j.jconrel.2014.12.030

Yuyama, Y., Tsujimoto, M., Fujimoto, Y., and Oku, N. (2000). Potential Usage of Thermosensitive Liposomes for Site-Specific Delivery of Cytokines. *Cancer Lett.* 155 (1), 71–77. doi: 10.1016/S0304-3835(00)00410-9

Conflict of Interest: The authors declare that the research was conducted in the absence of any commercial or financial relationships that could be construed as a potential conflict of interest.

frontiers in Pharmacology

ORIGINAL RESEARCH
published: 16 January 2020
doi: 10.3389/fphar.2019.01562

Enhanced Amikacin Diffusion With Ultrasound and Microbubbles in a Mechanically Ventilated Condensed Lung Rabbit Model

Fabien Espitalier[1,2], François Darrouzain[3,4], Jean-Michel Escoffre[1], David Ternant[3,4], Eric Piver[5], Ayache Bouakaz[1†] and Francis Remerand[1,2†]*

[1] UMR 1253, iBrain, Université de Tours, Inserm, Tours, France, [2] Pôle Anesthésie Réanimations, Hôpital Trousseau, CHRU de Tours, Tours, France, [3] Laboratoire de Pharmacologie-Toxicologie, Hôpital Bretonneau, CHRU de Tours, Tours, France, [4] Équipe PATCH, EA 7501 GICC, Tours, France, [5] Laboratoire de Biochimie, Hôpital Trousseau, CHRU de Tours, Tours, France

OPEN ACCESS

Edited by:
Marc Derieppe,
Princess Maxima Center for Pediatric Oncology, Netherlands

Reviewed by:
Erzsébet Bartolák-Suki,
Boston University, United States
Chin Moi Chow,
University of Sydney, Australia

***Correspondence:**
Francis Remerand
francis.remerand@univ-tours.fr

†These authors have contributed equally to this work

Specialty section:
This article was submitted to Translational Pharmacology, a section of the journal Frontiers in Pharmacology

Received: 15 July 2019
Accepted: 03 December 2019
Published: 16 January 2020

Citation:
Espitalier F, Darrouzain F, Escoffre J-M, Ternant D, Piver E, Bouakaz A and Remerand F (2020) Enhanced Amikacin Diffusion With Ultrasound and Microbubbles in a Mechanically Ventilated Condensed Lung Rabbit Model. Front. Pharmacol. 10:1562. doi: 10.3389/fphar.2019.01562

The poor diffusion of intravenous antibiotics in lung tissue makes nosocomial pneumonia challenging to treat, notably in critical patients under mechanical ventilation. The combination of ultrasound and microbubbles (USMB) is an emerging method for non-invasive and targeted enhancement of uptake of various drugs in several organs. This study aims to evaluate if USMB may increase amikacin concentration in condensed lung tissues in a mechanically ventilated rabbit model. When applied 60 or 160 min after the beginning of an intravenous amikacin infusion, USMB increased amikacin concentration in the condensed lung tissue by 1.33 ($p = 0.025$) or 1.56-fold ($p = 0.028$) respectively. When applied 70 min after the beginning of an intravenous amikacin infusion, USMB increased amikacin concentration in the muscle tissue by 2.52 ($p = 0.025$). In conclusion, this study demonstrates that USMB is a promising method for the targeted delivery of amikacin in mechanically ventilated condensed lung, thus opening new therapeutic fields against lung infections.

Keywords: sonoporation, ultrasound, microbubbles, antibiotic therapy, lung, amikacin

INTRODUCTION

Hospital-acquired and ventilator associated pneumonia (VAP) are among the most common infections in intensive care units (ICU) (Leone et al., 2018). They increase morbidity, and ICU and hospital length of stay (Rello et al., 2002; Koulenti et al., 2017). In ICU, most of pneumonia are VAP (American Thoracic Society et Infectious Diseases Society of America, 2005). They are frequently due to multidrug-resistant bacteria, which lead to poor therapeutic outcomes (Martin-Loeches et al., 2013). Aminoglycosides are recommended to treat these patients (Leone et al., 2018). Most intravenous (iv) antibiotics (*e.g.*, aminoglycosides) diffuse poorly in the lung tissue, making pneumonia challenging to treat. Moreover, the risk of systemic toxicity limits the use of high dose of iv antibiotics. To overcome these limitations, the development of innovative targeted delivery methods is required to increase the local concentration of antibiotics in infected lung tissues, while minimizing general side effects related to the systemic antibiotherapy.

Ultrasound contrast agents (UCAs) are microbubbles consisting of a gaseous core surrounded by a biocompatible shell. UCAs are currently used for diagnostic medical ultrasounds (Sennoga et al., 2017).

Beyond these diagnostic practices, new promising applications of UCAs have emerged for targeted drug delivery (Kooiman et al., 2014). When UCAs and the targeted drug are intravenously co-injected and both exposed to ultrasound, it provides unprecedented possibilities for a selective therapeutic action known as sonoporation (Geers et al., 2012). Sonoporation denotes a process in which ultrasonically-activated microbubbles (USMB) pulsations induce a transient permeabilization of nearby endothelial barriers (*e.g.*, blood-tumor barrier, blood-brain barrier) (Escoffre and Bouakaz, 2018). This increases vascular permeability and so extravasation of drugs from blood into surrounding tissues (Carpentier et al., 2016; Dimcevski et al., 2016). In comparison with other physical drug delivery methods, sonoporation is a non-invasive, easy to apply, and cost-effective method. Thus, it provides a high potential for the delivery of a wide range of drugs to superficial and deep organs under the guidance ultrasonic imaging (Escoffre et al., 2013; Zhang et al., 2015; Yu et al., 2016).

Few studies investigated the therapeutic benefit of antibiotic treatments combined with USMB for improving antibiotic activity against bacterial infections (He et al., 2011; Shih et al., 2013; Lin et al., 2015; Shang et al., 2015; Dong et al., 2018; Sugiyama et al., 2018). Thus, USMB enhanced the antibacterial effect of free vancomycin against *Staphylococcus epidermidis in-vivo* biofilms compared to antibiotic treatment alone (He et al., 2011; Dong et al., 2018). In addition, USMB stimulated the release of vancomycin from vancomycin-loaded polymethyl methacrylate (PMMA) cement, thus increasing the *in-vitro* and *in-vivo* antibacterial effects on *Staphylococcus aureus* (Lin et al., 2015). Two other preclinical investigations also demonstrated that USMB improved the concentration of cefuroxime in rat prostate tissue (Shang et al., 2015) and of gentamicin in the inner ear of guinea pig (Shih et al., 2013). Recently, Sugiyama *et al.* reported that USMB significantly increased the gentamicin concentration in lung tissue in a bilateral diffuse lung infection model in spontaneously breathing mice, thus decreasing bacterial growth (Sugiyama et al., 2018). However, in clinical practice, pneumonia can show a diffuse pattern or be localized (they usually are limited to a lower lung lobe). In addition, in ICU, 80% of nosocomial pneumonia are VAP (Koulenti et al., 2017). Both localized pneumonia and lung aeration due to mechanical ventilation may limit ultrasound penetration in the lung tissue, and so USMB efficacy. Whether USMB can increase antibiotic diffusion in these conditions is a crucial preliminary question to answer, before further *in vivo* or clinical studies. Our present *in vivo* study aimed to evaluate if USMB may increase aminoglycoside diffusion in condensed lung tissue of mechanically ventilated rabbits. To establish that USMB worked well under controlled conditions, the diffusion of aminoglycoside was also evaluated in skeletal muscles.

MATERIALS AND METHODS

Animal Preparation and Animal Model

All procedures were performed according to the ethical guidelines and were approved by the Animal Care and Regional Committee for Ethics in Animal Experiments, Val-de-Loire (2015020312576994). Forty healthy female adult New Zealand rabbits were purchased from Charles Rivers (Écully, France). Rabbits were maintained at constant room temperature with 12 h light cycle in isolation cages. At the start of the experiments, rabbits were 16–18 weeks old, weighing between 2.3 and 4.9 kg.

The rabbits were anesthetized by inhaling 3% isoflurane (Isoflurane Belamont, Paris, France) and oxygen *via* a facial oxygen mask. They were then positioned in supine position on a thermostatically controlled pad in order to maintain body temperature at about 37°C. During the whole procedure, the body temperature was monitored with a rectal temperature probe. Heart rate and pulse oximetry were continuously measured using a handheld pulse oximeter (PC-66V, Shenzhen Creative Industry, Shenzhen, China). The marginal vein of an ear was cannulated with a Jelco® 22 G catheter (length 25 mm, diameter 0.95 mm; Smiths Medical International Ltd, Lancashire, UK). This catheter was used to intravenously inject atropine (100 μg/ml in saline). Subsequently, through the catheter, continuous infusions of sufentanil (1 μg/ml in saline, 3 μg/h) and propofol (5 mg/ml saline, 15 mg/h) were performed independently of rabbit body weight. *Via* a tracheotomy, the trachea was intubated (Portex® tracheal tube with 2.5 mm internal diameter, without cuff; Smiths Medical International Ltd, Hythe, UK). The 40 rabbits were mechanically ventilated (Servo 300A, Siemens Elema, Solna Sweden) in a volume control support mode (inspired fraction of oxygen of 1.0, tidal volume of 8 ml/kg, no end-expiratory pressure, respiratory rate of 50 to 65 breaths per minute to maintain arterial CO_2 in a normal range). Neuromuscular blockade was achieved using iterative iv atracurium boli (10 mg) every 45 min. The right femoral artery was cannulated using Seldinger method with a Leadercath arterial catheter (20 G, 4 cm length; Vygon, Écouen, France) for continuous arterial pressure monitoring (GE Datex-Ohmeda S/5, GE Datex-Ohmeda, Helsinki, Finland) and blood sample collection.

Lung Condensation Model

Just before USMB, the right lung was flooded by saline. Briefly, a 19G epidural catheter (Vygon, Écouen, France) was inserted between the trachea and the intratracheal tube. The rabbit was positioned on its right side and 9 ml of saline were instilled into the trachea through the catheter. The flooding (and so the condensation) of the right lung but also the absence of flooding of the left lung were verified using lung echography (Logiq Book XP, General Electric Healthcare).

Ultrasound Setup

Ultrasound waves for sonoporation were generated using a single-element lab-made ultrasound transducer with a center frequency of 1 MHz. The transducer had a diameter of 14 mm and was naturally focused at 25 mm. It was driven by an electrical signal generated from an arbitrary waveform generator (Agilent, Santa Clara, CA), then amplified by a power amplifier (ADECE, Artannes-sur-Indre, France). As previously described (Escoffre et al., 2010), the peak negative pressure was measured in a separate setup using a calibrated polyvinylidene fluoride needle hydrophone (diameter 0.2 mm; Precision Acoustics Ltd., Dorchester, UK) at the natural focal distance of the transducer. The lung and muscle tissues (exact anatomical locations are described in *Study Design* section) were

sonicated at 1 MHz with a pulse repetition period of 100 μs, 40 cycles per pulse at peak-negative pressure of 600 kPa for a period of 3 min (Escoffre et al., 2013).

Pharmacokinetic Analysis of Amikacin

In a set of 11 mechanically ventilated anesthetized rabbits, the beginning of amikacin infusion (Mylan SAS, Saint Priest, France, 15 mg/kg in 5 ml saline during 30 min) set as time T0. The lung was not condensed and neither microbubbles nor ultrasound were used in this pharmacokinetics (PKs) experiment. Blood samples were collected at T30 (discontinuation of amikacin infusion), T60, T90, T150, T210, and T510 minutes. Total blood samples were centrifuged (2,000 tr.min^{-1} during 10 min) after coagulation and amikacin concentrations were determined in the obtained serum by fluorescence polarization immunoassay using the chemistry analyzer Cobas Integra 400+ (Cobas Integra 400+, Roche Diagnostics, Basel Switzerland) (Domke et al, 2000). Amikacin PKs analysis allowed to set the timing of ultrasound application for the two following experiments: high serum amikacin concentration [AMK] experiment and low serum [AMK] experiment.

Study Design

High [AMK] Sonoporation Experiment (N = 8 Rabbits)

Once amikacin infusion was started, the thorax, the ventral side of the abdomen, and both anterior legs of the rabbits were shaved. A right laparophrenotomy was performed. At T55 minutes the right lung was flooded.

Sonoporation of the Lung

At T60 minutes, the ultrasound transducer was placed in close contact with the right pulmonary lower lobe through the laparophrenotomy. Two milliliters of saline in the pleural space allowed ultrasound transmission between probe and lung tissue. An iv bolus of 400 μl of gas microbubbles (Vevo MicroMarker, FUJIFILM-VisualSonics Inc., Amsterdam, NL) was injected followed by 1 ml saline flush. One minute after microbubbles injection, ultrasound was applied to the lung using the ultrasound parameters described above. Each rabbit was then positioned in supine position and lung reaeration was checked using echography.

Sonoporation of the Muscle

The transducer was placed in contact with a shaved anterior leg (right or left legs were randomly chosen using a computer-generated random list) covered with ultrasound transmission gel. To ensure an accurate position, four thin needles around the transducer were used to mark the sonoporation region. At T70 minutes, an iv bolus of 400 μl of microbubbles was injected. One minute later, ultrasound was applied to the skeletal muscle of the anterior leg. Exsanguination was performed at T90 minutes.

Low [AMK] Sonoporation Experiment (N = 7 Rabbits)

In a separate experiment and using the USMB protocol previously described, the right condensed lung was exposed to two USMB treatments at T150 and T160 minutes. At T150 and T160, the systemic amikacin concentration was about three-fold lower than the peak of systemic amikacin concentration (**Figure 2**). Microbubbles were renewed before the second application of ultrasound. Exsanguination was performed at T170 minutes. In this experiment, the muscle was not submitted to USMB, meaning that the low [AMK] experiment was not conducted in the muscle tissue.

The study design is presented in **Figure 1**.

Sacrifice and Post Mortem Analysis

Each rabbit was exsanguinated *via* the arterial cannula. Through a cervicothoracic incision, both lungs were carefully dissected and separated. Their ventral and dorsal sides were photographed before removing the main vessels and bronchus. Then, two muscle samples (5 to 10 mm diameter, without serosa) were excised, one in the center of the sonicated area of the anterior leg, and the other one in the similar area on the contralateral leg (as a control sample). All lung and muscle samples were weighed with a micrometric balance. Lung and muscle samples were mechanically grinded within 5 ml of saline using Ultra-Turrax T10 device (IKA-Werke, GmbH & Co., Staufen, Germany), frozen and stored at −20°C for further analysis.

Amikacin Concentration Assessment in Tissues

After they defrosted, grinded tissue samples were mechanically homogenized using a disperser, followed by 10 min ultrasonication. Then samples were centrifuged (2,000 tr.min^{-1} during 10 min) and amikacin was quantified in the obtained supernatant, following dilution with Roche diluent to meet the measurement accuracy range if necessary. Amikacin concentrations in tissues were determined by fluorescence polarization immunoassay (one measurement done per sample) using the chemistry analyzer Cobas Integra 400+ (Cobas Integra 400+, Roche Diagnostics, Basel Switzerland) (Domke et al, 2000). Aiming to validate the assay technique, lung and muscle supernatants containing no amikacin were used. The supernatants were divided into 10 samples. In each sample, a known dose of amikacin was added. This dose of amikacin increased from the 1st to the 10th sample. Then, in each sample, the amount of amikacin present in the supernatant was measured by the fluorescence polarization immunoassay. The same method was applied in parallel to virgin amikacin blood serum. The results obtained for each medium (blood serum, lung, or muscle supernatant) were compared with each other for each dose of amikacin added. The results of the assays in the lung supernatant and in the blood serum were commutative, which means that the assay of amikacin by the fluorescence polarization immunoassay in the lung and muscle supernatants gave exactly the same result as in the blood serum, reference medium of this technique.

Statistics

Because of trapping of the sodium chloride used to flood the right lung, its weight was artificially increased, underestimating the amikacin concentration in this lung tissue. This "dilution effect" was corrected as follow: in a set of 14 female New Zealand rabbits without any lung flooding, right and left lungs were weighed in similar experimental conditions than previously

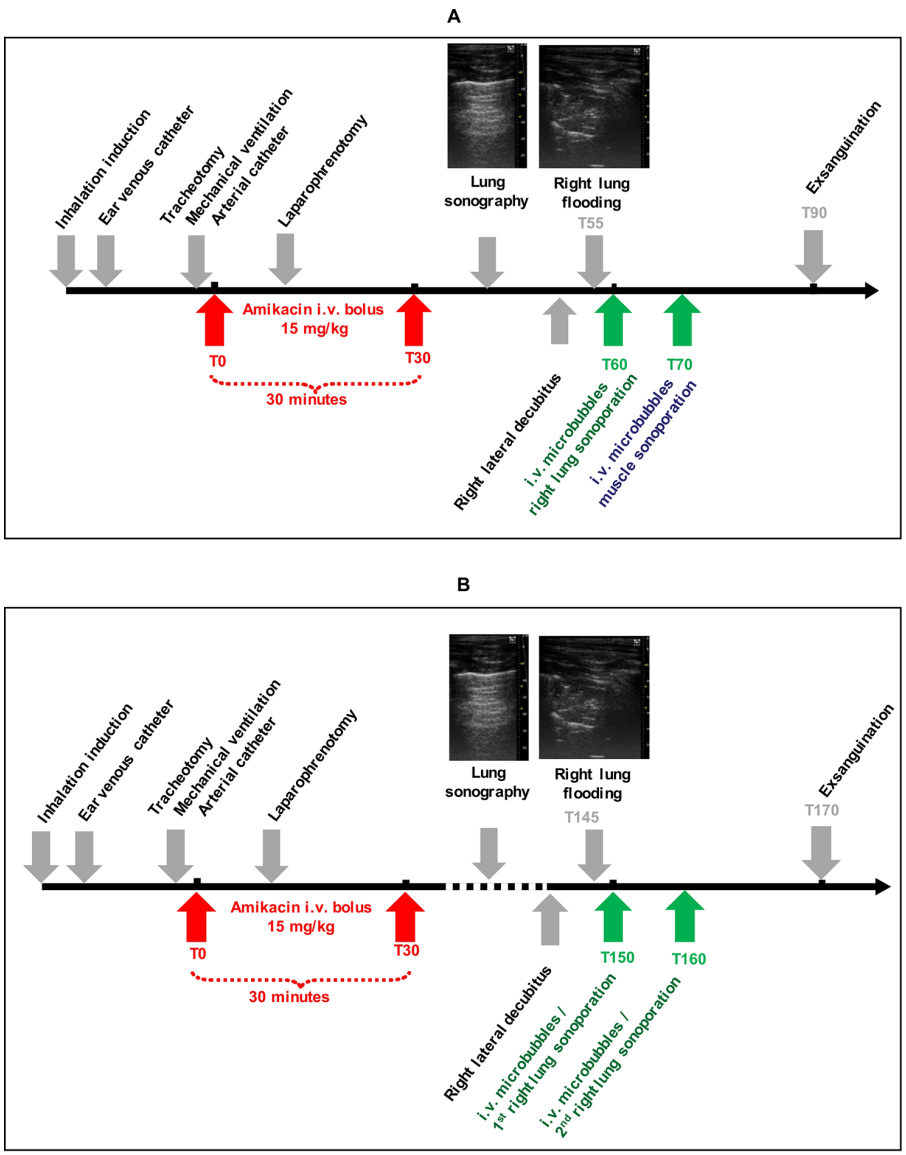

FIGURE 1 | Study design with high **(A)** and low **(B)** amikacin concentrations.

described. The mean (standard deviation) of the ratio between right lung weight (5.803 ± 0.605 g) and left lung weight (4.047 ± 0.558 g) was 1.458 (±0.123). Amikacin concentration in the right lung was therefore corrected as follows:

$$Corrected \quad [AMK]_{RL} = \frac{W_{RL} \times Measured \quad [AMK]_{RL}}{W_{LL} \times 1,458}$$

with $[AMK]_{RL}$, amikacin concentration in the right lung; W_{RL}, weight of the right lung; W_{LL}, weight of the left lung.

Finally, the following comparisons were made: 1) lung uptake of amikacin between sonicated and non-sonicated lung, in the presence of high [AMK] concentration, and in the presence of low [AMK] concentration, 2) muscle uptake of amikacin between sonicated and non-sonicated muscle in the presence of high [AMK] concentration. In each of these situations, the amikacin concentrations dosed in the supernatants of tissue samples were compared using a Wilcoxon test (each rabbit being its own control). A p value < 0.05 was considered as significant. Statistical tests were performed using SPSS 25 (IBM France statistics, Bois-Colombes, France). Neither statistical test was performed to compare amikacin lung concentration in low [AMK] concentration experiment with the one in high [AMK] concentration experiment, nor between amikacin concentration in lung and in muscle.

Because blood amikacin concentration was measured at T30, T60, T90, T150, T210, and T510, a PK modeling was needed to precisely determine the peak of blood amikacin concentration to optimize the administration of USMB in the experiments.

Amikacin PKs was assessed using population PK modeling (MonolixSuite 2018, Lixoft®, Orsay, France). One and two-compartment models with first order absorption and elimination rate constants were tested.

RESULTS

Amikacin Pharmacokinetics

The blood amikacin concentrations were measured over time by fluorescence polarization immunoassay after iv infusion of 15 mg/kg amikacin in mechanically ventilated anesthetized rabbits. Subsequently, amikacin PKs was assessed using population PKs modeling. As shown in **Figure 2**, a one-compartment PKs model described adequately amikacin PKs. Thus, the highest amikacin concentration (40.2 ± 5.3 mg/L) was measured at 60 min after the beginning of iv amikacin infusion. Model-fitted concentration peak occurred at 48 min. Average estimates of absorption rate constant, volume of distribution, clearance, and elimination half-life constants were 0.072 min^{-1}, 0.81 L, 0.01 $L.min^{-1}$, and 56 min, respectively. Inter-subject variability of PKs parameters was <9% and none of PKs parameters was related to the body weight.

In-Vivo Amikacin Delivery in Condensed Lung and Muscle Using Sonoporation

At T60 min (high [AMK] sonoporation experiment), the amikacin concentration in the right condensed lung tissue exposed to USMB was 1.33-fold higher (+33%) compared with the left non-sonicated lung (14.1 [10.3–15.4] *versus* 10.6 [8.5–14.0] µg/g; $p = 0.025$).

At T70 min, the amikacin concentration in muscle exposed to USMB was 2.52-fold higher (+152%) compared with non-sonicated muscle (6.3 [3.4–11.0] *versus* 2.5 [1.9–6.0] µg/g; $p = 0.025$).

At T160 min (low [AMK] sonoporation experiment), the amikacin concentration in the right condensed lung tissue exposed to USMB was 1.56-fold higher (+56%) compared with the left non-sonicated lung (6.1 [4.6–8.2] *versus* 3.9 [3.6–4.2] µg/g; $p = 0.028$).

The results are shown in **Figure 3**.

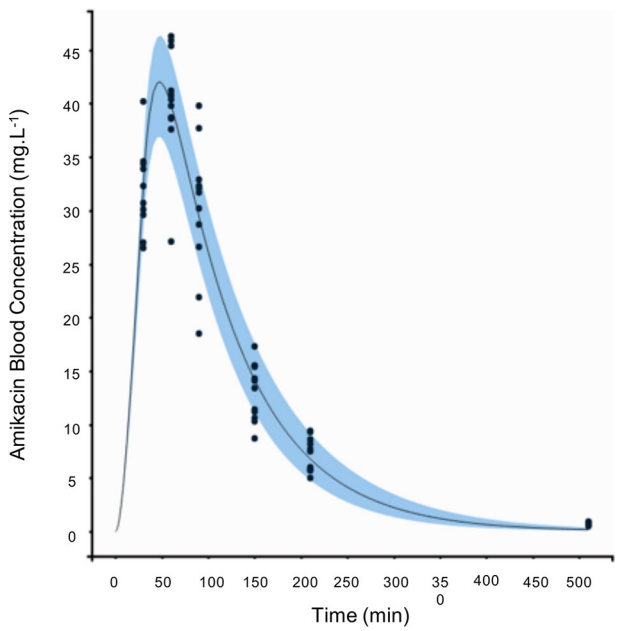

FIGURE 2 | Amikacin pharmacokinetics (PKs) in mechanically ventilated anesthetized rabbits (N = 11 rabbits). T0 was set as the beginning of intravenous (iv) amikacin infusion (15 mg/kg over 30 min).

DISCUSSION

The present study investigated the efficacy of USMB to improve amikacin diffusion in the mechanically ventilated condensed lung in a rabbit model. It demonstrated that focal USMB significantly increased amikacin concentration in the mechanically ventilated condensed lung but also in the muscle. However, the real effect of USMB was probably underestimated in lungs because of anatomical limitations of the rabbit model and instrumental limitations of our experimental setup.

The effect of an ultrasound-based treatment applied to pneumonia may appear as unpredictable. First, the multiple air/tissue interfaces in lungs may dramatically limit ultrasound propagation into the lung and so USMB efficiency. Second, in the opposite way, in case of pneumonia, inflammatory interstitial edema increases and many alveoli are progressively filled with exudate. These conditions may ease ultrasound propagation into the lung. Third, in clinical practice, the increase in hypoxemia requires mechanical ventilation to recruit alveoli, to decrease breathing work, and to increase fraction of inspired oxygen. During mechanical ventilation, positive pressure is continuously applied in the airways to insufflate gas into the lungs and to reaerate alveoli (during spontaneous breathing, this pressure is negative during inspiration, and very low during expiration). Mechanical ventilation may therefore decrease ultrasound propagation in the lung tissue. In the present study, a model of condensed lung under mechanical ventilation was specifically developed. In our laboratory, the rabbit was the smallest available animal allowing easy mechanical ventilation. By definition, inducing a clinically relevant VAP would have required several days of mechanical ventilation, with a possible important mortality rate. This would have been time and resources consuming. So we considered it was mandatory to document the pharmacologic step before such clinical step. Two main approaches can mimic quickly a lung condensation: lung atelectasis and lung flooding. From a pathological point of view, the lung flooding model is more appropriate. Moreover, this model gives very similar echographic aspect than pneumonia in human clinical practice (see **Figure 1**). Last but not least, each rabbit was its own control, limiting interindividual variability impact. In this model, a key methodological point was the timing of both USMB and amikacin infusion. To our knowledge, the amikacin PKs has not been described in a rabbit model before.

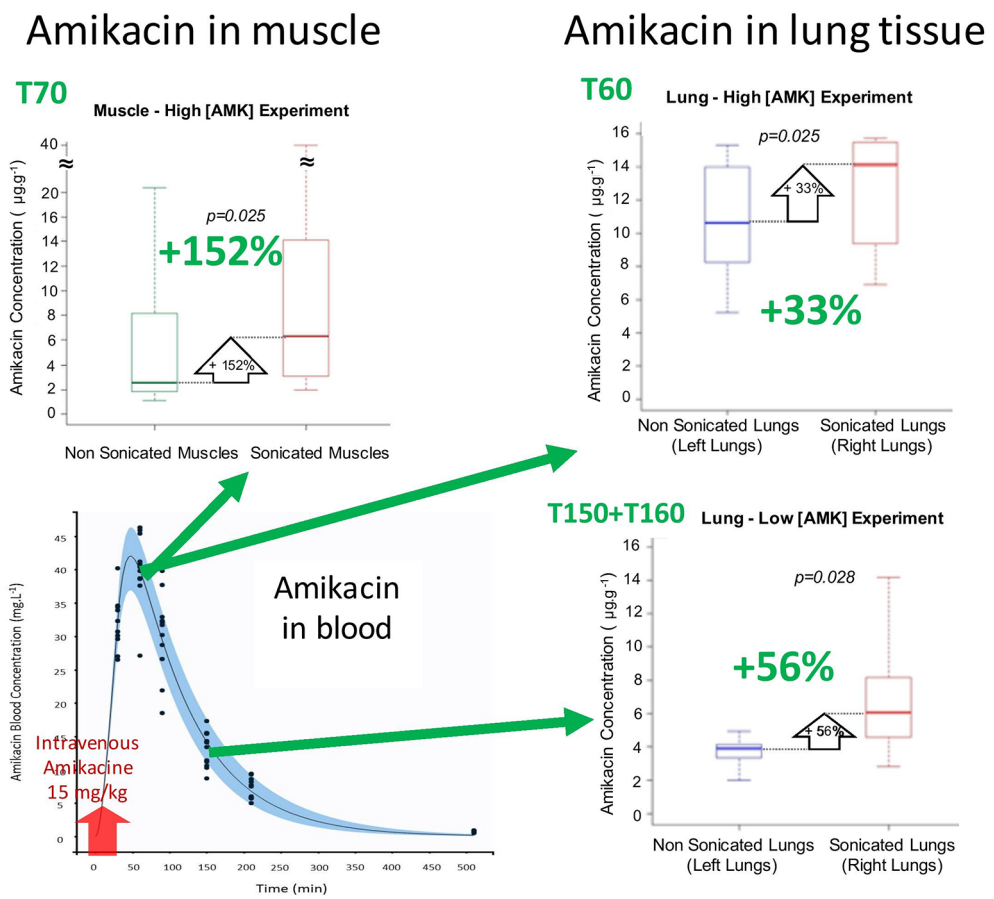

FIGURE 3 | Boxplots of amikacin concentration in lung and muscle tissues (N = 7–8 rabbits/condition; each rabbit was its own control). Green arrows indicate on the PKs curve the amikacin blood concentration at the time of sonoporation.

So, it had to be performed in ours. Amikacin PKs was very reproducible, since inter-individual variability was very low (< 9%), and did not depend on the rabbit weight. This PKs study allowed us to perform the USMB protocol at the highest plasmatic concentration of amikacin, in the high [AMK] experiment, when the effect should be maximal. It also allowed us to perform the USMB protocol when amikacin concentration decreased by 66%, in the so called "low [AMK] experiment." It aimed to test if the increased diffusion was potentially dependent from the amikacin concentration.

Our main findings are USMB increased amikacin lung concentration by 33% in the high [AMK] experiment ($p = 0.025$) and by 56% in the low [AMK] experiment ($p = 0.028$), and by 152% ($p = 0.025$) in the muscle tissue. Amikacin therapeutic effect on bacteria is mainly observed during the period of high amikacin concentration. So, in the aim to optimize amikacin efficacy, the more relevant timing to apply an USMB protocol is probably the one chosen in the high [AMK] experiment, or slightly before (in theory at T48). However, our findings revealed also that USMB was effective in increasing amikacin diffusion in lung, whatever the amikacin concentration. In another approach, USMB could maintain the amikacin therapeutic effect on bacteria in the lungs while reducing its posology, in the aim to decrease its systemic toxicity.

The relative increase in amikacin concentration due to USMB was +152% in muscle tissue compared to +33 and +56% in the lung. The apparent higher efficiency of USMB in muscle than in lung tissue should be challenged: first, the spread of ultrasound is better in muscle because of the lack of tissue/gas interfaces in this tissue; second, the muscle is more superficial than lung, making it easier to sonicate; third, the accurate localization of the probe and of its beam in the muscle tissue allowed us to collect muscle tissue sample mainly in the sonicated area, leading to a better evaluation of the USMB effect on amikacin diffusion in muscle than in lung. Indeed, the real effect of USMB is probably underestimated in lungs because of anatomical limitations of the rabbit model and instrumental limitations of our experimental setup. Therefore, with appropriate ultrasonic probe for lung sonoporation, an increase of antibiotics diffusion in lung similar to the one observed in muscle should be reachable.

Due to the particular anatomy of the rabbits, with a narrow chest and a central heart, only a direct application of the probe

on the right lung allowed the lung sonication while avoiding heart sonication. We presumed that if lung and heart were sonicated simultaneously, the microbubbles would have been extensively disrupted in cardiac cavities, before reaching the lung. This is the main reason why a transthoracic approach was not performed in the present study. In this rabbit model, we chose a focal application of ultrasound. The size of the probe (14 mm external diameter and a natural focus at 25 mm) allowed only limited sweeping motion once in the right hemithorax of the rabbits. Therefore, the volume of lung sonicated in our protocol with this probe (5 mm diameter beam and about 15 mm lung depth) was far less than 1 ml. It has to be compared with the median right lung weight in similar healthy female rabbits in this study (5.8 g), or with the median volume of the right lung measured on computed tomography in ten 7 month old female rabbits (30 ml) (Müllhaup et al., 2017). In the present study, the measured amikacin concentration in the whole right lung is therefore the mean of less than 1 ml of treated lung and of 5 to 30 ml of untreated lung. An accurate localization of the sonicated area could have circumvented this pitfall. This was not possible due to the cumbersome footprint of the probe, and to the respiratory lung mobility during USMB. At bedside, human lower lobes can easily be explored using transthoracic ultrasound, without visualizing the heart. So, non-invasive lung sonoporation should be feasible in clinical practice.

In mice in spontaneous ventilation, the relative increase of aminoglycoside (gentamicin) concentration in lung tissue induced by USMB was +100% (Sugiyama et al., 2018). This may appear more important than under mechanical ventilation (+33 or +56%), as showed in our study. Our results have to be challenged since they are largely underestimated (see above). Moreover, Sugiyama's animal model and aminoglycoside studied were different from our experiments. In addition, in Sugiyama's murine model, the whole thorax was sonicated (Sugiyama et al., 2018). Such large sonication is difficult to conceive in clinical practice. Our model was a non-infected one, so we were not able to directly demonstrate the anti-bacterial therapeutic effect related to the increase of lung amikacin concentration as recently reported with gentamicin (Sugiyama et al., 2018).

The conclusions drawn from our study should not be extended to other antibiotic classes. Indeed, the pharmacological and physicochemical properties (*e.g.*, molecular weight, spatial conformation, ionic charge, *etc.*) strongly vary from an antibiotic to another and the impact on the molecule diffusion after sonoporation cannot be predicted.

USMB is a new and original therapeutic approach. Its safety has to be explored. In theory, increasing vascular permeability may increase lung edema, and so increase hypoxemia. Whether this effect is negligible, additive, or synergistic with preexisting increased vascular permeability in inflamed lungs (induced by mechanical ventilation and/or infection) has to be questioned. At bedside, no harm has been attributed to diagnostic lung ultrasounds, while they have been largely used for more than 20 years, including in injured lungs (Lichtenstein et al., 1997). USMB seems to be safe during the hours following application: in agreement with Sugiyama's study, pulse oximetry was not modified by lung ultrasound application in our study (data not shown). Nevertheless, delayed deleterious effects of USMB cannot be excluded. This aspect will have to be explored in further studies on this topic, with a prolonged follow-up.

CONCLUSIONS

USMB increased amikacin concentration in mechanically ventilated condensed rabbit lung. Nevertheless, further technological developments are still required to potentiate this effect, and to validate the efficacy and the safety of therapeutic protocol in a rabbit lung infection model. Future works should study if USMB could improve the efficacy of current antibiotherapy for the treatment of pulmonary diseases, specifically in hospital-acquired and ventilator associated pneumonia.

DATA AVAILABILITY STATEMENT

The datasets generated for this study are available on request to the corresponding author.

ETHICS STATEMENT

The animal study was reviewed and approved by Animal Care and Regional Committee for Ethics in Animal Experiments, Val-de-Loire, France (2015020312576994).

AUTHOR CONTRIBUTIONS

AB, FR, J-ME, and FE conceived the project and the design of experiments. FE and FR performed the experiments. FE, EP, and FD performed the amikacin concentration dosing. FD and DT performed the modeling of the pharmacokinetics of amikacin. FE and FR analyzed the results, and wrote the manuscript. All authors reviewed the manuscript.

FUNDING

This work was supported by institutional funds from Inserm and Université de Tours.

ACKNOWLEDGMENTS

We acknowledge Prof. Laffon (Department of Anesthesiology and Surgical Reanimation, CHRU de Tours, Tours, France) for his assistance in establishing the rabbit model, Dr. Bruno (Laboratoire de Pharmacologie-Toxicologie, Hôpital

Bretonneau, CHRU de Tours, Tours, France) for the technical assistance in dosing amikacin concentration; Mr. Jean Yves Tartu (Inserm U1253) for his technical assistance, and Mrs Valérie Schubnel and Mr. Jérôme Montharu (PST Animalerie, Université de Tours, Tours, France) for their help in handling animals.

REFERENCES

American Thoracic Society, Infectious Diseases Society of America (2005). Guidelines for the management of adults with hospital-acquired, ventilator-associated, and healthcare-associated pneumonia. *Am. J. Respir. Crit. Care Med.* 171, 388–416. doi: 10.1164/rccm.200405-644ST

Carpentier, A., Canney, M., Vignot, A., Reina, V., Beccaria, K., Horodyckid, C., et al. (2016). Clinical trial of blood-brain barrier disruption by pulsed ultrasound. *Sci. Transl. Med.* 8, 343re2. doi: 10.1126/scitranslmed.aaf6086

Dimcevski, G., Kotopoulis, S., Bjånes, T., Hoem, D., Schjott, J., Gjertsen, B. T., et al. (2016). A human clinical trial using ultrasound and microbubbles to enhance gemcitabine treatment of inoperable pancreatic cancer. *J. Control Release* 243, 172–181. doi: 10.1016/j.jconrel.2016.10.007

Domke, I., Cremer, P., and Huchtemann, M. (2000). Therapeutic drug monitoring on COBAS INTERGA 400—evaluation result. *Clin. Lab.* 46, 509–515.

Dong, Y., Li, J., Li, P., and Yu, J. (2018). Ultrasound microbubbles enhance the activity of vancomycin against Staphylococcus epidermidis biofilms in vivo. *J. Ultrasound Med.* 37, 1379–1387. doi: 10.1002/jum.14475

Escoffre, J. M., and Bouakaz, A. (2018). Mini-review – Biophysical mechanisms of cell membrane sonopermeabilization: knows and unknows. *Langmuir*. 35, 10151–10165. doi: 10.1021/acs.langmuir.8b03538

Escoffre, J. M., Kaddur, K., Rols, M. P., and Bouakaz, A. (2010). In vitro gene transfer by electrosonoporation. *Ultrasound Med. Biol.* 36, 1746–1755. doi: 10.1016/j.ultrasmedbio.2010.06.019

Escoffre, J. M., Novell, A., Serrière, S., Lecomte, T., and Bouakaz, A. (2013). Irinotecan delivery by microbubble-assisted ultrasound: in vitro validation and a pilot preclinical study. *Mol. Pharm.* 10, 2667–2675. doi: 10.1021/mp400081b

Geers, B., Dewitte, H., De Smedt, S. C., and Lentacker, I. (2012). Crucial factors and emerging concepts in ultrasounds-triggered drug delivery. *J. Control Release* 164, 248–255. doi: 10.1016/j.jconrel.2012.08.014

He, N., Hu, J., Liu, H., Zhu, T., Huang, B., Wang, X., et al. (2011). Enhancement of vancomycin activity against biofilms by using ultrasound-targeted microbubble destruction. *Antimicrob. Agents Chemother.* 55, 5331–5337. doi: 10.1128/AAC.00542-11

Kooiman, K., Vos, H. J., Versluis, M., and de Jong, N. (2014). Acoustic behavior of microbubbles and implications for drug delivery. *Adv. Drug Deliv. Rev.* 72, 28–48. doi: 10.1016/j.addr.2014.03.003

Koulenti, D., Tsigou, E., and Rello, J. (2017). Nosocomial pneumonia in 27 ICUs in Europe: perspectives from the EU-VAP/CAP study. *Eur. J. Clin. Microbiol. Infect. Dis.* 36, 1999–2006. doi: 10.1007/s10096-016-2703-z

Leone, M., Bouadma, L., Bouhemad, B., Brissaud, O., Dauger, S., Gibot, S., et al. (2018). Hospital acquired pneumonia in ICU. *Anaesth. Crit. Care Pain Med.* 37, 83–98. doi: 10.1016/j.accpm.2017.11.006

Lichtenstein, D., Mézière, G., Biderman, P., Gepner, A., and Barré, O. (1997). The comet-tail artifact. An ultrasound sign of alveolar-interstitial syndrome. *Am. J. Respir. Crit. Care Med.* 156, 1640–1646. doi: 10.1164/ajrccm.156.5.96-07096

Lin, T., Cai, X. Z., Shi, M. M., Ying, Z. M., Hu, B., Zhou, C. H., et al. (2015). In vitro and in vivo evaluation of vancomycin-loaded PMMA cement in combination with ultrasound and microbubbles-mediated. *BioMed. Res. Int.* 2015, 309739. doi: 10.1155/2015/309739

Müllhaupt, D., Wenger, S., Kircher, P., Pfammatter, N., Hatt, J. M., and Ohlerth, S. (2017). Computed tomography of the thorax in rabbits: a prospective study in ten clinically healthy New Zealand White rabbits. *Acta Vet. Scand.* 59, 72–80. doi: 10.1186/s13028-017-0340-x

Martin-Loeches, I., Deja, M., Koulenti, D., Dimopoulos, G., Marsh, B., Torres, A., et al. (2013). Potentially resistant microorganisms in intubated patients with hospital-acquired pneumonia: the interaction of ecology, shock and risk factors. *Intensive Care Med.* 39, 672–681. doi: 10.1007/s00134-012-2808-5

Rello, J., Ollendorf, D. A., Oster, G., Vara-Llonch, M., Bellm, L., Redman, R., et al. (2002). Epidemiology and outcomes of ventilator-associated pneumonia in a large US database. *Chest* 122, 2115–2121. doi: 10.1378/chest.122.6.2115

Sennoga, C. A., Kanbar, E., Auboire, L., Dujardin, P. A., Fouan, D., Escoffre, J. M., et al. (2017). Microbubble-mediated ultrasound drug-delivery and therapeutic monitoring. *Expert Opin. Drug Deliv.* 14, 1031–1043. doi: 10.1080/17425247.2017.1266328

Shang, Y., Dong, X., Han, G., Li, J., Cui, D., Liu, C., et al. (2015). The roles of tight junctions and Claudin-1 in the microbubble-mediated ultrasound-induced enhancement of drug concentrations in rat prostate. *J. Membr. Biol.* 248, 1167–1173. doi: 10.1007/s00232-015-9834-5

Shih, C. P., Chen, H. C., Chen, H. H., Chiang, M. C., Sytwu, H. K., Lin, Y. C., et al. (2013). Ultrasound-aided microbubbles facilitate the delivery of drugs to the inner ear via the round window membrane. *J. Control Release* 167, 167–174. doi: 10.1016/j.jconrel.2013.01.028

Sugiyama, M., Mintsopoulos, V., Raheel, H., Goldenberg, N. M., Batt, J. E., Brochard, L., et al. (2018). Lung ultrasound and microbubbles enhance aminoglycoside efficacy and delivery to the lung in Escherichia coli-induced pneumonia and acute respiratory distress syndrome. *Am. J. Respir. Crit. Care Med.* 198, 404–408. doi: 10.1164/rccm.201711-2259LE

Yu, F. T., Chen, X., Wang, J., Qin, B., and Villanueva, F. S. (2016). Low intensity ultrasound mediated liposomal doxorubicin delivery using polymer microbubbles. *Mol. Pharm.* 13, 55–64. doi: 10.1021/acs.molpharmaceut.5b00421

Zhang, Y., Chang, S., Sun, J., Zhu, S., Pu, C., Li, Y., et al. (2015). Targeted Microbubbles for ultrasound mediated short hairpin RNA plasmid transfection to inhibit survivin gene expression and induce apoptosis of ovarian cancer A2780/DDP Cells. *Mol. Pharm.* 12, 3137–3145. doi: 10.1021/mp500835z

Conflict of Interest: The authors declare that the research was conducted in the absence of any commercial or financial relationships that could be construed as a potential conflict of interest.

The handling editor is currently organizing a Research Topic with one of the authors J-ME, and confirms the absence of any other collaboration.

frontiers in Pharmacology

ORIGINAL RESEARCH
published: 28 January 2020
doi: 10.3389/fphar.2019.01651

Micro-Particle Image Velocimetry Investigation of Flow Fields of SonoVue Microbubbles Mediated by Ultrasound and Their Relationship With Delivery

Penglin Zou[1†], Mengqi Li[2†], Ziqi Wang[1], Guoxiu Zhang[3], Lifang Jin[1], Yan Pang[2], Lianfang Du[1], Yourong Duan[4], Zhaomiao Liu[2*] and Qiusheng Shi[1*]*

[1] Department of Ultrasound, Shanghai General Hospital, Shanghai Jiao Tong University School of Medicine, Shanghai, China, [2] College of Mechanical Engineering and Applied Electronics Technology, Beijing University of Technology, Beijing, China, [3] Department of Emergency, The First Affiliated Hospital of Henan University of Science and Technology, Luoyang, China, [4] State Key Laboratory of Oncogenes and Related Genes, Shanghai Cancer Institute, Renji Hospital, Shanghai Jiao Tong University School of Medicine, Shanghai, China

The flow fields generated by the acoustic behavior of microbubbles can significantly increase cell permeability. This facilitates the cellular uptake of external molecules in a process known as ultrasound-mediated drug delivery. To promote its clinical translation, this study investigated the relationships among the ultrasound parameters, acoustic behavior of microbubbles, flow fields, and delivery results. SonoVue microbubbles were activated by 1 MHz pulsed ultrasound with 100 Hz pulse repetition frequency, 1:5 duty cycle, and 0.20/0.35/0.70 MPa peak rarefactional pressure. Micro-particle image velocimetry was used to detect the microbubble behavior and the resulting flow fields. Then HeLa human cervical cancer cells were treated with the same conditions for 2, 4, 10, 30, and 60 s, respectively. Fluorescein isothiocyanate and propidium iodide were used to quantitate the rates of sonoporated cells with a flow cytometer. The results indicate that (1) microbubbles exhibited different behavior in ultrasound fields of different peak rarefactional pressures. At peak rarefactional pressures of 0.20 and 0.35 MPa, the dispersed microbubbles clumped together into clusters, and the clusters showed no apparent movement. At a peak rarefactional pressure of 0.70 MPa, the microbubbles were partially broken, and the remainders underwent clustering and coalescence to form bubble clusters that exhibited translational oscillation. (2) The flow fields were unsteady before the unification of the microbubbles. After that, the flow fields showed a clear pattern. (3) The delivery efficiency improved with the shear stress of the flow fields increased. Before the formation of the microbubble/bubble cluster, the maximum shear stresses of the 0.20, 0.35, and 0.70 MPa groups were 56.0, 87.5 and 406.4 mPa, respectively, and the rates of the reversibly sonoporated cells were 2.4% ± 0.4%, 5.5% ± 1.3%, and 16.6% ± 0.2%. After the cluster formation, the maximum shear stresses of the three groups were 9.1, 8.7, and 71.7 mPa, respectively. The former two could not mediate sonoporation, whereas the

OPEN ACCESS

Edited by:
Jean-Michel Escoffre, INSERM U1253Imagerie et Cerveau (iBrain), France

Reviewed by:
Michiel Postema, University of the Witwatersrand, South Africa
Anthony Novell, UMR8081 Imagerie par Résonance Magnétique Médicale et Multi-Modalités (IR4M), France

***Correspondence:**
Yourong Duan
yrduan@shsci.org
Zhaomiao Liu
lzm@bjut.edu.cn
Qiusheng Shi
sqs19631989@163.com

[†]These authors have contributed equally to this work

Specialty section:
This article was submitted to Translational Pharmacology, a section of the journal Frontiers in Pharmacology

Received: *30 July 2019*
Accepted: *16 December 2019*
Published: *28 January 2020*

Citation:
Zou P, Li M, Wang Z, Zhang G, Jin L, Pang Y, Du L, Duan Y, Liu Z and Shi Q (2020) Micro-Particle Image Velocimetry Investigation of Flow Fields of SonoVue Microbubbles Mediated by Ultrasound and Their Relationship With Delivery. Front. Pharmacol. 10:1651. doi: 10.3389/fphar.2019.01651

last one could. These findings demonstrate the critical role of flow fields in ultrasound-mediated drug delivery and contribute to its clinical applications.

Keywords: flow field, microbubble, delivery, ultrasound, shear stress

INTRODUCTION

A microbubble population driven by ultrasound can enhance the delivery of external molecules through a process called ultrasound-mediated drug delivery (UMDD) (Tang et al., 2017). Numerous preclinical studies have proven the feasibility of UMDD and its advantages of safety, efficiency, and convenience (Shi et al., 2014; Xing et al., 2016; Lin et al., 2018). Through further research and development, UMDD has entered the clinical trial stage. Good therapeutic effect and no significant adverse effects have been observed (Carpentier et al., 2016; Dimcevski et al., 2016), which indicates that UMDD has great clinical potential. However, many obstacles still need to be overcome before clinical application can be achieved. One of the most important obstacles is that the exact mechanism has not been elucidated (Helfield et al., 2016b).

Cavitation, the creation and subsequent dynamic behavior of microbubbles, has been shown to play a key role in UMDD (De Cock et al., 2016; Huang et al., 2018; Pereno et al., 2018). According to the morphological changes of microbubbles, cavitation can be divided into two types: stable and transient. Stable cavitation refers to the periodic expansion and contraction of microbubbles around their equilibrium radius in a low-pressure sound field. Transient cavitation refers to the large expansion and rapid collapse of microbubbles in a high-pressure sound field (Huang et al., 2018). Because microbubbles are located within a medium or blood, the above behavior inevitably disturbs the surrounding liquid to form flow fields. The flow fields exert shear and normal stresses on the plasma membranes and induce pore formation (Rong et al., 2018). This process called sonoporation is the primary mechanism of UMDD (Mehier-Humbert et al., 2005; Kooiman et al., 2014; Qin et al., 2018). Depending on the duration of existence of the pores, sonoporation is divided into two types: reversible and irreversible (Wu et al., 2002; Lentacker et al., 2014; Nejad et al., 2016; Qin et al., 2018). The former refers to the formation of reparable pores on cell membranes, while the latter refers to irreparable pores. Both pore types can facilitate the cellular uptake of external impermeable macromolecules, but the former does not have a significant effect on cell viability, while the latter leads to cell death. Current research suggests that the duration of pores which varies from the order of milliseconds to minutes (Deng et al., 2004; Qin et al., 2016) depends on the pore size. The pore size varies from the order of nanometers to micrometers (Mehier-Humbert et al., 2005; Yun et al., 2009) and depends on the bubble-cell distance and peak negative pressure (PRP). For details of the spatiotemporal characteristics of pores, see Refs. (Qin et al., 2018). The acoustic behavior of microbubbles and the cell responses during the delivery process have been extensively studied, but the role of flow fields in delivery is largely unknown (Kooiman et al., 2014).

There have been few experimental studies on the flow fields of ultrasound-activated microbubbles, which may be due to the difficulty of quantitative analysis of microscale flow fields with sufficient spatial and temporal resolution. Optical microscopy can only observe the dynamic behavior of individual microbubbles and microbubble groups (Fan et al., 2014; Nejad et al., 2016; van Rooij et al., 2016) but cannot detect the velocity fields around them. Gelderblom (2012) used ultra-high-speed fluorescence imaging to capture acoustic streaming around liposome-loaded microbubbles, but this was only a qualitative study, and they did not provide detailed information. Marmottant and Hilgenfeldt (2003) added lipid vesicles as a tracer to a cuvette with oscillating bubbles attached and depicted the streamlines by tracking the trajectories of the vesicles. However, the size of the vesicles was 10–100 μm, which resulted in poor followability and significant interference to the flow fields. Thus, there was a large difference between the measured and calculated values of the flow fields. None of the above methods can meet the requirements of microscale flow field detection. Thus, flow visualization technology is required for in-depth research.

Micro-particle image velocimetry (Micro-PIV) is a microscale flow measurement technique developed in the 1990s (Raffel et al., 2007). It combines traditional PIV technology with optical microscopy and can accurately measure two-dimensional microscale velocity fields without interference. Currently, other measurement techniques such as micro-laser Doppler velocimetry, Raman scattering, and molecular tagging velocimetry do not provide a resolution and measurement accuracy comparable to micro-PIV. Tho et al. (2007) and Collis et al. (2010) used micro-PIV to study the flow fields around a bubble undergoing stable cavitation; they found that many different microstreaming patterns were possible around a bubble, and each pattern generated different shear stress and stretch/compression distributions. Reuter et al. (2017) used micro-PIV and high-speed cameras to study the flow fields and vortex dynamics of bubbles collapsing near a solid boundary. Their results showed that the flow patterns of transient cavitation included free and wall vortices and depended on the bubble stand-off distance. These experiments demonstrated the feasibility and accuracy of micro-PIV, but the research objects were individual unencapsulated bubbles of several hundred microns in diameter. In contrast, UMDD uses encapsulated microbubbles with a diameter of 10 μm or less. Cho et al. (2015) measured the movement speed of SonoVue microbubbles caused by primary and secondary radiation forces in a blood vessel model, but they ignored the flow fields generated by the oscillation of microbubbles and microbubble clusters. Pereno et al. (2018) developed an device called a layered acoustofluidic resonator. This device could optically and

acoustically characterize cavitation dynamics, microstreaming, and biological effects simultaneously and was therefore an ideal system to study the interactions between UMDD and tissue. However, only the feasibility of the device was verified. The relationships among the detected objects were not studied, and no follow-up studies have been reported yet. Therefore, further research is needed on the flow fields of ultrasound-activated microbubbles.

In this study, bright field and fluorescence imaging were used on the micro-PIV system to capture the acoustic behavior and flow fields of SonoVue microbubbles driven by ultrasound, respectively. The relationships among the ultrasound parameters, acoustic behavior of microbubbles, and flow fields were clarified through qualitative and quantitative analyses of the flow patterns and shear microenvironment. Fluorescein isothiocyanate (FITC) was then delivered to HeLa human cervical cancer cells under the same experimental conditions, and the uptake efficiency and cell viability were analyzed with a flow cytometer. Based on the micro-PIV results and flow cytometry data, the role of the flow fields in UMDD was discussed. This study explored the mechanism of UMDD from the perspective of fluid dynamics, which not only contributes to the optimization, design, and future clinical transformation of this technology but also breaks a new path for research on its mechanism.

MATERIALS AND METHODS

Ultrasound Exposure Device

The authors developed a custom device to facilitate ultrasound exposure of the SonoVue microbubbles, as shown in **Figure 1A**. Polydimethylsiloxane was used to fabricate a tank filled with degassed water for coupling the ultrasound. A cylindrical cell culture chamber (**Figure 1B**) made of borosilicate glass was placed at the bottom of the tank. The thickness of the glass was 0.13 mm, and the basal diameter and height of the chamber were 14 mm and 1.6 mm, respectively. A flat transmitting transducer (Physioson-Basic, PHYSIOMED Elektro-medizin, Germany) was vertically immersed in the degassed water using a three-dimensional fixator. The transducer had a diameter of 17.8 mm and completely covered the chamber. The distance of the acoustic near field in this experiment was about 54.9 mm. The sound pressure in the near field fluctuated greatly. Therefore, the chamber was placed in the far field at a distance of 60 mm from the incident surface of the transducer.

Acoustic Calibration

PRP is one of the main influencing factors of sonoporation (Kotopoulis and Postema, 2010; Lin et al., 2017; Qin et al., 2018), so it was chosen as the research variable. Before the experiment proper commenced, the PRP was determined with a hydrophone (HGL-0200, ONDA, USA) at different output intensities. All experiments were carried out at a room temperature of 25 °C unless noted otherwise. Please see the **Supplementary Material** for details of the calibration.

Microbubble Preparation

SonoVue microbubbles (Bracco, Italy) consist of phospholipid shells filled with sulfur hexafluoride and have a diameter of 2–7 μm. According to the manufacturer's specifications, the microbubbles were freshly reconstituted in 5 mL of physiological saline solution to form a suspension with a concentration of 2–5 × 10^8/mL (Correas et al., 2001). The reconstituted SonoVue microbubbles were diluted in phosphate buffer saline (PBS) to a concentration of 20% (v/v).

Experimental Grouping

The control groups for the studies consisted of the PBS group, US group, and MB group. The fluids to be tested of the three groups were PBS, PBS, and diluted microbubble suspension, respectively. And only the US group was exposed to ultrasound at a PRP of 0.70 MPa. The experimental groups had the same test fluid as the MB group, with ultrasound irradiation at PRPs of 0.20, 0.35, and 0.70 MPa. The PRP for UMDD typically ranges from 0.06 to 0.60 MPa (Fan et al., 2014; Qin et al., 2016; Pereno et al., 2018), with early *in vitro* studies reporting sonoporation at PRPs as high as 1.32 MPa (Lai et al., 2006). Within this range, we selected a number of PRP levels for pre-experiments. The results showed that 0.20 MPa was below the transient cavitation threshold and shear stress threshold for sonoporation, 0.35 MPa was below the transient cavitation threshold and above the shear stress threshold for sonoporation, 0.70 MPa was above the transient cavitation threshold and shear stress threshold for sonoporation. Therefore, we selected the above three levels with typical characteristics for formal experiments and reporting. The other ultrasound parameters were fixed to optimized values that were more suitable for delivery (Chen et al., 2016; Lin et al., 2018), including a center frequency of 1 MHz, pulse repetition frequency of 100 Hz, and duty cycle of 1:5.

Micro-PIV Detection

The micro-PIV system (Dantec Dynamics, Denmark) consisted of an inverted microscope, double-pulse Nd : YAG laser, metal halide lamp, digital charge-coupled device camera, and computer (**Figure 1B**). The laser produced a laser beam with a wavelength of 532 nm. The laser beam was reflected by a dichroic mirror and then focused by the objective lens into the fluid to be tested in the cell culture chamber on the stage. After being excited by the laser beam, the tracer particles dispersed in the fluid emitted fluorescence at a wavelength of 612 nm, which was recorded by the camera. The computer processed the fluorescence and calculated the fluid velocity of the detected plane. The optical path of the metal halide lamp was similar to that of the laser and was mainly used for the bright field imaging of the acoustic behavior of the microbubble groups.

Monolayer cells are only few microns thick, which cannot significantly affect the acoustic interaction (Brujan et al., 2001). Therefore, cells were not seeded in the chamber in this section to ensure the accuracy of the micro-PIV detection. 0.02 mL of tracer particle suspension (Fluoro-Max, Thermo Fisher

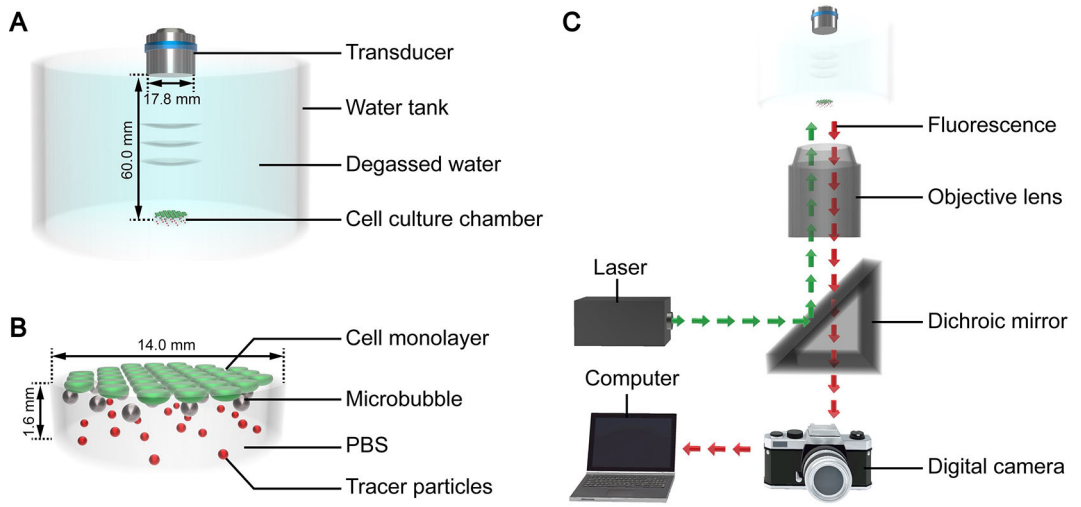

FIGURE 1 | 3D schematic diagram of the **(A)** ultrasound exposure device, **(B)** cell culture chamber, and **(C)** micro-PIV system.

Scientific, USA) was added to each milliliter of the fluid to be tested. The ultrasound exposure device was placed on the stage of the micro-PIV system. Then, the mixed suspension was added into the chamber and allowed to stand for 100 s to ensure that all microbubbles floated to the top of the chamber. Subsequently, the vertical height of the objective lens was adjusted to focus on the plane of the microbubbles, which was the detection plane. The metal halide lamp and ultrasound were then simultaneously turned on to capture the bright field images of the microbubbles. Finally, the new mixed suspension was replaced, and the fluorescence of the detection plane was induced with laser irradiation.

The tracer particles used for flow visualization were 1 μm diameter polystyrene fluorescent microspheres that were coated in a red dye with an excitation wavelength of 532 nm. The size and dosage of the tracer particles were determined based on our previous researches (Liu et al., 2017; Liu et al., 2019) and pre-experiments in order to ensure the measurement accuracy. The numerical aperture of the objective lens was 0.4, and the magnification was 10 ×. The depth of correlation is given by $\delta_{DOC} = 2\{\frac{(1-\sqrt{\epsilon})}{\sqrt{\epsilon}}[\frac{n_o^2 d_p^2}{4d} + \frac{5.95(M+1)^2\lambda^2 n_o^4}{16M^2 d^4}]\}^{1/2}$, where d_p is the particle diameter, λ is the laser wavelength, M is the magnification, n_o is the refractive index of the infiltrating liquid of the objective lens, d is the numerical aperture, and ϵ is the weight limit value (Olsen and Adrian, 2000). Thus, the depth of correlation in this experiment was 18 μm. The digital camera was used to acquire the bright and flow field images in single and dual frame modes, respectively, at a frequency of 6.1 Hz. The time interval between the two images in the dual frame mode was set according to different flow conditions from 50 to 3,000 μs (Liu et al., 2017; Liu et al., 2019). The fluorescence signal was analyzed with a standard cross-correlation algorithm implemented in commercial PIV software. The interrogation area size was 32 × 32 pixels with an overlap of 50%.

Shear Stress Calculation

The velocity gradients were calculated from the measured velocities with the least squares method. Based on the velocity gradients, the shear rates were estimated as $\epsilon = \frac{\partial \bar{u}}{\partial y} + \frac{\partial \bar{v}}{\partial x}$ (Ma et al., 2015). The shear stress τ was calculated as $\tau = \eta\epsilon$, where η was the fluid viscosity and set to 1.05 ± 0.01 mPa·s (Helfield et al., 2016a).

UMDD Delivery

HeLa cells are commonly used for UMDD (Lai et al., 2006; Qin et al., 2014; Fan et al., 2017) because they have a fast proliferation rate and are easy to operate experimentally. Therefore, these cells were selected in this study for the delivery experiments. HeLa cells were obtained from the Institute of Biochemistry and Cell Biology of the Chinese Academy of Sciences (Shanghai, China). Cells were seeded in the cell culture chamber and cultured in Dulbecco's modified Eagle medium (DMEM; Hyclone, USA) supplemented with 10% fetal bovine serum (Gibco, USA) in a humidified incubator at 37°C with 5% CO_2. After the cells reached 60–70% confluence, the DMEM was removed. Then, a mixture of FITC (Invitrogen, USA) and the fluid to be tested was added. The final concentration of FITC was 2 mg/mL. After standing for 100 s, each sample was subjected to ultrasound irradiation. The irradiation duration was 60 s for the US group and 2, 4, 10, 30, or 60 s for the UMDD groups. After exposure to ultrasound, samples were placed in an incubator for 30 min.

Evaluation of the FITC Uptake Efficiency and Cell Viability

To assess the cell viability after UMDD treatments, propidium iodide (PI; Invitrogen, USA) was added to the chamber at a concentration of 2 μM to stain the dead cells for 10 min. After being washed twice with PBS, the cells were trypsinized and

collected for measurement of the FITC uptake efficiency and cell viability *via* fluorescence activated cell-sorting (Beckman Coulter, Miami, Florida).

Statistical Analysis

All experiments were performed in triplicate. Statistical analysis of the fluorescence activated cell-sorting data was performed through one-way analysis of variance followed by Bonferroni multiple comparison with SPSS version 22.0. The significance level was set to a value of 0.05.

RESULTS AND DISCUSSION

Relationships Between the Ultrasound Parameters and Acoustic Behavior of Microbubbles

After the suspension was added to the chamber and allowed to stand for 100 s, bright field imaging showed that the microbubbles of each group were uniformly and stably suspended at the detection plane (**Figure 2A**). The flow tracers were evenly dispersed throughout the fluid, and no significant floating or sinking occurred (**Figure 2B**). This was because that the particles matched the density of the surrounding fluid, which could minimize the measurement error caused by gravity and buoyancy (Tho et al., 2007).

Figures 3A, **4A**, and **5A** show the acoustic behavior of the microbubbles of the three experimental groups in the ultrasound field. Once ultrasound was applied, the dispersed microbubbles in the 0.20 and 0.35 MPa groups rapidly aggregated into small clusters. The small clusters then gathered together to form several honeycombed microbubble clusters of different sizes at 3.93 and 1.96 s, respectively. Some researchers have referred to this kind of microbubble cluster as a microbubble cloud (Kotopoulis and Postema, 2010). The resulting microbubble clouds were relatively static and showed no obvious movement. For the 0.70 MPa group, it was found that the concentration of microbubbles in the second image frame (0.16 s in **Figure 5A**) is approximately 32.2% lower than that in the first image frame (0.00 s in **Figure 5A**) by evaluating the changes in the number of pixels occupied by the microbubbles. This indicates that the microbubbles were partially destroyed. Subsequently, the remaining microbubbles underwent clustering and coalescence. The clustering refers to the deduction of distance among microbubbles, while the coalescence means the fusion of two or more microbubbles. Finally, the microbubbles formed several bubble clusters which underwent translating oscillation along a single axis (1.80–2.78 s in **Figure 5A**) (Tho et al., 2007).

The action of mechanical force caused the above microbubble behavior. In this experimental system, the microbubbles were mainly affected by five kinds of mechanical forces: the buoyancy, gravity, primary radiation force, secondary radiation force, and sound pressure. The primary radiation force acts on an object in a sound field parallel to the direction of the sound (Dayton et al., 1997; Dayton et al., 2002). Therefore, the microbubbles were subjected to the downward gravity and primary radiation force as well as the upward buoyancy. With ultrasound irradiation, no

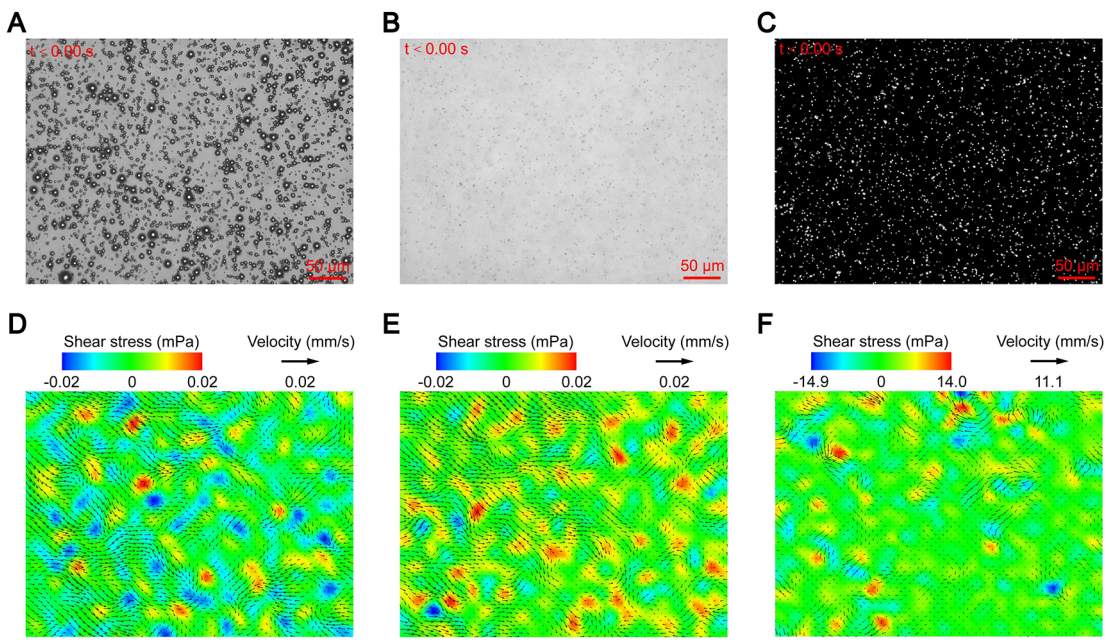

FIGURE 2 | Micro-PIV results of the control groups: **(A)** suspended microbubbles at the detection plane; **(B)** flow tracers dispersed throughout the fluid; **(C)** fluorescent image of flow tracers at the detection plane; and maximum flow velocity and corresponding shear stress of the **(D)** PBS group, **(E)** MB group, and **(F)** US group.

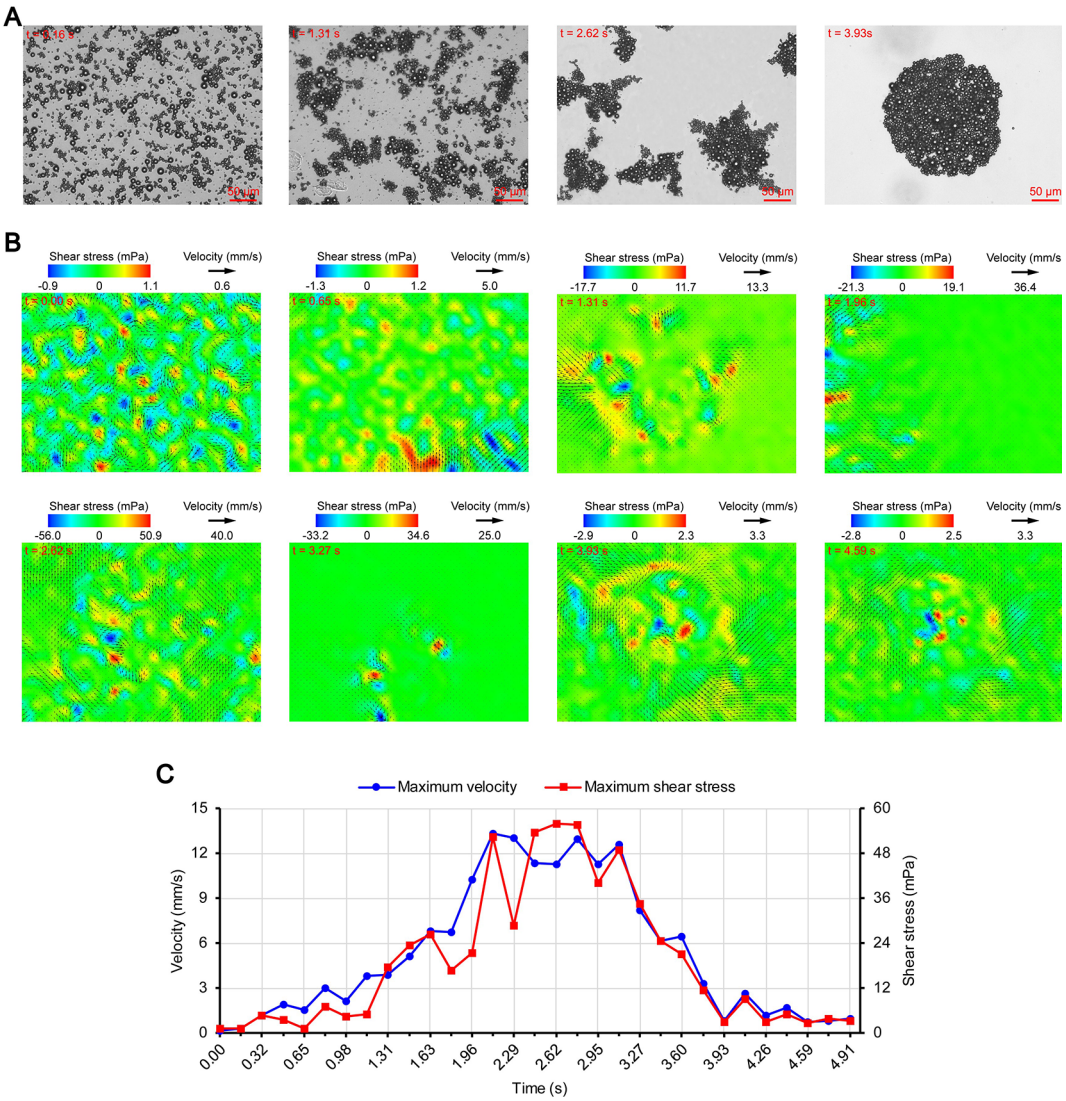

FIGURE 3 | Micro-PIV results of the 0.20 MPa group. **(A)** Acoustic behavior of the microbubbles. The effect of the microbubbles on light was attenuated with accumulation, and the brightness of the images gradually increased. **(B)** Temporal evolution and spatial distribution of the velocity fields and shear stress. **(C)** Time variation of the maximum shear stress and maximum flow velocity.

sinking microbubbles were obvious in the other planes of the fluid, which indicates that the buoyancy was greater than the sum of the gravity and primary radiation force. This caused the microbubbles to always float on the detection plane. Therefore, the behavior induced by these three mechanical forces was slight.

As described in the introduction, sound pressure with positive and negative variations causes cavitation of microbubbles. Although the details of the microbubble oscillations could not be observed because of the low magnification of the objective lens, the type of cavitation could be distinguished depending on whether or not the microbubbles were broken. Therefore, the 0.20 and 0.35 MPa groups underwent stable cavitation, while the 0.70 MPa group underwent transient cavitation in the initial stage of ultrasound irradiation. This was consistent with the report by Lin et al. (2017) on the transient cavitation threshold of SonoVue microbubbles. We also noticed that the smaller microbubbles preferentially ruptured, probably due to their lower transient cavitation threshold (Kooiman et al., 2014). In addition to the cavitation, sound pressure also induces microbubble coalescence (**Figure 5A**). The expansion or collision of adjacent microbubbles can result in flattening and thinning of the phospholipid coatings at the contact (Postema et al., 2004). These deformations continue until a critical thickness of about 0.1 μm is reached, at which the van der Waals force results in coating rupture and microbubble coalescence (Kotopoulis and Postema, 2010). The degree of deformation is positively correlated

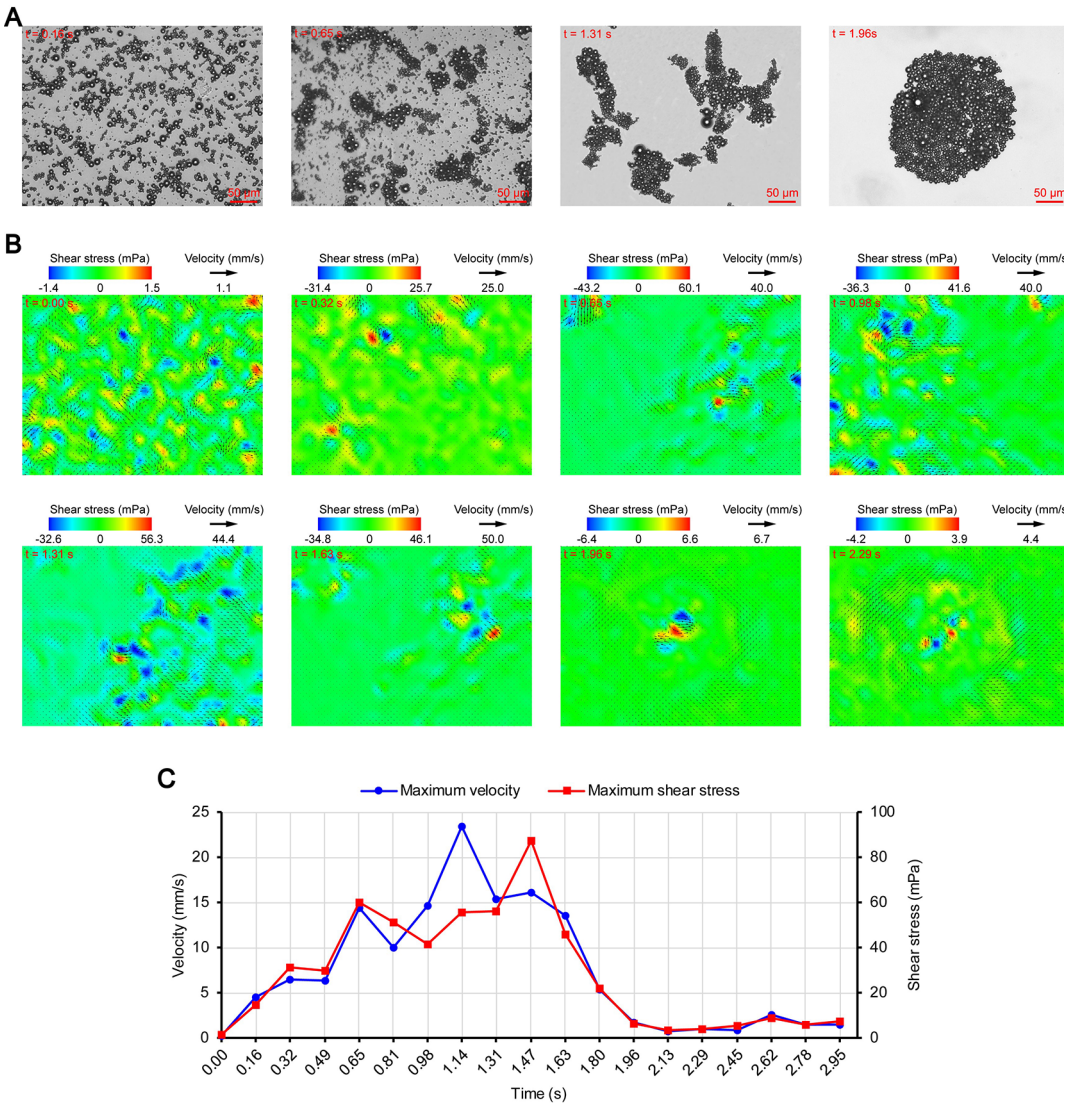

FIGURE 4 | Micro-PIV results of the 0.35 MPa group. **(A)** Acoustic behavior of the microbubbles. **(B)** Temporal evolution and spatial distribution of the velocity fields and shear stress. **(C)** Time variation of the maximum shear stress and maximum flow velocity.

with the PRP (Kotopoulis and Postema, 2010), so obvious coalescence was observed only in the 0.70 MPa group.

The secondary radiation force is also called the Bjerknes force and is generated by the scattering effect of the incoming ultrasonic waves from the liquid-gas interface (Hashmi et al., 2012), which causes the originally dispersed satellite bubbles to gather toward the core bubbles and form microbubble clusters (Fan et al., 2014). Kotopoulis and Postema (2010) demonstrated that the time required for clustering was inversely proportional to the square of the PRP. However, the clustering time ratio of the 0.35 MPa group to the 0.20 MPa group was 1.96/3.93 = 0.4987, which did not match the ratio of the square of the PRP ($0.35^2/0.20^2$ = 3.0625). The main reason may be that the boundary layer limited the acceleration of the microbubble clustering. Another possible reason is that the attraction of the microbubbles to the tracer particles reduces the measurement accuracy. Under the secondary radiation force, the particles are attracted toward the microbubbles (Hashmi et al., 2012), which may cause the measured value of the flow velocity to be lower than the true value. In order to avoid this influence, we chose particles that were smaller than those used by Cho et al. (2015). The PRP of the 0.70 MPa group was significantly higher than that of the 0.35 MPa group, but the clustering time of the two groups were very close. This may be because the concentration of the microbubbles decreased significantly after transient cavitation and the secondary radiation force decreased accordingly.

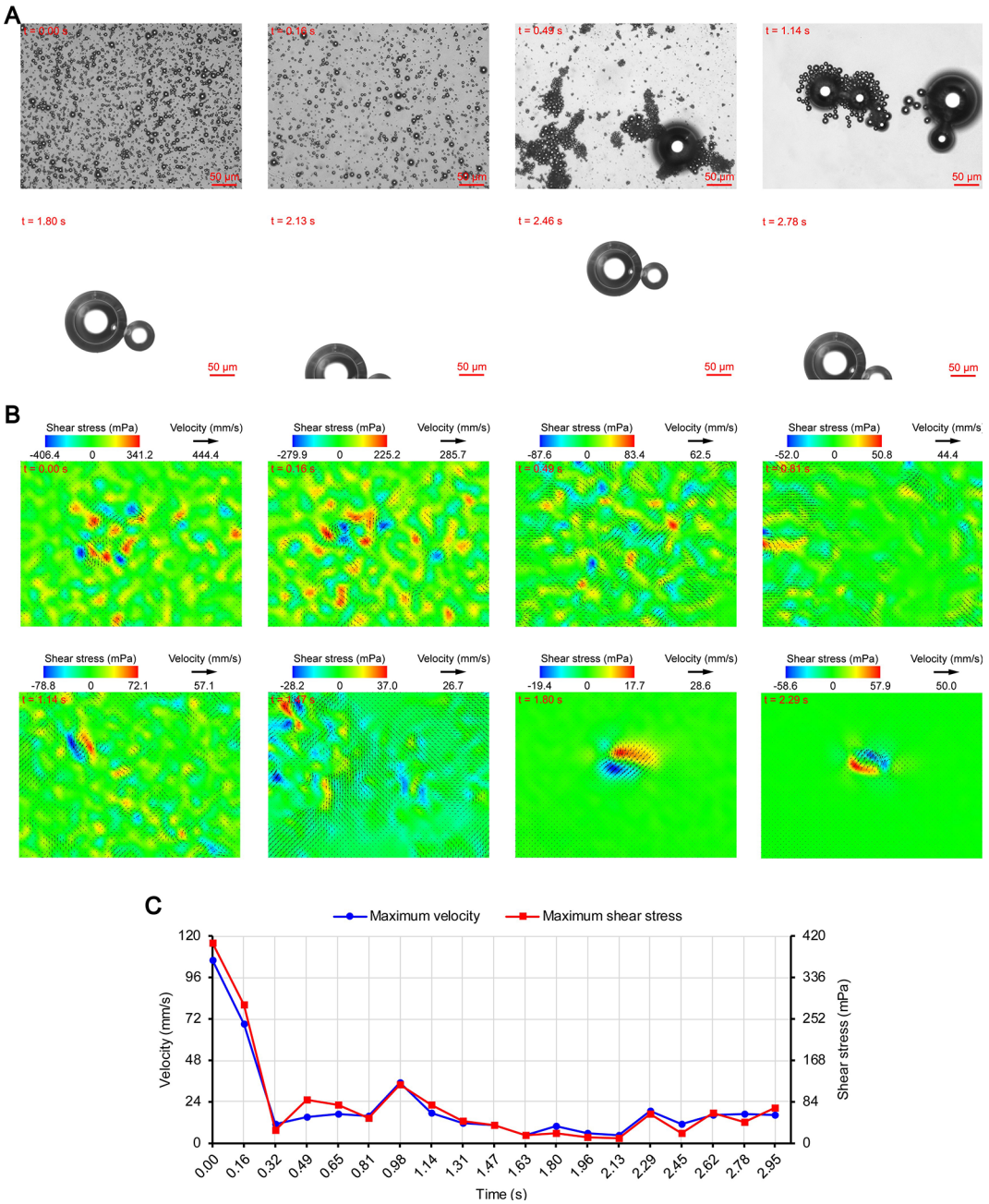

FIGURE 5 | Micro-PIV results of the 0.70 MPa group. **(A)** Acoustic behavior of the microbubbles. **(B)** Temporal evolution and spatial distribution of the velocity fields and shear stress. **(C)** Time variation of the maximum shear stress and maximum flow velocity.

Relationships Between the Acoustic Behavior of Microbubbles and Flow Fields

After the laser was turned on, the flow tracers of the detection plane emitted dot-like fluorescence, and no obvious aggregation was observed (**Figure 2C**). The instantaneous velocities of the detection plane were obtained through analysis of the fluorescence signal. The maximum velocities of the PBS and MB groups were 0.006 and 0.008 mm/s, respectively, and the maximum shear stress of both groups was 0.02 mPa (**Figures 2D, E**). The average uncertainty of the measured velocity is 5.6×10^{-2} mm/s, which is calculated by estimating an uncertainty in pixel displacement to be ±0.1 pixels (Raffel et al., 2007; Liu et al., 2019). Thus, the maximum velocities of the flow fields were less than the detection range of the micro-PIV when no ultrasound was applied, and the measured velocities should be regarded as background noise. For the US group, although no

microbubbles were added, the flow fields changed significantly with a maximum velocity of 4.5 mm/s and maximum shear stress of 14.9 mPa after ultrasound was applied (**Figure 2F**). This may have been due to the cavitation of the naturally dissolved air in the fluid. In order to test the hypothesis, the suspension of the US group was degassed and subjected to ultrasound again. The flow fields recovered to the levels of the PBS and MB groups, which confirmed the above conjecture.

Figures 3B, **4B**, and **5B** show the temporal evolution and spatial distribution of the velocity fields and shear stress of the three experimental groups. Before the formation of microbubble or bubble clusters (0.00–3.93 s in **Figure 3B**, 0.00–1.96 s in **Figure 4B** and 0.00–1.80 s in **Figure 5B**), none of the three groups showed obvious flow pattern and shear stress distribution law. Experimental studies have shown that the flow fields generated by the dynamic behavior of a single bubble have a specific pattern (Tho et al., 2007; Collis et al., 2010; Reuter et al., 2017). Although the bubbles they studied differ from the SonoVue microbubbles in size and shell, Collis et al. (2010) argued that nonlinear phenomena such as microstreaming are similar. However, when the flow fields of multiple microbubbles are superimposed on each other, the respective patterns are masked, which results in an unsteady flow overall without a specific pattern.

After the clustering was completed, multiple microbubbles formed a whole body that performed a unified motion, and the flow fields showed a relatively clear pattern as follows. The fluids of the 0.20 and 0.35 MPa groups diverged around the microbubble cloud, and the fluid velocity and shear stress decreased with increasing distance from the microbubble clouds. For the 0.70 MPa group, the flow direction was consistent with the movement direction of the bubble clusters, and the fluid velocity decreased with increasing distance from the bubble clusters. The shear stress on both sides of the bubble cluster was symmetrically distributed with similar values and opposite directions (1.80 s in **Figure 5B**). When the movement direction was reversed, the flow direction was simultaneously reversed, and eddy currents formed on both sides of the bubble cluster. Meanwhile, the direction of the shear stress also reversed and was still symmetrically distributed (2.29 s in **Figure 5B**).

The relationship between UMDD and delivery has often been discussed in the literature, and the shear stress threshold for sonoporation is one of the most commonly studied parameters (Wu et al., 2002; Fan et al., 2014; Helfield et al., 2016b; Nejad et al., 2016; Rong et al., 2018). **Figures 3C**, **4C**, and **5C** show the time variation of the maximum shear stress. Although not absolute, a high shear stress tends to correspond to high flow velocity, so the time variation of the maximum flow velocity is also shown in these figures. In the early stage of the 0.20 and 0.35 MPa groups (0.00–2.13 s in **Figure 3C** and 0.00–0.65 s in **Figure 4C**), the maximum velocity and maximum shear stress gradually increased to a high level, and the acceleration of both increased with time. The main reason was that, as the microbubbles continued to gather, the secondary radiation force increased accordingly (Fan et al., 2014), which in turn produced greater acceleration. After a brief fluctuation at a high level, the maximum velocity and maximum shear stress decreased rapidly, which indicated that the momentum of each cluster was significantly offset in the final stage of clustering. Although microbubbles can undergo linear and nonlinear oscillation at a PRP that is lower than the transient cavitation threshold, no obvious movement of the microbubble clouds was observed, and the shear stress were also very weak (9.1 mPa and 8.7 mPa, respectively). Studies (Caskey et al., 2007; Garbin et al., 2007; Overvelde et al., 2011) have shown that, when a bubble is near a wall, its cavitation is significantly suppressed. Therefore, the reason for the above phenomenon appears to be that the stacking and squeezing of microbubbles inhibited the oscillation.

Once ultrasound was applied, the maximum velocity and maximum shear stress of the 0.70 MPa group were immediately increased to 105.8 mm/s and 406.4 mPa, respectively. The sound pressure and secondary radiation force act on microbubbles at the same time, but the time scales of the two actions are completely different. After ultrasound was turned on, ultrahigh-speed microscopy was used to observe the occurrence of transient cavitation within tens of microseconds (Prentice et al., 2005), while the clustering take several seconds (Kotopoulis and Postema, 2010). Therefore, in the initial stage of ultrasound irradiation, the microjets generated by transient cavitation were the main components of the flow fields. When the microjets were perpendicular to the detection plane (Brujan et al., 2001), their accompanying eddy currents could be detected by micro-PIV (Reuter et al., 2017). Although the eddy currents were much weaker than the microjets which ranged in speed from a few meters per second (Prentice et al., 2005; Reuter et al., 2017) to hundreds of meters per second (Brujan et al., 2001), the former still had the highest flow velocity and shear stress measured in this study. The duration of the eddy currents was short, so the maximum velocity and maximum shear stress rapidly decreased to a low level (0.00–0.32 s in **Figure 5C**). Thereafter, the maximum velocity and maximum shear stress gradually increased to a high level and then rapidly decreased, and fluctuated between 9.9–71.7 mPa (0.32–2.95 s in **Figure 5C**).

The acoustic behavior of the microbubble group is very complicated because of the influence of the incident ultrasound, acoustic scattering, acoustic radiation force, and other factors (Lin et al., 2017); thus, flow field data measured under the same conditions may vary greatly. To account for this, the present study focused on the change law of the flow velocity and shear stress rather than the magnitude of specific values. The flow field detection of each group was repeated three times, and the change law was basically the same.

Relationship Between the Flow Fields and Delivery

FITC was used as a fluorescence marker for identifying sonoporated cells (Lin et al., 2018) in this study because it normally would not permeate through the cell membrane unless the membrane permeability is increased by sonoporation. PI, a cell viability detected agent, was used to distinguish the type of sonoporation (Lin et al., 2018) because the two types of sonoporation had different effects on cell viability. In

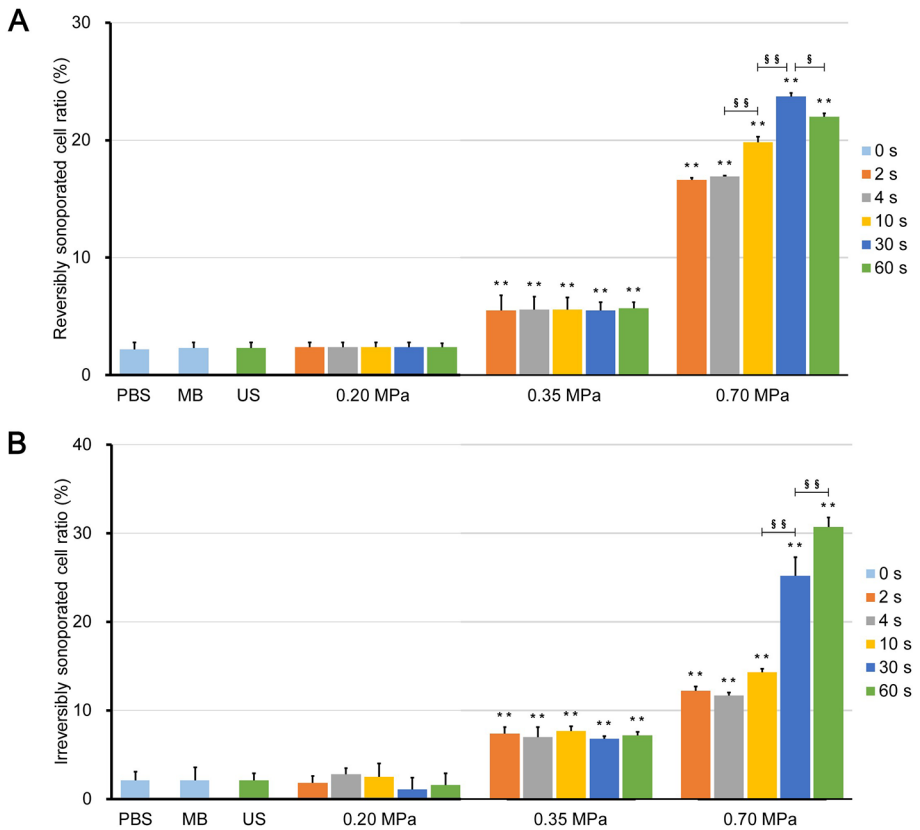

FIGURE 6 | Ratio of **(A)** reversibly sonoporated and **(B)** irreversibly sonoporated cells. Data are shown as the mean ± SEM (n = 3). ** $p < 0.01$ vs the control and 0.20 MPa group; $^{\S}p < 0.05$, $^{\S\S}p < 0.01$.

conclusion, both FITC and PI positive indicates the occurrence of irreversible sonoporation, while FITC positive and PI negative represent reversible sonoporation.

Figures 6A, B show the rates of reversibly and irreversibly sonoporated cells, respectively. The two rates of the three control groups were very low, which indicates that no significant FITC uptake and cell death occurred. Although the flow fields of the US group were completely different from those of the PBS and MB groups, there was no statistical difference between the three control groups ($p > 0.05$), which indicated that ultrasound combined with naturally dissolved air cannot cause obvious biological effects.

There was also no significant difference between the 0.20 MPa group and control groups ($p > 0.05$), which indicates that the maximum shear stress (**Figure 3C**) was less than the shear stress threshold for sonoporation. Although both the magnitude of the shear stress and the exposure time are important factors for sonoporation, the experimental results showed that prolonging the ultrasound exposure time to 60 s did not change the FITC uptake efficiency and cell viability significantly ($p > 0.05$) because of the weak shear stress generated by microbubble clouds.

After ultrasound irradiation for 2 s, the rates of the reversibly and irreversibly sonoporated cells of the 0.35 MPa group increased to 5.5% ± 1.3% and 7.4% ± 0.7%, respectively. This suggests that the maximum shear stress of the 0.35 MPa group exceeded the shear stress threshold for sonoporation in the accumulation stage, and both types of sonoporation occurred. The magnitude of the shear stress generated by microbubbles driven by low acoustic pressure and the shear stress threshold for sonoporation vary widely with a range from millipascals to kilopascals (Wu et al., 2002; Fan et al., 2014; Helfield et al., 2016b; Nejad et al., 2016; Rong et al., 2018). The primary reason for this difference is that the researchers used different calculation models and the current experimental or theoretical methods cannot account for all stress components (Ma et al., 2015). In the present study, the wall shear rate was estimated from the near-wall velocity, which may have affected the measurement of the wall shear stress (Cho et al., 2015). Despite this, the variation in the shear stress was credible. In addition, prolonging the ultrasound exposure time also failed to significantly change the flow cytometry results of the 0.35 MPa group for the same reason as the 0.20 MPa group.

The 0.70 MPa group underwent transient cavitation, and microjets directed toward cells were formed when microbubbles collapsed. The shear stress of the microjets was on the order of megapascals (Liang et al., 2010; Kooiman et al., 2014), which far exceeded the sonoporation shear stress threshold. Therefore, after ultrasound irradiation for 2 s, the rates of reversibly and

irreversibly sonoporated cells further increased to 16.6% ± 0.2% and 12.2% ± 0.5%, respectively. It should be noted that there are differences between *in vitro* cell experiments and practical applications *in vivo*. Typically, the elastic modulus of vessels is below 1 MPa, which indicates that the microjets are more likely to point away from the vessel wall (Brujan et al., 2001). This has been experimentally verified in *ex vivo* rat mesentery (Chen et al., 2011). Borosilicate glass with an elastic modulus of 7.2×10^4 MPa was used in the present study which caused the microjets to point towards the glass. When the exposure time to 30 s, both rates continued to increase to 23.7% ± 0.3% and 25.2% ± 2.1%, respectively; this indicated that the flow fields generated by the finally formed bubble clusters could induce sonoporation. When the exposure time was further increase to 60 s, the rate of irreversibly sonoporated cells increased to 30.7% ± 1.1%, while the rate of reversibly sonoporated cells decreased to 22.0% ± 0.3%. The reason may be that, under the action of shear stress, reversible sonoporation occurs first; as the action time increases, the reversible pores turn into irreversible ones, which leads to cell death. This is consistent with the point proposed by Wu et al. (Wu et al., 2002) that the mechanisms of reversible and irreversible sonoporation may be similar, but the degree of damage to cell membranes is different. A major challenge to the application of UMDD is both to obtain high delivery and to maintain good cell viability (Mehier-Humbert et al., 2005), and the above findings may be helpful in resolving this issue.

CONCLUSION

UMDD is a complex process and research on its mechanism requires cooperation between multiple disciplines. In this study, flow visualization technology was used to explore the change law of the flow fields generated by SonoVue microbubbles and the relationships among the ultrasound parameters, acoustic behavior of microbubbles, flow fields, and delivery results. Results indicate that under different ultrasonic conditions, SonoVue microbubbles exhibit different acoustic behavior that generate various flow fields which lead to distinct delivery results. These findings effectively serve to substantiate the causal relationship between flow fields and sonoporation and contribute to the clinical application of UMDD.

One limitation of this study is that only the PRP was selected as the variable. Other ultrasound parameters may also have an effect on the sonoporation. For example, when excited by ultrasound at resonance frequency, a bubble will result in the maximum acoustic radiation forces and the maximum shear stress (Kooiman et al., 2014). However, there is not one single resonance frequency for a polydisperse population of microbubbles. This means that only a subset of microbubbles will resonate and the oscillation amplitude of other microbubbles is much lower. Moreover, this study did not delve into the temporal and spatial relationships between the flow fields and cellular response, which will be the main objective of future research.

DATA AVAILABILITY STATEMENT

The datasets generated for this study are available on request to the corresponding author.

AUTHOR CONTRIBUTIONS

PZ and ML conducted the micro-PIV experiments. PZ drafted the manuscript. PZ, ZW, and GZ carried out the UMDD delivery experiments. YP, LD, YD, ZL, and QS contributed to conception and design of the study. All authors contributed to manuscript revision and approved the submitted version.

FUNDING

This work was supported by the National Natural Science Foundation of China (No. 81571677) and the Three-year Plan for Clinical Skills and Innovation in Municipal Hospitals (No. 16CR3093B).

SUPPLEMENTARY MATERIAL

The Supplementary Material for this article can be found online at: https://www.frontiersin.org/articles/10.3389/fphar.2019.01651/full#supplementary-material

REFERENCES

Brujan, E. A., Nahen, K., Schmidt, P., and Vogel, A. (2001). Dynamics of laser-induced cavitation bubbles near elastic boundaries: influence of the elastic modulus. *J. Fluid Mech.* 433, 283–314. doi: 10.1017/S0022112000003335

Carpentier, A., Canney, M., Vignot, A., Reina, V., Beccaria, K., Horodyckid, C., et al. (2016). Clinical trial of blood-brain barrier disruption by pulsed ultrasound. *Sci. Transl. Med.* 8, 343re2. doi: 10.1126/scitranslmed.aaf6086

Caskey, C. F., Stieger, S. M., Qin, S., Dayton, P. A., and Ferrara, K. W. (2007). Direct observations of ultrasound microbubble contrast agent interaction with the microvessel wall. *J. Acoust. Soc Am.* 122, 1191–1200. doi: 10.1121/1.2747204

Chen, H., Kreider, W., Brayman, A. A., Bailey, M. R., and Matula, T. J. (2011). Blood vessel deformations on microsecond time scales by ultrasonic cavitation. *Phys. Rev. Lett.* 106, 034301. doi: 10.1103/PhysRevLett.106.034301

Chen, H. H., Matkar, P. N., Afrasiabi, K., Kuliszewski, M. A., and Leong-Poi, H. (2016). Prospect of ultrasound-mediated gene delivery in cardiovascular applications. *Expert Opin. Biol. Th.* 16, 815–826. doi: 10.1517/14712598.2016.1169268

Cho, E., Chung, S. K., and Rhee, K. (2015). Streaming flow from ultrasound contrast agents by acoustic waves in a blood vessel model. *Ultrasonics* 62, 66–74. doi: 10.1016/j.ultras.2015.05.002

Collis, J., Manasseh, R., Liovic, P., Tho, P., Ooi, A., Petkovic-Duran, K., et al. (2010). Cavitation microstreaming and stress fields created by microbubbles. *Ultrasonics* 50, 273–279. doi: 10.1016/j.ultras.2009.10.002

Correas, J. M., Bridal, L., Lesavre, A., Mejean, A., Claudon, M., and Helenon, O. (2001). Ultrasound contrast agents: properties, principles of action, tolerance, and artifacts. *Eur. Radiol.* 11, 1316–1328. doi: 10.1007/s003300100940

Dayton, P. A., Morgan, K. E., Klibanov, A., Brandenburger, G., Nightingale, K. R., and Ferrara, K. W. (1997). A preliminary evaluation of the effects of primary

and secondary radiation forces on acoustic contrast agents. *IEEE T. Ultrason. Ferr.* 44, 1264–1277. doi: 10.1109/58.656630

Dayton, P. A., Allen, J. S., and Ferrara, K. W. (2002). The magnitude of radiation force on ultrasound contrast agents. *J. Acoust. Soc Am.* 112, 2183–2192. doi: 10.1121/1.1509428

De Cock, I., Lajoinie, G., Versluis, M., De Smedt, S. C., and Lentacker, I. (2016). Sonoprinting and the importance of microbubble loading for the ultrasound mediated cellular delivery of nanoparticles. *Biomaterials* 83, 294–307. doi: 10.1016/j.biomaterials.2016.01.022

Deng, C. X., Fred, S., Hua, P., and Jianmin, C. (2004). Ultrasound-induced cell membrane porosity. *Ultrasound Med. Biol.* 30, 519–526. doi: 10.1016/j.ultrasmedbio.2004.01.005

Dimcevski, G., Kotopoulis, S., Bjanes, T., Hoem, D., Schjott, J., Gjertsen, B. T., et al. (2016). A human clinical trial using ultrasound and microbubbles to enhance gemcitabine treatment of inoperable pancreatic cancer. *J. Control. Release* 243, 172–181. doi: 10.1016/j.jconrel.2016.10.007

Fan, Z. Z., Chen, D., and Deng, C. X. (2014). Characterization of the dynamic activities of a population of microbubbles driven by pulsed ultrasound exposure in sonoporation. *Ultrasound Med. Biol.* 40, 1260–1272. doi: 10.1016/j.ultrasmedbio.2013.12.002

Fan, P., Yi, Z., Xiasheng, G., Chenliang, C., Maochen, W., Dongxin, Y., et al. (2017). Cell-cycle-specific Cellular Responses to Sonoporation. *Theranostics* 7, 4894–4908. doi: 10.7150/thno.20820

Garbin, V., Cojoc, D., Ferrari, E., Di Fabrizio, E., Overvelde, M., van der Meer, S. M., et al. (2007). Changes in microbubble dynamics near a boundary revealed by combined optical micromanipulation and high-speed imaging. *Appl. Phys. Lett.* 90, 114103. doi: 10.1063/1.2713164

Gelderblom, E. C. (2012). *Ultra-high-speed fluorescence imaging* (Enschede: Universiteit Twente).

Hashmi, A., Yu, G., Reilly-Collette, M., Heiman, G., and Xu, J. (2012). Oscillating bubbles: a versatile tool for lab on a chip applications. *Lab. Chip* 12, 4216–4227. doi: 10.1039/c2lc40424a

Helfield, B., Black, J. J., Qin, B., Pacella, J., Chen, X. C., and Villanueva, F. S. (2016a). Fluid viscosity affects the fragmentation and inertial cavitation threshold of lipid-encapsulated microbubbles. *Ultrasound Med. Biol.* 42, 782–794. doi: 10.1016/j.ultrasmedbio.2015.10.023

Helfield, B., Chen, X. C., Watkins, S. C., and Villanueva, F. S. (2016b). Biophysical insight into mechanisms of sonoporation. *P. Natl. Acad. Sci. U.S.A.* 113, 9983–9988. doi: 10.1073/pnas.1606915113

Huang, H., Chen, Y. S., and Rupenthal, I. D. (2018). Overcoming ocular drug delivery barriers through the use of physical forces. *Adv. Drug Deliver. Rev.* 126, 96–112. doi: 10.1016/j.addr.2017.09.008

Kooiman, K., Vos, H. J., Versluis, M., and de Jong, N. (2014). Acoustic behavior of microbubbles and implications for drug delivery. *Adv. Drug Deliver. Rev.* 72, 28–48. doi: 10.1016/j.addr.2014.03.003

Kotopoulis, S., and Postema, M. (2010). Microfoam formation in a capillary. *Ultrasonics* 50, 260–268. doi: 10.1016/j.ultras.2009.09.028

Lai, C., Wu, C., Chen, C., and Li, P. (2006). Quantitative relations of acoustic inertial cavitation with sonoporation and cell viability. *Ultrasound Med. Biol.* 32, 1931–1941. doi: 10.1016/j.ultrasmedbio.2006.06.020

Lentacker, I., De Cock, I., Deckers, R., De Smedt, S. C., and Moonen, C. (2014). Understanding ultrasound induced sonoporation: Definitions and underlying mechanisms. *Adv. Drug Deliver. Rev.* 72, 49–64. doi: 10.1016/j.addr.2013.11.008

Liang, H. D., Tang, J., and Halliwell, M. (2010). Sonoporation, drug delivery, and gene therapy. *P. I. Mech. Eng. H* 224, 343–361. doi: 10.1243/09544119JEIM565

Lin, Y. T., Lin, L. Z., Cheng, M. W., Jin, L. F., Du, L. F., Han, T., et al. (2017). Effect of acoustic parameters on the cavitation behavior of SonoVue microbubbles induced by pulsed ultrasound. *Ultrason. Sonochem.* 35, 176–184. doi: 10.1016/j.ultsonch.2016.09.016

Lin, L. Z., Fan, Y., Gao, F., Jin, L. F., Li, D., Sun, W. J., et al. (2018). UTMD-promoted co-delivery of gemcitabine and miR-21 inhibitor by dendrimer-entrapped gold nanoparticles for pancreatic cancer therapy. *Theranostics* 8, 1923–1939. doi: 10.7150/thno.22834

Liu, Z. M., Zhang, L. X., Pang, Y., Wang, X., and Li, M. Q. (2017). Micro-PIV investigation of the internal flow transitions inside droplets traveling in a rectangular microchannel. *Microfluid. Nanofluid.* 21, 180. doi: 10.1007/s10404-017-2019-z

Liu, Z. M., Li, M. Q., Pang, Y., Zhang, L. X., Ren, Y. L., and Wang, J. (2019). Flow characteristics inside droplets moving in a curved microchannel with rectangular section. *Phys. Fluids* 31, 022004. doi: 10.1063/1.5080373

Ma, S. H., Sherwood, J. M., Huck, W., and Balabani, S. (2015). The microenvironment of double emulsions in rectangular microchannels. *Lab. Chip* 15, 2327–2334. doi: 10.1039/c5lc00346f

Marmottant, P., and Hilgenfeldt, S. (2003). Controlled vesicle deformation and lysis by single oscillating bubbles. *Nature* 423, 153–156. doi: 10.1038/nature01613

Mehier-Humbert, S., Bettinger, T., Yan, F., and Guy, R. H. (2005). Plasma membrane poration induced by ultrasound exposure: Implication for drug delivery. *J. Control. Release* 104, 213–222. doi: 10.1016/j.jconrel.2005.01.007

Nejad, S. M., Hosseini, H., Akiyama, H., and Tachibana, K. (2016). Reparable cell sonoporation in suspension: theranostic potential of microbubble. *Theranostics* 6, 446–455. doi: 10.7150/thno.13518

Olsen, M. G., and Adrian, R. J. (2000). Out-of-focus effects on particle image visibility and correlation in microscopic particle image velocimetry. *Exp. Fluids* 29S, S166–S174. doi: 10.1007/s003480070018

Overvelde, M., Garbin, V., Dollet, B., de Jong, N., Lohse, D., and Versluis, M. (2011). Dynamics of coated microbubbles adherent to a wall. *Ultrasound Med. Biol.* 37, 1500–1508. doi: 10.1016/j.ultrasmedbio.2011.05.025

Pereno, V., Aron, M., Vince, O., Mannaris, C., Seth, A., de Saint Victor, M., et al. (2018). Layered acoustofluidic resonators for the simultaneous optical and acoustic characterisation of cavitation dynamics, microstreaming, and biological effects. *Biomicrofluidics* 12(3), 034109. doi: 10.1063/1.5023729

Postema, M., Marmottant, P., Lancee, C. T., Hilgenfeldt, S., and De Jong, N. (2004). Ultrasound-induced microbubble coalescence. *Ultrasound Med. Biol.* 30, 1337–1344. doi: 10.1016/j.ultrasmedbio.2004.08.008

Prentice, P., Cuschierp, A., Dholakia, K., Prausnitz, M., and Campbell, P. (2005). Membrane disruption by optically controlled microbubble cavitation. *Nat. Phys.* 1, 107–110. doi: 10.1038/nphys148

Qin, P., Xu, L., Hu, Y., Zhong, W., Cai, P., Du, L., et al. (2014). Sonoporation-Induced Depolarization of Plasma Membrane Potential: Analysis of Heterogeneous Impact. *Ultrasound Med. Biol.* 40, 979–989. doi: 10.1016/j.ultrasmedbio.2013.11.024

Qin, P., Xu, L., Han, T., Du, L., and Yu, A. C. H. (2016). Effect of non-acoustic parameters on heterogeneous sonoporation mediated by single-pulse ultrasound and microbubbles. *Ultrason. Sonochem.* 31, 107–115. doi: 10.1016/j.ultsonch.2015.12.001

Qin, P., Han, T., Yu, A., and Xu, L. (2018). Mechanistic understanding the bioeffects of ultrasound-driven microbubbles to enhance macromolecule delivery. *J. Control. Release* 272, 169–181. doi: 10.1016/j.jconrel.2018.01.001

Raffel, M. C., Willert, C. E., and Kompenhans, J. (2007). *Particle Image Velocimetry: A Practical Guide*. (Berlin Heidelberg: Springer Science & Business Media).

Reuter, F., Gonzalez-Avila, S. R., Mettin, R., and Ohl, C. D. (2017). Flow fields and vortex dynamics of bubbles collapsing near a solid boundary. *Phys. Rev. Fluids* 2, 064202. doi: 10.1103/PhysRevFluids.2.064202

Rong, N., Zhou, H., Liu, R. M., Wang, Y., and Fan, Z. Z. (2018). Ultrasound and microbubble mediated plasmid DNA uptake: A fast, global and multi-mechanisms involved process. *J. Control. Release* 273, 40–50. doi: 10.1016/j.jconrel.2018.01.014

Shi, Q. S., Liu, P. F., Sun, Y., Zhang, H. P., Du, J., Li, F., et al. (2014). siRNA delivery mediated by copolymer nanoparticles, phospholipid stabilized sulphur hexafluoride microbubbles and ultrasound. *J. Biomed. Nanotechnol.* 10, 436–444. doi: 10.1166/jbn.2014.1728

Tang, H. L., Zheng, Y. Y., and Chen, Y. (2017). Materials chemistry of nanoultrasonic biomedicine. *Adv. Mater.* 29, UNSP 1604105. doi: 10.1002/adma.201604105

Tho, P., Manasseh, R., and Ooi, A. (2007). Cavitation microstreaming patterns in single and multiple bubble systems. *J. Fluid Mech.* 576, 191–233. doi: 10.1017/S0022112006004393

van Rooij, T., Skachkov, I., Beekers, I., Lattwein, K. R., Voorneveld, J. D., Kokhuis, T., et al. (2016). Viability of endothelial cells after ultrasound-mediated sonoporation: Influence of targeting, oscillation, and displacement of microbubbles. *J. Control. Release* 238, 197–211. doi: 10.1016/j.jconrel.2016.07.037

Wu, J. R., Ross, J. P., and Chiu, J. F. (2002). Reparable sonoporation generated by microstreaming. *J. Acoust. Soc Am.* 111, 1460–1464. doi: 10.1121/1.1420389

Xing, L. X., Shi, Q. S., Zheng, K. L., Shen, M., Ma, J., Li, F., et al. (2016). Ultrasound-mediated microbubble destruction (UMMD) facilitates the delivery of CA19-9 targeted and paclitaxel loaded mPEG-PLGA-PLL nanoparticles in pancreatic cancer. *Theranostics* 6, 1573–1587. doi: 10.7150/thno.15164

Yun, Z., Kumon, R. E., Cui, J., and Deng, C. X. (2009). The Size of Sonoporation Pores on the Cell Membrane. *Ultrasound Med. Biol.* 35, 1756–1760. doi: 10.1016/j.ultrasmedbio.2009.05.012

Conflict of Interest: The authors declare that the research was conducted in the absence of any commercial or financial relationships that could be construed as a potential conflict of interest.

frontiers in Pharmacology

ORIGINAL RESEARCH
published: 28 January 2020
doi: 10.3389/fphar.2019.01580

Ultrastructural Changes Associated With the Enhanced Permeability of the Round Window Membrane Mediated by Ultrasound Microbubbles

Yi-Chun Lin[1], Hsin-Chien Chen[2], Hang-Kang Chen[3], Yuan-Yung Lin[1,2], Chao-Yin Kuo[2], Hao Wang[2], Chia-Lien Hung[3], Cheng-Ping Shih[2] and Chih-Hung Wang[1,2,4*]*

[1] Graduate Institute of Medical Sciences, National Defense Medical Center, Taipei, Taiwan, [2] Department of Otolaryngology-Head and Neck Surgery, Tri-Service General Hospital, National Defense Medical Center, Taipei, Taiwan, [3] Teaching and Research Section, Taichung Armed Forces General Hospital, Taichung, Taiwan, [4] Taichung Armed Forces General Hospital, Taichung, Taiwan

OPEN ACCESS

Edited by:
Jean-Michel Escoffre, INSERM U1253Imagerie et Cerveau (iBrain), France

Reviewed by:
Xinxing Duan, University of Waterloo, Canada
Noboru Sasaki, Hokkaido University, Japan
Roel Deckers, University Medical Center Utrecht, Netherlands

***Correspondence:**
Cheng-Ping Shih
zhengping_shi@yahoo.com.tw
Chih-Hung Wang
chw@ms3.hinet.net

Specialty section:
This article was submitted to Translational Pharmacology, a section of the journal Frontiers in Pharmacology

Received: *30 July 2019*
Accepted: *05 December 2019*
Published: *28 January 2020*

Citation:
Lin Y-C, Chen H-C, Chen H-K, Lin Y-Y, Kuo C-Y, Wang H, Hung C-L, Shih C-P and Wang C-H (2020) Ultrastructural Changes Associated With the Enhanced Permeability of the Round Window Membrane Mediated by Ultrasound Microbubbles. Front. Pharmacol. 10:1580. doi: 10.3389/fphar.2019.01580

The round window membrane (RWM) is the most common entryway for local drug and gene delivery into the inner ear, but its permeability can change the treatment outcome. We previously demonstrated a feasible and highly efficient approach using ultrasound-aided microbubble (USMB) cavitation to enhance the permeability of the RWM. Here, we investigated the safety of USMB exposure and the association between temporal changes in RWM permeability and ultrastructure. Experimental guinea pigs were divided into two treatment groups: a control group receiving round window soaking (RWS) with MBs and treatment (USM) groups undergoing 3 (USM-3) or 5 (USM-5) consecutive USMB exposures (1 min/exposure) at an acoustic intensity of 3 W/cm^2 and 1 MHz frequency. The trans-RWM delivery efficiency of biotin-fluorescein isothiocyanate conjugates, used as permeability tracers, revealed a greater than 7-fold higher delivery efficiency for the USM groups immediately after 3 or 5 exposures than for the RWS group. After 24 h, the delivery efficiency was 2.4-fold higher for the USM-3 group but was 6.6-fold higher for the USM-5 group (and 3.7-fold higher after 48 h), when compared to the RWS group. Scanning electron microscopy images of the RWM ultrastructure revealed USMB-induced sonoporation effects that could include the formation of heterogeneous pore-like openings with perforation diameters from 100 nm to several micrometers, disruption of the continuity of the outer epithelial surface layer, and loss of microvilli. These ultrastructural features were associated with differential permeability changes that depended on the USMB exposure course. Fourteen days after treatment, the pore-like openings had significantly decreased in number and the epithelial defects were healed either by cell expansion or by repair by newly migrated epithelial cells. The auditory brainstem response recordings of the animals following the 5-exposure USMB treatment indicated no deterioration in the hearing thresholds at a 2-month follow-up and no significant hair cell damage or apoptosis, based on scanning electron microscopy, surface preparations, and TUNEL assays. USMBs

therefore appear to be safe and effective for inner ear drug delivery. The mechanism of enhanced permeability may involve a disruption of the continuity of the outer RWM epithelial layer, which controls transmembrane transport of various substances.

Keywords: ultrasound, microbubble, round window membrane (RWM), permeability, inner ear, ultrastructure, scanning electron microscope (SEM), transmission electron microscope (TEM)

INTRODUCTION

The delivery of drugs and genes into the human inner ear remains a current challenge, not only because of the anatomically complex structure of the inner ear but also due to its inaccessibility and vulnerability as a sensory organ (**Figure 1**). Although several inner ear diseases can be managed with the systemic drug administration, the pre-existing blood-labyrinth barrier and the potentially adverse effects of systemic medication all hamper an effective therapeutic dosage from reaching the inner ear. Local administration provides the advantage of precise targeting and avoids the risk of systemic adverse events (El Kechai et al., 2015; Li et al., 2017; Hao and Li, 2019; Piu and Bishop, 2019). The methods of local drug administration to the inner ear include intratympanic and intracochlear approaches, where the latter offers a direct delivery route to achieve a greater drug bioavailability by either penetrating right through the round window membrane (RWM) or through an opening in the cochlear bony wall (El Kechai et al., 2015; Mäder et al., 2018). However, the intracochlear approach poses a high risk of inner ear damage and hearing loss and is therefore mainly employed as a combined procedure during cochlear implant surgery (Mccall et al., 2010; Chin and Diaz, 2019).

Intratympanic medication injection, by way of the RWM as a transfer site for medication delivery into the cochlea, is currently the most common clinical procedure used for inner ear drug delivery. For example, intratympanic injections of corticosteroids are effective for treating sudden sensorineural hearing loss, and aminoglycoside injection is used to treat Meniere's disease (Jackson and Silverstein, 2002; Rauch et al., 2011; Li et al., 2017). These injection procedures are minimally invasive; however, effective therapeutic outcomes may require repeated injections, avoidance of swallowing by the patient, or placing the patient's head slightly lower than the body because medications in the middle ear cavity usually drain out through the Eustachian tube (Shih et al., 2019). To overcome the short residence times for contact with the RWM, several delivery devices, such as the MicroWick, microcathers, and osmotic pumps, have been developed to prolong the duration of medication contact with the RWM. Delivery materials and agents such as gelfoam, hyaluronic acid hydrogels, histamine, nanoparticles, and nanovesicles can also provide a sustained inner ear delivery *via* the RWM (El Kechai et al., 2015; Mäder et al., 2018; Creber et al., 2019).

Recently, ultrasound (US) combined with a microbubble (MB) contrast agent has been demonstrated to target or control drug release to tissues and cells (Tang et al., 2002; Smith et al., 2003; Hernot and Klibanov, 2008). In 2013, our research team demonstrated that trans-membrane drug delivery into the inner ear can be assisted and enhanced by sonophoresis with US-aided MBs (USMBs) (Shih et al., 2013). This technique not only increases the permeability of the RWM and facilitates drug delivery into the inner ear, but the preliminary results also show no resulting damage to the integrity of the RWM or deterioration of the hearing thresholds, as assessed by auditory brainstem responses. Furthermore, in 2014, we demonstrated that USMBs were effective at facilitating gene transfer to auditory cells *in vitro* (Liao et al., 2014) and that the size-dependent MB oscillation behavior in the presence of US plays a role in enhancing gene transfer. In addition, dexamethasone delivery to the round window of animals with the aid of USMBs has a greater efficacy in protecting the inner ear from noise-exposed

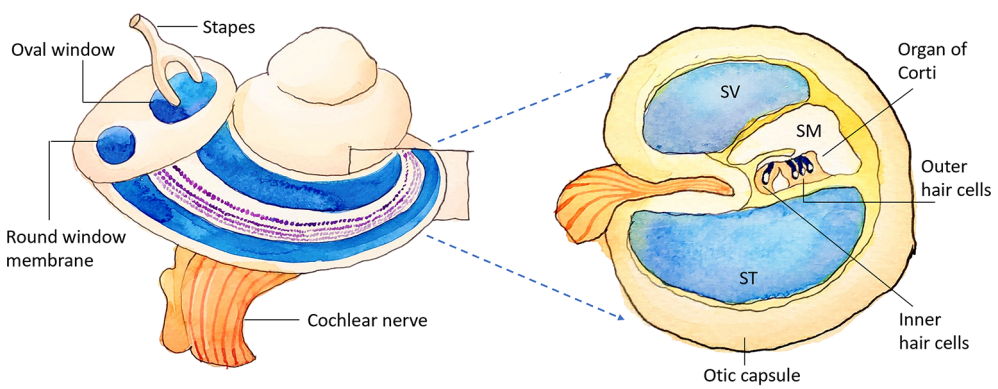

FIGURE 1 | Schematic illustration of the inner ear. SV, scala vestibuli; SM, scala media; ST, scala tympani.

injury when compared to a simple soaking with the drug (Shih et al., 2019).

In the cochlea, the RWM not only serves a membranous barrier between the inner ear and the middle ear cavity, but it also provides the main route for local drug and gene delivery into the inner ear. The RWM is made up of an outer epithelial layer, a middle connective tissue layer, and an inner epithelial layer (Goycoolea and Lundman, 1997). Of these three layers, the outer epithelial layer is believed to prevent the passage of substances from the middle ear to the inner ear. Substance transport across the RWM can involve several cellular processes: diffusion down a concentration gradient, pinocytosis, or transcellular movement through channels. The anatomical characteristics of the outer epithelium include absorbent microvilli and lateral interdigitations, tight junctions between cells, a continuous basement membrane, abundant mitochondria and rough endoplasmic reticulum, and a well-developed Golgi complex (Paparella et al., 1983; Goycoolea and Lundman, 1997; Goycoolea, 2001). All these features contribute to the permeability of the RWM (Goycoolea et al., 1988).

Our previous studies on animal models suggested that the USMB technique is both practical and successful. However, translating this technique to the clinic requires exploration of the USMB-induced RWM permeability changes and identification of any safety issues. The aim of the present study was therefore to evaluate a possible association between the number of USMB exposure courses, the permeability changes in the targeted RWM and its related ultrastructural alterations, and the safety concerns regarding application of USMBs to the middle ear cavity for inner ear drug delivery.

MATERIALS AND METHODS

Animals and Study Design

Guinea pigs with normal Preyer's reflex, weighing 250–350 g, were divided into two groups: 1) an ultrasound microbubble (USM) group: animals receiving 3 (USM-3) or 5 (USM-5) courses of USMB application and 2) a round window soaking (RWS) group that served as the control and received MBs soaked into the tympanic bulla. In the USM groups, the animal's tympanic bulla was filled with 200 μl of MBs, followed by three or five consecutive US exposures. In the RWS group, the animal's tympanic bulla was filled as above with the same volume of MBs but no US treatment was given. After the treatment, the cochleae of all animals were soaked for 10 min with biotin-fluorescein isothiocyanate conjugates (FITC; 40 μg/ml) at each of the examined time points. The collected samples were evaluated for permeability and ultrastructure of the RWM, and the safety of the procedure was tested by auditory brainstem response (ABR) and distortion product otoacoustic emission (DPOAE) evaluations. Under this protocol, a total of 58 animals were tested, including technical failures. A flow chart of the study design is presented in **Figure 2**.

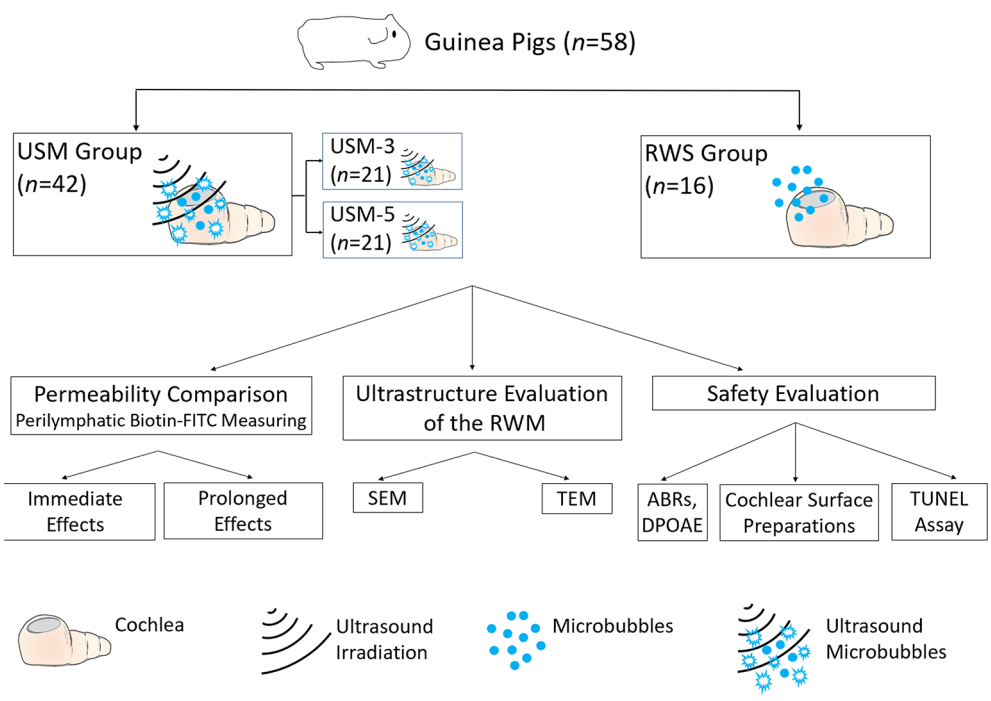

FIGURE 2 | Flow chart of the study design and animal groups. USM, ultrasound microbubble treatment; RWS, round window membrane soaking treatment; RWM, round window membrane; SEM, scanning electron microscopy; TEM, transmission electron microscopy; ABR, auditory brainstem response; DPOAE, distortion product otoacoustic emission; TUNEL, terminal deoxynucleotidyl transferase dUTP nick end labeling.

Microbubble Preparation and Ultrasound Exposure

SonoVue® (Bracco, Milano, Italy) phospholipid MBs containing sulfur hexafluoride were freshly reconstituted prior to use by mixing the lyophilizate with 5 ml of 0.9% saline to form a suspension containing 2–5 × 10^8 bubbles/ml. The ultrasound device (ST2000V, Nepa Gene, Chiba, Japan) equipped with a 6-mm-diameter transducer was used for irradiation. The optimal US exposure settings had been predetermined in our previous report (Shih et al., 2019). Briefly, the mode was set as follows: frequency 1 MHz, burst rate 250 Hz, burst duration 2 ms, acoustic intensity 3 W/cm^2 (mechanical index [MI] = 0.254) for three or five consecutive 1-min courses; and a 50% duty cycle. The transducer was positioned at the level of the mastoid bone with opened tympanic bulla, which was at least 5 mm away from, but in alignment with, the RWM.

Surgery

As described and schematically illustrated in our previous study (Shih et al., 2019), guinea pigs were administered xylazine i.m. (Rompun; Bayer, Leverkusen, Germany) at 10 mg/kg and ketamine (Imalgene; Merial, Lyon, France) at 80 mg/kg. After making a post-auricular skin incision, a 4-mm-diameter fenestration was created in the tympanic bulla by drilling to expose the cochlea and round window under an operating microscope (F-170; Carl Zeiss, Germany). Ultrasound irradiation was then applied to the MBs filling the bulla through the bony fenestration (**Figure 3**). At the end of the final US exposure, the MBs were removed from both the USM and RWS groups. For immediate permeability comparisons, 200 µl of biotin-FITC was filled into tympanic bulla and soaked for 10 min. For permeability comparisons at other time points, the USM animal's surgical wound was sutured by layers. At each examined time point, the closed surgical wound was re-opened, the tympanic bulla was filled with same volume of biotin-FITC, and soaked for 10 min.

Perilymphatic Fluid Collection and Biotin-FITC Fluorescence Measurements

To assess the amount of biotin-FITC delivered to the cochlea, the guinea pigs were euthanized using CO_2 gas and their cochleae were harvested from within the tympanic bulla. A 10-µl pipette microtip was gently inserted through a cochleostomy inferior to the RWM for perilymphatic fluid collection (Shih et al., 2013). The aspirated perilymphatic samples were centrifuged immediately and stored at −80°C until used for fluorescence intensity analysis using a fluorometer (excitation/emission: 485/528 nm; Fluoroskan Ascent FL, Thermo Labsystems, Finland).

Cochlear Surface Preparation

After deep anesthesia with intraperitoneal injection of pentobarbital sodium 100 mg/kg, the animals were transcardially perfused with 4% paraformaldehyde in phosphate buffered saline (PBS; ChemCruz, Santa Cruz Biotechnology, Inc., Dallas, TX) and the cochleae were removed from the tympanic bulla and post-fixed with the same fixative at 4°C overnight, followed by dissection under a dissecting microscope to excise the cochlear lateral wall and Reissner's membrane. The Corti sensory epithelium was permeabilized with 0.3% Triton X-100 and stained with 2% Alexa Fluor 488-conjugated phalloidin (Molecular Probes/ThermoFisher Scientific, Waltham, MA) to confirm hair cells, while 4,6-diamidino-2-phenylindole (DAPI; Molecular Probes/ThermoFisher Scientific; 5 mg/ml) was used to stain the nuclei. The entire length of the Corti sensory epithelium was cut into pieces and examined with a confocal laser scanning microscope (LSM880, Zeiss, Oberkochen, Germany).

Scanning Electron Microscopy (SEM)

The removed cochleae were placed in fixative (2.5% glutaraldehyde with 2% paraformaldehyde in 0.1% sodium cacodylate buffer) overnight at 4°C, and then given three 10 min washes with cold PBS (0.1 M, pH 7.4). For RWM preparation, the specimens were trimmed, leaving the RWM tissue intact. Samples were then given three 15 min washes with 0.1 M cacodylate buffer containing 7% sucrose. After post-fixing in 1% osmium tetroxide (Electron Microscopy Science) and 1% thiocarbohydrizide (TCH; EMS) for 2 h, the samples were again given three 15 min washes with 0.1 M cacodylate buffer containing 7% sucrose. The specimens were dehydrated through a graded ethanol series (35%–to absolute ethanol) at 10 min intervals and then finished in a critical point dryer. The processed specimens were viewed and photographed using a

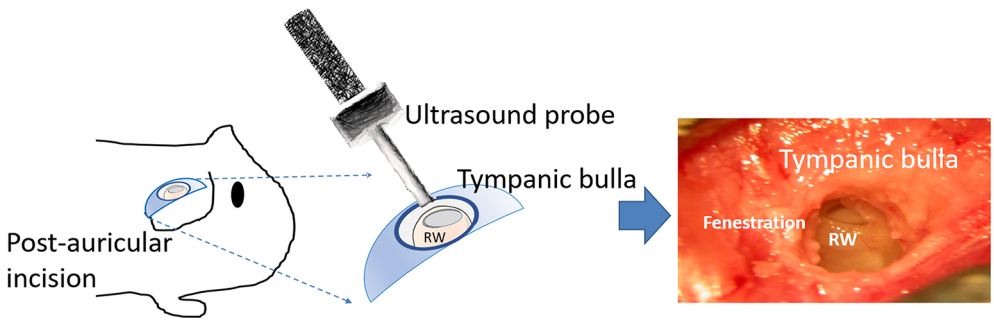

FIGURE 3 | Schematic illustration of the surgery and ultrasound exposure. RW, round window.

SU3500 scanning electron microscope (Hitachi, Tokyo, Japan) at 15 kV.

Transmission Electron Microscopy (TEM)

As was done for SEM, the cochleae, following fixation at 4℃ overnight and washing with cold PBS, were trimmed to leave the intact RWM soft tissue only. The whole RWM was post-fixed in 1% osmium tetroxide for 2 h, given three 15 min washes with 0.1M PBS, dehydrated in an ethanol series, and infiltrated with Spurr's resin. The polymerized samples were sectioned with an ultramicrotome (Leica EM UC7) at a 90 nm thickness. Images were obtained using a transmission electron microscope (FEI Tecnai 20 G2 S-Twin).

Terminal Deoxynucleotidyl Transferase dUTP Nick End Labeling (TUNEL) Assays

Paraffin-embedded cochlear sections were dewaxed in xylene and rehydrated through a graded ethanol series and double-distilled water, followed by PBS washes. Positive control sections were incubated with 100 U/ml DNase I diluted in a buffer containing 20 mM Tris-HCl (pH 7.0), 10 mM $MnCl_2$, and 1 M NaCl at room temperature for 10 min. The TUNEL assay utilizing the In Situ Cell Death Detection Kit, POD (Roche, Basel, Switzerland) was carried out following the instructions supplied by the manufacturer. Deparaffinized slides were incubated with 3% hydrogen peroxidase in methanol for 10 min to block endogenous peroxidase activity and then washed with PBS. As described in our previous report (Chen et al., 2018), the tissue sections were permeabilized first, blocked for 30 min at room temperature with the supplied blocking buffer, and then incubated with the TUNEL reaction mixture for 60 min at 37°C in a humidified atmosphere in the dark. After PBS Tween-20 (PBST) washing, the tissues were stained with Converter-POD for an additional 30 min and washed with PBST. The diaminobenzidine chromogen was then applied for 10 min to label apoptotic cells. For histological analysis, the tissue sections were counterstained with hematoxylin and viewed with an Olympus BX50 brightfield/fluorescence microscope (Olympus Corp., Tokyo, Japan) equipped with a digital camera (Olympus DP74).

Auditory Brainstem Response (ABR) Recording

The animal's auditory function was evaluated by recording the ABRs, as described previously (Lin et al., 2011). Briefly, guinea pigs were anesthetized and kept warm with a heating pad in a sound-attenuating chamber. Subcutaneous needle electrodes were inserted at the vertex (positive electrode), below the pinna of the ear (negative electrode), and at the back (ground electrode). Specific stimuli (clicks and 8, 16, and 32 kHz tone bursts) were generated using SigGen software (Tucker-Davis Technologies, Alachua, FL) and delivered *via* an earphone inserted into the external auditory canal. The average responses from 1,024 stimuli for each frequency were obtained by reducing the sound intensity in 5-dB steps until reaching a threshold. The resulting ABR thresholds were defined as the lowest intensity at which a reproducible deflection in the evoked response trace could be recognized.

Distortion Product Otoacoustic Emission Measurements

The distortion product otoacoustic emissions (DPOAEs) were measured at the center frequencies (FCs) of 8, 16, 20, 24, and 32 kHz with a Real-time Signal Processing System (Tucker-Davis Technologies), as reported previously (Chen et al., 2018). Briefly, two simultaneous continuous pure tones, F1 and F2 were calculated using the FC to yield a frequency of primary 1 (Tone 1) and primary 2 (Tone 2). The two primary tones were presented at the same intensity (L1 = L2 = 65 dB SPL) and at a frequency ratio (F2/F1) of 1.2. The primary tones produced by two separate speakers (EC1 close-field speakers; Tucker-Davis Technologies) were introduced into the animal's ear canal. The DPOAE recordings were made with a low-noise microphone (ER 10B; Etymotic Research, Elk Grove Village, IL) and averaged 512 times at each frequency. The peak of the cubic difference distortion product (2F1 − F2) at different FCs was accepted as a DPOAE if it was 3 dB above the noise floor, and the difference was referred to as the signal-to-noise ratio (SNR).

Monitoring of Cochlear and Tympanic Cavity Temperature Changes

The temperature changes in the cochlea and tympanic cavity after various courses of USMB exposures were monitored using a thermometer coupled to a fine sensor probe (Center-301 type K; CENTER Technology Corp., New Taipei City, Taiwan), with a resolution of 0.1°C. The sensor probe was inserted at different depths into the tympanic cavity filled with MBs and would concomitantly touch the nearby cochlea to measure the temperature before USMB treatment and at the end of various USMB courses. The three designed locations for temperature measurements, from the top to the bottom of the tympanic cavity, were the cochlear basal turn near the RWM, the middle turn, and the apex. Temperature measurements began at the cochlea, then in the tympanic cavity, and then at the cochlea and were processed alternately. The temperature differences between the two measurements were recorded.

Statistical Analysis

Statistical analysis was performed using a two-tailed Student's *t* test for comparison of the means between two groups and the Kruskal-Wallis test or one-way ANOVA with *post hoc* Bonferroni correction for multigroup comparisons. Data were expressed as mean ± standard error of the mean.

RESULTS

Permeability Changes in the RWM Depend on the Number of Exposures to USMBs

We first examined the USMB-mediated RWM permeability changes by comparing the perilymphatic levels of delivered biotin-FITC at different time points. As shown in **Figure 4**,

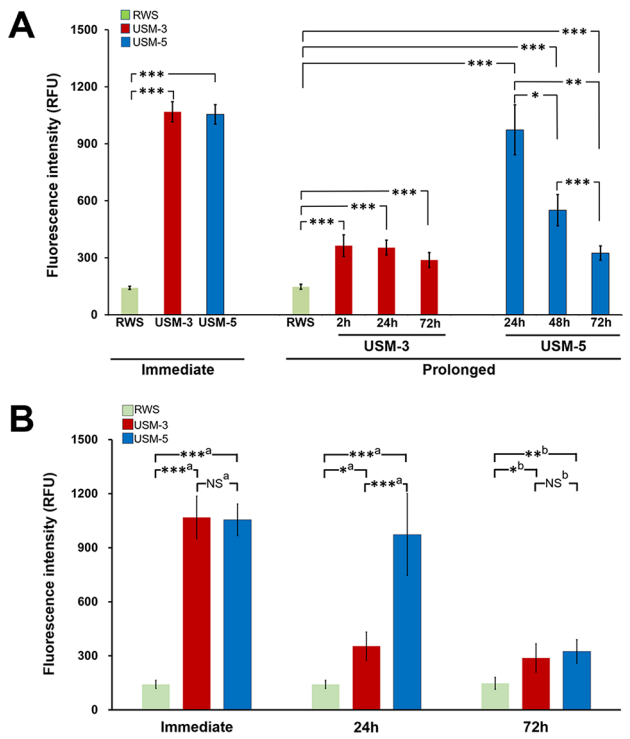

FIGURE 4 | Evaluation of the permeability changes of the round window membrane (RWM) following three or five ultrasound microbubble (USMB) treatments and a 10-min biotin-fluorescein isothiocyanate solution soaking of the tympanic bulla immediately after USMB treatment and at different time points post USMB treatment. **(A)** The bars indicate the mean maximum fluorescence in relative fluorescence units (RFU) of the assessed USM-3 (red) and USM-5 (blue) groups when compared with the control RWS group (green). **(B)** Multigroup comparisons using the Kruskal-Wallis test or one-way ANOVA, followed by *post hoc* Bonferroni tests. Values are expressed as mean ± SEM; n = 4 per group. a = Kruskal-Wallis test with Bonferroni correction; b = one-way ANOVA test with Bonferroni correction; USM, ultrasound microbubble treatment; RWS, round window soaking with microbubbles treatment; $^{*}p < 0.05$, $^{**}p < 0.01$, $^{***}p < 0.001$, NS, not significant.

comparison of the fluorescence intensity of the USM-3 and control groups at each time point, immediate (1068.4 ± 53.0 vs. 141.6 ± 8.5, $p < 0.001$), 2 h (363.9 ± 56.9 vs. 147.3 ± 13.5, $p < 0.01$), 24 h (353.7 ± 39.1 vs. 147.3 ± 13.5, $p < 0.01$), and 72 h (288.1 ± 39.3 vs. 147.3 ± 13.5, $p < 0.01$) revealed a significantly enhanced permeability of the RWM in the USM-3 group compared to the control group. In the USM-3 group, the measured fluorescence intensity showed its highest level (7.5-fold higher than control) at the 10 min time point immediately post USMB exposure, followed by a gradual decrease in fluorescence levels at subsequent post exposure time points (2.5-fold at 2 h, 2.4-fold at 24 h, and 2.0-fold at 72 h vs. the control) (**Table 1**).

In the USM-5 group, the delivered biotin-FITC level was also significantly higher at each time point immediately after USMB treatment and after 72 h when compare to the control (**Figure 4**). Like the USM-3 group, the USM-5 group also demonstrated a

TABLE 1 | Comparison of the efficiency of USMB exposure courses for inner ear drug delivery.

Time points post USMB	Exposure number of USMB	Delivered Biotin-FITC Fluorescence Intensity	Fold-increase of inner ear delivery (relative to control)
Immediate			
	3	1068.4 ± 53.0	7.5
	5	1055.0 ± 51.0	7.4
	Control	141.6 ± 8.5	–
Prolong			
2 h	3	363.9 ± 56.8	2.5
24 h	3	353.7 ± 39.1	2.4
72 h	3	288.1 ± 39.3	2.0
24 h	5	973.3 ± 131.6	6.6
48 h	5	550.5 ± 82.3	3.7
72 h	5	324.7 ± 37.3	2.2
72 h	Control	147.3 ± 13.5	–

post-USMB time-dependent permeability change of the RWM as shown by the gradually decreasing delivery of biotin-FITC from immediately after the USMB treatment to 72 h later. These data suggest that USMBs can effectively enhance the permeability of the RWM and that the enhancement could be maintained for at least 72 h. Five consecutive treatments with USMBs caused a similar immediate transmembrane delivery effect to that observed with 3 treatments (1055.0 ± 51.0 vs. 1068.4 ± 53.0, $p = 0.87$); however, after 24 h, the 5-course USMB treatment delivered a higher level of biotin-FITC than the 3-course treatment (973.3 ± 131.6 vs. 353.7 ± 39.1, $p = 0.004$), suggesting that 5 courses of USMB treatment may sustain a more enhanced permeability change in the RWM.

Ultrasound-Mediated MB Cavitation and Sonoporation on the Outer Epithelial Layer of the RWM Enhanced Permeability

SEM examination of the sequential changes of the RWM ultrastructural features at different time points after USMB treatments revealed a normal architecture of the outer epithelium in the control animals, with flat cells arranged in pentagonal or octagonal patterns and abundant microvilli (**Figures 5A–A"**). The RWM in the USM-3 group immediately after USMB treatment showed various degrees of heterogeneous pore-like openings, with sizes from 100 nm to several microns, on the epithelial surface. Some areas even showed separation of the epithelial cells, with fissures appearing on the cell boundaries where the tight junctions between adjacent cells were originally located (**Figures 5B–B"**). The USM-5 samples showed more extensive pore-like defects and disruption of the continuity of the cell membrane on the epithelial surface, as well as a significant loss of microvilli (**Figures 5C–C"**). All these observations suggest a direct involvement of cavitation-enhanced sonoporation on the targeted RWM.

Figure 6 shows the TEM views of cross-sections of the RWM after USMB. Microbubble cavitation resulted in various degree of disruption on the outer epithelial cells, including the formation of pits of different sizes and rising of the cell membranes (**Figures**

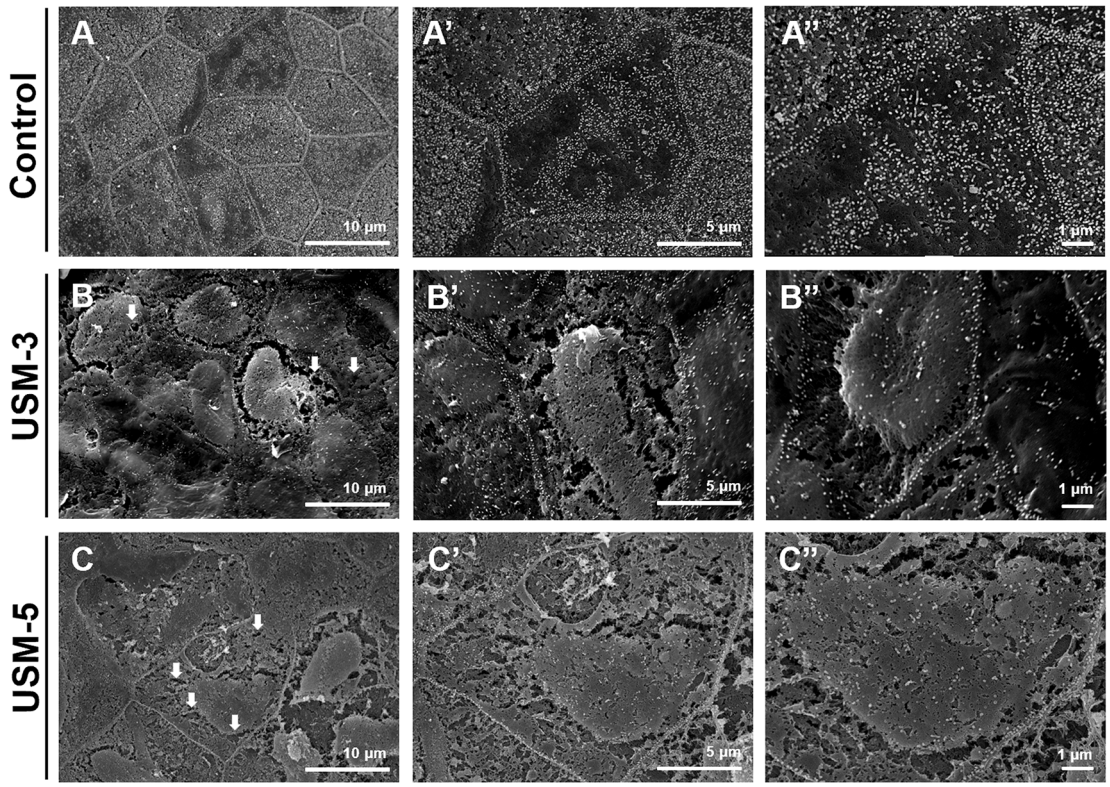

FIGURE 5 | Scanning electron microscopy (SEM) view of the epithelial surface of the round window membrane (RWM) under different magnifications. **(A–A")** RWM from a control animal after microbubbles (MBs) soaking for 10 min without ultrasound (US) exposure. **(B–B")** Samples were immediately taken from the animal after three ultrasound microbubble (USMB) treatments. **(C–C")** After five USMB treatments. The white arrows indicate pore-like defects.

6B–B', arrows). Extensive disruptions of the outer epithelial cells and membrane defects were noted in the USM-5 group (**Figures 6C–C'**, arrows). However, the sonoporation effects seemed to disturb only the outer epithelial layer of the RWM, because the basement membrane along the outer epithelial cells remained intact (**Figures 6B–C**, arrowheads).

Post-Cavitation Epithelial Wound Healing

A series of SEM images taken at different time points after USMB treatment demonstrated outer epithelial barrier disruption (**Figure 7**). On day 7 after USMB treatment, the previously sonoporation-induced breaches between adjacent cells began to fill up in the USM-3 group (**Figures 7A–A"**), whereas many gaps remained in the USM-5 group (although the size and area of the gaps had significantly reduced) (**Figures 7D–D"**). On day 14 after USMB treatment, the epithelial wounds in the USM-3 group had almost fully healed with a cell-expansion-like pattern (**Figures 7B–B"**), whereas regenerative epithelial cell migration was observed in the USM-5 group and had begun to cover the wound area (**Figures 7E–E", asterisk)**. By day 28, microvillus regrowth was evident on the outer epithelial surface of the USM-3 group (**Figures 7C–C"**), the TEM images also revealed a completely recovered outer epithelial layer in the USM-3 group (**Figures 6D–D'**). By contrast, only a limited number of microvilli were found in the USM-5 group (**Figures 7F–F"**). Taken together, the results indicate that 3 or 5 courses of USMB treatment caused a reversible epithelial wounding that healed without damaging the basement membrane. These ultrastructural changes of the outer epithelium were associated with a differential permeability of the RWM that depended on the USMB exposure.

Thermal Effects of USMBs Applied to the Tympanic Cavity

Figure 8 shows the range of temperature increases for both the cochlea and the tympanic cavity after various courses of USMBs. One or two courses of USMBs resulted in a slight drift in the temperature rise of around 0.8°C–1.5°C on the cochlea and in the tympanic cavity. By contrast, three or more courses of irradiation caused rapid increases in temperature and greater heating over the cochlear basal turn and its adjacent upper tympanic cavity (2.0°C–2.7°C) than over the cochlear apical turn and the adjacent lower tympanic cavity (1.2°C–1.8°C). This finding indicated an attenuated temperature gradient in the USMB-exposed tympanic cavity, which displayed the greatest temperature elevation at the top and the least elevation at the bottom of the

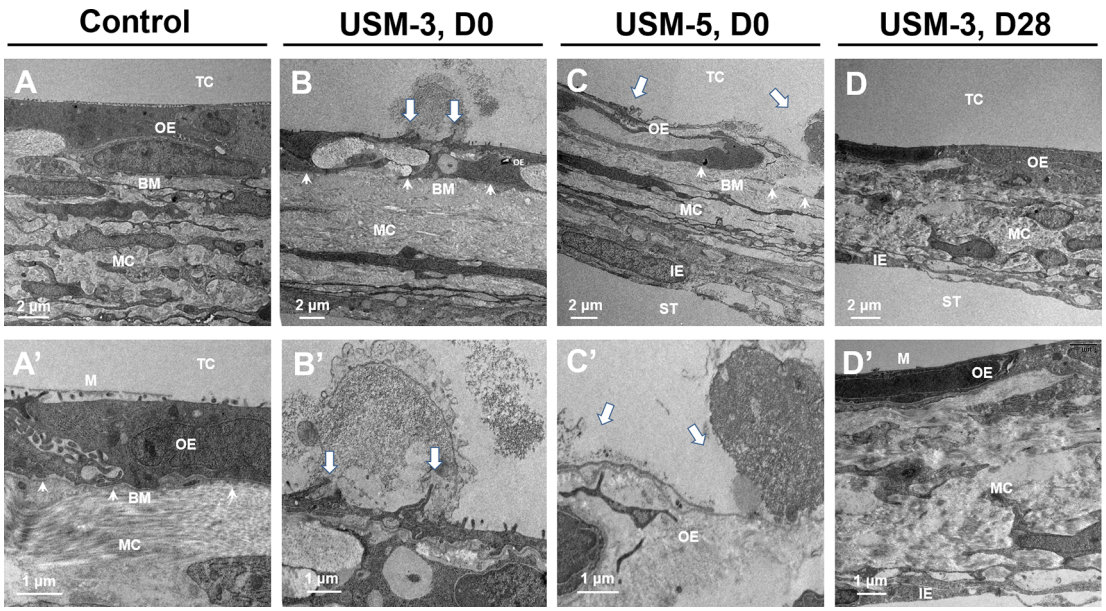

FIGURE 6 | Cross-sectional transmission electron microscope (TEM) images of the round window membrane (RWM) under different magnifications. **(A–A')** RWM from the control animal after soaking with microbubbles (MBs) for 10 min without ultrasound (US) exposure. **(B–B')** Samples immediately taken from animal after three ultrasound microbubble (USMB) treatments. **(C–C')** Samples after five USMB treatments. **(D–D')** Samples taken from animals 28 days after receiving 3 courses of USMB treatment. The white arrows indicate outer epithelial membrane defects. The white arrowheads indicate basement membrane. TC, tympanic cavity; OE, outer epithelial layer; MC, middle connective tissue layer; IE, inner epithelial layer; BM, basement membrane; ST, scala tympani; M, microvilli; D0, day 0; D28, day 28.

cavity. The temperature also tended to be lower, by about 0.2°C, in the tympanic cavity than on the cochlea after more than 3 courses of irradiation, implying a much greater heat deposition at the bone surface than in the MB solution in the cavity. These data suggest that ultrasound absorption by the bony cochlea or by the surrounding MBs solution is greatest on the exposed surface of the tissue close to the transducer face and decreases with increased propagation distance or depth.

Preservation of Hearing Thresholds and Cochlear Integrity After USMB Treatment

We also performed ABRs on the treated animals to evaluate whether USMB intervention compromised the animals' hearing thresholds. In an earlier paper, we described that a two-course USMB treatment did not cause hearing threshold shifts or damage to the cochlear hair cells (Shih et al., 2013). In this study, hearing assessments were only performed on animals of the RWS and USM-5 groups to reduce the number of animals used. The results of the ABR hearing assessments, to both click-evoked and tone burst-evoked sounds at a frequency of 8, 16, and 32 kHz, showed that the hearing in animals that received 5 courses of USMB treatment did not differ from that of the controls that had MBs soaking during a two-month follow up (**Figure 9A**). The signal-to-noise ratio (SNR) of the distortion product (DP) measurements immediately after 5 courses of USMB at frequencies from 4 kHz to 32 kHz among the treatment and control groups also did not differ (**Figure 9B**).

To determine if the USMB treatment cause cellular damage inside the cochlea, a TUNEL-assay was performed in the cochlear structures 24 h after USMB treatment. TUNEL-positive cells were nearly absent in the organ of Corti and spiral ganglion of both the USM and control groups (**Figure 10**). Cochlear sensory epithelial surface preparations obtained from guinea pigs four weeks after USMB treatment showed no significant hair cell damage (**Figure 11**). Taken together, these data suggest that the current protocol for application of USMB for 3 or 5 courses would not damage the receiver's hearing or their cochlear structure.

DISCUSSION

The permeability of the RWM can directly reflect the efficacy of inner ear drug delivery *via* RWM transit. In the work reported here, we demonstrated that the sonoporation-enhanced RWM permeability changes may depend on the number of USMB courses, with the highest delivery efficiency observed immediately after USMB treatment. This is followed by a gradual decay in the delivery but a prolonged enhancement still remains for at least 72 h. Concerning the question of whether different temporal profiles of USMB treatments would impact on the measured delivery amounts between USM-3 and USM-5 groups (3 min vs. 5 min), the time difference of 2 min was considered negligible because both groups reached a similar (~7.5-

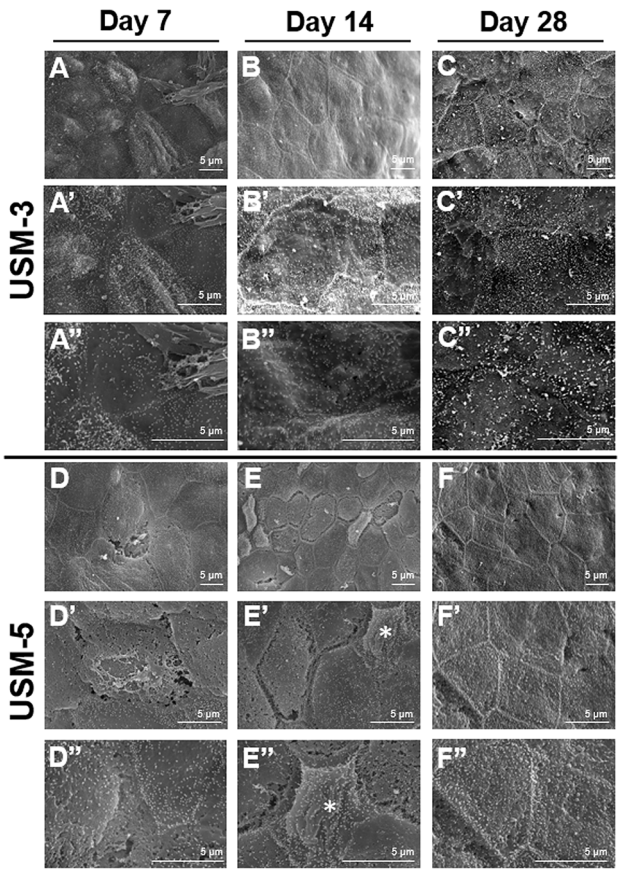

FIGURE 7 | Scanning electron microscopy (SEM) view of the epithelial surface of the round window membrane (RWM) under different magnifications at different time points post ultrasound microbubble (USMB) treatment. **(A–A")** RWM after 3 courses of USMBs for 7 days, **(B–B")** 14 days, and **(C–C")** 28 days. **(D–D")** Samples after 5 courses of USMBs for 7 days, **(E–E")** 14 days, and **(F–F")** 28 days.

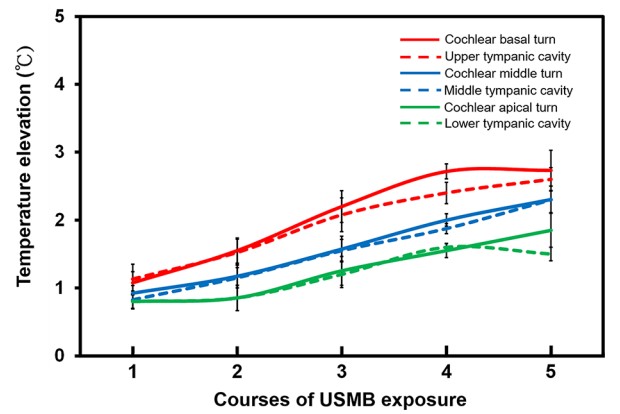

FIGURE 8 | The elevation of the cochlea and tympanic cavity temperature after different courses of ultrasound microbubble (USMB) exposure. The results are expressed as the mean ± SEM; n = 5 for each point.

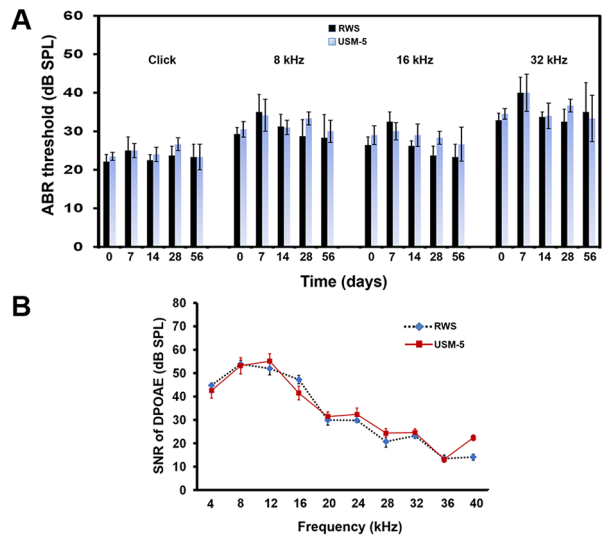

FIGURE 9 | Hearing assessment in guinea pigs after 5 courses (USM-5) of ultrasound microbubble (USMB) treatments. **(A)** The auditory brainstem response (ABR) threshold recordings in the round window soaking (RWS) and USM-5 groups before (day 0) and at a two-month follow up after USMB treatments. **(B)** Signal-to-noise ratios (SNRs) of the cubic difference distortion product ($2F_1–F_2$) at different center frequencies (F_C) for each group. The results are expressed as the mean ± standard error of the mean (SEM), with n = 4 for each bar.

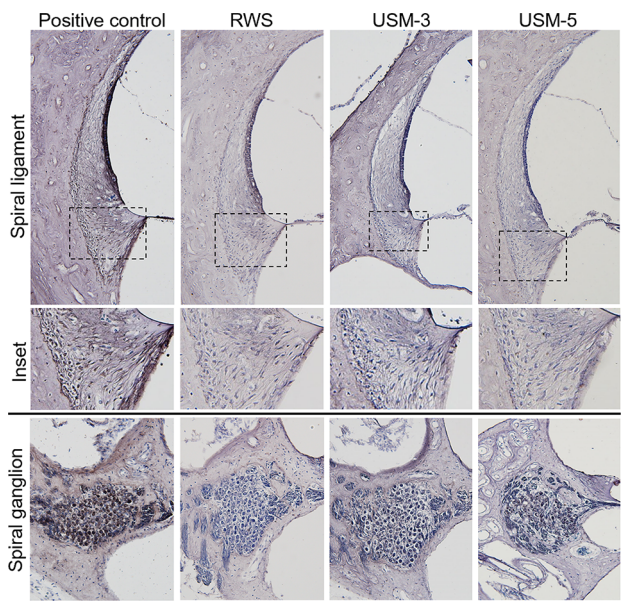

FIGURE 10 | Effects of various ultrasound microbubble (USMB) courses on cell death in the target inner ear. Representative photos of the spiral ligament and spiral ganglion examined by Transferase dUTP Nick End Labeling (TUNEL) assays following round window soaking (RWS) and USMB treatment (original magnification ×200). A section treated with DNase I served as a positive control.

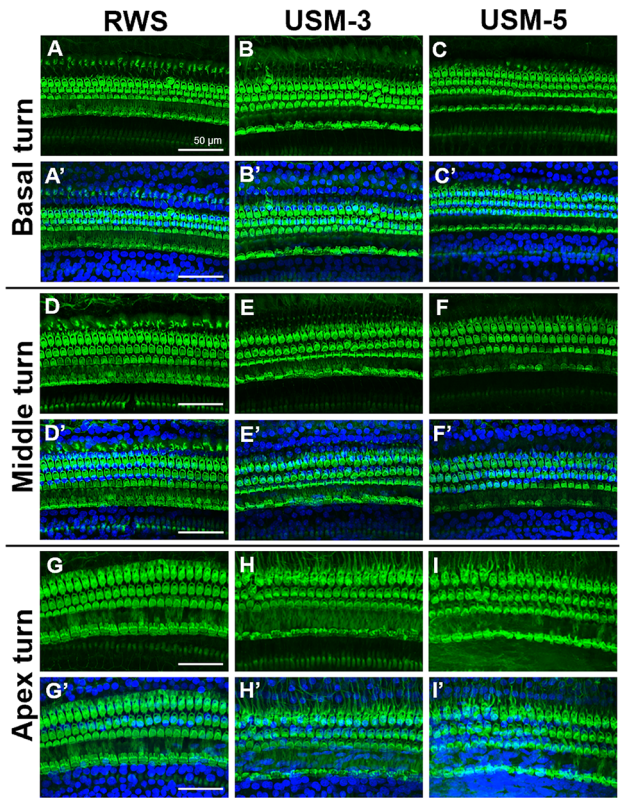

FIGURE 11 | Cochlear sensory epithelial surface preparations were obtained from guinea pigs four weeks after ultrasound microbubble (USMB) treatment. Representative images in panels **(A–I)** are labeled with phalloidin, panels **(A'–I')** show the merged DAPI staining images. Immunofluorescence staining shows the nuclei (blue, DAPI) and filamentous actin (green, phalloidin). Scale bars = 50 μm; DAPI, 4,6-diamidino-2-phenylindole; RWS, round window soaking with microbubbles treatment; USM, ultrasound microbubble treatment.

fold) transmembrane delivery efficiency within 10 min after USMB treatments. We demonstrated that the sonoporation-enhanced permeability change in the RWM may already reach a plateau with a course consisting of between 3 to 5 exposures.

Further exploration of the surface ultrastructure of the RWM after USMB treatment revealed that the MB cavitation and sonoporation effects on the outer epithelial layer also depended on the course of irradiations. The area of epithelial membrane disruption, the membranous pore formation, the gaps or defects between adjacent cells, and the depth of the epithelial breakage were more severe in the group receiving 5 exposures than in the group receiving 3 exposures. These findings were consistent with the results for the USM-3 and USM-5 groups for the biotin-FITC delivery efficiency. As mentioned earlier, although RWM transit may involve several cellular processes, the outer epithelial layer is considered the main barrier to the passage of substances and is directly responsible for membrane permeability (Goycoolea, 2001; Wang et al., 2012; Liu et al., 2013). Our findings in the current study also support this viewpoint, as the USMB-induced permeability enhancement was associated with the physical breakdown of the main barrier, either by disruption of the tight junctions or the creation of membranous holes on the outer epithelial surface of the RWM.

We were the first to extend the application of USMBs to inner ear drug delivery (Shih et al., 2013). In our previous study using confocal laser scanning microscopy, we demonstrated that a fluorescent tracer, when passing through the RWM after USMB treatment, manifested within the cytoplasm of the outer epithelial layer. In addition, this tracer staining was co-localized with actin in the apposed plasma membranes between epithelial cells, i.e., at the cell boundary where tight junctions are formed with the closest contact between adjacent cells (Shih et al., 2013). In this study, the SEM and TEM observations showed that US-induced MB cavitation and sonoporation of the RWM resulted in membrane pore formations and disruption of the continuity and junctions of the outer epithelium, in agreement with our previous histological confocal imaging findings (Shih et al., 2013).

A characteristic of sonoporation treatment is a transient disruption of the cell membrane and an increase in membrane permeability due to acoustic MB cavitation (Mehier-Humbert et al., 2005). This process generates membrane pores ranging in diameter from hundreds of nanometers to microns and is highly associated with the volume expansion, contraction, fragmentation, and collapse of MBs (Kudo et al., 2009; Wang et al., 2013; Fan et al., 2014). Moreover, the change in cell membrane permeability is directly associated with the pore distribution that results from MB cavitation-induced membrane rupture and depends on the ultrasound irradiation applied (Zhou et al., 2012). Our current study revealed an association between sonoporation, membrane permeability, and cavitation-targeted structural changes and is the first to reveal the ultrastructural changes of the RWM after USMB exposure.

The vital roles of the outer epithelium in controlling the permeability of the RWM and subsequent regulation of transport have been described in previous studies (Nomura, 1984; Goycoolea et al., 1988; Suzuki et al., 2003; Wang et al., 2012; Liu et al., 2013). Damaging the outer epithelium with collagenase digestion or phenol treatment were shown to facilitate the delivery of viral vectors (Suzuki et al., 2003; Wang et al., 2012). Interestingly, even after this type of localized enzymatic manipulation had disrupted and eliminated most of the epithelial cells, experimental samples taken 3 or 4 weeks later showed complete recovery and could not be distinguished from the untreated controls (Wang et al., 2012), indicating the high regenerative capacity of epithelial cells. The basement membrane, positioned between the epithelial cells and connective tissue, plays a crucial role in wound healing and in the remodeling process following tissue injury (Brown et al., 2006). The USMB protocol described in the current study showed various degrees of damage that perturbed the outer epithelium and enhanced RWM permeability. However, the treatment still preserved the integrity of the basement membrane, thereby protecting the RWM from sonoporation damage and ensuring its subsequent regeneration.

The underlying mechanisms of USMB treatment have been investigated and involve US-induced MB cavitation that increases the permeability of the targeted cell membranes and capillaries to drugs (Pitt et al., 2004). The acoustic cavitation of MBs can be further classified into stable and inertial cavitation: the former generates a microstreaming and the latter produces a shock wave. An asymmetrical collapse of MBs can even produce a microjet that moves at sonic speed toward the cell surface, accompanied by a shear stress that creates transient but nonlethal micropores in the cell membrane to facilitate the passage of the drug or gene (Pitt et al., 2004; Hernot and Klibanov, 2008). In our related experiments, we have confirmed that US sonication at a suitably diluted MB concentration and a power density of 3 W/cm^2, as set in this study, induces a cavitation that arises predominantly from the inertial type (unpublished data). Because the current protocol of applying USMBs to an animal's tympanic cavity required placement of the ultrasound transducer 5 mm away from, but facing, the RWM (Shih et al., 2013), the additional sonoporation effect evoked by direct irradiation may be combined with the effect of MB cavitation, as shown in this study.

The thermal effect occurring during USMB administration is an important issue. In general, a temperature rise of 1.0°C –1.5°C over an indefinite time interval is not considered a safety concern for non-obstetric examinations (Ter Haar, 2011; Harris et al., 2016). A previous report showed the following logarithmic relationship between temperature elevation and the exposure time needed to produce adverse biological effects in animal fetuses for temperatures below 43°C: the necessary exposure time was reduced by a factor of four for every 1°C increase in temperature (Miller and Ziskin, 1989). Applying this logarithmic rule, the maximum safe exposure time would be 4 min for a temperature elevation of 4°C, 16 min for 3°C, 64 min for 2°C, and 256 min for 1°C (Harris et al., 2016). A reduction from a 256 min maximum exposure time to 120 min has been suggested as a safety precaution to reflect the present limited knowledge about possible subtle thermal bioeffects. However, the results from the present study showed that the temperature on the cochlear basal turn increased by 2.0°C–2.7°C and that of the cochlear apex increased by 1.2°C–1.8°C during sonication with 3–5 courses of USMBs, indicating that temperatures are unlikely to extend beyond the normal physiological range. Our investigation of hearing assessment and our histological examinations, including ABRs, DPOAE, surface preparations, and TUNEL assays, also indicated that this USMB technique is not harmful when applied as a method for inner ear drug delivery. Nevertheless, taking ultrasonic thermal safety precautions against any adverse bioeffects is always imperative, especially when a sensory organ is exposed to a prolonged duration of elevated temperature.

The conveyance of substances through the RWM to the inner ear primarily relied on a passive process, while active transport was assumed to be in charge of larger molecules and particles (Goycoolea, 2001; Salt and Plontke, 2005). When placed on the RWM, the substances may undergo nonspecific pinocytosis or pass through different channels between epithelial cells to traverse through the cytoplasm, undergo phagocytosis by the connective tissue cells, and then either penetrate blood vessels in the connective tissue layer or flow further into the perilymph (Goycoolea and Lundman, 1997; Duan and Chen, 2009). In addition to the physical alterations observed in the ultrastructural evaluations by TEM and SEM, the interactions between cavitation events and targeted cells also evoke a series of spatiotemporal molecular responses and biological effects that provide a temporary and reversible time window for drug delivery and repair of cavitation-induced membrane perforations (Qin et al., 2018). For example, receptor and caveolin-mediated endocytosis, a specific and active route for drug delivery, can be stimulated by acoustic cavitation (Zeghimi et al., 2015). The Ca^{2+}-gated ion channels are transiently activated and the intracellular Ca^{2+} transients can be detected after cavitation; these responses are temporally correlated with the occurrence of sonoporation (Fan et al., 2014; Qin et al., 2018). Changes in membrane potential, cytoskeleton dynamics, and in the production of reactive oxygen species were also reported after sonoporation (Qin et al., 2018).

The mechanisms for resealing USMB-mediated membrane perforations may rely on exocytosis and endocytosis (Fan et al., 2014; Qin et al., 2018). A large membrane perforation can trigger exocytosis of intracellular vesicles that, in turn, reseal the perforation with fused exocytotic vesicles. A small membrane perforation can be eliminated *via* endocytosis initiated by Ca^{2+} influx. This study focused on investigating sonoporation-induced ultrastructural alterations that may explain in part the mechanism of the observed permeability changes. Further exploration of the molecular biological mechanisms involved in cavitation-regulated membrane repair and prolonged permeability will be needed in the future.

CONCLUSION

Our findings demonstrated that the application of USMBs for the delivery of drugs to the inner ear was a safe, feasible, and effective approach to enhance RWM permeability. Scanning and transmission electron microscopy revealed the morphological changes that corresponded to the increased RWM permeability and indicated that the enhanced RWM permeability can result directly from MB cavitation-induced disruption of the barrier formed by the outer epithelial layer of the RWM. The sonoporation effects on the targeted cells and the prolonged effects on membrane permeability were dependent on the USMB irradiation course. Although epithelial cells were transiently disrupted by cavitation, their basement membranes remained intact and could completely recover within one month. Our findings provide a better understanding of how to develop therapeutic USMBs for inner ear drug and gene delivery for use in future clinical trials.

DATA AVAILABILITY STATEMENT

All datasets generated for this study are included in the article.

ETHICS STATEMENT

This study was carried out in accordance with relevant institutional and national guidelines for the care and use of laboratory animals. The experimental protocol was approved by the Institutional Animal Care and Use Committee of the National Defense Medical Center, Taipei, Taiwan (ethic code: IACUC-15-165; permission date: 1 August 2015).

AUTHOR CONTRIBUTIONS

Y-CL completed the main experiment and wrote the first draft of the paper. H-CC and H-KC participated in planning and analyzed the data. Y-YL, C-YK, and HW performed the surgery. C-LH assisted with statistical analysis. C-PS and C-HW initiated the project and designed the experiments. C-HW edited and revised the manuscript. All authors have reviewed the final version of the manuscript and approved it for publication.

FUNDING

This work was supported in part by grants from the Ministry of Science and Technology, Taiwan (MOST107-2314-B-016-027 and MOST 108-2314-B-016-038 to C-PS and MOST107-2314-B-663-001-MY3 to C-HW), the Tri-Service General Hospital grants (TSGH-C108-011 to C-PS and TSGH-C107-009 to C-HW), the Taichung Armed Forces General Hospital grant (108A14 to C-HW), and the Teh-Tzer Study Group for Human Medical Research Foundation (A1041001 and A1061019 to C-HW).

ACKNOWLEDGMENTS

The authors would like to thank Miss Yu-Jie Cai for her helpful schematic illustration, and Ms. Huei-Min Chen and Mr. Chi-Ming Lee for their excellent technical support of scanning electron microscopy at Core Facility Center, Office of Research and Development, Taipei Medical University.

REFERENCES

Brown, B., Lindberg, K., Reing, J., Stolz, D. B., and Badylak, S. F. (2006). The basement membrane component of biologic scaffolds derived from extracellular matrix. *Tissue Eng.* 12, 519–526. doi: 10.1089/ten.2006.12.519

Chen, H. K., Zhang, S. M., Chang, J. L., Chen, H. C., Lin, Y. C., Shih, C. P., et al. (2018). Insonation of systemically delivered Cisplatin-loaded microbubbles significantly attenuates nephrotoxicity of chemotherapy in experimental models of head and neck cancer. *Cancer (Basel)* 10. doi: 10.3390/cancers10090311

Chin, O. Y., and Diaz, R. C. (2019). State-of-the-art methods in clinical intracochlear drug delivery. *Curr. Opin. Otolaryngol. Head Neck Surg.* 27, 381–386. doi: 10.1097/MOO.0000000000000566

Creber, N. J., Eastwood, H. T., Hampson, A. J., Tan, J., and O'leary, S. J. (2019). Adjuvant agents enhance round window membrane permeability to dexamethasone and modulate basal to apical cochlear gradients. *Eur. J. Pharm. Sci.* 126, 69–81. doi: 10.1016/j.ejps.2018.08.013

Duan, M. L., and Chen, Z. Q. (2009). Permeability of round window membrane and its role for drug delivery: our own findings and literature review. *J. Otol.* 4, 34–43. doi: 10.1016/S1672-2930(09)50006-2

El Kechai, N., Agnely, F., Mamelle, E., Nguyen, Y., Ferrary, E., and Bochot, A. (2015). Recent advances in local drug delivery to the inner ear. *Int. J. Pharmaceut.* 494, 83–101. doi: 10.1016/j.ijpharm.2015.08.015

Fan, Z., Kumon, R. E., and Deng, C. X. (2014). Mechanisms of microbubble-facilitated sonoporation for drug and gene delivery. *Ther. Deliv.* 5, 467–486. doi: 10.4155/tde.14.10

Goycoolea, M. V., and Lundman, L. (1997). Round window membrane. Structure function and permeability: a review. *Microscopy Res. Tech.* 36, 201–211. doi: 10.1002/(SICI)1097-0029(19970201)36:3<201::AID-JEMT8>3.0.CO;2-R

Goycoolea, M. V., Muchow, D., and Schachern, P. (1988). Experimental studies on round window structure: function and permeability. *Laryngoscope* 98, 1–20. doi: 10.1288/00005537-198806001-00002

Goycoolea, M. V. (2001). Clinical aspects of round window membrane permeability under normal and pathological conditions. *Acta Otolaryngol.* 121, 437–447. doi: 10.1080/000164801300366552

Hao, J., and Li, S. K. (2019). Inner ear drug delivery: recent advances, challenges, and perspective. *Eur. J. Pharm. Sci.* 126, 82–92. doi: 10.1016/j.ejps.2018.05.020

Harris, G. R., Church, C. C., Dalecki, D., Ziskin, M. C., and Bagley, J. E. (2016). Comparison of thermal safety practice guidelines for diagnostic ultrasound exposures. *Ultrasound Med. Biol.* 42, 345–357. doi: 10.1016/j.ultrasmedbio.2015.09.016

Hernot, S., and Klibanov, A. L. (2008). Microbubbles in ultrasound-triggered drug and gene delivery. *Adv. Drug Delivery Rev.* 60, 1153–1166. doi: 10.1016/j.addr.2008.03.005

Jackson, L. E., and Silverstein, H. (2002). Chemical perfusion of the inner ear. *Otolaryngolog. Clinics North America* 35, 639–653. doi: 10.1016/s0030-6665(02)00023-3

Kudo, N., Okada, K., and Yamamoto, K. (2009). Sonoporation by single-shot pulsed ultrasound with microbubbles adjacent to cells. *Biophys. J.* 96, 4866–4876. doi: 10.1016/j.bpj.2009.02.072

Li, L., Chao, T., Brant, J., O'malley, B. Jr., Tsourkas, A., and Li, D. (2017). Advances in nano-based inner ear delivery systems for the treatment of sensorineural hearing loss. *Adv. Drug Deliv. Rev.* 108, 2–12. doi: 10.1016/j.addr.2016.01.004

Liao, A. H., Hsieh, Y. L., Ho, H. C., Chen, H. K., Lin, Y. C., Shih, C. P., et al. (2014). Effects of microbubble size on ultrasound-mediated gene transfection in auditory cells. *BioMed. Res. Int.* 2014, 840852. doi: 10.1155/2014/840852

Lin, Y.-S., Chen, C.-M., Soong, B.-W., Wu, Y.-R., Chen, H.-M., Yeh, W.-Y., et al. (2011). Dysregulated brain creatine kinase is associated with hearing impairment in mouse models of Huntington disease. *J. Clin. Invest.* 121, 1519–1523. doi: 10.1172/JCI43220

Liu, H., Chen, S., Zhou, Y., Che, X., Bao, Z., Li, S., et al. (2013). The effect of surface charge of glycerol monooleate-based nanoparticles on the round window membrane permeability and cochlear distribution. *J. Drug Target* 21, 846–854. doi: 10.3109/1061186X.2013.829075

Mäder, K., Lehner, E., Liebau, A., and Plontke, S. K. (2018). Controlled drug release to the inner ear: concepts, materials, mechanisms, and performance. *Hearing Res.* 368, 49–66. doi: 10.1016/j.heares.2018.03.006

Mccall, A. A., Swan, E. E. L., Borenstein, J. T., Sewell, W. F., Kujawa, S. G., and Mckenna, M. J. (2010). Drug delivery for treatment of inner ear disease: current state of knowledge. *Ear Hearing* 31, 156. doi: 10.1097/AUD.0b013e3181c351f2

Mehier-Humbert, S., Bettinger, T., Yan, F., and Guy, R. H. (2005). Plasma membrane poration induced by ultrasound exposure: implication for drug delivery. *J. Controlled Release* 104, 213–222. doi: 10.1016/j.jconrel.2005.01.007

Miller, M. W., and Ziskin, M. C. (1989). Biological consequences of hyperthermia. *Ultrasound Med. Biol.* 15, 707–722. doi: 10.1016/0301-5629(89)90111-7

Nomura, Y. (1984). Otological significance of the round window. *Adv. Otorhinolaryngol.* 33, 1–162.

Paparella, M. M., Schachern, P. A., and Choo, Y. B. (1983). The round window membrane: otological observations. *Ann. Otolog. Rhinolog. Laryngolog.* 92, 629–634. doi: 10.1177/000348948309200619

Pitt, W. G., Husseini, G. A., and Staples, B. J. (2004). Ultrasonic drug delivery–a general review. *Expert Opin. Drug Deliv.* 1, 37–56. doi: 10.1517/17425247.1.1.37

Piu, F., and Bishop, K. M. (2019). Local drug delivery for the treatment of neurotology disorders. *Front. Cell Neurosci.* 13, 238. doi: 10.3389/fncel.2019.00238

Qin, P., Han, T., Yu, A. C. H., and Xu, L. (2018). Mechanistic understanding the bioeffects of ultrasound-driven microbubbles to enhance macromolecule delivery. *J. Control Release* 272, 169–181. doi: 10.1016/j.jconrel.2018.01.001

Rauch, S. D., Halpin, C. F., Antonelli, P. J., Babu, S., Carey, J. P., Gantz, B. J., et al. (2011). Oral vs intratympanic corticosteroid therapy for idiopathic sudden sensorineural hearing loss: a randomized trial. *Jama* 305, 2071–2079. doi: 10.1001/jama.2011.679

Salt, A. N., and Plontke, S. K. (2005). Local inner-ear drug delivery and pharmacokinetics. *Drug Discovery Today* 10, 1299–1306. doi: 10.1016/S1359-6446(05)03574-9

Shih, C. P., Chen, H. C., Chen, H. K., Chiang, M. C., Sytwu, H. K., Lin, Y. C., et al. (2013). Ultrasound-aided microbubbles facilitate the delivery of drugs to the inner ear *via the* round window membrane. *J. Control Release* 167, 167–174. doi: 10.1016/j.jconrel.2013.01.028

Shih, C. P., Chen, H. C., Lin, Y. C., Chen, H. K., Wang, H., Kuo, C. Y., et al. (2019). Middle-ear dexamethasone delivery *via* ultrasound microbubbles attenuates noise-induced hearing loss. *Laryngoscope* 129, 1907–1914. doi: 10.1002/lary.27713

Smith, N. B., Lee, S., Maione, E., Roy, R. B., Mcelligott, S., and Shung, K. K. (2003). Ultrasound-mediated transdermal transport of insulin *in vitro* through human skin using novel transducer designs. *Ultrasound Med. Biol.* 29, 311–317. doi: 10.1016/s0301-5629(02)00706-8

Suzuki, M., Yamasoba, T., Suzukawa, K., and Kaga, K. (2003). Adenoviral vector gene delivery *via the* round window membrane in guinea pigs. *Neuroreport* 14, 1951–1955. doi: 10.1097/00001756-200310270-00014

Tang, H., Wang, C. C., Blankschtein, D., and Langer, R. (2002). An investigation of the role of cavitation in low-frequency ultrasound-mediated transdermal drug transport. *Pharm. Res.* 19, 1160–1169. doi: 10.1023/a:1019898109793

Ter Haar, G. (2011). Ultrasonic imaging: safety considerations. *Interface Focus* 1, 686–697. doi: 10.1098/rsfs.2011.0029

Wang, H., Murphy, R., Taaffe, D., Yin, S., Xia, L., Hauswirth, W. W., et al. (2012). Efficient cochlear gene transfection in guinea-pigs with adeno-associated viral vectors by partial digestion of round window membrane. *Gene Ther.* 19, 255–263. doi: 10.1038/gt.2011.91

Wang, T.-Y., Wilson, K. E., Machtaler, S., and Willmann, J. K. (2013). Ultrasound and microbubble guided drug delivery: mechanistic understanding and clinical implications. *Curr. Pharmaceut. Biotechnol.* 14, 743–752. doi: 10.2174/1389201014666131226114611

Zeghimi, A., Escoffre, J., and Bouakaz, A. (2015). Role of endocytosis in sonoporation-mediated membrane permeabilization and uptake of small molecules: a electron microscopy study. *Phys. Biol.* 12, 066007. doi: 10.1088/1478-3975/12/6/066007

Zhou, Y., Yang, K., Cui, J., Ye, J., and Deng, C. (2012). Controlled permeation of cell membrane by single bubble acoustic cavitation. *J. Controlled Release* 157, 103–111. doi: 10.1016/j.jconrel.2011.09.068

Conflict of Interest: The authors declare that the research was conducted in the absence of any commercial or financial relationships that could be construed as a potential conflict of interest.

frontiers in Pharmacology

ORIGINAL RESEARCH
published: 30 January 2020
doi: 10.3389/fphar.2019.01540

Bactericidal Activity of Lipid-Shelled Nitric Oxide-Loaded Microbubbles

Maxime Lafond[1*], *Himanshu Shekhar*[1], *Warunya Panmanee*[2], *Sydney D. Collins*[1], *Arunkumar Palaniappan*[1], *Cameron T. McDaniel*[2], *Daniel J. Hassett*[2] *and Christy K. Holland*[1,3]

[1] Department of Internal Medicine, Division of Cardiovascular Health and Disease, University of Cincinnati, Cincinnati, OH, United States, [2] Department of Molecular Genetics, Biochemistry and Microbiology, University of Cincinnati College of Medicine, Cincinnati, OH, United States, [3] Department of Biomedical Engineering, University of Cincinnati, Cincinnati, OH, United States

OPEN ACCESS

Edited by:
Marc Derieppe,
Princess Maxima Center for Pediatric Oncology, Netherlands

Reviewed by:
Francesca Cavalieri,
The University of Melbourne, Australia
Virginie Papadopoulou,
University of North Carolina at Chapel Hill, United States

***Correspondence:**
Maxime Lafond
lafondme@ucmail.uc.edu

Specialty section:
This article was submitted to Translational Pharmacology, a section of the journal Frontiers in Pharmacology

Received: 29 August 2019
Accepted: 27 November 2019
Published: 30 January 2020

Citation:
Lafond M, Shekhar H, Panmanee W, Collins SD, Palaniappan A, McDaniel CT, Hassett DJ and Holland CK (2020) Bactericidal Activity of Lipid-Shelled Nitric Oxide-Loaded Microbubbles. Front. Pharmacol. 10:1540. doi: 10.3389/fphar.2019.01540

The global pandemic of antibiotic resistance is an ever-burgeoning public health challenge, motivating the development of adjunct bactericidal therapies. Nitric oxide (NO) is a potent bioactive gas that induces a variety of therapeutic effects, including bactericidal and biofilm dispersion properties. The short half-life, high reactivity, and rapid diffusivity of NO make therapeutic delivery challenging. The goal of this work was to characterize NO-loaded microbubbles (MB) stabilized with a lipid shell and to assess the feasibility of antibacterial therapy *in vitro*. MB were loaded with either NO alone (NO-MB) or with NO and octafluoropropane (NO-OFP-MB) (9:1 v/v and 1:1 v/v). The size distribution and acoustic attenuation coefficient of NO-MB and NO-OFP-MB were measured. Ultrasound-triggered release of the encapsulated gas payload was demonstrated with 3-MHz pulsed Doppler ultrasound. An amperometric microelectrode sensor was used to measure NO concentration released from the MB and compared to an NO-OFP-saturated solution. The effect of NO delivery on the viability of planktonic (free living) *Staphylococcus aureus* (SA) USA 300, a methicillin-resistant strain, was evaluated in a 96 well-plate format. The co-encapsulation of NO with OFP increased the total volume and attenuation coefficient of MB. The NO-OFP-MB were destroyed with a clinical ultrasound scanner with an output of 2.48 MPa peak negative pressure (*in situ* MI of 1.34) but maintained their echogenicity when exposed to 0.02 MPa peak negative pressure (*in situ* MI of 0.01. The NO dose in NO-MB and NO-OFP-MB was more than 2-fold higher than the NO-OFP-saturated solution. Delivery of NO-OFP-MB increased bactericidal efficacy compared to the NO-OFP-saturated solution or air and OFP-loaded MB. These results suggest that encapsulation of NO with OFP in lipid-shelled MB enhances payload delivery. Furthermore, these studies demonstrate the feasibility and limitations of NO-OFP-MB for antibacterial applications.

Keywords: nitric oxide delivery, lipid-shelled microbubbles, bactericide, USA 300 *Staphylococcus aureus*, bioactive gas delivery, echocontrast agent, ultrasound

INTRODUCTION

Antibiotic resistance is a leading public health challenge of the 21st century (Nolte, 2014; Tacconelli and Pezzani, 2019). Multidrug-resistant bacteria have emerged in both community and nosocomial settings (van Duin and Paterson, 2016), partly due to the misuse of antibiotics in animals and humans as well as horizontal gene transfer (Ventola, 2015). Furthermore, recent efforts toward the development of novel antibiotics have produced diminishing returns (Coates et al., 2011), motivating the need to develop alternative and adjunct strategies for treating bacterial infections. Nitric oxide (NO) is a potent bioactive gas that plays important roles in physiology, including the regulation of vasodilation, platelet activation, and neurotransmission (Elnaggar et al., 2017). NO is downregulated in pathological conditions, such as hypertension, atherosclerosis, and chronic kidney disease (Ahmad et al., 2018). Additionally, NO demonstrates antibacterial activity against a variety of microorganisms (Schairer et al., 2012). Specifically, NO exhibits dose-dependent activity that can not only disperse biofilms but also kill bacteria (Barraud et al., 2009; Schairer et al., 2012; Barraud et al., 2014). Therapeutic exogenous NO delivery has the potential for efficacy against both common and antibiotic-resistant microbial strains *via* reactive intermediates that exert nitrosative and oxidative stresses (Schairer et al., 2012). NO could be used either as a standalone therapy or in combination with other antibacterial agents.

Therapeutic applications of NO are limited by the lack of successful delivery strategies (Elnaggar et al., 2017). NO donors, such as nitroglycerin, are used in the clinic to manage acute hypertension (Flaherty et al., 1982). However, nitroglycerin can cause side effects, such as a systemic reduction in blood pressure, which precludes broad usage (Bloch et al., 2007). Inhalation of NO has been used to treat hypoxemia and pulmonary arterial hypertension in full-term and near-term neonates (Ichinose et al., 2004; Bloch et al., 2007). Additionally, recent studies suggest that NO inhalation can prevent chronic lung disease in premature infants and alleviate ischemia-reperfusion injury (Bloch et al., 2007; Kida and Ichinose, 2014). However, inhalation is expensive, cumbersome and suitable for a limited number of applications (Thunberg et al., 2015). Therefore, the development of site-specific and triggered delivery of NO is an active area of research (Elnaggar et al., 2017). Biomaterials, such as dendrimers (Sun et al., 2012), sol-gels (Robbins and Schoenfisch, 2003), polymers (Studenovsky et al., 2018), and lipids (Elnaggar et al., 2017), are under investigation as carriers for NO donors. Loading of NO in micron-sized microbubbles (MB) is another strategy for delivery of this bioactive gas (Wang et al., 2013; Sutton et al., 2014; Grishenkov et al., 2015). Echogenic liposomes containing MB encapsulated in multilamellar structures or monolayers have also been used for NO delivery (Huang et al., 2009; Kim et al., 2014; Lee et al., 2014).

The theoretical considerations for NO delivery using MB and ultrasound have been explored previously (Postema et al., 2006). Intravenous release of NO from lipid-shelled MB was shown to accelerate the resolution of deep vein thrombosis in a murine model (Wang et al., 2013). NO-loaded MB have been used with stem cells for regenerating ischemic tissue after myocardial infarction (Tong et al., 2013). NO-loaded echogenic liposomes (NO-ELIP) have been tested for the treatment of breast cancer *in vitro* (Lee et al., 2014). NO-ELIP were also explored to trigger vasodilation (Kim et al., 2014), and to reduce neointimal hyperplasia (Huang et al., 2009). In a review on ultrasound-mediated therapeutic delivery for the treatment of biofilm in chronic wounds, LuTheryn et al. (2019a) describe the potency of NO for biofilm dispersion and bactericide applications, and highlight the need for site specific delivery of NO. LuTheryn et al. suggest sonosensitive NO-loaded MB as a strategy for controlled delivery. The same group notably reported preliminary data on biofilm dispersion using NOMB (LuTheryn et al., 2019b).

Recent studies on bioactive gas delivery suggest that the bioactive gas payload can be stabilized by the co-encapsulation of perfluorocarbon gases (Kwan et al., 2012; Yang et al., 2018; Shekhar et al., 2019b). Whether co-encapsulation of a perfluorocarbon gas can stabilize NO payload within MB has not been determined previously.

In this study, we evaluated the amount of NO loading, acoustic response, and stability of MB synthesized with either NO alone (NO-MB), or with NO and OFP at different volume fractions: 90% NO and 10% OFP (NO-OFP-MB 9:1 v/v), or 50% NO and 50% OFP (NO-OFP-MB 1:1 v/v). The size distribution and acoustic attenuation of NO-loaded MB were characterized. The NO dose delivered using these agents also was measured. Next, the imaging and release of the gaseous payload of MB was demonstrated using a commercial ultrasound scanner, exhibiting compatibility of this technique in a clinical setting. Finally, we evaluated the feasibility of killing the USA 300 strain of *Staphylococcus aureus* (*S. aureus*) using NO-loaded MB *in vitro*.

MATERIALS AND METHODS

Preparation of Lipid-Shelled MB

All lipids were purchased from Avanti Polar Lipids (Alabaster, AL, USA). NO (99.99%) and OFP (99.9%) gases were sourced from Wright Brothers (Ohio, USA) and Advanced Specialty Gases (Reno, NV, USA), respectively. Bovine serum albumin (BSA), propylene glycol, and glycerol were acquired from Sigma Aldrich (St. Louis, MO, USA). To prepare NO-loaded MB, 1,2-distearoyl-sn-glycero-3-phosphocholine (DSPC), and 1,2-distearoyl-sn-glycero-3-phosphoethanolamine-N-[methoxy (polyethylene glycol)-2000] (18:0 PEG2000 PE) were combined in a molar ratio of 9:1. The procedure for preparing these lipid-shelled MB has been reported in detail previously (Shekhar et al., 2019b). Briefly, a thin lipid film was formed in a round bottom flask using a rotary evaporator (N-1001, Eyela, Bohemia, NY). Thereafter, the residual solvents were removed by overnight lyophilization (Labconco FreeZone 2.5, Labconco, Kansas City, MO, USA). Subsequently, the lipids were rehydrated using a solution of PBS:propylene glycol:glycerol at 16:3:1 volume ratio that was pre-warmed to 60°C to obtain a lipid concentration of 1 mg/ml. After rehydration, the lipid suspension was sonicated

(Branson 3510, Branson Ultrasonics, Danbury, CT, USA) for 30 min to obtain a lipid dispersion. Aliquots (1.4 ml) of this dispersion were transferred into serum glass vials (3 ml total volume, item# 223683, Wheaton, Millville, NJ USA), sealed using gas-tight butyl-rubber stoppers, and crimped. Similarly, 1.4-ml aliquots of the buffer solution were stored in 3-ml serum vials, sealed, and crimped. The air in the headspace of each vial was evacuated for 30 s to a pressure of 40 mmHg using a vacuum pump (model number: 8803, Welch Vacuum Technologies Inc., Mt. Prospect, IL, USA). Subsequently, the vials were refrigerated at 4°C and used for experiments within 2 weeks.

Vials were warmed to room temperature for 1 h before adding the gases. NO and OFP gases were collected in 0.5-L gas-sampling bags (Tedlar®, Zefon International, Ocala, FL, USA). The 1.6-ml vial headspace was filled with either NO only, or a mixture of NO and OFP (9:1 and 1:1 v/v), or a mixture of air and OFP 9:1 v/v using a 3-ml syringe fitted with a 30-G needle. Thereafter, the vials were activated by high-shear mixing for 45 s with a VIALMIX™ device (Lantheus Medical Imaging, N. Billerica, MA, USA) to produce NO-MB and NO-OFP-MB. As the high-shear mixing process generated heat, the vials were allowed to cool for 15 min to room temperature before use.

Size Distribution Assessment

A Coulter counter (Multisizer 4, Beckman Coulter, Brea, CA, USA), equipped with a 30-μm aperture, was used to measure the size distributions of NO-MB and NO-OFP-MB, as described previously (Shekhar et al., 2018) at room temperature. NO-MB or NO-OFP-MB were diluted 1,000 and 20,000-fold in air-saturated PBS, respectively. The size distributions of three vials of each type of microbubble were assessed (n = 3). The volume-weighted size distribution histograms were obtained and adjusted for the degree of dilution. The total volume of gas in the MB was calculated from the volume-weighted size distribution measurements.

Differential Interference Contrast Microscopy

Differential interference contrast (DIC) microscopy was performed to assess the morphology of lipid-shelled MB. Either NO-MB, or NO-OFP-MB at 1:1 or 9:1 v/v NO-OFP ratio (10 μl, undiluted) were added to a polystyrene (plasma-treated) microscope slide (Ted Pella, Redding, CA, USA), covered with a glass coverslip, and visualized with DIC microscopy using an Axioplan two imaging microscope (Zeiss, Thornwood, NY, USA). A 63× oil-immersion objective (Plan Apochromat, Zeiss, Thornwood, NY, USA) with a numerical aperture of 1.4 was used along with a charged coupled device camera (Axiocam MRM, Zeiss, Thornwood, NY, USA) to acquire images. Images of Definity®, an FDA-approved echo-contrast agent, were also acquired under the same conditions for comparison.

Acoustic Attenuation and Ultrasound-Triggered Release

Broadband attenuation spectroscopy was used to measure the acoustic attenuation coefficient of NO-MB and NO-OFP-MB from 2 to 25 MHz at 37 °C as reported previously (Raymond et al., 2014). The attenuation spectroscopy system is shown in **Figure 1**. Briefly, the agents were diluted 2,000-fold in a 37 ± 0.5 °C solution of 0.5% BSA in air-saturated PBS. The through-transmission attenuation spectrum was measured using a broadband transducer pair (PI-20, Olympus NDT, Waltham, MA, USA). The same system was used along with two ultrasound insonation schemes to assess the ultrasound-triggered release of the gas payload from NO-OFP-MB. Specifically, the NO-OFP-MB (9:1 or 1:1 v/v) diluted in BSA were perfused through a 1-mm inner diameter ethyl vinyl acetate tube (McMaster-Carr, Aurora, OH, USA) at a rate of 11.7 ml/min, filling the cell-culture cassette serving as a measurement chamber (CLINIcell 25, Mabio, Tourcoing, France) in approximately 30 s. A C5-1 transducer array (Phillips, Bothell, MA, USA) with a center frequency of 3.41 MHz attached to a clinical ultrasound scanner (EPIQ 7G, Philips Healthcare, Bothell, WA USA) was positioned 1 cm away from the tube. The acoustic attenuation of NO-OFP-MB was measured after exposure to either sham (no ultrasound), B-mode ultrasound at an on-screen MI of 0.04 (Porter et al., 2006; Radhakrishnan et al., 2012), or Duplex Doppler ultrasound at an on-screen MI of 1.2. Exposure or sham exposure was performed in the tube between the syringe and the measurement chamber shown in **Figure 1**. The peak negative pressure and *in situ* MI within the tube were measured using a 0.2 μm needle hydrophone (Precision Acoustics, Dorchester, UK). The NO-OFP-MB were exposed to B-mode pulses at a peak negative pressure of 0.02 MPa (or an *in situ* MI of 0.01), or Duplex Doppler ultrasound at a peak negative pressure of 2.48 MPa (or *in situ* MI of 1.34). Complete attenuation loss was used to indicate gas payload release from lipid-shelled MB. All the attenuation measurements were performed in triplicate.

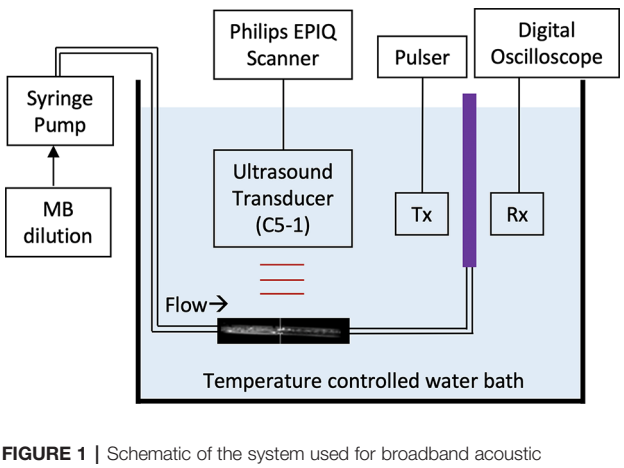

FIGURE 1 | Schematic of the system used for broadband acoustic attenuation spectroscopy. The purple region denotes the CLINIcell sample chamber. Tx and Rx denotes the transmitting and receiving transducers, respectively.

Quantification of NO Loading

The NO dose in the MB was quantified using an amperometric microelectrode sensor (Apollo 4000 with ISO-NOP electrode; World Precision Instruments, Sarasota, FL, USA), which had a response time of about 5 to 7 s, using the experimental set-up shown in **Figure 2** at room temperature. NO and OFP gases were removed from compressed lecture bottle-sized cylinders and transferred to gas sampling bags. Standard solutions with known gas volume fractions (v/v) were created by diluting NO-saturated water in PBS. The concentration of NO in NO-saturated water was calculated based on the published solubility coefficient at room temperature, 1.91 mM. The peak electrode response was evaluated for a range of NO-saturated solution volumes between 2 µl and 20 µl. A linear regression was performed to obtain a calibration curve relating the concentration of NO with the measured peak response of the amperometric microelectrode sensor.

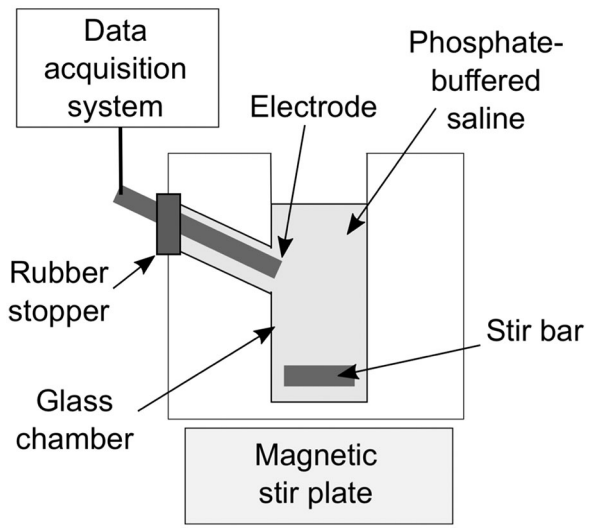

FIGURE 2 | Schematic of the experimental set-up with the amperometric microelectrode sensor that was used to measure the NO dose.

To determine the NO dose in NO-OFP-MB, 10 µl of the dispersion were added to 2.5 ml of PBS in a glass measurement chamber, with and without destroying the MB. A protocol based on injection of NO-OFP-MB through a 30-G needle into the glass measurement chamber was used to destroy the MB and release the gas payload. A preliminary experiment was performed to validate this injection protocol (**Figure 3**). A 10-µl aliquot of NO-saturated solution was drawn into a glass syringe through a 19-G needle and injected into the measurement chamber through the same needle. Next, a 19-G needle was used to draw the solution and the syringe was replaced with a 30-G needle, ensuring that a 15-µl solution was present in the syringe before injection. This procedure allowed us to account for the dead volume difference between the 30-G and the 19-G needles (5 µl). Thus, 10-µl solution was delivered into the measurement chamber. Both injection techniques resulted in the same current response from the amperometric microelectrode sensor ($p > 0.05$, **Figure 3A**, n = 3). Next, it was determined whether injection through a 30-G needle destroyed the MB (**Figure 3B**). The attenuation coefficient of NO-OFP-MB 9:1 v/v was determined after injection using a 19-G and a 30-G needle into BSA (1:3000 dilution, n = 3). These measurements showed almost complete loss of attenuation of NO-OFP-MB 9:1 v/v after injection through a 30-G needle (**Figure 3B**).

Subsequent to the validation of the injection protocol, the NO dose in NO-OFP-MB (9:1 v/v and 1:1 v/v) was measured using the amperometric microelectrode sensor (n = 9 except for NO-OFP-MB 9:1 v/v with 30-G needle: n = 10). The concentration of

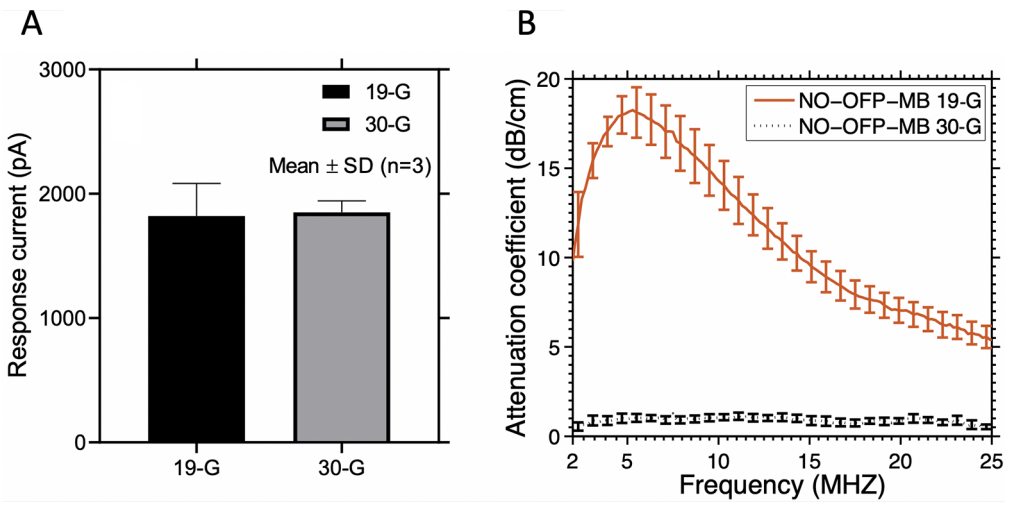

FIGURE 3 | (A) The response current of the amperometric microelectrode sensor to NO-saturated solution obtained after injection through a 19-G or 30-G needle. **(B)** Attenuation coefficient of NO-OFP-MB 9:1 v/v obtained after injection through a 19-G or a 30-G needle. Injection through a 30-G needle resulted in a sharp decrease in the attenuation coefficient, and release of the gas payload. The mean ± 1 standard deviation is depicted (n = 3 per group) in each case.

NO measured by the amperometric microelectrode sensor was corrected for the dilution factor and reported in terms of in vial concentration in mM. As an alternate measurement method, the NO concentration was also determined from the size measurements obtained using the Coulter counter. The size measurement was performed after diluting the bubbles in an air-saturated PBS solution, which initiated gas diffusion into and out of the MB across the lipid shell with a concomitant change of microbubble size. Hence, NO-OFP-MB size and gas content dynamics of the bubbles injected in the PBS for measurement were modeled using a multi-gas bubble model taking into account the NO-OFP loading in an air-saturated fluid (oxygen plus nitrogen) (Kwan et al., 2012). Briefly, this model describes gas exchange through the bubble layers (1) and the expression for the mechanical equilibrium (2):

$$\frac{dn_i}{dt} = -\frac{4\pi R^2 K_{H,i}}{\Omega_{s,i} + \Omega_{w,i} + R_{PEG}} \left(P_H + P_L - \frac{3BT}{4\pi R^3} \sum_j^N n_j - f_i P_{sat} \right) \quad (1)$$

$$\frac{3BT}{4\pi R^3} \sum_{i=1}^{N} n_i = \frac{2\sigma}{R} + P_H, \quad (2)$$

where n is the moles of gas inside the bubble, R is the bubble radius, K_H is the Henry's constant of each gas (denoted by the subscript i). P_H is the hydrostatic pressure (101325 Pa), P_{sat} is the saturation pressure, $P_L=2\sigma/R$ is the Laplace pressure with σ the surface tension, and f is the gas saturation fraction in the medium surrounding the bubble. B is the ideal gas constant, and T is the temperature. N is the number of gas species considered. The subscript j denotes a different gas species ($j \neq i$). Ω_s, and R_{PEG} denote resistance to gas diffusion from the lipid shell, and the pegylation (Borden and Longo, 2002), respectively. $\Omega_{w,i}=R/D_i$ is the resistance of gas diffusion in the bulk medium, and D is the diffusivity of each gas species, i, in the bulk medium. The resistance to diffusion (in s/cm), $\Omega_{s,i}$, was implemented in an energy barrier model by Kwan et al. (Kwan et al., 2012):

$$\Omega_{s,i} = \Omega_n e^{\frac{\pi a_i^2}{k_B T}(\sigma_0 - \sigma)}, \quad (3)$$

where $\Omega_n=133 s/cm$ (Kwan et al., 2012) is a constant associated with the lipid encapsulation, a_i is the collision diameter of the gas molecule, k_B is the Boltzman constant, and $\sigma_0=0.073 N/m$ is the surface tension of the gas-liquid interface. Custom code was written in Matlab® (MathWorks), run on a desktop personal computer, and used to solve equations (1) and (2) iteratively. Equation (1) was solved using a finite difference scheme. The polynomial equation (2) was solved by finding the eigenvalues of the companion matrix in rational canonical form using the Matlab® function "root" and selecting the only real and positive solution. Initial bubble radii between 0.5 and 30 µm were modeled. The gas properties used in the computation are listed in **Table 1**. We assumed that the MB reached minimum sizes before measurement with the Multisizer 4 (Pu et al., 2006). Thus, the measured bubble size distribution was corrected for this size change due to gas diffusion and used to calculate the expected NO dose. The kinetics of the reaction of NO with oxygen in aqueous solution was modeled using the following set of equations adapted from Lewis and Deen (1994):

$$\frac{d[NO]}{dt} = -4k_1[NO]^2[O_2] + \left(\frac{k_G A_G}{V}\right)_{NO} \left([NO]^* - [NO]\right), \quad (4)$$

$$\frac{d[O_2]}{dt} = -k_1[NO]^2[O_2] + \left(\frac{k_G A_G}{V}\right)_{O_2} \left([O_2]^* - [O_2]\right), \quad (5)$$

where k_1 is the rate constant of the reaction ($2.1\times10^6 M^{-2}s^{-1}$), and $k_G A_G/V$ is the volumetric mass-transfer coefficient ($2.8\times10^{-3}s^{-1}$ and $2.5\times10^{-3}s^{-1}$ for NO and oxygen, respectively). The asterisks denote the concentrations in the gas phase. The concentration of NO in the gas phase, $[NO]^*$, was assumed to be negligible. The expected NO dose was derived from the size distribution measurements (n = 3) and assumed to be the initial NO concentration.

The stability of the "in vial" NO dose was assessed by successive measurements 15 min, 2, 4, and 6 h after vial activation (n = 3). The NO dose in a 96 well-plate was measured between 15 and 340 s (n = 3). The results were compared with the model of gas diffusion including the reaction of NO with oxygen.

Susceptibility of *Staphylococcus Aureus* Strain USA300 to NO-OFP-MB

The susceptibility of *S. aureus* USA300, a methicillin-resistant strain, to NO-OFP-MB 9:1 v/v was evaluated *in vitro*. Because NO-OFP-MB 9:1 v/v had the highest NO dose determined by the

TABLE 1 | Gas properties used in the simulations.

Gas properties	Oxygen	Nitrogen	Octafluoropropane	Nitric oxide
Henry's constant - K_H [$mol.m^{-3}.Pa^{-1}$] ($\times10^{-6}$), derived from Ostwald coefficients (Wilhelm et al., 1977; Kwan et al., 2012)	7.56	7.14	0.21	19.00
Collision diameter - a [Å]	3.46 (Ismail et al., 2015)	3.64 (Ismail et al., 2015)	6.95 (Siebert and Knobler, 1971; Sarkar et al., 2009)	3.17 (Ismail et al., 2015)
Diffusivity – $D[m^2.s^{-1}]$ ($\times10^{-9}$)	2.10 (Cussler and Cussler, 2009)	1.88 (Cussler and Cussler, 2009)	0.745 (Sarkar et al., 2009)	2.21 (Zacharia and Deen, 2005)

experiments described in section 2.5, this formulation was used for bactericidal assessment. Air-OFP-MB 9:1 v/v served as a control to assess the effect of pegylated lipid-shelled MB without NO on the bacteria. *S. aureus* strain USA300 bacteria were grown on Luria-Bertani (LB) agar and maintained at 37 °C overnight. Thereafter, a single colony of bacteria was used to inoculate Mueller Hinton (MH) broth for 18 h then 100-fold diluted with 20% MH broth in a 96 well-plate. Subsequently, 100 µl of either air-saturated solution (consisting of PBS, propylene glycol, and Glycerol mixed at 16:3:1 v/v ratio), or NO-saturated solution, or air-OFP-MB 9:1 v/v, or NO-OFP-MB 9:1 v/v were added to each well plate to obtain a total volume of 200 µl. Each vial was sealed and vented to a bag of the corresponding gas mixture to avoid degradation of NO by O_2 between replicates. The plates were incubated 24 h at 37°C, and the viability of the cells was counted using the serial dilution method. A 20 µl aliquot of each sample was transferred into each well of a 96 well-plate. Subsequently, bacteria were diluted 10-fold in PBS, and 10 µl of each diluted sample was spotted on an LB agar plate. After incubation at 37 °C for 18 h, bacteria colonies were counted and reported as colony forming units (CFU)/ml. At least nine independent bactericide experiments were performed using fresh vials and a different colony of bacteria each time over three different days of experiments.

Statistical Analysis

All statistical analyses were performed on GraphPad Prism version 8.0.2 for MacOS (GraphPad Software, San Diego, CA, USA). The data are reported as the mean ± 1 standard deviation. To determine whether the differences in particle volume and payload of NO in NO-MB or NO-OFP-MB (9:1 v/v or 1:1 v/v) were statistically significant, ANOVA tests with Dunn's multiple comparison correction were employed after testing for normality using a Kolmogorov-Smirnov test. No outliers were detected using the robust regression and outlier removal (ROUT) method with the parameter Q set to 1% (recommended setting in GraphPad Prism). For bacteria killing experiments, the data were tested against a normal distribution using the Kolmogorov-Smirnov normality test and three outliers were removed using the ROUT method. The Kruskal-Wallis test was used to compare the CFU/ml obtained with air-saturated solution, NO-OFP 9:1 v/v saturated solution and air-OFP-MB against NO-OFP-MB. Post-hoc Dunn's multiple comparison test was used to obtain adjusted *p*-values. A *p*-value less than 0.05 was considered statistically significant.

RESULTS

Figure 4 shows the volume-weighted size distributions of NO-MB and NO-OFP-MB (9:1 and 1:1 v/v). The shape of the volume size distribution of NO-OFP-MB was similar for the 1:1 and 9:1 ratio of NO and OFP. However, the total volume of NO-MB was significantly lower than NO-OFP-MB ($p < 0.01$).

Simulations of the gas content and radial changes of a 3.5-µm diameter bubble immersed in air-saturated water are shown in **Figure 5A**. In the first 2 s, NO diffused out of the microbubble,

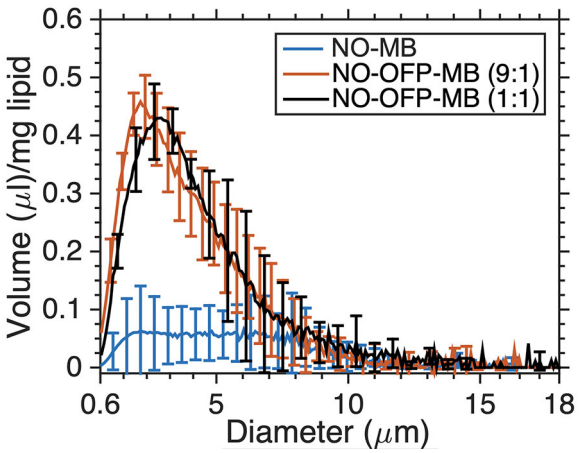

FIGURE 4 | The volume-weighted size distribution of NO-MB and NO-OFP-MB (9:1 v/v and 1:1 v/v). The mean ± 1 standard deviation is depicted (n = 3 per group).

and the radius dropped by 44%. Conversely, oxygen and nitrogen diffused into the microbubble. OFP diffusion is not significant over 30s. **Figure 5B** shows the predicted and measured concentration of NO in a 96-well plate. This predicted drop in NO concentration is higher than the measured values by a factor of approximately 2–3.

DIC images of NO-OFP-MB are shown in **Figure 6**. NO-MB were not visible on the microscope. The NO-OFP-MB 9:1 v/v are both smaller and sparser than the NO-OFP-MB 1:1 v/v. Both agents were polydisperse in size, consistent with the high-shear mixing process of preparation (Borden, 2016).

Figure 7 shows the attenuation coefficient of NO-MB and NO-OFP-MB. The attenuation coefficient of NO-MB was substantially lower than NO-OFP-MB. However, the attenuation coefficient of NO-OFP-MB prepared with the 1:1 and 9:1 v/v ratio of NO and OFP was similar. In **Figure 8** the frequency-dependent attenuation coefficient of NO-OFP-MB 9:1 v/v before and after exposure to B-mode (0.02 MPa peak negative pressure or *in situ* MI of 0.01), and 3-MHz pulsed duplex Doppler ultrasound (2.48 MPa peak negative pressure or *in situ* MI of 1.34), is plotted. The MB retained attenuation after exposure to B-mode ultrasound at an *in situ* MI of 0.01. However, a precipitous loss in attenuation was observed after exposure to pulsed duplex Doppler ultrasound (*in situ* MI of 1.34).

Figure 9 shows the measured concentration of NO in NO-OFP-MB (9:1 and 1:1 v/v) per ml of solution. Water saturated with a combination of NO and OFP either at 1:1 or 9:1 v/v mixture ratio contains 0.96 or 1.72 mM NO at room temperature (Manahan, 2017). The NO dose of NO-OFP-MB 1:1 and 9:1 v/v was 3.1 and 2.8-fold higher than that of water saturated with an equivalent NO and OFP mixture ratio. The NO dose in NO-OFP-MB measured after injection with a 30-G needle was higher than the dose after injection with a 19-G needle for both the 9:1 ($p < 0.01$) and 1:1 NO-OFP payloads. However, the difference for

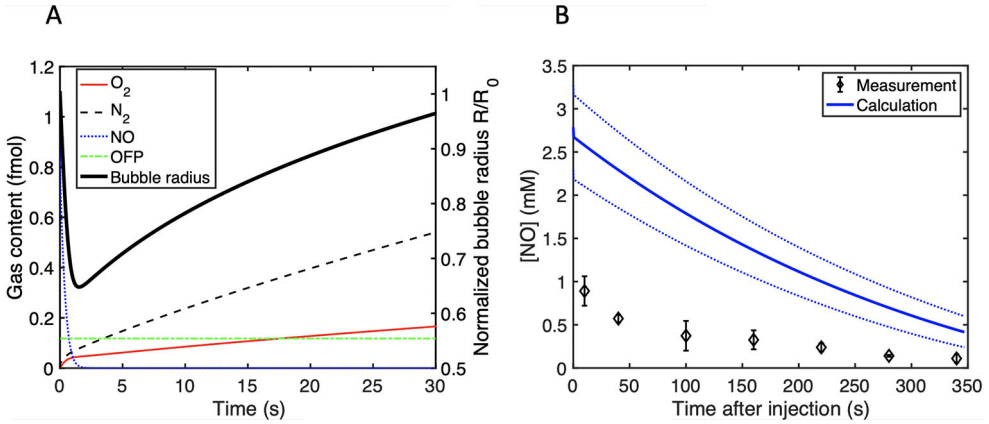

FIGURE 5 | (A) The gas content in femtomoles inside a single 3.5-μm diameter bubble and the normalized radius as a function of time after immersion in air-saturated water. **(B)** Calculation of the time-dependent NO concentration in the 96 well-plate used to assess bactericidal activity. The initial NO concentration was determined from the size measurements. The dotted lines represent the range of the NO concentration calculated based on the standard deviation in the size distribution measurements.

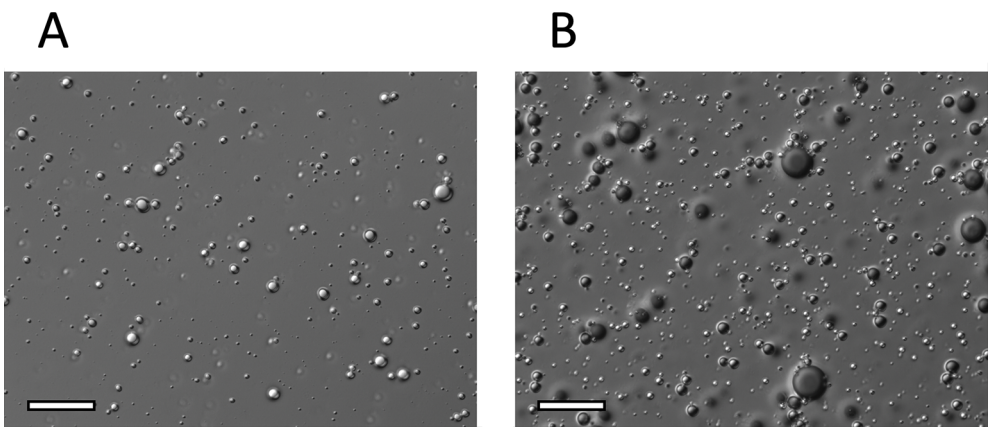

FIGURE 6 | Representative DIC microscopy images (x 63) of **(A)**, NO-OFP-MB 9:1 v/v, and **(B)**, NO-OFP-MB 1:1 v/v. Scale bar = 20 μm. NO-OFP-MB, Nitric oxide and octafluoropropane microbubbles.

the NO-OFP-MB 1:1 v/v was not statistically significant (p = 0.12). For the NO-OFP-MB 9:1 v/v payload, the dose measured with the amperometric microelectrode sensor was 4.78 ± 1.03 mM and that derived from the size measurements was 5.57 ± 0.98 mM. The NO dose for the NO-OFP-MB 9:1 v/v payload measured with the sensor and the NO dose calculated from the size distribution measurements were not significantly different (p = 0.20). For the NO-OFP-MB 1:1 v/v payload, the dose measured with the sensor was 2.96 ± 0.61 mM and the dose derived from the size measurements was 2.02 ± 0.56 mM, which were also not significantly different (p = 0.20).

Figure 10A shows the NO dose in NO-OFP-MB measured at 15 min, 2, 4, or 6 h after activation. No change was observed in the dose over this period, which indicated "in vial" stability of the agent after activation at room temperature. **Figure 9B** shows the concentration of NO measured in air-saturated MH broth between 10 s and 340 s. A drop in the concentration of NO was observed over this period, with a half-life of approximately 50 s.

Figure 11 depicts the viability of *S. aureus* strain USA 300 after exposure to the MB solution, NO-saturated solution, air-OFP-MB 9:1 v/v, or NO-OFP-MB 9:1 v/v. NO-OFP-MB caused a statistically significant decrease in CFU of bacterial cells over air-OFP-MB ($p < 0.05$) and the NO-OFP-saturated solution ($p < 0.05$). There was no noticeable difference between the results of the experiments on three different days.

DISCUSSION

The frequency-dependent attenuation of NO-MB was substantially lower than NO-OFP-MB (**Figures 4** and **7**). Co-

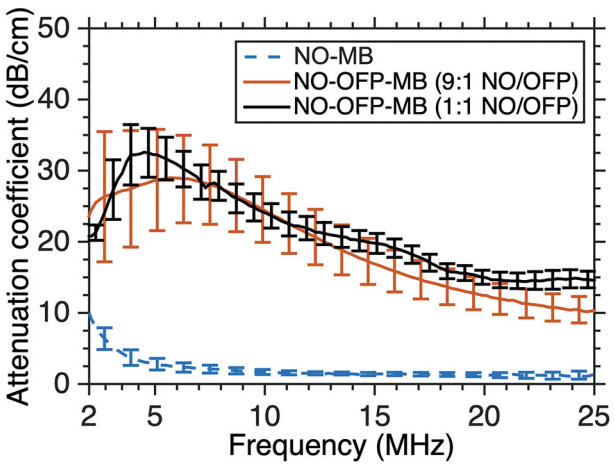

FIGURE 7 | The frequency-dependent attenuation spectra of NO-MB and NO-OFP-MB (9:1 v/v and 1:1 v/v). The mean ± 1 standard deviation is depicted (n = 3 per group). NO-OFP-MB, Nitric oxide and octafluoropropane microbubbles.

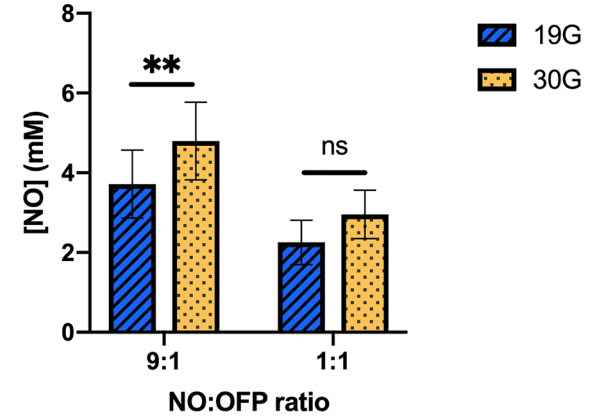

FIGURE 9 | The NO concentration in the NO-OFP-MB (9:1 and 1:1 v/v). The mean ± 1 standard deviation is depicted. n = 9 per group except for 9:1 30-G (n = 10). The symbols 'ns', and '**' represent *p*-values > 0.05, and < 0.01, respectively. NO-OFP-MB, Nitric oxide and octafluoropropane microbubbles. The difference between panel A and B is that A is 9:1 v/v and B is 1:1 v/v. Please change caption to read, "(Panel A: 9:1 v/v, Panel B: 1:1 v/v)".

encapsulation of OFP, a perfluorocarbon gas was postulated to improve the stability of bioactive gas-loaded MB during the high-shear mixing process by allowing unshelled MB to persist until the formation of a lipid shell (Kwan et al., 2012). The osmotic and co-surfactant effect of OFP could be responsible for the enhancement of bubble formation and stability. The attenuation and total volume of NO-OFP-MB 9:1 v/v were similar to that of NO-OFP-MB 1:1 v/v, demonstrating that increasing the relative amount of OFP beyond 10% did not improve the gas loading. Nonetheless, it was demonstrated that the encapsulation of NO and OFP in MB enhanced bioactive gas loading relative to NO- and OFP-saturated solutions.

We have previously reported the ability to show ultrasound-responsive vasodilation in the presence of hemoglobin with NO-loaded cationic MB (or "bubble liposomes") (Sutton et al., 2014). This agent had DPPC as the main lipid constituent. These cationic MB may help adhere to targets such as the vascular endothelium. The release of NO in close proximity to the target can help enhance delivery because NO is scavenged rapidly in the presence of hemoglobin or oxygen. However, cationic MB may also carry a higher risk for detrimental effects such as thrombosis.

In the present study, MB were prepared using DSPC (18-carbon long-chain lipid) as the primary constituent, which may enhance stability over DPPC (Borden and Longo, 2002). DIC images (**Figure 6**) reveal that our manufactured MB have a similar structure as

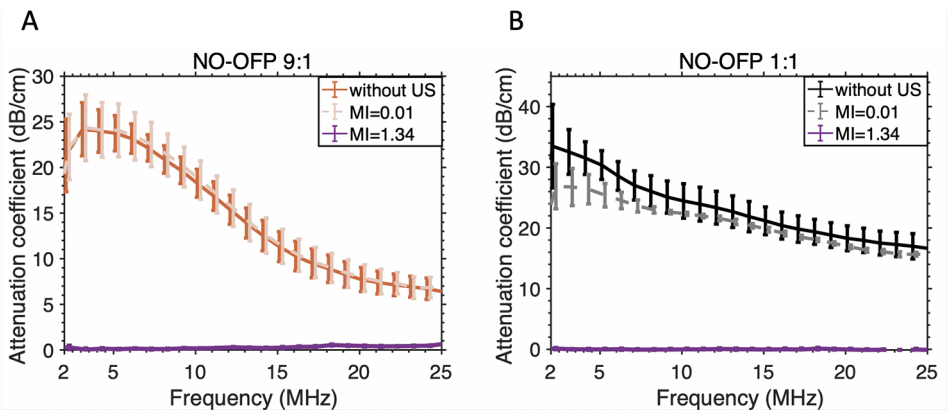

FIGURE 8 | Attenuation-coefficient of NO-OFP-MB [**(A)** 9:1 v/v, **(B)** 1:1v/v] without ultrasound or after exposure to ultrasound at MI=0.01 (used for imaging) or MI=1.34 (ultrasound-triggered gas payload release). The mean ± 1 standard deviation is depicted (n = 3). NO-OFP-MB, Nitric oxide and octafluoropropane microbubbles.

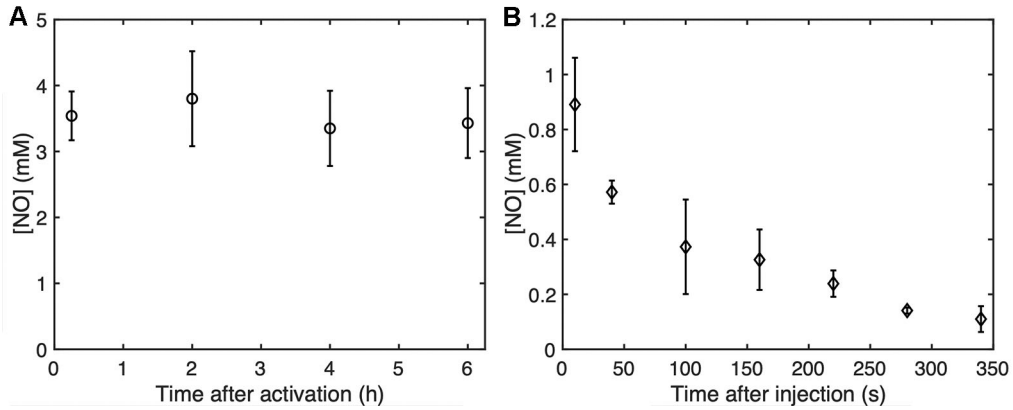

FIGURE 10 | (A) The "in vial" concentration of NO-OFP-MB 9:1 v/v measured up to 6 hours after activation. **(B)** The NO concentration as a function of time up to 340 s after the addition of NO-OFP-MB 9:1 v/v in the 96 well-plate. The mean ± 1 standard deviation is depicted (n = 3 measurements for each time point). NO-OFP-MB, Nitric oxide and octafluoropropane microbubbles.

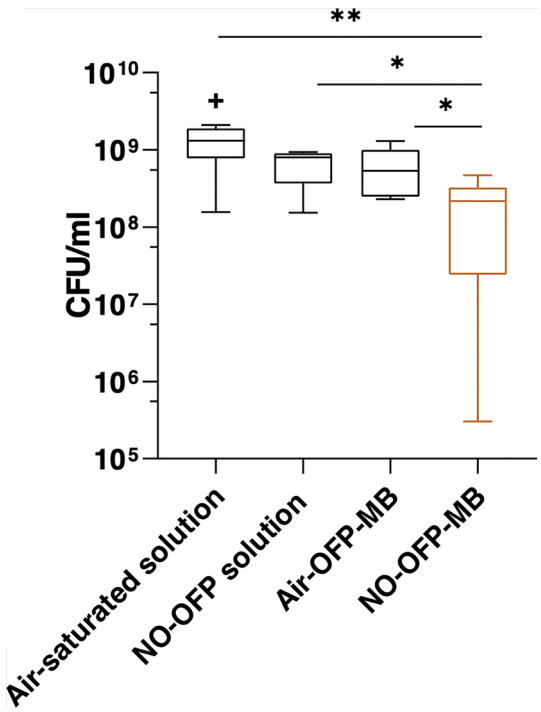

FIGURE 11 | Measurement of bacteria colony forming units (CFU) after treatment with the solvent only (n = 10), NO-OFP-saturated solvent 9:1 v/v, (n = 9), air-OFP-MB 9:1 v/v, (n = 12), and NO-OFP-MB 9:1 v/v, (n = 12). The horizontal lines represent the median, the boxes represent the interquartile range, the whiskers represent 1.5-times the interquartile range. The symbols "*" and "**" represent *p*-values < 0.05, and < 0.01, respectively. The "+" sign represents a data point that lies outside the interquartile range by a factor > 1.5. NO-OFP-MB, Nitric oxide and octafluoropropane microbubbles.

Definity® as previously reported (Shekhar et al., 2019a). A previous study employed the Griess assay in combination with serial dialysis for NO dose assessment within liposomes (Huang et al., 2009). This approach relies on colorimetric quantification of NO degradation products (nitrate and nitrite). This method is precise, but lacks temporal resolution and is based on indirect measurements. Our group has employed vasodilation of a viable artery *ex vivo* to assess the concentration of NO within MB (Sutton et al., 2014). This method has excellent temporal resolution, but lacks quantitative dose assessment. In the present study we used amperometric electrode sensing for direct measurements of NO concentration, which is highly specific to NO but has only moderate temporal resolution, approximately 5 s according to the manufacturer specifications. The dose measured with the NO sensor agreed with that calculated from the size measurement despite the high variability in both of these methods.

In this study, only a fraction of the NO payload was retained within the MB. Recent studies have shown the ability to stabilize bioactive gas payloads by co-encapsulating a small percentage of a perfluorocarbon gas (5%–20%) (Kwan et al., 2012; Yang et al., 2018). There are two main reasons why OFP does not diffuse across the lipid shell rapidly. The first reason is the very low solubility of OFP in water. This characteristic is expressed in Eq. 1 in the form of the Henry's constant. The solubility of OFP is 60-fold lower in water than oxygen and 200-fold lower than NO. This ratio proportionally impacts the quantity of gas escaping the bubble at each iteration of the simulation. Secondly, OFP is a bigger molecule than the other gases modelled. The collision diameter of OFP is twice that of NO or O_2. As described in Eq. 3, the energy barrier created by the lipid layer induces a resistance to diffusion that depends on the exponential of the square of the collision diameter. The difference in collision diameters results in the lipid barrier retarding OFP diffusion by several orders of magnitude compared to smaller gases. However, the efficacy of perfluorocarbon gases for stabilizing payloads may depend on the physical properties of the bioactive gas. Perfluorocarbon gases with higher molecular weights than OFP could also be explored for stabilizing NO payloads.

The lipid-shelled agents used in the present study were pegylated. PEG brushes serve as emulsifying agents, preventing MB aggregation (Chen and Borden, 2010). The presence of PEG has been reported to cause a loss of viability in bacterial culture (Chirife et al., 1983; Nalawade et al., 2015), which could explain the drop in CFU/ml in the air-OFP-MB group relative to the air-saturated solution (**Figure 11**). This decrease was not statistically significant ($p = 0.15$). We hypothesize that the small amount of PEG used in the present formulation was likely not sufficient to have a demonstrable antibacterial effect. Nonetheless, NO-OFP-MB showed a statistically significant enhancement in bactericidal activity beyond both air-OFP-MB and NO-OFP-saturated solution. The variability in the efficacy could be attributed to variability of the fluid mixing inherent to the manual syringe injection of the solution into the well plates, and the variability in NO-loading of the MB (see **Figure 9**). Although the decrease in CFU/ml was modest, the present study provides a proof-of-principle for using NO encapsulated in a lipid-shelled agent for bactericidal applications.

NO is a highly diffusive gas, which makes it challenging to prevent passive release of the gas through a microbubble shell an over extended timescale. In this study, the temporal response of the amperometric microelectrode sensor combined with the time taken to stir the solution was slow (~5–7 s). Therefore, the passive release profile of NO from the agent could not be determined precisely. In addition, the interaction of NO with dissolved oxygen and the rapid degradation of NO made the assessment of the passive release profile challenging. MB stabilized with other types of shell materials, such as polymers (McEwan et al., 2014), dextran (Cavalli et al., 2009a), surfactants (Eisenbrey et al., 2015; Eisenbrey et al., 2018), or chitosan (Cavalli et al., 2009b) shells, may increase the timescale of gas diffusion across the shell, with or without the addition of osmotic gases for payload stabilization. The efficacy and biocompatibility of such agents for encapsulating NO could also be compared to lipid-shelled MB.

In the present study, both the NO dose assessment and bactericidal experiments were performed in an aerobic environment because the antibacterial effect of NO has been reported to require an aerobic environment to form reactive nitrosative and oxidative intermediates (Fang, 1997). However, NO also degrades rapidly following second-order kinetics in the presence of dissolved oxygen to form nitrate and nitrite (Howlin et al., 2017). Therefore, oxygen plays a paradoxical role in NO-mediated bactericidal applications.

NO-OFP-MB were stable inside the vial for at least 6 h after activation (**Figure 10**). After formation of the MB, the vial solution (mixture of PBS, propylene glycol and glycerol) likely became saturated with NO. The NO-saturated environment could have reduced the diffusion gradient and kept the MB stable. If dilution of NO-OFP-MB is required for antibacterial applications, the agent may be diluted in NO and OFP-saturated solutions to keep the agent stable before ultrasound-mediated release. Due to the presence of oxygen in air-saturated media, the concentration of NO in the plate wells decreased rapidly over 340 s. A similar result was obtained by calculating the NO diffusion and scavenging by oxygen in water. The measured NO concentration was lower, which could be due to additional mixing caused by pipetting while transferring the sample from the 96 well-plate to the NO measurement chamber. The bacteria were likely exposed to NO only for a 5–6 min, which could explain why only a modest enhancement in bacterial killing was observed in this study. Note that previous studies have relied on prolonged exposure to NO, albeit at lower concentrations for antibacterial therapy (Barraud et al., 2009; Schairer et al., 2012; Barraud et al., 2014; Howlin et al., 2017).

This study evaluated the antibacterial efficacy on a single *S. aureus* strain, USA 300, which is one of the most common community-associated Methicillin-resistance (MRSA). This organism causes skin and soft issue infections, along with more invasive conditions such as bacteremia, endocarditis, osteomyelitis, and severe necrotizing pneumonia (Tenover and Goering, 2009). Future studies will be needed to evaluate the effect of NO-OFP-MB on other common bacterial strains. Furthermore, bactericidal effects of NO-OFP-MB were evaluated in a planktonic culture. Further research should be conducted to assess this strategy on the dispersal and killing of biofilms. Although we demonstrated a statistically significant enhancement in bacterial killing with respect to air-OFP-MB and NO-OFP-saturated solution, the effect of this therapy on host cells also needs to be evaluated to assess off-target effects. Studies using *in vivo* models should be performed to assess the therapeutic efficacy of NO-OFP-MB. These agents could also be combined with antibiotics (Ren et al., 2016) and other antimicrobial agents (Privett et al., 2010; Worley et al., 2014; Storm et al., 2015) to enhance therapeutic efficacy.

The reduction in ultrasound-triggered attenuation showed the feasibility of releasing the bioactive gas payload by destroying the lipid-shelled MB (**Figure 8**). The rapid release of NO from NO-OFP-MB for over either milliseconds (using ultrasound) or several seconds (passively) at the target site could avoid unwanted systemic effects, such as hypotension, which are a limitation of chemical NO donors. The rapid passive release of NO from lipid-shelled MB is a "double-edged sword" as it dictates that these agents should be delivered in the vicinity of the target using either direct injection or a catheter, but limits potential off-target effects. NO-OFP-MB may be useful for various applications, such as treating infections related to dialysis vascular access (Saeed Abdulrahman et al., 2002), and for infections in the urinary tract (Pietropaolo et al., 2018), in which the target tissue may be easily accessible. The formulation could be delivered directly to the target site using a catheter, and the gas payload released either rapidly using ultrasound, or passively by diffusion. Either a bolus or a diluted bolus in NO-saturated saline could be employed to retard loss of gas due to diffusion before reaching the target. Indwelling catheters could also be treated using this route of administration. NO-OFP-MB could also be used to treat biofilms on infected skin wounds with topical administration along with ultrasound exposure at the site of interest.

In summary, we demonstrated that NO can be loaded into lipid-shelled MB with OFP gas that increased the NO dose relative to NO- and OFP-saturated solutions. The attenuation and total volume of NO-OFP-MB was higher than lipid-shelled bubbles fabricated with NO alone. The feasibility of antibacterial

therapy with NO-OFP-MB against a resistant USA 300 strain was demonstrated. A statistically significant enhancement in bacterial killing over NO-OFP-saturated solution and air-OFP-MB was demonstrated *in vitro* with NO-OFP-MB. These results suggest that lipid-shelled MB loaded with NO and OFP could be useful for bactericidal applications.

DATA AVAILABILITY STATEMENT

The datasets generated for this study are available on request to the corresponding author.

AUTHOR CONTRIBUTIONS

HS, ML, WP, AP, SC, and CM performed experiments and data analysis. ML performed the numerical modeling with CH guidance. CH and DH guided the experimental design. HS and ML wrote the first draft of the manuscript, which was critically revised and approved by all authors.

FUNDING

This work was funded by the U.S. National Institutes of Health, National Institute of Neurological Diseases and Stroke through grant R01 NS047603. DH was supported by ARCH Biopartners, Inc. (Toronto, CA). The funder was not involved in the study design, collection, analysis, interpretation of data, the writing of this article or the decision to submit it for publication.

ACKNOWLEDGMENTS

The authors are grateful to Begona Campos for sharing her expertise on nitric oxide dose measurements in the initial stage of this work. We also acknowledge Profs. Shaoling Huang and Kevin Haworth for the useful suggestions.

REFERENCES

Ahmad, A., Dempsey, S., Daneva, Z., Azam, M., Li, N., Li, P.-L., et al. (2018). Role of nitric oxide in the cardiovascular and renal systems. *Int. J. Mol. Sci.* 19, 2605. doi: 10.3390/ijms19092605

Barraud, N., Schleheck, D., Klebensberger, J., Webb, J. S., Hassett, D. J., Rice, S. A., et al. (2009). Nitric oxide signaling in Pseudomonas aeruginosa Biofilms mediates phosphodiesterase activity, decreased cyclic Di-GMP levels, and enhanced dispersal. *J. Bacteriol.* 191, 7333–7342. doi: 10.1128/JB.00975-09

Barraud, N., Kelso, M., Rice, S., and Kjelleberg, S. (2014). Nitric oxide: a key mediator of biofilm dispersal with applications in infectious diseases. *Curr. Pharm. Des.* 21, 31–42. doi: 10.2174/1381612820666140905112822

Bloch, S., Ichinose, F., Roberts, J. D., and Zapol, W. M. (2007). Inhaled NO as a therapeutic agent. *Cardiovasc. Res.* 75, 339–348. doi: 10.1016/j.cardiores.2007.04.014

Borden, M. A., and Longo, M. L. (2002). Dissolution behavior of lipid monolayer-coated, air-filled microbubbles: effect of lipid hydrophobic chain length. *Langmuir* 18, 9225–9233. doi: 10.1021/la026082h

Borden, M. A. (2016). "Lipid-Coated Nanodrops and Microbubbles," in *Handbook of Ultrasonics and Sonochemistry* (Singapore: Springer Singapore), 1075–1100. doi: 10.1007/978-981-287-278-4_26

Cavalli, R., Bisazza, A., Giustetto, P., Civra, A., Lembo, D., Trotta, G., et al. (2009a). Preparation and characterization of dextran nanobubbles for oxygen delivery. *Int. J. Pharm.* 381, 160–165. doi: 10.1016/J.IJPHARM.2009.07.010

Cavalli, R., Bisazza, A., Rolfo, A., Balbis, S., Madonnaripa, D., Caniggia, I., et al. (2009b). Ultrasound-mediated oxygen delivery from chitosan nanobubbles. *Int. J. Pharm.* 378, 215–217. doi: 10.1016/j.ijpharm.2009.05.058

Chen, C. C., and Borden, M. A. (2010). Ligand conjugation to bimodal Poly (ethylene glycol) brush layers on microbubbles. *Langmuir* 26, 13183–13194. doi: 10.1021/la101796p

Chirife, J., Herszage, L., Joseph, A., Bozzini, J. P., Leardini, N., and Kohn, E. S. (1983). In vitro antibacterial activity of concentrated polyethylene glycol 400 solutions. *Antimicrob. Agents Chemother.* 24, 409–412. doi: 10.1128/aac.24.3.409

Coates, A. R., Halls, G., and Hu, Y. (2011). Novel classes of antibiotics or more of the same? *Br. J. Pharmacol.* 163, 184–194. doi: 10.1111/j.1476-5381.2011.01250.x

Cussler, E. L., and Cussler, E. L. (2009). *Diffusion: mass transfer in fluid systems* (New York, NY: Cambridge University Press).

Eisenbrey, J. R., Albala, L., Kramer, M. R., Daroshefski, N., Brown, D., Liu, J.-B., et al. (2015). Development of an ultrasound sensitive oxygen carrier for oxygen delivery to hypoxic tissue. *Int. J. Pharm.* 478, 361–367. doi: 10.1016/J.IJPHARM.2014.11.023

Eisenbrey, J. R., Shraim, R., Liu, J.-B., Li, J., Stanczak, M., Oeffinger, B., et al. (2018). Sensitization of hypoxic tumors to radiation therapy using ultrasound-sensitive oxygen microbubbles. *Int. J. Radiat. Oncol.* 101, 88–96. doi: 10.1016/J.IJROBP.2018.01.042

Elnaggar, M. A., Subbiah, R., Han, D. K., and Joung, Y. K. (2017). Lipid-based carriers for controlled delivery of nitric oxide. *Expert Opin. Drug Deliv.* 14, 1341–1353. doi: 10.1080/17425247.2017.1285904

Fang, F. C. (1997). Perspectives Series : Host/Pathogen Interactions. *J. Clin. Invest.* 99, 2818–2825. doi: 10.1172/JCI119473

Flaherty, J. T., Magee, P. A., Gardner, T. L., Potter, A., and MacAllister, N. P. (1982). Comparison of intravenous nitroglycerin and sodium nitroprusside for treatment of acute hypertension developing after coronary artery bypass surgery. *Circulation* 65, 1072–1077. doi: 10.1161/01.cir.65.6.1072

Grishenkov, D., Gonon, A., Weitzberg, E., Lundberg, J., Harmark, J., Cerroni, B., et al. (2015). Ultrasound contrast agent loaded with nitric oxide as a theranostic microdevice. *Drug Des. Devel. Ther.* 9, 2409. doi: 10.2147/DDDT.S77790

Howlin, R. P., Cathie, K., Hall-Stoodley, L., Cornelius, V., Duignan, C., Allan, R. N., et al. (2017). Low-dose nitric oxide as targeted anti-biofilm adjunctive therapy to treat chronic Pseudomonas aeruginosa infection in cystic fibrosis. *Mol. Ther.* 25, 2104–2116. doi: 10.1016/j.ymthe.2017.06.021

Huang, S.-L., Kee, P. H., Kim, H., Moody, M. R., Chrzanowski, S. M., MacDonald, R. C., et al. (2009). Nitric oxide-loaded echogenic liposomes for nitric oxide delivery and inhibition of intimal hyperplasia. *J. Am. Coll. Cardiol.* 54, 652–659. doi: 10.1016/j.jacc.2009.04.039

Ichinose, F., Roberts, J. D., and Zapol, W. M. (2004). Inhaled nitric oxide: a selective pulmonary vasodilator: current uses and therapeutic potential. *Circulation* 109, 3106–3111. doi: 10.1161/01.CIR.0000134595.80170.62

Ismail, A. F., Khulbe, K. C., and Matsuura, T. (2015). Gas separation membranes. *Switz. Springer*. doi: 10.1007/978-3-319-01095-3

Kida, K., and Ichinose, F. (2014). Preventing ischemic brain injury after sudden cardiac arrest using NO inhalation. *Crit. Care Lond. Engl.* 18, 212. doi: 10.1186/cc13779

Kim, H., Britton, G. L., Peng, T., Holland, C. K., McPherson, D. D., and Huang, S.-L. (2014). Nitric oxide-loaded echogenic liposomes for treatment of vasospasm following subarachnoid hemorrhage. *Int. J. Nanomed.* 9, 155. doi: 10.2147/IJN.S48856

Kwan, J. J., Kaya, M., Borden, M. A., and Dayton, P. A. (2012). Theranostic oxygen delivery using ultrasound and microbubbles. *Theranostics* 2, 1174–1184. doi: 10.7150/thno.4410

Lee, S. Y., Rim, Y., McPherson, D. D., Huang, S.-L., and Kim, H. (2014). A novel liposomal nanomedicine for nitric oxide delivery and breast cancer treatment. *Biomed. Mater. Eng.* 24, 61–67. doi: 10.3233/BME-130784

Lewis, R. S., and Deen, W. M. (1994). Kinetics of the reaction of nitric oxide with oxygen in aqueous solutions. *Chem. Res. Toxicol.* 7, 568–574. doi: 10.1021/tx00040a013

LuTheryn, G., Glynne-Jones, P., Webb, J. S., and Carugo, D. (2019a). Ultrasound-mediated therapies for the treatment of biofilms in chronic wounds: a review of present knowledge. *Microb. Biotechnol.* doi: 10.1111/1751-7915.13471

LuTheryn, G., Hind, C., Glynne-Jones, P., Webb, J. S., Sutton, J. M., and Carugo, D. (2019b). Ultrasound-responsive bioactive-microbubbles for the eradication of biofilms. *24th Eur. Symp. Ultrasound Contrast Imaging*.

Manahan, S. (2017). *Environmental Chemistry* (CRC Press). doi: 10.1201/9781315160474

McEwan, C., Fowley, C., Nomikou, N., McCaughan, B., McHale, A. P., and Callan, J. F. (2014). Polymeric microbubbles as delivery vehicles for sensitizers in sonodynamic therapy. *Langmuir* 30, 14926–14930. doi: 10.1021/la503929c

Nalawade, T., Sogi, S. H. P., Bhat, K., Bhat, K., Sogi, S. H. P., Sogi, S. H. P., et al. (2015). Bactericidal activity of propylene glycol, glycerine, polyethylene glycol 400, and polyethylene glycol 1000 against selected microorganisms. *J. Int. Soc. Prev. Community Dent.* 5, 114. doi: 10.4103/2231-0762.155736

Nolte, O. (2014). Antimicrobial Resistance in the 21st Century: A Multifaceted Challenge. *Protein Pept. Lett.* 21, 330–335. doi: 10.2174/09298665113206660106

Pietropaolo, A., Jones, P., Moors, M., Birch, B., and Somani, B. K. (2018). Use and effectiveness of antimicrobial intravesical treatment for prophylaxis and treatment of recurrent urinary tract infections (UTIs): a Systematic Review. *Curr. Urol. Rep.* 19, 78. doi: 10.1007/s11934-018-0834-8

Porter, T. M., Smith, D. A. B., and Holland, C. K. (2006). Acoustic techniques for assessing the optison destruction threshold. *J. Ultrasound Med.* 25, 1519–1529. doi: 10.7863/jum.2006.25.12.1519

Postema, M., Bouakaz, A., ten Cate, F. J., Schmitz, G., de Jong, N., and van Wamel, A. (2006). Nitric oxide delivery by ultrasonic cracking: Some limitations. *Ultrasonics* 44, e109–e113. doi: 10.1016/J.ULTRAS.2006.06.003

Privett, B. J., Deupree, S. M., Backlund, C. J., Rao, K. S., Johnson, C. B., Coneski, P. N., et al. (2010). Synergy of Nitric Oxide and Silver Sulfadiazine against Gram-Negative, Gram-Positive, and Antibiotic-Resistant Pathogens. *Mol. Pharm.* 7, 2289–2296. doi: 10.1021/mp100248e

Pu, G., Borden, M. A., and Longo, M. L. (2006). Collapse and shedding transitions in binary lipid monolayers coating microbubbles. *Langmuir* 22, 2993–2999. doi: 10.1021/la0530337

Radhakrishnan, K., Haworth, K. J., Huang, S.-L., Klegerman, M. E., McPherson, D. D., and Holland, C. K. (2012). Stability of echogenic liposomes as a blood pool ultrasound contrast agent in a physiologic flow phantom. *Ultrasound Med. Biol.* 38, 1970–1981. doi: 10.1016/j.ultrasmedbio.2012.06.012

Raymond, J. L., Haworth, K. J., Bader, K. B., Radhakrishnan, K., Griffin, J. K., Huang, S.-L., et al. (2014). Broadband attenuation measurements of phospholipid-shelled ultrasound contrast agents. *Ultrasound Med. Biol.* 40, 410–421. doi: 10.1016/j.ultrasmedbio.2013.09.018

Ren, H., Wu, J., Colletta, A., Meyerhoff, M. E., and Xi, C. (2016). Efficient eradication of mature Pseudomonas aeruginosa biofilm *via* controlled delivery of nitric oxide combined with antimicrobial peptide and antibiotics. *Front. Microbiol.* 7, 1260. doi: 10.3389/fmicb.2016.01260

Robbins, M. E., and Schoenfisch, M. H. (2003). Surface-localized release of nitric oxide *via* Sol- Gel Chemistry. *J. Am. Chem. Soc* 125, 6068–6069. doi: 10.1021/ja034019o

Saeed Abdulrahman, I., Al-Mueilo, S. H., Bokhary, H. A., Ladipo, G. O. A., and Al-Rubaish, A. (2002). A prospective study of hemodialysis access-related bacterial infections. *J. Infect. Chemother.* 8, 242–246. doi: 10.1007/s10156-002-0184-8

Sarkar, K., Katiyar, A., and Jain, P. (2009). Growth and dissolution of an encapsulated contrast microbubble: effects of encapsulation permeability. *Ultrasound Med. Biol.* 35, 1385–1396. doi: 10.1016/j.ultrasmedbio.2009.04.010

Schairer, D. O., Chouake, J. S., Nosanchuk, J. D., and Friedman, A. J. (2012). The potential of nitric oxide releasing therapies as antimicrobial agents. *Virulence* 3, 271–279. doi: 10.4161/viru.20328

Shekhar, H., Smith, N. J., Raymond, J. L., and Holland, C. K. (2018). Effect of Temperature on the Size Distribution, Shell Properties, and Stability of Definity®. *Ultrasound Med. Biol.* 44, 434–446. doi: 10.1016/j.ultrasmedbio.2017.09.021

Shekhar, H., Kleven, R. T., Peng, T., Palaniappan, A., Karani, K. B., Huang, S., et al. (2019a). In vitro characterization of sonothrombolysis and echocontrast agents to treat ischemic stroke. *Sci. Rep.* 9, 1–13. doi: 10.1038/s41598-019-46112-z

Shekhar, H., Palaniappan, A., Peng, T., Lafond, M., Moody, M. R., Haworth, K. J., et al. (2019b). Characterization and imaging of lipid-shelled microbubbles for ultrasound-triggered Release of Xenon. *Neurotherapeutics*, 16, 878–890. doi: 10.1007/s13311-019-00733-4

Siebert, E. M. D., and Knobler, C. M. (1971). Interaction virial coefficients in hydrocarbon-fluorocarbon mixtures. *J. Phys. Chem.* 75, 3863–3870. doi: 10.1021/j100694a014

Storm, W. L., Johnson, J. A., Worley, B. V., Slomberg, D. L., and Schoenfisch, M. H. (2015). Dual action antimicrobial surfaces *via* combined nitric oxide and silver release. *J. Biomed. Mater. Res. A.* 103, 1974–1984. doi: 10.1002/jbm.a.35331

Studenovsky, M., Sivak, L., Sedlacek, O., Konefal, R., Horkova, V., Etrych, T., et al. (2018). Polymer nitric oxide donors potentiate the treatment of experimental solid tumours by increasing drug accumulation in the tumour tissue. *J. Controlled Release* 269, 214–224. doi: 10.1016/j.jconrel.2017.11.017

Sun, B., Slomberg, D. L., Chudasama, S. L., Lu, Y., and Schoenfisch, M. H. (2012). Nitric Oxide-Releasing Dendrimers as Antibacterial Agents. *Biomacromolecules* 13, 3343–3354. doi: 10.1021/bm301109c

Sutton, J. T., Raymond, J. L., Verleye, M. C., Pyne-Geithman, G. J., and Holland, C. K. (2014). Pulsed ultrasound enhances the delivery of nitric oxide from bubble liposomes to ex vivo porcine carotid tissue. *Int. J. Nanomed.* 9, 4671. doi: 10.2147/IJN.S63850

Tacconelli, E., and Pezzani, M. D. (2019). Public health burden of antimicrobial resistance in Europe. *Lancet Infect. Dis.* 19, 4–6. doi: 10.1016/S1473-3099(18)30648-0

Tenover, F. C., and Goering, R. V. (2009). Methicillin-resistant Staphylococcus aureus strain USA300: origin and epidemiology. *J. Antimicrob. Chemother.* 64, 441–446. doi: 10.1093/jac/dkp241

Thunberg, C. A., Morozowich, S. T., and Ramakrishna, H. (2015). Inhaled therapy for the management of perioperative pulmonary hypertension. *Ann. Card. Anaesth.* 18, 394. doi: 10.4103/0971-9784.159811

Tong, J., Ding, J., Shen, X., Chen, L., Bian, Y., Ma, G., et al. (2013). Mesenchymal stem cell transplantation enhancement in myocardial infarction rat model under ultrasound combined with nitric oxide microbubbles. *PloS One* 8, e80186. doi: 10.1371/journal.pone.0080186

van Duin, D., and Paterson, D. L. (2016). Multidrug-resistant bacteria in the community: trends and lessons learned. *Infect. Dis. Clin. North Am.* 30, 377–390. doi: 10.1016/J.IDC.2016.02.004

Ventola, C. L. (2015). The antibiotic resistance crisis: part 1: causes and threats. *P. T. Peer-Rev. J. Formul. Manage.* 40, 277–283.

Wang, C., Yang, F., Xu, Z., Shi, D., Chen, D., Dai, J., et al. (2013). Intravenous release of NO from lipidic microbubbles accelerates deep vein thrombosis resolution in a rat model. *Thromb. Res.* 131, e31–e38. doi: 10.1016/j.thromres.2012.11.002

Wilhelm, E., Battino, R., and Wilcock, R. J. (1977). Low-pressure solubility of gases in liquid water. *Chem. Rev.* 77, 219–262. doi: 10.1021/cr60306a003

Worley, B. V., Slomberg, D. L., and Schoenfisch, M. H. (2014). Nitric Oxide-Releasing Quaternary Ammonium-Modified Poly(amidoamine) Dendrimers as Dual Action Antibacterial Agents. *Bioconjug. Chem.* 25, 918–927. doi: 10.1021/bc5000719

Yang, C., Xiao, H., Sun, Y., Zhu, L., Gao, Y., Kwok, S., et al. (2018). Lipid microbubbles as ultrasound-stimulated oxygen carriers for controllable oxygen release for tumor reoxygenation. *Ultrasound Med. Biol.* 44, 416–425. doi: 10.1016/J.ULTRASMEDBIO.2017.08.1883

Zacharia, I. G., and Deen, W. M. (2005). Diffusivity and Solubility of Nitric Oxide in Water and Saline. *Ann. Biomed. Eng.* 33, 214–222. doi: 10.1007/s10439-005-8980-9

Conflict of Interest: CH, HS, and AP are inventors on a patent application #15788224 entitled "Gas-Encapsulated Acoustically Responsive Stabilized Microbubbles and Methods for Treating Cardiovascular Disease" published on 8th February 2018.

The remaining authors declare that the research was conducted in the absence of any commercial or financial relationships that could be construed as a potential conflict of interest.

frontiers in Pharmacology

REVIEW
published: 31 January 2020
doi: 10.3389/fphar.2019.01650

Ultrasound-Responsive Materials for Drug/Gene Delivery

Xiaowen Cai[1], Yuan Jiang[1], Mei Lin[1], Jiyong Zhang[2], Huanhuan Guo[1], Fanwen Yang[3], Wingnang Leung[4] and Chuanshan Xu[1]**

[1] Key Laboratory of Molecular Target and Clinical Pharmacology, State Key Laboratory of Respiratory Disease, School of Pharmaceutical Sciences & Fifth Affiliated Hospital, Guangzhou Medical University, Guangzhou, China, [2] Department of Pediatrics, Shenzhen Maternity and Child Health Care Hospital, Shenzhen, China, [3] Department of Biomedical Engineering, School of Basic Medical Sciences, Guangzhou Medical University, Guangzhou, China, [4] Asia-Pacific Institute of Aging Studies, Lingnan University, Tuen Mun, Hong Kong, Hong Kong*

Ultrasound is one of the most commonly used methods in the diagnosis and therapy of diseases due to its safety, deep penetration into tissue, and non-invasive nature. In the drug/gene delivery systems, ultrasound shows many advantages in terms of site-specific delivery and spatial release control of drugs/genes and attracts increasing attention. Microbubbles are the most well-known ultrasound-responsive delivery materials. Recently, nanobubbles, droplets, micelles, and nanoliposomes have been developed as novel carriers in this field. Herein, we review advances of novel ultrasound-responsive materials (nanobubbles, droplets, micelles and nanoliposomes) and discuss the challenges of ultrasound-responsive materials in delivery systems to boost the development of ultrasound-responsive materials as delivery carriers.

Keywords: ultrasound-responsive materials, drug, gene, delivery, microbubbles

OPEN ACCESS

Edited by:
Marc Derieppe,
Princess Maxima Center for Pediatric Oncology, Netherlands

Reviewed by:
Christoph Eugen Hagemeyer,
Monash University, Australia
Abdallah El-Sayed Allam,
Tanta University, Egypt
Aditi Jhaveri,
AnTolRx Inc., United States

****Correspondence:***
Chuanshan Xu
xcshan@163.com
Wingnang Leung
awnleung@gmail.com

Specialty section:
This article was submitted to Translational Pharmacology, a section of the journal Frontiers in Pharmacology

Received: *31 July 2019*
Accepted: *16 December 2019*
Published: *31 January 2020*

Citation:
Cai X, Jiang Y, Lin M, Zhang J, Guo H, Yang F, Leung W and Xu C (2020) Ultrasound-Responsive Materials for Drug/Gene Delivery. Front. Pharmacol. 10:1650. doi: 10.3389/fphar.2019.01650

INTRODUCTION

Drugs are important agents for combating the ailments. Drugs are mainly divided into hydrophilic and lipophilic types according to solubility. Hydrophilic drugs, in general, have difficulties entering cells through passive diffusion because cell membranes are composed mainly of lipid bilayers (Thansandote et al., 2015). However, lipophilic drugs are often difficult to dissolve in water and have unsatisfactory bioavailability (Arnott and Planey, 2012). Recently, gene drugs including DNA drugs, RNA drugs have shown promise in treating mutant gene-associated diseases (Kaufmann et al., 2013). Different from chemical drugs, these gene drugs are much larger and have difficulties entering cells. Meanwhile, gene drugs are easily degraded by nucleases in blood stream or cells.

To address the shortcomings of chemical and gene drugs in clinical practices, drug-delivery carriers are used to encapsulate drugs to improve the water solubility of lipophilic drugs, enhance the penetration of hydrophilic drugs into cells, and decrease the side-effect of drugs. For example, the nanoliposomal encapsulation improve the water solubility and bioavailability of hydrophobic polyphenol curcumin (diferuloylmethane) and enhance anticancer activity of curcumin against breast cancer (Hasan et al., 2014). Additionally, delivery systems can also protect gene drugs from degradation by extracellular and intracellular enzymes, and promote therapeutic outcome (Cavalieri et al., 2015).

Advanced drug delivery systems (DDS) require a demand of dosage, spatial, and temporal control strategy (Liu et al., 2016b). Several studies have shown that microspheres and nanoparticles

can protect drugs or genes and further improve therapeutic outcomes (Nakamura and Harashima, 2017; Alkie et al., 2019; Holley et al., 2019; Yu et al., 2019). However, the uncontrolled release of drugs and genes at the disease site is the main limitation of microspheres and nanoparticles.

Since 1978, stimuli-responsive delivery systems have been widely investigated to control release of drugs and genes in targeted sites (Yatvin et al., 1978). Recently, the commonly used stimuli include microenvironment pH and enzymes in target tissues, as well as external stimuli such as photons, electromagnetic, and ultrasound waves. It supplies new perspective for the study of control release of drugs and genes in delivery system. Ultrasound wave is a promising physical stimulus for drug/gene delivery because of its safety, low cost, and portability of ultrasound instrument (Endo-Takahashi et al., 2013).

Ultrasound, including low frequency (<100 kHz) and high frequency (>100 kHz and MHz range) ultrasound (Ji et al., 2018; Matafonova and Batoev, 2019), as one of the most commonly used physical factors has been widely employed in the disease diagnosis and therapy (Witte et al., 2018). Since the mid-1990s, it has been demonstrated that ultrasound can enhance the permeability of agents into living cells (Lentacker et al., 2014). Ultrasound sonication improves the delivery efficiency of drugs/genes mainly through thermal and non-thermal effect (Husseini and Pitt, 2008a; Lentacker et al., 2010; De Temmerman et al., 2011; He et al., 2015; Tardoski et al., 2015; Endo-Takahashi et al., 2016; Liao et al., 2017). The thermal effects are produced from the absorption of acoustic energy in biological tissues. While the non-thermal effects are mainly generated from ultrasound pressure, acoustic streaming, shockwaves, liquid microjet, and ultrasound-induced oscillation or cavitation (Marin et al., 2002; Husseini et al., 2008a; Mannaris et al., 2020). In particular, in the presence of cavitation nuclei, a type of particles which can lower acoustic intensity to induce cavitation, ultrasound shows higher delivery efficiency (Miller et al., 1999; Ward et al., 1999; Peruzzi et al., 2018; Mannaris et al., 2020).

In view of the advantages of cavitation nuclei in ultrasound stimuli, microbubbles as cavitation nuclei have been used widely in ultrasound-mediated drug/gene delivery (Huang et al., 2012; Yan et al., 2015; Oishi et al., 2016; Wang et al., 2016; Zullino et al., 2018). The commonly used microbubbles have gaseous cores and outer shells composed of phospholipids, polymers or proteins. The size of microbubbles (about 1–10 μm) enables them to circulate with red blood cells (Jayaweera et al., 1994; Sirsi and Borden, 2012; Mulvana et al., 2017). Microbubbles, as proven ultrasound-responsive materials, have been applied in drug delivery in clinical trials (**Table 1**) (Hynynen et al., 2001; Dimcevski et al., 2016; He et al., 2016). These clinical trials confirmed the controllability of delivering the cargo like drugs

TABLE 1 | Clinical trials of materials assisting drug delivery under sonication [the datasets for this table can be found in the (ClinicalTrials.gov) (https://clinicaltrials.gov/)].

Materials	NCT number	Cargo	Center frequency	Therapeutic area
Microbubbles	NCT 03458975	Monoclonal antibodies in combination with chemotherapy	Not Provided	Colorectal Cancer, Hepatic Metastases
Microbubbles	NCT 03199274	Perflutren Protein-Type A Microspheres	Not Provided	Hepatocellular Carcinoma, Liver Cancer
Microbubbles	NCT 02233205	platinum and gemcitabine	1.9 MHz	Gastrointestinal Neoplasms
Microbubbles	NCT 01674556	Gemzar	1.9 MHz	Pancreatic Adenocarcinoma
Microbubbles	NCT 01678495	Recombinant tissue plasminogen activator	Not Provided	Cerebrovascular Stroke
Liposomes	NCT 03749850	Lyso-thermosensitive liposomal doxorubicin and Cyclophosphamide	Not Provided	Metastatic Breast Cancer, Breast Cancer Breast, Neoplasms, Stage IV Breast Cancer, Metastatic Cancer, Invasive Ductal Carcinoma of Female Breast, Invasive Ductal Breast Cancer, Adenocarcinoma Breast
Liposomes	NCT 02536183	Lyso-thermosensitive liposomal doxorubicin	Not Provided	Pediatric Cancer, Solid Tumors, Rhabdomyosarcoma, Ewing Sarcoma, Soft Tissue Sarcomas, Osteosarcoma, Neuroblastoma Wilms Tumor, Hepatic Tumor, Germ Cell Tumors
Liposomes	NCT 02181075	Lyso-thermosensitive liposomal (LTSL) doxorubicin	0.96 MHz	Liver Tumor

and gene materials with ultrasonic switch and visualization of treatment. Most noteworthy, many preclinical studies were also under study. Kuo et al. (2019) used doxorubicin-loaded microbubbles in combination with ultrasound (1 MHz) to facilitate the entering of doxorubicin into osteosarcoma cells and exhibited 3.7-fold inhibition of cancer growth compared to doxrubicin-loaded microbubbles without sonication, and simultaneously in combination with contrast-enhanced ultrasound imaging doxorubicin-loaded microbubbles were used to monitor the perfusion and volume of cancer. Lee et al. (2016) delivered miR-29b-3p to enhance fracture healing using ultrasound microbubbles system. Even in articular cartilage to which it is difficult to deliver drugs, ultrasound-responsive microbubbles can also improve the drug delivery efficiency (Nieminen et al., 2017). However, microbubbles have a short circulation time in blood because their sizes restrict their passage through the barrier between blood vessels and targeted tissues. For example, tumor tissues permit only smaller particles (<1 μm) to enter their interior (Zullino et al., 2018). In particular, nanoparticles of size 1–100 nm can have high accumulation in tumor tissues *via* the enhanced permeability and retention (EPR) effect (Maeda, 2001; Baghbani and Moztarzadeh, 2017).

Along with the rapid development of nanomaterials, nanoscale bubbles, droplets, micelles and nanoliposomes have been developed as novel nanomaterials in ultrasound-responsive drug-delivery systems (Ulrich, 2002; Ahmed et al., 2015). Some liposomes have been applied for drug delivery under ultrasound in clinical trials (**Table 1**).

Herein, we will introduce several of the major nanoscale ultrasound-responsive materials used in drug/gene delivery. Furthermore, we will discuss the challenges and the development of ultrasound-responsive materials in drug/gene delivery.

NOVEL ULTRASOUND-RESPONSIVE MATERIALS

Nanobubbles

Nanobubbles are a type of nanoscale bubbles (1–1,000 nm) with gaseous cores and outer shells. As a ultrasound-responsive material, nanobubbles were designed originally as contrast agents to enhance ultrasound imaging, and developed as drug-delivery carriers later (Cavalli et al., 2016).

In tumor tissues, the endothelial gaps range from 380 nm to 780 nm (Hobbs et al., 1998). Microbubbles with the size of 1–10 μm cannot generally extravasate from blood vessels to tumor tissues. However, "leaky" tumor vessels and obstructive lymphatic drainage make nanobubbles with the size of 10–780 nm extravasate through endothelial gaps and accumulate in tumor tissue *via* the EPR effect (Fernandes et al., 2018). Therefore, nanobubbles show great potential in drug/gene delivery for the diagnosis and therapy of cancer because they can accumulate in tumor tissues and interact with tumor cells directly. Upon ultrasound sonication, nanobubble-induced sonoporation on cells can also enhance the efficiency of drug/gene delivery (Xing et al., 2016). As early as 2009, Watanabe et al. (2010) used ultrasound-responsive nanobubbles to control the delivery of gene to skeletal muscle both in BALB/c mice. This is the first report to use isotopic imaging (PET or SPECT) to realize visualization of gene transfection and to provide an easy way to detect the transfection of gene in clinic especially in vascular diseases and muscular dystrophy. Wu et al. (2017a) used poly(lactide-co-glycolic acid) (PLGA) as the shell and octafluoropropane (C_3F_8) gas as core of nanobubbles to load paclitaxel, and further modified them with A10-3.2 aptamer to target prostate cell-specific membrane antigen (PSMA) for therapy of prostate cancer. Under low-frequency ultrasound stimuli, the nanobubble (PTX-A10-3.2-PLGA NB) achieved high drug release that induced significant apoptosis *in vitro* and significant inhibition of growth of tumor cells in BALB/c nude mice with xenograft tumors, and provided biological imaging of prostate-cancer cells. Subsequently in 2018, this research team synthesized cationic nanobubbles (CNBs) with same gas core decorated with A10-3.2 aptamer (siFoxM1-Apt-CNBs) for anti-tumor-targeted delivery of siRNA-FoxM1 (Forkhead box M1) (Wu et al., 2018a). The transfection efficiency of siRNA was improved significantly, whereas FoxM1 expression was reduced significantly after siFoxM1-Apt-CNBs combined with ultrasound stimuli in xenograft tumors in nude mice as well as in PSMA-positive LNCaP cells *in vivo*. These actions led to significant inhibition of tumor growth and prolonged mice survival.

Cai et al. (2018) used C_3F_8 gas as the core and phospholipids as shells to prepare nanobubbles for delivering isocitrate dehydrogenase 1 (IDH1)-siRNA to gliomas. The siRNA-loaded nanobubbles interfered significantly expression of IDH1 *in vitro* and *in vivo* under ultrasound sonication. Shen et al. (2018a) modified ultrasound-mediated resveratrol-embedded nanobubbles containing C_3F_8 core with anti-N-cadherin 2 antibody (which is regarded as a specific binding ligand of nucleus pulposus cells in intervertebral disks) to increase the drug concentration in intervertebral disks for slowing down their degeneration *in vivo*. Song et al. (2018b) developed low-frequency ultrasound-responsive nanobubbles composed of C_3F_8 core and PEGylated lipid shell to deliver a plasmid, the expression vector of brain-derived neurotrophic factor (BDNF) for treating acute injury to the spinal cord, and microtubule-associated protein 2 (MAP-2) antibody to modify the nanobubbles to enhance the targeting. They found that combined treatment of ultrasound and nanobubbles increased BDNF expression significantly *in vitro* and *in vivo*, and improved recovery of spinal-cord injury, indicating that nanobubbles are potential ultrasound-responsive materials in drug/gene delivery. Some other studies are enumerated in **Table 2**.

Droplets

Droplets are especially ultrasound-responsive liquid nanomaterials consisting of volatile perfluorocarbons (PFCs). It can undergo a phase transition through ultrasound-induced acoustic droplet vaporization or heat. After ultrasound stimulation, droplets can expand and convert into nanobubbles. This characteristic feature improves the ultrasonic contrast and triggers the release of loading agents specifically. Moreover droplets are more stable than gas

TABLE 2 | Summaries of the studies on ultrasound-responsive nanobubbles.

Core	Shell	Cargo	Ultrasonic frequency	Therapeutic area	Study
Gas-generating calcium carbonate	PEG-PAsp	Doxorubicin	40 MHz	Squamous Cell Carcinoma	(Min et al., 2015)
C_3F_8	Herceptin-PEGylated phospholipid-shell	No cargo	5–12 MHz	Her-2-positive Breast Cancers	(Jiang et al., 2016)
CF_4	PLGA	Doxorubicin	1 MHz	VX2 Liver Tumor	(Meng et al., 2016)
C_3F_8	Herceptin-PEG-PLGA	Paclitaxel	1 MHz and 40 MHz	Breast Cancer	(Song et al., 2017)
C_5F_{12}	Glycine/PEG/RGD-modified poly(methacrylic acid)	Doxorubicin	Not Provided	Liver Tumor	(Li et al., 2017)
Oxygen	Sodium carboxymethylcellulose	Mitomycin-C	40 MHz	Bladder Cancer	(Bhandari et al., 2018)
C_3F_8 + UCNP–CN	DPPC, DSPE-PEG2k and DPPA	Doxorubicin	7 MHz	Tongue Squamous Carcinoma	(Chan et al., 2018)
C_3F_8	Mix of DPPC and DPPA	pc DNA3.1(+)/PNP plasmid	1.3 MHz	Hepatocellular Carcinoma	(Zhang et al., 2018a)
C_3F_8	Folate-conjugated N-palmitoyl chitosan	No cargo	7 MHz	Oral Epidermoid Cancer Cells, Cervical Cancer, Lung Cancer	(Shen et al., 2018b)
C_3F_8	Mix DSPC, DSPE-PEG2000 and DSPE-PEG2000-biotin	Apatinib	1 MHz	Liver Tumor	(Tian et al., 2018)
$C_5H_2F_{10}$	Polymer shell composing of chitosan and lecithin	Paclitaxel and survivin inhibitor sepantronium bromide	3 MHz	Lung Cancer	(Baspinar et al., 2019)
C_3F_8	PLA-PEG-NH_2	No cargo	9.0 MHz	Breast Cancer	(Shang et al., 2019)
1% CO_2	Protein	The pEGFP and pCMV-Luc reporter plasmids	18 MHz	Breast Cancer	(Tayier et al., 2019)

bubbles in blood circulation at 37°C because droplets maintain their liquid core in the circulation avoiding gas dissolution (Lanza and Wickline, 2001; Lea-Banks et al., 2019). Stable PFC emulsions, commonly used droplets, can be prepared to ~200 nm in diameter (Fabiilli et al., 2010), which is beneficial for circulating for a longer time *in vivo*, passing into tissues or cells, and enhancing the EPR effect (Shpak et al., 2016). More interestingly, Lattin et al. (2015) supposed that the disruption of droplets may break down the membrane of endosome to aid the escape from the endosome endocytosis pathway of macromolecules such as genes. Their findings provide a new strategy for delivering therapeutic agents especially large molecules like genes upon ultrasound sonication.

Droplets, in general, are used to load lipophilic drugs, such as 10-hydroxycamptothecin (HCPT). HCPT is an efficacious anticancer drug but has limited clinical application due to its poor hydrophilicity. Encapsulation of lipophilic materials could improve the therapeutic efficacy of HCPT against cancer (Zhang et al., 2008; Li et al., 2012; Yang et al., 2013; Liu et al., 2015; Liu et al., 2016a). Based on this information, Liu et al. (2018) prepared an ultrasound-responsive droplet consisting of four parts: folic acid (FA) for overexpression of FA receptors on cancer cell membranes; superparamagnetic Fe_3O_4 for imaging; HCPT for cancer treatment; a PFC as the droplet core. The PFC core could undergo droplet vaporization upon sonication to cause HCPT release and enhance ultrasound imaging.

Rapoport et al. (2011) developed a novel nanoemulsion containing a perfluoro-15-crown-5-ether (PFCE) core with good stability and reversible transition from droplet to bubble. Moreover, the novel nanoemulsions could realize ultrasound and ^{19}Flourine magnetic resonance dual-mode imaging, and enhance the inhibitory efficiency of paclitaxel-loaded nanoemulsions on the growth and metastasis of breast and pancreatic cancer cells in mice.

Doplets were also investigated in the application of brain diseases. Chen et al. (2013) compared the safety of microbubbles and droplets for drug delivery to the brain under focused ultrasound. In their studies, the same lipid compositions were used as the outer shells of microbubbles and droplets: perfluorobutane as the microbubble core and PFC as the droplet core. The cavitation induced by droplets required a higher threshold and droplets could deliver the drug more safely and more effectively than microbubbles in the brain. In 2018, another study on the delivery of biomolecules into the brain using droplets was published by colleagues in the team (Wu et al., 2018a). These findings demonstrated that ultrasound droplet-mediated delivery was a novel approach to deliver drug/gene into the brain effectively. Other up-to-date researches are listed in **Table 3**.

Micelles

Micelles are, in general, generated through self-assembly of polymers containing a hydrophilic group and a hydrophobic alkane (Husseini et al., 2007). Moreover, the diameters of micelles, which range from 10 nm to 100 nm, will help their application in nanoformulations (Husseini and Pitt, 2008b; Xia et al., 2016). Amphiphilic structures enable hydrophilic drugs and hydrophobic drugs to be encapsulated readily in micelles. The moderate thermal effect induced by ultrasound can increase the cell membrane penetrability resulting in enhancing extravasation in targeted cells (Rapoport, 2012). And increasing evidence has shown that micelles can be destroyed

TABLE 3 | Summaries of the studies on ultrasound-responsive droplets.

Core	Shell	Cargo	Ultrasonic frequency	Therapeutic area	Study
C_6F_{14}	Alginate	Doxorubicin and curcumin	28 k Hz and 1 MHz	Multidrug Resistant Ovarian Cancer	(Baghbani and Moztarzadeh, 2017)
C_5F_{12}	PLGA	Cetuximab and 10-Hydroxycamptothecin	1 MHz	Anaplastic Thyroid Carcinoma	(Wang et al., 2018)
C_9F_{20}	Mix of DSPC and mPEG-DSPE	Lidocaine	2.25 MHz	Acute and Chronic Pain	(Soto et al., 2018)
C_5F_{12}	Perylene diimide	$ZnF_{16}Pc$	40 MHz	Malignant Glioblastoma	(Tang et al., 2018)
C_6F_{14}	Phosphatidyl ethanolamine	Ce6	1 MHz	Breast Cancer	(Yu et al., 2018)
C_3F_8	Mix of DSPE-PEG3400-t Ly P-1, DPPG, DPPC, and cholesterol	10-Hydroxycamptothecin	1 MHz	Breast Cancer	(Zhu et al., 2018)
C_5F_{12}	Mix of POPC, POPE, cholesterol, and DSPE-PEG-2000	Camptothecin	2 MHz	Melanoma	(Ho et al., 2018)
C_5F_{12}	Mix of DPPC, DSPE-m PEG2000, cholesterol	IR780	650 k Hz for treatment, 12 MHz for imaging	Breast Cancer	(Zhang et al., 2019)
C_6F_{14}	O-carboxymethyl chitosan	Doxorubicin	9.0 MHz	Prostatic Cancer	(Meng et al., 2019)
C_7F_{16}	Pluronic F68	Basic fibroblast growth factor	2.5 MHz	Ischemic Cardiovascular Diseases	(Dong et al., 2019)
C_6F_{14}	Polydopamine	No cargo	7.5 MHz	Breast Cancer	(Mannaris et al., 2020)

under shockwaves produced by ultrasound to release cargo loaded in micelles and deliver them to target tissues (Ahmed et al., 2015). Ultrasound-responsive micelles not only achieve the control of space release but also the quantity of release, since they can reassemble again when the ultrasound shuts off (Husseini et al., 2002; Tanbour et al., 2016). Hence, micelles are also potential materials for ultrasound-responsive delivery.

As early as in 2006, Chen et al. (2006) prepared micelles composed of three kinds of pluronics, F127, L61 and P85 as gene-delivery carriers under sonication. They found that, upon sonication, these three types of micelles enhanced the efficiency of gene transfection in 3T3-MDEI, C2C12, and CHO cell lines. Later, Wu et al. (2017b) developed a mixed micelle of pluronic P123/F127 polymers to encapsulate curcumin. They showed that curcumin was released at specific sites under ultrasound sonication, and that sonication increased cellular uptake of curcumin compared with that using free curcumin. *In vitro*, curcumin released from micelles increased along with increasing ultrasound intensity. Furthermore, curcumin-loaded micelles decreased the tumor weight by ~6.5-fold upon ultrasound sonication compared with the group without sonication exposure. Kang et al. (2019) studied doxorubicin (DOX) release with the help of high-intensity focused ultrasound (HIFU). The center frequency of the pre-clinical HIFU system they used was 1.5 MHz. Under high-intensity focused ultrasound, the structure of micelles loaded with DOX and hydrophobic 1,3-bis-(2,4,6-trimethylpheny l) imidazolylidene nitric oxide (IMesNO, a donor of nitric oxide, NO) was destroyed, and IMesNO was released from the micelles to produce NO. In cancer tissues, NO improved the EPR effect by expanding cancer blood vessels to increase blood blow, and subsequently enhanced the anticancer effect of DOX.

Nanoliposomes

Liposomes show excellent biocompatibility because they consist primarily of lipid bilayers (Schroeder et al., 2009). Liposomes can often load hydrophilic molecules and lipophilic molecules to improve their pharmacokinetics and reduce systemic toxicity (Torchilin, 2005; Allen and Cullis, 2013). Recently, accelerating evidence shows that nanoliposomes can deliver and release drugs/genes in target tissues upon ultrasound sonication (Dromi et al., 2007; Mannaris et al., 2013; Ta et al., 2014; Lyon et al., 2017). In general, nanoliposomes do not contain gas, so they are not particularly responsive to ultrasound. To achieve a particular response to ultrasound, nanoliposomes can be designed to contain vapor-phase molecules or encapsulated emulsions that can vaporize under ultrasound (Huang, 2008; Geers et al., 2012). When being exposed to ultrasound, cavitation or thermal effects can increase the release of drug/gene-loaded in nanoliposomes. Usually under sonication at high frequency, thermal effect takes the main role of delivery process. While under low frequency, cavitation plays an important role (Huang and MacDonald, 2004; Kopechek et al., 2008; Smith et al., 2010; Lattin et al., 2012).

To improve the targeting ability of ultrasound-responsive nanoliposomes, Negishi et al. (2013) used an AG73 peptide targeting syndecan (which is highly expressed in neovascular vessels) to modify liposomes with a perfluoropropane core. This AG73 peptide-modification endowed liposomes with a perfluoropropane core to have good targeting ability to tumor cells and deliver plasmids to them effectively. In 2018, a new liposome-encapsulating gas, phosphorodiamidate morpholino oligomer, was used to induce antisense oligonucleotide-mediated "exon skipping" for treating Duchenne muscular dystrophy (Negishi et al., 2018). This new liposome could deliver the antisense oligonucleotide to diseased muscles and release it upon ultrasound sonication.

Nowadays, a mixture of liposomes and microbubbles termed a "liposome–microbubble complex" (LMC) has been reported. The LMC has the high drug-loading ability of liposomes and ultrasound-responsive property of microbubbles. Zhang et al. (2018b) fabricated a LMC as a drug vehicle to deliver paclitaxel. To overcome the disadvantage that LMC was effective *in vitro* but not *in vivo*, they used iRGD peptide, a nine-unit cyclic

tumor-homing and tissue-penetrating peptide, to modify the LMC to achieve better permeability into blood vessels and tissues in a tumor-specific manner. This modified LMC showed higher toxicity to 4T1 breast cancer cells and antitumor efficacy in a subcutaneous tumor model.

CHALLENGES

Ultrasound-responsive material-based drug/gene delivery has been explored widely in treating cancer (Khokhlova et al., 2015; Qin et al., 2016; Fan et al., 2017; Yue et al., 2018; Jing et al., 2019), cardiovascular diseases (Hua et al., 2014; Dixon et al., 2015; Castle and Feinstein, 2016), orthopedic diseases (Le et al., 2016; Pullan et al., 2017; Kuo et al., 2019), ocular diseases (Aptel and Lafon, 2012; Wan et al., 2015a; Wan et al., 2015b; Lafond et al., 2017) and brain diseases (Timbie et al., 2015; Song et al., 2018a), and also applied in vaccine immunization (Tachibana et al., 1997; Escoffre et al., 2016). However, application of ultrasound-responsive materials in drug/gene delivery faces certain challenges.

First, the prerequisite for treating diseases is a sufficient amount of drug/gene delivered and released in diseased tissues. Most ultrasound-responsive materials need an ultrasound-responsive core (gaseous, PFC, or gas-generating). These ultrasound-responsive cores consume a lot of space in ultrasound-responsive materials (microbubbles, nanobubbles, or droplets), which makes lower drug/gene-loaded contents, and decrease the amount of drug/gene delivered to diseased tissues, and eventually lead to limited therapeutic efficacy (Klibanov et al., 2010; Fabiilli et al., 2010; Shende and Jain, 2019). Second, nanoscale ultrasound-responsive materials have advantages over microbubbles with regard to targeted delivery of drugs and genes, but these nanomaterials are less responsive than microbubbles (Sirsi and Borden, 2014). So nanomaterials require higher ultrasound intensity to induce cavitation for effective release of drugs/genes from nanomaterials. But ultrasound of high intensity can cause damage to neighboring healthy tissues. High-intensity ultrasound also induces the rapid collapse of bubbles and rapid release of the drug/gene loaded in the bubbles, which may not meet the need for sustained release of some drugs (e.g., insulin).

The last but not the least, ultrasonic parameters are still noticeable issues. Low- and high-frequency ultrasound can damage biologic tissues when sonication-induced heating is too high, and the pore formation on cell membranes is irreversible (Mehier-Humbert et al., 2005). Therefore, the intensity and duration of ultrasound sonication must be controlled. Kovacs et al. (2017) found that pulsed-focused ultrasound induced the opening of the blood–brain barrier and was accompanied by increased expression of heat-shock protein 70, interleukin-1, interleukin-18, tumor necrosis factor-α, and inflammation of brain tissues, suggesting that application of ultrasound-responsive materials in drug/gene delivery to the brain system should be done with extreme caution.

CONCLUSIONS

Ultrasound-responsive materials can deliver drugs/genes to targeted tissues, and induce the release of drugs/genes in specific sites upon ultrasound sonication. However, most evidence has arisen from *in vitro* and *in vivo* animal experiments. Few clinical trials have investigated the role of ultrasound-responsive materials in drug/gene delivery. Thus, more clinical trials should be conducted to confirm the outlook of ultrasound-responsive materials in drug/gene delivery.

Recent studies have revealed that the major reason limiting application of ultrasound-responsive materials is their low drug/gene-loaded content. Enhancing the drug/gene-loaded content in ultrasound-responsive materials will be a "hotspot" for clinical translation of ultrasound-responsive materials.

In addition, sonoporation is regarded to be the main reason that ultrasound-responsive materials enhance the release of loaded drugs/genes. However, the interaction of ultrasound and ultrasound-responsive materials is complicated, and can induce mechanical forces, sonoporation, heating, and sonochemical effects. Therefore, better understanding of how ultrasound-responsive materials enhance release of loaded drugs/genes will lay a solid foundation to boost development of ultrasound-responsive materials in drug/gene delivery.

DATA AVAILABILITY STATEMENT

The datasets generated for this study can be found in the ClinicalTrials.gov database (https://clinicaltrials.gov/).

AUTHOR CONTRIBUTIONS

XC, YJ, and CX contributed to the conception and design of the study. XC wrote the first draft of the manuscript. YJ wrote sections of the manuscript. All authors contributed to manuscript revision and approved the submitted version.

FUNDING

This work was supported by the Fund of Talents for High-level University in the Construction of Guangzhou (B195002009025) and the Science and Technology Project of Guangdong Province (2017B090911012).

ACKNOWLEDGMENTS

We express our sincere gratitude to Dr. Qicai Xiao for the helpful assistance.

REFERENCES

Ahmed, S. E., Martins, A. M., and Husseini, G. A. (2015). The use of ultrasound to release chemotherapeutic drugs from micelles and liposomes. *J. Drug Targeting* 23, 16–42. doi: 10.3109/1061186X.2014.954119

Alkie, T. N., de Jong, J., Jenik, K., Klinger, K. M., and DeWitte-Orr, S. J. (2019). Enhancing innate antiviral immune responses in rainbow trout by double stranded RNA delivered with cationic phytoglycogen nanoparticles. *Sci. Rep.* 9, 13619. doi: 10.1038/s41598-019-49931-2

Allen, T. M., and Cullis, P. R. (2013). Liposomal drug delivery systems: from concept to clinical applications. *Adv. Drug Deliv. Rev.* 65, 36–48. doi: 10.1016/j.addr.2012.09.037

Amani, A., Kabiri, T., Shafiee, S., and Hamidi, A. (2019). Preparation and characterization of PLA-PEG-PLA/PEI/DNA nanoparticles for improvement of transfection efficiency and controlled release of DNA in gene delivery systems. *Iran. J. Pharm. Res.* 18, 125–141.

Aptel, F., and Lafon, C. (2012). Therapeutic applications of ultrasound in ophthalmology. *Int. J. Hyperthermia* 28, 405–418. doi: 10.3109/02656736.2012.665566

Arnott, J. A., and Planey, S. L. (2012). The influence of lipophilicity in drug discovery and design. *Expert Opin. Drug Discovery* 7, 863–875. doi: 10.1517/17460441.2012.714363

Baghbani, F., and Moztarzadeh, F. (2017). Bypassing multidrug resistant ovarian cancer using ultrasound responsive doxorubicin/curcumin co-deliver alginate nanodroplets. *Colloids Surf. B Biointerfaces* 153, 132–140. doi: 10.1016/j.colsurfb.2017.01.051

Baspinar, Y., Erel-Akbaba, G., Kotmakci, M., and Akbaba, H. (2019). Development and characterization of nanobubbles containing paclitaxel and survivin inhibitor YM155 against lung cancer. *Int. J. Pharm.* 566, 149–156. doi: 10.1016/j.ijpharm.2019.05.039

Bhandari, P., Novikova, G., Goergen, C. J., and Irudayaraj, J. (2018). Ultrasound beam steering of oxygen nanobubbles for enhanced bladder cancer therapy. *Sci. Rep.* 8, 3112. doi: 10.1038/s41598-018-20363-8

Cai, W., Lv, W., Feng, Y., Yang, H., Zhang, Y., Yang, G., et al. (2018). The therapeutic effect in gliomas of nanobubbles carrying siRNA combined with ultrasound-targeted destruction. *Int. J. Nanomed.* 13, 6791–6807. doi: 10.2147/IJN.S164760

Castle, J., and Feinstein, S. B. (2016). Drug and gene delivery using sonoporation for cardiovascular disease. *Adv. Exp. Med. Biol.* 880, 331. doi: 10.1007/978-3-319-22536-4_18

Cavalieri, F., Beretta, G. L., Cui, J., Braunger, J. A., Yan, Y., Richardson, J. J., et al. (2015). Redox-sensitive PEG-polypeptide nanoporous particles for survivin silencing in prostate cancer cells. *Biomacromolecules* 16, 2168–2178. doi: 10.1021/acs.biomac.5b00562

Cavalli, R., Soster, M., and Argenziano, M. (2016). Nanobubbles: a promising efficient tool for therapeutic delivery. *Ther. Deliv.* 7, 117–138. doi: 10.4155/tde.15.92

Chan, M. H., Pan, Y. T., Chan, Y. C., Hsiao, M., Chen, C. H., Sun, L., et al. (2018). Nanobubble-embedded inorganic 808 nm excited upconversion nanocomposites for tumor multiple imaging and treatment. *Chem. Sci.* 9, 3141–3151. doi: 10.1039/c8sc00108a

Chen, Y. C., Liang, H. D., Zhang, Q. P., Blomley, M. J., and Lu, Q. L. (2006). Pluronic block copolymers: novel functions in ultrasound-mediated gene transfer and against cell damage. *Ultrasound Med. Biol.* 32, 131–137. doi: 10.1016/j.ultrasmedbio.2005.10.002

Chen, C. C., Sheeran, P. S., Wu, S. Y., Olumolade, O. O., Dayton, P. A., and Konofagou, E. E. (2013). Targeted drug delivery with focused ultrasound-induced blood-brain barrier opening using acoustically-activated nanodroplets. *J. Control. Release* 172, 795–804. doi: 10.1016/j.jconrel.2013.09.025

De Temmerman, M. L., Dewitte, H., Vandenbroucke, R. E., Lucas, B., Libert, C., Demeester, J., et al. (2011). mRNA-Lipoplex loaded microbubble contrast agents for ultrasound-assisted transfection of dendritic cells. *Biomaterials* 32, 9128–9135. doi: 10.1016/j.biomaterials.2011.08.024

Dimcevski, G., Kotopoulis, S., Bjanes, T., Hoem, D., Schjott, J., Gjertsen, B. T., et al. (2016). A human clinical trial using ultrasound and microbubbles to enhance gemcitabine treatment of inoperable pancreatic cancer. *J. Control. Release* 243, 172–181. doi: 10.1016/j.jconrel.2016.10.007

Dixon, A. J., Kilroy, J. P., Dhanaliwala, A. H., Chen, J. L., Phillips, L. C., Ragosta, M., et al. (2015). Microbubble-mediated intravascular ultrasound imaging and drug delivery. *IEEE Trans. Ultrason. Ferroelectr. Freq. Control* 62, 1674–1685. doi: 10.1109/TUFFC.2015.007143

Dong, X., Lu, X., Kingston, K., Brewer, E., Juliar, B. A., Kripfgans, O. D., et al. (2019). Controlled delivery of basic fibroblast growth factor (bFGF) using acoustic droplet vaporization stimulates endothelial network formation. *Acta Biomater.* 97, 409–419. doi: 10.1016/j.actbio.2019.08.016

Dromi, S., Frenkel, V., Luk, A., Traughber, B., Angstadt, M., Bur, M., et al. (2007). Pulsed-high intensity focused ultrasound and low temperature-sensitive liposomes for enhanced targeted drug delivery and antitumor effect. *Clin. Cancer Res.* 13, 2722–2727. doi: 10.1158/1078-0432.CCR-06-2443

Endo-Takahashi, Y., Negishi, Y., Nakamura, A., Suzuki, D., Ukai, S., Sugimoto, K., et al. (2013). pDNA-loaded bubble liposomes as potential ultrasound imaging and gene delivery agents. *Biomaterials* 34, 2807–2813. doi: 10.1016/j.biomaterials.2012.12.018

Endo-Takahashi, Y., Negishi, Y., Suzuki, R., Maruyama, K., and Aramaki, Y. (2016). MicroRNA imaging in combination with diagnostic ultrasound and bubble liposomes for microRNA delivery. *Methods Mol. Biol.* 1372, 209–213. doi: 10.1007/978-1-4939-3148-4_16

Escoffre, J. M., Deckers, R., Bos, C., and Moonen, C. (2016). Bubble-assisted ultrasound: application in immunotherapy and vaccination. *Adv. Exp. Med. Biol.* 880, 243–261. doi: 10.1007/978-3-319-22536-4_14

Fabiilli, M. L., Haworth, K. J., Sebastian, I. E., Kripfgans, O. D., Carson, P. L., and Fowlkes, J. B. (2010). Delivery of chlorambucil using an acoustically-triggered perfluoropentane emulsion. *Ultrasound Med. Biol.* 36, 1364–1375. doi: 10.1016/j.ultrasmedbio.2010.04.019

Fan, P., Zhang, Y., Guo, X., Cai, C., Wang, M., Yang, D., et al. (2017). Cell-cycle-specific cellular responses to sonoporation. *Theranostics* 7, 4894–4908. doi: 10.7150/thno.20820

Fernandes, C., Suares, D., and Yergeri, M. C. (2018). Tumor microenvironment targeted nanotherapy. *Front. Pharmacol.* 9, 1230. doi: 10.3389/fphar.2018.01230

Geers, B., Dewitte, H., De Smedt, S. C., and Lentacker, I. (2012). Crucial factors and emerging concepts in ultrasound-triggered drug delivery. *J. Control. Release* 164, 248–255. doi: 10.1016/j.jconrel.2012.08.014

Hasan, M., Belhaj, N., Benachour, H., Barberi-Heyob, M., Kahn, C. J., Jabbari, E., et al. (2014). Liposome encapsulation of curcumin: physico-chemical characterizations and effects on MCF7 cancer cell proliferation. *Int. J. Pharm.* 461, 519–528. doi: 10.1016/j.ijpharm.2013.12.007

He, Y., Bi, Y., Ji, X. J., and Wei, G. (2015). Increased efficiency of testicular tumor chemotherapy by ultrasound microbubble-mediated targeted transfection of siMDR1. *Oncol. Rep.* 34, 2311–2318. doi: 10.3892/or.2015.4262

He, X., Wu, D. F., Ji, J., Ling, W. P., Chen, X. L., and Chen, Y. X. (2016). Ultrasound microbubble-carried PNA targeting to c-myc mRNA inhibits the proliferation of rabbit iliac arterious smooth muscle cells and intimal hyperplasia. *Drug Deliv.* 23, 2482–2487. doi: 10.3109/10717544.2015.1014947

Ho, Y. J., Chiang, Y. J., Kang, S. T., Fan, C. H., and Yeh, C. K. (2018). Camptothecin-loaded fusogenic nanodroplets as ultrasound theranostic agent in stem cell-mediated drug-delivery system. *J. Control. Release* 278, 100–109. doi: 10.1016/j.jconrel.2018.04.001

Hobbs, S. K., Monsky, W. L., Yuan, F., Roberts, W. G., Griffith, L., Torchilin, V. P., et al. (1998). Regulation of transport pathways in tumor vessels: role of tumor type and microenvironment. *Proc. Natl. Acad. Sci. U. S. A.* 95, 4607–4612. doi: 10.1073/pnas.95.8.4607

Holley, C. K., Kang, Y. J., Kuo, C. F., Abidian, M. R., and Majd, S. (2019). Development and *in vitro* assessment of an anti-tumor nano-formulation. *Colloids Surf. B Biointerfaces* 184, 110481. doi: 10.1016/j.colsurfb.2019.110481

Hua, X., Zhou, L., Liu, P., He, Y., Tan, K., Chen, Q., et al. (2014). In vivo thrombolysis with targeted microbubbles loading tissue plasminogen activator in a rabbit femoral artery thrombus model. *J. Thromb. Thromb.* 38, 57–64. doi: 10.1007/s11239-014-1071-8

Huang, S. L., and MacDonald, R. C. (2004). Acoustically active liposomes for drug encapsulation and ultrasound-triggered release. *Biochim. Biophys. Acta* 1665, 134–141. doi: 10.1016/j.bbamem.2004.07.003

Huang, Q., Deng, J., Wang, F., Chen, S., Liu, Y., Wang, Z., et al. (2012). Targeted gene delivery to the mouse brain by MRI-guided focused ultrasound-induced blood-brain barrier disruption. *Exp. Neurol.* 233, 350–356. doi: 10.1016/j.expneurol.2011.10.027

Huang, S. L. (2008). Liposomes in ultrasonic drug and gene delivery. *Adv. Drug Deliv. Rev.* 60, 1167–1176. doi: 10.1016/j.addr.2008.03.003

Husseini, G. A., and Pitt, W. G. (2008a). Micelles and nanoparticles for ultrasonic drug and gene delivery. *Adv. Drug Delivery Rev.* 60, 1137–1152. doi: 10.1016/j.addr.2008.03.008

Husseini, G. A., and Pitt, W. G. (2008b). The use of ultrasound and micelles in cancer treatment. *J. Nanosci. Nanotechnol.* 8, 2205–2215. doi: 10.1166/jnn.2008.225

Husseini, G. A., Christensen, D. A., Rapoport, N. Y., and Pitt, W. G. (2002). Ultrasonic release of doxorubicin from Pluronic P105 micelles stabilized with an interpenetrating network of N,N-diethylacrylamide. *J. Control. Release* 83, 303–305. doi: 10.1016/s0168-3659(02)00203-1

Husseini, G. A., Diaz, D. L. R. M., Gabuji, T., Zeng, Y., Christensen, D. A., and Pitt, W. G. (2007). Release of doxorubicin from unstabilized and stabilized micelles under the action of ultrasound. *J. Nanosci. Nanotechnol.* 7, 1028–1033. doi: 10.1166/jnn.2007.218

Hynynen, K., Pomeroy, O., Smith, D. N., Huber, P. E., McDannold, N. J., Kettenbach, J., et al. (2001). MR imaging-guided focused ultrasound surgery of fibroadenomas in the breast: a feasibility study. *Radiology* 219, 176–185. doi: 10.1148/radiology.219.1.r01ap02176

Jayaweera, A. R., Edwards, N., Glasheen, W. P., Villanueva, F. S., Abbott, R. D., and Kaul, S. (1994). *In vivo* myocardial kinetics of air-filled albumin microbubbles during myocardial contrast echocardiography. Comparison with radiolabeled red blood cells. *Circ. Res.* 74, 1157–1165. doi: 10.1161/01.res.74.6.1157

Ji, R., Pflieger, R., Virot, M., and Nikitenko, S. I. (2018). Multibubble sonochemistry and sonoluminescence at 100 kHz: the missing link between low- and high-frequency ultrasound. . *J. Phys. Chem. B* 122, 6989–6994. doi: 10.1021/acs.jpcb.8b04267

Jiang, Q., Hao, S., Xiao, X., Yao, J., Ou, B., Zhao, Z., et al. (2016). Production and characterization of a novel long-acting Herceptin-targeted nanobubble contrast agent specific for Her-2-positive breast cancers. *Breast Cancer-Tokyo* 23, 445–455. doi: 10.1007/s12282-014-0581-8

Jing, Y., Xiu-Juan, Z., Hong-Jiao, C., Zhi-Kui, C., Qing-Fu, Q., En-Sheng, X., et al. (2019). Ultrasound-targeted microbubble destruction improved the antiangiogenic effect of Endostar in triple-negative breast carcinoma xenografts. *J. Cancer Res. Clin. Oncol.* 145, 1191–1200. doi: 10.1007/s00432-019-02866-7

Kang, Y., Kim, J., Park, J., Lee, Y. M., Saravanakumar, G., Park, K. M., et al. (2019). Tumor vasodilation by N-Heterocyclic carbene-based nitric oxide delivery triggered by high-intensity focused ultrasound and enhanced drug homing to tumor sites for anti-cancer therapy. *Biomaterials* 217, 119297. doi: 10.1016/j.biomaterials.2019.119297

Kaufmann, K. B., Buning, H., Galy, A., Schambach, A., and Grez, M. (2013). Gene therapy on the move. *EMBO Mol. Med.* 5 (11), 1642–1661. doi: 10.1002/emmm.201202287

Khokhlova, T. D., Haider, Y., and Hwang, J. H. (2015). *Therapeutic potential of ultrasound microbubbles in gastrointestinal oncology: recent advances and future prospects* (London, England: SAGE Publications).

Klibanov, A. L., Shevchenko, T. I., Raju, B. I., Seip, R., and Chin, C. T. (2010). Ultrasound-triggered release of materials entrapped in microbubble-liposome constructs: a tool for targeted drug delivery. *J. Control. Release* 148, 13–17. doi: 10.1016/j.jconrel.2010.07.115

Kopechek, J. A., Abruzzo, T. M., Wang, B., Chrzanowski, S. M., Smith, D. A., Kee, P. H., et al. (2008). Ultrasound-mediated release of hydrophilic and lipophilic agents from echogenic liposomes. *J. Ultrasound Med.* 27, 1597–1606. doi: 10.7863/jum.2008.27.11.1597

Kovacs, Z. I., Kim, S., Jikaria, N., Qureshi, F., Milo, B., Lewis, B. K., et al. (2017). Disrupting the blood-brain barrier by focused ultrasound induces sterile inflammation. *Proc. Natl. Acad. Sci. U. S. A.* 114, E75–E84. doi: 10.1073/pnas.1614777114

Kuo, T. T., Wang, C. H., Wang, J. Y., Chiou, H. J., Fan, C. H., and Yeh, C. K. (2019). Concurrent osteosarcoma theranostic strategy using contrast-enhanced ultrasound and drug-loaded bubbles. *Pharmaceutics* 11, 223. doi: 10.3390/parmaceutics11050223

Lafond, M., Aptel, F., Mestas, J. L., and Lafon, C. (2017). Ultrasound-mediated ocular delivery of therapeutic agents: a review. *Expert Opin. Drug Deliv.* 14, 539–550. doi: 10.1080/17425247.2016.1198766

Lanza, G. M., and Wickline, S. A. (2001). Targeted ultrasonic contrast agents for molecular imaging and therapy. *Prog. Cardiovasc. Dis.* 44, 13–31. doi: 10.1053/pcad.2001.26440

Lattin, J. R., Pitt, W. G., Belnap, D. M., and Husseini, G. A. (2012). Ultrasound-induced calcein release from eLiposomes. *Ultrasound Med. Biol.* 38, 2163–2173. doi: 10.1016/j.ultrasmedbio.2012.08.001

Lattin, J. R., Javadi, M., McRae, M., and Pitt, W. G. (2015). Cytosolic delivery *via* escape from the endosome using emulsion droplets and ultrasound. *J. Drug Targeting* 23, 469–479. doi: 10.3109/1061186X.2015.1009074

Lea-Banks, H., O'Reilly, M. A., and Hynynen, K. (2019). Ultrasound-responsive droplets for therapy: a review. *J. Control. Release* 293, 144–154. doi: 10.1016/j.jconrel.2018.11.028

Lee, W. Y., Li, N., Lin, S., Wang, B., Lan, H. Y., and Li, G. (2016). miRNA-29b improves bone healing in mouse fracture model. *Mol. Cell. Endocrinol.* 430, 97–107. doi: 10.1016/j.mce.2016.04.014

Lentacker, I., Geers, B., Demeester, J., De Smedt, S. C., and Sanders, N. N. (2010). Design and evaluation of doxorubicin-containing microbubbles for ultrasound-triggered doxorubicin delivery: cytotoxicity and mechanisms involved. *Mol. Ther.* 18, 101–108. doi: 10.1038/mt.2009.160

Lentacker, I., De Cock, I., Deckers, R., De Smedt, S. C., and Moonen, C. T. (2014). Understanding ultrasound induced sonoporation: definitions and underlying mechanisms. *Adv. Drug Deliv. Rev.* 72, 49–64. doi: 10.1016/j.addr.2013.11.008

Li, P., Zheng, Y., Ran, H., Tan, J., Lin, Y., Zhang, Q., et al. (2012). Ultrasound triggered drug release from 10-hydroxycamptothecin-loaded phospholipid microbubbles for targeted tumor therapy in mice. *J. Control. Release* 162, 349–354. doi: 10.1016/j.jconrel.2012.07.009

Li, Y., Wan, J., Zhang, Z., Guo, J., and Wang, C. (2017). Targeted soft biodegradable glycine/PEG/RGD-modified poly(methacrylic acid) nanobubbles as intelligent theranostic vehicles for drug delivery. *ACS Appl. Mater. Interfaces* 9, 35604–35612. doi: 10.1021/acsami.7b11392

Liao, W. H., Hsiao, M. Y., Lo, C. W., Yang, H. S., Sun, M. K., Lin, F. H., et al. (2017). Intracellular triggered release of DNA-quaternary ammonium polyplex by ultrasound. *Ultrason. Sonochem.* 36, 70–77. doi: 10.1016/j.ultsonch.2016.11.002

Liu, M., Chen, D., Wang, C., Chen, X., Wen, Z., Cao, Y., et al. (2015). Intracellular target delivery of 10-hydroxycamptothecin with solid lipid nanoparticles against multidrug resistance. *J. Drug Targeting* 23, 800–805. doi: 10.3109/1061186X.2015.1020427

Liu, M., Chen, D., Mukerabigwi, J. F., Chen, S., Zhang, Y., Lei, S., et al. (2016a). Intracellular delivery of 10-hydroxycamptothecin with targeted nanostructured lipid carriers against multidrug resistance. *J. Drug Targeting* 24, 433–440. doi: 10.3109/1061186X.2015.1086358

Liu, D., Yang, F., Xiong, F., and Gu, N. (2016b). The smart drug delivery system and its clinical potential. *Theranostics* 6 (9), 1306–1323. doi: 10.7150/thno.14858

Liu, J., Xu, F., Huang, J., Xu, J., Liu, Y., Yao, Y., et al. (2018). Low-intensity focused ultrasound (LIFU)-activated nanodroplets as a theranostic agent for noninvasive cancer molecular imaging and drug delivery. *Biomater. Sci.* 6, 2838–2849. doi: 10.1039/c8bm00726h

Lyon, P. C., Griffiths, L. F., Lee, J., Chung, D., Carlisle, R., Wu, F., et al. (2017). Clinical trial protocol for TARDOX: a phase I study to investigate the feasibility of targeted release of lyso-thermosensitive liposomal doxorubicin (ThermoDox (R)) using focused ultrasound in patients with liver tumours. *J. Ther. Ultrasound* 5, 28. doi: 10.1186/s40349-017-0104-0

Maeda, H. (2001). The enhanced permeability and retention (EPR) effect in tumor vasculature: the key role of tumor-selective macromolecular drug targeting. *Adv. Enzyme Regul.* 41, 189–207. doi: 10.1016/s0065-2571(00)00013-3

Mannaris, C., Efthymiou, E., Meyre, M. E., and Averkiou, M. A. (2013). In vitro localized release of thermosensitive liposomes with ultrasound-induced hyperthermia. *Ultrasound Med. Biol.* 39, 2011–2020. doi: 10.1016/j.ultrasmedbio.2013.06.001

Mannaris, C., Yang, C., Carugo, D., Owen, J., Lee, J. Y., Nwokeoha, S., et al. (2020). Acoustically responsive polydopamine nanodroplets: a novel theranostic agent. *Ultrason. Sonochem.* 60, 104782. doi: 10.1016/j.ultsonch.2019.104782

Marin, A., Sun, H., Husseini, G. A., Pitt, W. G., Christensen, D. A., and Rapoport, N. Y. (2002). Drug delivery in pluronic micelles: effect of high-frequency ultrasound on drug release from micelles and intracellular uptake. *J. Control. Release* 84, 39–47. doi: 10.1016/s0168-3659(02)00262-6

Matafonova, G., and Batoev, V. (2019). Review on low- and high-frequency sonolytic, sonophotolytic and sonophotochemical processes for inactivating pathogenic microorganisms in aqueous media. *Water Res.* 166, 115085. doi: 10.1016/j.watres.2019.115085

Mehier-Humbert, S., Bettinger, T., Yan, F., and Guy, R. H. (2005). Plasma membrane poration induced by ultrasound exposure: implication for drug delivery. *J. Control. Release* 104, 213–222. doi: 10.1016/j.jconrel.2005.01.007

Meng, M., Gao, J., Wu, C., Zhou, X., Zang, X., Lin, X., et al. (2016). Doxorubicin nanobubble for combining ultrasonography and targeted chemotherapy of rabbit with VX2 liver tumor. *Tumour Biol.* 37, 8673–8680. doi: 10.1007/s13277-015-4525-5

Meng, D., Guo, L., Shi, D., Sun, X., Shang, M., Zhou, X., et al. (2019). Charge-conversion and ultrasound-responsive O-carboxymethyl chitosan nanodroplets for controlled drug delivery. *Nanomed. (Lond.)* 14, 2549–2565. doi: 10.2217/nnm-2019-0217

Miller, D. L., Bao, S., and Morris, J. E. (1999). Sonoporation of cultured cells in the rotating tube exposure system. *Ultrasound Med. Biol.* 25, 143–149. doi: 10.1016/s0301-5629(98)00137-9

Min, K. H., Min, H. S., Lee, H. J., Park, D. J., Yhee, J. Y., Kim, K., et al. (2015). pH-controlled gas-generating mineralized nanoparticles: a theranostic agent for ultrasound imaging and therapy of cancers. *ACS Nano* 9, 134–145. doi: 10.1021/nn506210a

Mulvana, H., Browning, R. J., Luan, Y., de Jong, N., Tang, M. X., Eckersley, R. J., et al. (2017). Characterization of contrast agent microbubbles for ultrasound imaging and therapy research. *IEEE Trans. Ultrason. Ferroelectr. Freq. Control* 64, 232–251. doi: 10.1109/TUFFC.2016.2613991

Nakamura, T., and Harashima, H. (2017). Integration of nano drug-delivery system with cancer immunotherapy. *Ther. Delivery* 8, 987–1000. doi: 10.4155/tde-2017-0071

Negishi, Y., Tsunoda, Y., Hamano, N., Omata, D., Endo-Takahashi, Y., Suzuki, R., et al. (2013). Ultrasound-mediated gene delivery systems by AG73-modified Bubble liposomes. *Biopolymers* 100, 402–407. doi: 10.1002/bip.22246

Negishi, Y., Ishii, Y., Nirasawa, K., Sasaki, E., Endo-Takahashi, Y., Suzuki, R., et al. (2018). PMO delivery system using bubble liposomes and ultrasound exposure for duchenne muscular dystrophy treatment. *Methods Mol. Biol.* 1687, 185–192. doi: 10.1007/978-1-4939-7374-3_13

Nieminen, H. J., Barreto, G., Finnila, M. A., Garcia-Perez, A., Salmi, A., Ranjan, S., et al. (2017). Laser-ultrasonic delivery of agents into articular cartilage. *Sci. Rep.* 7 (1), 3991. doi: 10.1038/s41598-017-04293-5

Oishi, Y., Kakimoto, T., Yuan, W., Kuno, S., Yamashita, H., and Chiba, T. (2016). Fetal gene therapy for ornithine transcarbamylase deficiency by intrahepatic plasmid DNA-micro-bubble injection combined with hepatic ultrasound insonation. *Ultrasound Med. Biol.* 42, 1357–1361. doi: 10.1016/j.ultrasmedbio.2015.10.007

Peruzzi, G., Sinibaldi, G., Silvani, G., Ruocco, G., and Casciola, C. M. (2018). Perspectives on cavitation enhanced endothelial layer permeability. *Colloids Surf. B Biointerfaces* 168, 83–93. doi: 10.1016/j.colsurfb.2018.02.027

Pullan, J. E., Bullan, A. T., Taylor, V. B., Brooks, B. B., Ewert, D., and Brooks, A. E. (2017). Energy-triggering drug release from polymer nanoparticles for orthopedic applications. *Ther. Deliv.* 8, 5–14. doi: 10.4155/tde-2016-0066

Qin, J., Wang, T. Y., and Willmann, J. K. (2016). Sonoporation: applications for cancer therapy. *Adv. Exp. Med. Biol.* 880, 263–291. doi: 10.1007/978-3-319-22536-4_15

Rapoport, N., Nam, K. H., Gupta, R., Gao, Z., Mohan, P., Payne, A., et al. (2011). Ultrasound-mediated tumor imaging and nanotherapy using drug loaded, block copolymer stabilized perfluorocarbon nanoemulsions. *J. Control. Release* 153, 4–15. doi: 10.1016/j.jconrel.2011.01.022

Rapoport, N. (2012). Ultrasound-mediated micellar drug delivery. *Int. J. Hyperthermia* 28, 374–385. doi: 10.3109/02656736.2012.665567

Schroeder, A., Kost, J., and Barenholz, Y. (2009). Ultrasound, liposomes, and drug delivery: principles for using ultrasound to control the release of drugs from liposomes. *Chem. Phys. Lipids* 162, 1–16. doi: 10.1016/j.chemphyslip.2009.08.003

Shang, M., Wang, K., Guo, L., Duan, S., Lu, Z., and Li, J. (2019). Development of novel ST68/PLA-PEG stabilized ultrasound nanobubbles for potential tumor imaging and theranostic. *Ultrasonics* 99, 105947. doi: 10.1016/j.ultras.2019.105947

Shen, J., Zhuo, N., Xu, S., Song, Z., Hu, Z., Hao, J., et al. (2018a). Resveratrol delivery by ultrasound-mediated nanobubbles targeting nucleus pulposus cells. *Nanomed. (Lond)* 13, 1433–1446. doi: 10.2217/nnm-2018-0019

Shen, S., Li, Y., Xiao, Y., Zhao, Z., Zhang, C., Wang, J., et al. (2018b). Folate-conjugated nanobubbles selectively target and kill cancer cells *via* ultrasound-triggered intracellular explosion. *Biomaterials* 181, 293–306. doi: 10.1016/j.biomaterials.2018.07.030

Shende, P., and Jain, S. (2019). Polymeric nanodroplets: an emerging trend in gaseous delivery system. *J. Drug Targeting* 27, 1035–1045. doi: 10.1080/1061186X.2019.1588281

Shpak, O., Verweij, M., de Jong, N., and Versluis, M. (2016). Droplets, bubbles and ultrasound interactions. *Adv. Exp. Med. Biol.* 880, 157–174. doi: 10.1007/978-3-319-22536-4_9

Sirsi, S. R., and Borden, M. A. (2012). Advances in ultrasound mediated gene therapy using microbubble contrast agents. *Theranostics* 2, 1208–1222. doi: 10.7150/thno.4306

Sirsi, S. R., and Borden, M. A. (2014). State-of-the-art materials for ultrasound-triggered drug delivery. *Adv. Drug Deliv. Rev.* 72, 3–14. doi: 10.1016/j.addr.2013.12.010

Smith, D. A., Vaidya, S. S., Kopechek, J. A., Huang, S. L., Klegerman, M. E., McPherson, D. D., et al. (2010). Ultrasound-triggered release of recombinant tissue-type plasminogen activator from echogenic liposomes. *Ultrasound Med. Biol.* 36, 145–157. doi: 10.1016/j.ultrasmedbio.2009.08.009

Song, W., Luo, Y., Zhao, Y., Liu, X., Zhao, J., Luo, J., et al. (2017). Magnetic nanobubbles with potential for targeted drug delivery and trimodal imaging in breast cancer: an *in vitro* study. *Nanomed. (Lond.)* 12, 991–1009. doi: 10.2217/nnm-2017-0027

Song, K. H., Harvey, B. K., and Borden, M. A. (2018a). State-of-the-art of microbubble-assisted blood-brain barrier disruption. *Theranostics* 8, 4393–4408. doi: 10.7150/thno.26869

Song, Z., Ye, Y., Zhang, Z., Shen, J., Hu, Z., Wang, Z., et al. (2018b). Noninvasive, targeted gene therapy for acute spinal cord injury using LIFU-mediated BDNF-loaded cationic nanobubble destruction. *Biochem. Biophys. Res. Commun.* 496, 911–920. doi: 10.1016/j.bbrc.2018.01.123

Soto, F., Jeerapan, I., Silva-Lopez, C., Lopez-Ramirez, M. A., Chai, I., Xiaolong, L., et al. (2018). Noninvasive transdermal delivery system of lidocaine using an acoustic droplet-vaporization based wearable patch. *Small* 14, e1803266. doi: 10.1002/smll.201803266

Ta, T., Bartolak-Suki, E., Park, E. J., Karrobi, K., McDannold, N. J., and Porter, T. M. (2014). Localized delivery of doxorubicin *in vivo* from polymer-modified thermosensitive liposomes with MR-guided focused ultrasound-mediated heating. *J. Control. Release* 194, 71–81. doi: 10.1016/j.jconrel.2014.08.013

Tachibana, K., Uchida, T., Hisano, S., and Morioka, E. (1997). Eliminating adult T-cell leukaemia cells with ultrasound. *Lancet* 349, 325. doi: 10.1016/S0140-6736(97)24005-5

Tanbour, R., Martins, A. M., Pitt, W. G., and Husseini, G. A. (2016). Drug delivery systems based on polymeric micelles and ultrasound: a review. *Curr. Pharm. Des.* 22, 2796–2807. doi: 10.2174/1381612822666160217125215

Tang, W., Yang, Z., Wang, S., Wang, Z., Song, J., Yu, G., et al. (2018). Organic semiconducting photoacoustic nanodroplets for laser-activatable ultrasound imaging and combinational cancer therapy. *ACS Nano* 12, 2610–2622. doi: 10.1021/acsnano.7b08628

Tardoski, S., Gineyts, E., Ngo, J., Kocot, A., Clezardin, P., and Melodelima, D. (2015). Low-intensity ultrasound promotes clathrin-dependent endocytosis for drug penetration into tumor cells. *Ultrasound Med. Biol.* 41, 2740–2754. doi: 10.1016/j.ultrasmedbio.2015.06.006

Tayier, B., Deng, Z., Wang, Y., Wang, W., Mu, Y., and Yan, F. (2019). Biosynthetic nanobubbles for targeted gene delivery by focused ultrasound. *Nanoscale* 11, 14757–14768. doi: 10.1039/c9nr03402a

Thansandote, P., Harris, R. M., Dexter, H. L., Simpson, G. L., Pal, S., Upton, R. J., et al. (2015). Improving the passive permeability of macrocyclic peptides: Balancing permeability with other physicochemical properties. *Bioorg. Med. Chem.* 23, 322–327. doi: 10.1016/j.bmc.2014.11.034

Tian, Y., Liu, Z., Zhang, L., Zhang, J., Han, X., Wang, Q., et al. (2018). Apatinib-loaded lipid nanobubbles combined with ultrasound-targeted nanobubble destruction for synergistic treatment of HepG2 cells *in vitro*. *Oncol. Targets Ther.* 11, 4785–4795. doi: 10.2147/OTT.S170786

Timbie, K. F., Mead, B. P., and Price, R. J. (2015). Drug and gene delivery across the blood-brain barrier with focused ultrasound. *J. Control. Release* 219, 61–75. doi: 10.1016/j.jconrel.2015.08.059

Torchilin, V. P. (2005). Recent advances with liposomes as pharmaceutical carriers. *Nat. Rev. Drug Discovery* 4, 145–160. doi: 10.1038/nrd1632

Ulrich, A. S. (2002). Biophysical aspects of using liposomes as delivery vehicles. *Biosci. Rep.* 22, 129–150. doi: 10.1023/a:1020178304031

Wan, C., Li, F., and Li, H. (2015a). Gene therapy for ocular diseases meditated by ultrasound and microbubbles (Review). *Mol. Med. Rep.* 12, 4803–4814. doi: 10.3892/mmr.2015.4054

Wan, C., Qian, J., Li, F., and Li, H. (2015b). Ultrasound-targeted microbubble destruction enhances polyethylenimine-mediated gene transfection *in vitro* in human retinal pigment epithelial cells and *in vivo* in rat retina. *Mol. Med. Rep.* 12, 2835–2841. doi: 10.3892/mmr.2015.3703

Wang, P., Yin, T., Li, J., Zheng, B., Wang, X., Wang, Y., et al. (2016). Ultrasound-responsive microbubbles for sonography-guided siRNA delivery. *Nanomedicine-UK* 12, 1139–1149. doi: 10.1016/j.nano.2015.12.361

Wang, Y., Sui, G., Teng, D., Wang, Q., Qu, J., Zhu, L., et al. (2018). Low intensity focused ultrasound (LIFU) triggered drug release from cetuximab-conjugated phase-changeable nanoparticles for precision theranostics against anaplastic thyroid carcinoma. *Biomater. Sci.* 7, 196–210. doi: 10.1039/c8bm00970h

Ward, M., Wu, J., and Chiu, J. F. (1999). Ultrasound-induced cell lysis and sonoporation enhanced by contrast agents. *J. Acoust. Soc. Am.* 105, 2951–2957. doi: 10.1121/1.426908

Watanabe, Y., Horie, S., Funaki, Y., Kikuchi, Y., Yamazaki, H., Ishii, K., et al. (2010). Delivery of Na/I symporter gene into skeletal muscle using nanobubbles and ultrasound: visualization of gene expression by PET. *J. Nucl. Med.* 51 (6), 951–958. doi: 10.2967/jnumed.109.074443

Witte, R. S., Karunakaran, C., Zuniga, A. N., Schmitz, H., and Arif, H. (2018). Frontiers of cancer imaging and guided therapy using ultrasound, light, and microwaves. *Clin. Exp. Metastasis* 35, 413–418. doi: 10.1007/s10585-018-9923-9

Wu, M., Wang, Y., Wang, Y., Zhang, M., Luo, Y., Tang, J., et al. (2017a). Paclitaxel-loaded and A10-3.2 aptamer-targeted poly(lactide-co-glycolic acid) nanobubbles for ultrasound imaging and therapy of prostate cancer. *Int. J. Nanomed.* 12, 5313–5330. doi: 10.2147/IJN.S136032

Wu, P., Jia, Y., Qu, F., Sun, Y., Wang, P., Zhang, K., et al. (2017b). Ultrasound-responsive polymeric micelles for sonoporation-assisted site-specific therapeutic action. *ACS Appl. Mater. Interfaces* 9, 25706–25716. doi: 10.1021/acsami.7b05469

Wu, M., Zhao, H., Guo, L., Wang, Y., Song, J., Zhao, X., et al. (2018a). Ultrasound-mediated nanobubble destruction (UMND) facilitates the delivery of A10-3.2 aptamer targeted and siRNA-loaded cationic nanobubbles for therapy of prostate cancer. *Drug Deliv.* 25, 226–240. doi: 10.1080/10717544.2017.1422300

Wu, S. Y., Fix, S. M., Arena, C. B., Chen, C. C., Zheng, W., Olumolade, O. O., et al. (2018b). Focused ultrasound-facilitated brain drug delivery using optimized nanodroplets: vaporization efficiency dictates large molecular delivery. *Phys. Med. Biol.* 63, 035002. doi: 10.1088/1361-6560/aaa30d

Xia, H., Zhao, Y., and Tong, R. (2016). Ultrasound-mediated polymeric micelle drug delivery. *Adv. Exp. Med. Biol.* 880, 365–384. doi: 10.1007/978-3-319-22536-4_20

Xing, L., Shi, Q., Zheng, K., Shen, M., Ma, J., Li, F., et al. (2016). Ultrasound-mediated microbubble destruction (UMMD) facilitates the delivery of CA19-9 targeted and paclitaxel loaded mPEG-PLGA-PLL nanoparticles in pancreatic cancer. *Theranostics* 6, 1573–1587. doi: 10.7150/thno.15164

Yan, C., Zhu, D., Huang, D., and Xia, G. (2015). Role of ultrasound and microbubble-mediated heat shock protein 72 siRNA on ischemia-reperfusion liver injury in rat. *Int. J. Clin. Exp. Med.* 8, 5746–5752.

Yang, Z., Luo, X., Zhang, X., Liu, J., and Jiang, Q. (2013). Targeted delivery of 10-hydroxycamptothecin to human breast cancers by cyclic RGD-modified lipid-polymer hybrid nanoparticles. *Biomed. Mater.* 8, 025012. doi: 10.1088/1748-6041/8/2/025012

Yatvin, M. B., Weinstein, J. N., Dennis, W. H., and Blumenthal, R. (1978). Design of liposomes for enhanced local release of drugs by hyperthermia. *Science* 202, 1290–1293. doi: 10.1126/science.364652

Yu, M., Xu, X., Cai, Y., Zou, L., and Shuai, X. (2018). Perfluorohexane-cored nanodroplets for stimulations-responsive ultrasonography and O2-potentiated photodynamic therapy. *Biomaterials* 175, 61–71. doi: 10.1016/j.biomaterials.2018.05.019

Yu, Y., Wang, B., Guo, C., Zhao, F., and Chen, D. (2019). Protoporphyrin IX-loaded laminarin nanoparticles for anticancer treatment, their cellular behavior, ROS detection, and animal studies. *Nanoscale Res. Lett.* 14, 316. doi: 10.1186/s11671-019-3138-0

Yue, P., Gao, L., Wang, X., Ding, X., and Teng, J. (2018). Ultrasound-triggered effects of the microbubbles coupled to GDNF- and Nurr1-loaded PEGylated liposomes in a rat model of Parkinson's disease. *J. Cell. Biochem.* 119, 4581–4591. doi: 10.1002/jcb.26608

Zhang, X., Pan, W., Gan, L., Zhu, C., Gan, Y., and Nie, S. (2008). Preparation of a dispersible PEGylate nanostructured lipid carriers (NLC) loaded with 10-hydroxycamptothecin by spray-drying. *Chem. Pharm. Bull. (Tokyo)* 56, 1645–1650. doi: 10.1248/cpb.56.1645

Zhang, B., Chen, M., Zhang, Y., Chen, W., Zhang, L., and Chen, L. (2018a). An ultrasonic nanobubble-mediated PNP/fludarabine suicide gene system: a new approach for the treatment of hepatocellular carcinoma. *PloS One* 13, e0196686. doi: 10.1371/journal.pone.0196686

Zhang, J., Wang, S., Deng, Z., Li, L., Tan, G., Liu, X., et al. (2018b). Ultrasound-triggered drug delivery for breast tumor therapy through iRGD-targeted paclitaxel-loaded liposome-microbubble complexes. *J. Biomed. Nanotechnol.* 14, 1384–1395. doi: 10.1166/jbn.2018.2594

Zhang, L., Yi, H., Song, J., Huang, J., Yang, K., Tan, B., et al. (2019). Mitochondria-targeted and ultrasound-activated nanodroplets for enhanced deep-penetration sonodynamic cancer therapy. *ACS Appl. Mater. Interfaces* 11, 9355–9366. doi: 10.1021/acsami.8b21968

Zhu, L., Zhao, H., Zhou, Z., Xia, Y., Wang, Z., Ran, H., et al. (2018). Peptide-functionalized phase-transformation nanoparticles for low intensity focused ultrasound-assisted tumor imaging and therapy. *Nano Lett.* 18, 1831–1841. doi: 10.1021/acs.nanolett.7b05087

Zullino, S., Argenziano, M., Stura, I., Guiot, C., and Cavalli, R. (2018). From micro- to nano-multifunctional theranostic platform: effective ultrasound imaging is not just a matter of scale. *Mol. Imaging* 17, 153601211877821. doi: 10.1177/1536012118778216

Conflict of Interest: The authors declare that the research was conducted in the absence of commercial or financial relationships that could be construed as a potential conflict of interest.

frontiers in Pharmacology

ORIGINAL RESEARCH
published: 20 February 2020
doi: 10.3389/fphar.2020.00075

Theranostic Attributes of Acoustic Cluster Therapy and Its Use for Enhancing the Effectiveness of Liposomal Doxorubicin Treatment of Human Triple Negative Breast Cancer in Mice

Nigel Bush[1], Andrew Healey[2], Anant Shah[1], Gary Box[3], Vladimir Kirkin[3], Sue Eccles[3], Per Christian Sontum[2], Spiros Kotopoulis[2], Svein Kvåle[2], Annemieke van Wamel[4], Catharina de Lange Davies[4] and Jeffrey Bamber[1]*

[1] Joint Department of Physics, Institute of Cancer Research, London, United Kingdom, [2] Phoenix Solutions AS, Oslo, Norway, [3] Department of Physics, CRUK Cancer Therapeutics Unit, The Institute of Cancer Research, London, United Kingdom, [4] Norwegian University of Science and Technology (NTNU), Trondheim, Norway

OPEN ACCESS

Edited by:
Heike Wulff,
University of California,
Davis, United States

Reviewed by:
Noboru Sasaki,
Hokkaido University, Japan
Marc Derieppe,
Princess Maxima Center for Pediatric Oncology, Netherlands

***Correspondence:**
Nigel Bush
Nigel@icr.ac.uk

Specialty section:
This article was submitted to Translational Pharmacology, a section of the journal Frontiers in Pharmacology

Received: 31 July 2019
Accepted: 24 January 2020
Published: 20 February 2020

Citation:
Bush N, Healey A, Shah A, Box G, Kirkin V, Eccles S, Sontum PC, Kotopoulis S, Kvåle S, van Wamel A, Davies CdL and Bamber J (2020) Theranostic Attributes of Acoustic Cluster Therapy and Its Use for Enhancing the Effectiveness of Liposomal Doxorubicin Treatment of Human Triple Negative Breast Cancer in Mice. Front. Pharmacol. 11:75. doi: 10.3389/fphar.2020.00075

Introduction: Acoustic cluster therapy (ACT) comprises co-administration of a formulation containing microbubble/microdroplet clusters (PS101), together with a regular medicinal drug (*e.g.*, a chemotherapeutic) and local ultrasound (US) insonation of the targeted pathological tissue (*e.g.*, the tumor). PS101 is confined to the vascular compartment and, when the clusters are exposed to regular diagnostic imaging US fields, the microdroplets undergo a phase-shift to produce bubbles with a median diameter of 22 µm when unconstrained by the capillary wall. *In vivo* these bubbles transiently lodge in the tumor's microvasculature. Low frequency ultrasound (300 kHz) at a low mechanical index (MI = 0.15) is then applied to drive oscillations of the deposited ACT bubbles to induce a range of biomechanical effects that locally enhance extravasation, distribution, and uptake of the co-administered drug, significantly increasing its therapeutic efficacy.

Methods: In this study we investigated the therapeutic efficacy of ACT with liposomal doxorubicin for the treatment of triple negative breast cancer using orthotopic human tumor xenografts (MDA-MB-231-H.luc) in athymic mice (ICR-NCr-Foxn1^{nu}). Doxil® (6 mg/kg, *i.v.*) was administered at days 0 and 21, each time immediately followed by three sequential ACT (20 ml/kg PS101) treatment procedures (n = 7–10). B-mode and nonlinear ultrasound images acquired during the activation phase were correlated to the therapeutic efficacy.

Results: Results show that combination with ACT induces a strong increase in the therapeutic efficacy of Doxil®, with 63% of animals in complete, stable remission at end of study, *vs*. 10% for Doxil® alone ($p < 0.02$). A significant positive correlation ($p < 0.004$) was found between B-mode contrast enhancement during ACT activation and therapy response. These observations indicate that ACT may also be used as a theranostic

agent and that ultrasound contrast enhancement during or before ACT treatment may be employed as a biomarker of therapeutic response during clinical use.

Keywords: acoustic cluster therapy, microbubbles, ultrasound, drug delivery, doxorubicin, breast cancer

INTRODUCTION

A prerequisite for successful therapy with a medicinal drug is that the active substance reaches its target pathology and that toxicity to healthy tissue and non-targeted organs is limited. Once a drug is administrated systemically, the mononuclear phagocyte system, the vascular endothelium, the disrupted tumor blood flow, the tumor stroma, endosomal escape, and drug efflux pumps are a few among a multitude of other biological barriers that severely restrict its effective delivery from the vascular compartment into the tissue of the targeted pathology (Nizzero et al., 2018). In effect: for a number of drugs, the current, passive transvascular delivery paradigm is inefficient, insufficient, and often results in therapeutic agents failing to reach effective local concentrations due to poor tumor penetration. In combination with low therapeutic indexes, increasing the dosages is not a viable strategy due to serious and widespread adverse effects, overall severely limiting the clinical utility of a range of potent drugs.

While the lack of sufficient extravasation of drug to the targeted pathology is an issue over the range of medicinal therapeutic sectors, this is in particular the case within medicinal treatment of cancers. Regular chemotherapeutics and a range of more novel immune therapies induce severe side effects at partially effective doses and typically, these medicinal regimes are not terminated because the cancer is eradicated, but because the body cannot tolerate more treatment. The outcome is palliative benefit or life prolongation instead of a cure. In conditions such as triple negative breast cancer (TNBC) treated with standard of care chemotherapy, this is unfortunately the case. Specifically, TNBC is a cancer that lacks the expression of estrogen, progesterone, and human epidermal growth factor 2 receptors and is strongly correlated with a poorer outcome when compared to other breast cancer subtypes (Bianchini et al., 2016). This is primarily due to the inherently aggressive clinical behavior, lack of recognized molecular targets for therapy, and heterogenous response to therapy. In 2018, there were estimated to be over 2 million new cases of breast cancer making it the second largest cancer occurrence worldwide (Bray et al., 2018). While significant progress has been made for treatment of breast cancer, there is still a 20% overall mortality ratio at over 620,000 patients per year. The survival impact of TNBC is even worse and commonly referred to as the "kiss of death" (Jitariu et al., 2017) as it is unfortunately deadly in most cases. Specifically, patients diagnosed with TBNC have a mortality incidence from 40 to 50% (Foulkes et al., 2010; Gonçalves et al., 2018) This clearly indicates an important need to improve the therapeutic efficacy for the treatment of breast cancer and even more so of TNBC.

To resolve this fundamental problem, over the past decades, a wide range of concepts to improve the pathology-specific drug uptake (targeted drug delivery) have been explored (Devarajan and Jain, 2015). Within oncology, numerous drug carrier concepts, e.g., liposomes, micelles, dendrimers, and nanoparticles have been employed, either to passively make use of the enhanced permeability and retention (EPR) effect (Maeda et al., 2000), or in combination with surface ligands that actively promote accumulation in tumor tissue through biochemical affinity to specifically expressed target groups. However, even though huge resources have been spent on finding functional concepts for targeted drug delivery over the last two decades, and despite promising pre-clinical results for several of these, there has been very limited transition to drug products and clinical practice. In truth, the objective remains essentially unresolved in current standard-of-care medicinal therapy.

In recent years, several concepts for ultrasound (US) mediated drug delivery have been investigated, some with quite encouraging results (Tsutsui et al., 2004; Martin and Dayton, 2013; Unga and Hashida, 2014). Most of these concepts explore the use of regular US contrast microbubbles such as SonoVue®, Optison™, or Definity®, either loaded with or co-injected with various active ingredients. Insonation of the target pathology containing microbubbles in vascular compartments leads to a variety of biomechanical effects that enhance extravasation and distribution of drug molecules to target tissue (Kooiman et al., 2014; Lentacker et al., 2014) Co-injection of Gemcitabine and SonoVue®, with localized US insonation for a hypothesized enhanced drug uptake and therapeutic effect during treatment of pancreatic cancer (PDAC) has been explored in clinical trials with encouraging results (Dimcevski et al., 2016). A similar approach is being investigated for treatment of glioblastoma in humans (Carpentier et al., 2016). Whereas various drug delivery approaches exploring the use of regular US contrast agents have shown some promise, their effectiveness is hampered by several issues. Being small, the magnitude of the biomechanical work that microbubbles of 1-8μm diameter can induce is relatively limited. In addition, as they are free flowing, they display limited contact with the endothelial wall, further reducing the level and range of any biomechanical effects (Kooiman et al., 2014). Furthermore, microbubbles are typically cleared from vascular compartments within 2–3 min and, finally, to produce sufficient biomechanical work and effect levels, microbubbles often need a high US intensity and as a consequence will potentially induce inertial cavitation, with ensuing potential safety issues.

More recently, a new microbubble concept, specifically designed to improve on the shortcomings of regular contrast microbubbles for targeted drug delivery, has been developed: acoustic cluster therapy (ACT) (Sontum et al., 2015; Healey et al., 2016). ACT addresses important deficiencies of microbubble contrast agents. In brief, ACT is defined as the co-administration of a drug together with a dispersion of microbubble/microdroplet clusters (PS101), followed by a two-

step, local activation, and delivery-enhancement procedure targeted by ultrasound directed at the tumor. The microbubble in cluster acts as a vaporization seed, *i.e.,* the US activation forces the microbubble to oscillate which induces a liquid-to-gas phase shift of the microdroplet component and the formation of a large (22-μm diameter) bubbles. If the microbubble in the cluster was not present, the microdroplet would not phase shift at low acoustic MIs. The ACT bubbles produced by droplet vaporisation are designed to transiently lodge at the microvascular level of the vascular tree due to their size. The subsequent US enhancement step induces controlled volume oscillations that lead to enhanced local permeability of the vasculature, allowing for improved extravasation and distribution of drug into the tumor tissue extracellular matrix. The ACT bubbles, being 1,000 times larger (by volume) than regular contrast microbubbles, will induce in the range of three orders of magnitude greater biomechanical work. When lodged in the vascular compartment, the ACT bubbles display close contact with the endothelial wall over significant vessel segments; and remain for approximately 5–10 min. This allows for prolonged insonation and biomechanical work and these effects are induced using low intensity and low MI (<0.3) US. The concept represents a novel approach to targeted drug delivery that may improve significantly the efficacy of *e.g.,* current chemotherapy regimens.

Previously, ACT has been explored in combination with a range of drugs for treatment of several cancers, including; Abraxane® (nab-paclitaxel) for treatment of prostate cancer (Van Wamel et al., 2016c) (Park, 2016) and paclitaxel for treatment of human pancreatic ductal carcinoma (PDAC) (Kotopoulis et al., 2017). In these earlier studies, a remarkable increase in the therapeutic efficacy over drug alone was observed when combined with the ACT procedure. In our work here we investigate the treatment of TNBC with liposomal doxorubicin (Doxil®) using two treatments of ACT. The therapeutic agent, Doxil, was chosen as it is considered a different drug class to the previously evaluated chemotherapeutic agents. Specifically, Doxil® is a liposomal nanoparticle while the other evaluated nanoparticulate agent (Abraxane®) was a protein bound agent. This allows us to determine to what extent ACT is therapeutic agent agnostic. In addition, in a clinical trial using Doxil® for treatment of metastatic breast cancer (O'Brien et al., 2004) Doxil® showed reduced toxicity over doxorubicin but with no difference in efficacy. Here were evaluate if ACT can help improve the therapeutic efficacy of Doxil®, potentially adding an additional option for the treatment of metastatic breast cancer.

Furthermore, we perform a *post-hoc* analysis to investigate the relationship between ultrasound imaging contrast during the activation step and treatment efficacy as a biomarker for prediction and monitoring of therapeutic efficacy.

MATERIALS AND METHODS

Cell Line and Tumor Model

The human TNBC cells MDA-MB-231.H-luc (American Type Culture Collection, Manassas, VA, USA, lot no. 8924081) were grown in Leibovitz's L-15 cell culture medium supplemented with 10% fetal bovine serum in a humidified atmosphere of 5% CO_2 at 37°C and passaged before renewal from frozen. Cells were regularly screened for mycoplasma by PCR using in-house primers.

Orthotopic tumors were established by injecting $3x10^6$ cells in 100 μl Matrigel:L-15 medium (1:4) into the thoracic mammary fat pad of 6-week old female athymic mice (ICR : NCr-Foxn1^{nu}), bred in-house. During xenografting, mice were anesthetized using 2% isoflurane (Zoetis UK Ltd, UK) in oxygen. Mice were housed in groups of five in individually ventilated cages and allowed access to food and water *ad libitum*. All mice were treated in accordance with the local Animal Welfare and Ethical Review Board, the UK Home Office Animals Scientific Procedures Act 1986 and with the United Kingdom National Cancer Research Institute guidelines for the welfare of animals in cancer research (Workman et al., 2010).

The tumors were allowed to grow for up to 3 weeks and treatment was initiated when tumor volumes surpassed 180 $(mm)^3$. The average (± SEM) starting volume was 209 ± 17 $(mm)^3$ while the range was 183–241 $(mm)^3$.

Therapeutics

Clinical grade liposomal doxorubicin (DOX) (Caelyx®/Doxil®, Janssen Pharmaceutica NV, Belgium) was stored at 2–8 °C and freshly diluted for each treatment in 5% dextrose to a concentration of 1.5 mg/ml and administered as an intravenous (*i.v.*) bolus *via* a tail vein catheter. Mice were treated with DOX doses of 6 and/or 8 mg/kg matching literature values (Working et al., 1994).

PS101 was provided by Phoenix Solutions AS, Oslo, Norway (Sontum et al., 2015). PS101 was prepared by reconstituting commercially available microbubbles, Sonazoid™ (GE Healthcare), with a microdroplet emulsion of perfluoromethylcylopentane (PFMCP, F2 Chemicals Ltd., UK) microdroplets. The reconstituted PS101 formulation consists of a suspension of small microbubble/microdroplet conjugates ("clusters") 6 x 10^7 clusters/ml, with a median diameter of 5 μm (Sontum et al., 2015). The content of PFMCP, which is defined as the active pharmaceutical ingredient (API) in PS101, is 6.8 mg/ml. For administration of low doses, to allow for acceptable injection volumes, PS101 was diluted in 0.9% saline prior to administration.

Treatment Protocol

Prior to each treatment anesthesia was induced by subcutaneous (*s.c.*) injection of fentanyl citrate +fluanisone (Hypnorm™, VetaPharma Ltd, Leeds, UK) and Midazolam (Hypnovel®, Roche Products Ltd, Welwyn Garden City, UK) (0.28:10:4.5 mg/kg). During treatments the mice were maintained on a mouse handling table (Vevo™, Fujifilm VisualSonics Inc., Toronto) and body temperature was controlled thermostatically, with vital signs carefully monitored. Following treatments mice were kept in a temperature-controlled recovery chamber until fully recovered.

Figure 1 shows a photograph (**Figure 1A**) and schematic explanation (**Figure 1B**) of the experimental setup used to image and treat the mice. The mice were placed in dorsal recumbency and ultrasound gel was applied to the tumor area only. An open polyethylene water bag was lowered until in contact with the

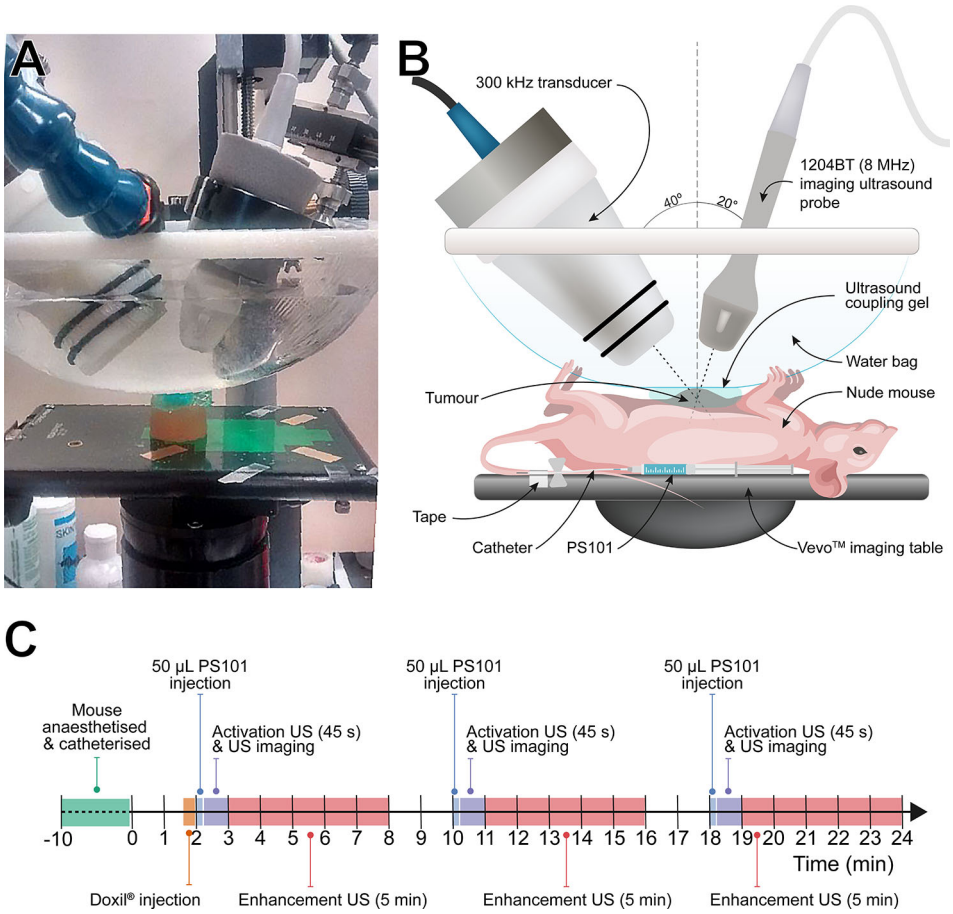

FIGURE 1 | Overview of the experimental setup and experimental timeline. Panel **(A)**: Photograph of the experimental setup. A sample block has been positioned in place of the animal. Panel **(B)**: Schematic overview of the experimental setup with primary equipment labeled. Panel **(C)**: Timeline for each treatment cycle using acoustic cluster therapy (ACT) with Doxil®. Sham ultrasound was used for the Doxil® group.

ultrasound gel. **Figure 1C** shows the chronological order of each treatment cycle.

A clinical US diagnostic scanner, Aplio XG ultrasound scanner (Toshiba Medical Systems Corporation, Tochigi, Japan) combined with a 1204BT linear array ultrasound probe was used to both image the tumors and provide 45 s of "activation" ultrasound to phase-shift the PS101. The clinical system was set to an MI of 0.33 at a center frequency of 8 MHz at 20 fps. The clinical scanner operating in dual imaging mode permits visualization of the PS101 (Sonazoid component) inflow using non-linear contrast imaging, and ACT bubble formation (Healey et al., 2016; Van Wamel et al., 2016b) using B-mode imaging. At the end of the activation period, ultrasound output was switched to enhancement ultrasound applied *via* a custom made 300 kHz, 55 mm diameter, single element focused transducer (Imasonic SAS, Voray-sur-l'Ognon, France) for 5 min at an MI of 0.15 with two cycles of excitation every 125 ms. The 300 kHz ultrasound transducer was driven by an Analogic 2045 polynomial waveform synthesizer (Analogic Corp, USA) amplified by a pulsed radio frequency (RF) amplifier, BT00500 (Tomco Technologies, Australia) power amplifier. The acoustic conditions were chosen based on *a-priori in-vitro* and *in-vivo* experiments (Healey et al., 2016; Van Wamel et al., 2016a)

During activation, both B-mode and contrast-mode images were acquired for correlation with therapeutic response. The two transducers were fixed and aligned in relation to each other so that the imaging focus of the diagnostic array and the acoustic focus of 300 kHz transducer coincided without interfering with the acoustic propagation of the other transducer. Specifically, the 1204BT array was placed at 20° off the vertical axis and the 300 kHz array −40° off the vertical axis. Once the mouse was in place, both ultrasound sources where lowered so that the acoustic foci aligned with the center of the tumor, and the transducers' front surfaces were within the water bag. The acoustic pressures of the 300 kHz transducer were calibrated *a priori in situ* using a 200-µm lipstick hydrophone (HGL-200, Onda Corporation, Sunnyvale, CA, USA). The hydrophone was spot calibrated in-house at 300 kHz by comparing to a fully calibrated needle hydrophone (1-mm, Precision Acoustics Ltd, Dorchester, Dorset, UK). The scanner's on-screen values were used for the 8-MHz transducer.

For PS101 and drug delivery a catheter was assembled by combining a winged infusion set, Surflo® 27G butterfly needle

(Terumo Europe, Leuven, Belgium), a 70 mm length of polyethylene tubing, 0.4 mm i.d. (Biochrom Ltd, Cambridge, UK) and a 27G, 0.5" hypodermic needle. It was validated *a priori* using established methods (Sontum et al., 2015), that this exact injection procedure did not affect the size distribution or activation potential of the PS101 (**Supplemental Figure 1**, **Supplemental Table 3**). The catheter, primed with a 0.9% saline solution, was inserted into the lateral tail vein of the mouse and patency checked by injecting a small volume of saline solution <5 µl. The hub of the cannula was then filled with 0.9% saline and closed with a cap and taped to the animal's tail with surgical tape, which resulted in a "dead space" of 10 µl to be accounted for in subsequent injections. Just prior to each new injection, PS101 was freshly drawn up into a 1 ml syringe and 60 µl (50 µl effective dose, plus 10 µl to allow for dead space) was injected intravenously into the animal's lateral tail vein *via* the preplaced catheter. Three injections of PS101 followed by activation and enhancement ultrasound were performed for each treatment cycle.

Treatment Groups

Table 1 summarizes the treatment groups evaluated in this study. Animals were randomized into cohorts of 8–10 mice randomly, depending on when the tumors reached the required starting volume. Group 1 was only PS101 followed by activation and enhancement ultrasound. Group 2, treated with Doxil® only, employed a reduced Doxil® dose during the second treatment cycle to match the lower doses employed in group 3, ACT with Doxil®, where dose was lowered during the first treatment cycle to compensate for apparent toxicity encountered when treating the first animals with a dose of 8 mg/kg in the first treatment cycle. This toxicity manifested as a failure to recover from the anesthetic procedure. Hence the dose reduced to 6 mg/kg was used in the ACT with Doxil® group and maintained for both treatment days.

Disease Development Evaluation

Animal health status was monitored daily. Tumor volumes were obtained *via* caliper measurement four to five times a week up to 175 days from study start. Tumor volumes were calculated using the ellipsoid equation $\frac{4}{3}\pi(\frac{a}{4}+\frac{b}{4})^3$.

Tumor size is reported as fold increase normalized to the day of the first treatment, *i.e.,* day 0. Values were linearly interpolated to single day values for graphing purposes.

Following the 3Rs of ethical research and EU directives (Directive 2010/63/EU, 2010) a drug + US only group was not included in the study as the US exposure levels are well below those which might cause bioeffects (Miller et al., 2008; Nelson et al., 2009). Similarly, Sonazoid™ and saline in the absence of US are not expected to affect tumor growth, and such groups were not included.

Mice that showed no visible sign of the tumors at the end of the study (day 175) were considered complete responders while mice that were sacrificed prior to the end of the study were considered non-responders. To minimize experimental bias and animal suffering, a score sheet was used to determine when to sacrifice an animal based on ulceration and tumor size (**Supplemental Table 1**)

TABLE 1 | Summary of the treatment groups: number of mice, name, and Doxil® and acoustic cluster therapy (ACT) doses; t_1 and t_2 indicate the doses at the fist (day 0) and second (day 21) treatment cycle.

Group	Name	Number of animals	Treatment doses		US exposure
			Doxil® (mg/kg) $t_1 \rightarrow t_2$ (total)	ACT 3×(ml/kg) t1→t2	
1	PS101 +US	9	–	2.00→2.00	✓
2	Doxil®	10	8→6 [14]	–	×
3	ACT with Doxil®	8	6→6 [12]	2.00→2.00	✓

Response Assessment

Contrast Enhancement Ranking

Contrast enhancement ranking (*i.e.,* Imaging rank) was determined from the ultrasound images recorded during activation following post-processing in MATLAB 2014a (MathWorks, Massachusetts, NA, USA). Specifically, an ROI is manually defined within the tumor core in the contrast image. The average image intensity for frame 1 (reference image pre-PS101 injection) and frame 300 (contrast enhanced image 15 s after PS101 injection) and the difference between frame 1 and frame 300, was calculated. This was repeated for all three PS101 injections on day 0 and day 21. The average of these six values (three from each treatment day over two treatment days) was used as the contrast metric, and determined the imaging rank. These values were then used to produce a ranked score of contrast enhancement by sorting them in increasing order of contrast enhancement where a larger average contrast value is a higher imaging rank. The attained measured values were also used to evaluate if there were any changes in tumor perfusion over the three sequential treatments on either of the two treatment days.

Therapy Response Ranking

Non-responding animals, *i.e.,* animals that were sacrificed prior to 175 days, were ranked by survival time (shorter survival ranked lower). Complete responders were ranked by the day the tumor volume reached zero and stayed at zero *i.e.,* the shorter the time to reach zero tumor volume is a higher therapy rank. Both the contrast enhancement and therapy response ranking were performed by observers who were blinded to the other ranking.

Statistical Analysis

Results for average tumor normalized volume are expressed as mean ± standard error. Survival was compared using a Log-rank (Mantel-Cox) test between two groups. Contrast enhancement for comparing perfusion changes was evaluated using a simple linear regression. Therapy and imaging rank correlation was performed using nonparametric Pearsons correlation. A contingency table was used to compare the number of complete responders *via* Fishers exact test. A p-value less than 0.05 was considered statistically significant. All statistical analysis was performed in Prism 8.3.0 (GraphPad Software Inc, San Diego, CA, USA).

RESULTS

Tumor Growth and Development

Figure 2 shows the normalized tumor growth as a function of time for all three groups. For ease of visualization, markers are plotted every 4 days. **Supplemental Figure 2** shows the exact tumor volumes as a function of time.

When treated with PS101+US (**Figure 2A**) no therapeutic response was observed, as expected. The tumor growth curves in this group show a bimodal distribution; in one population 2 out of 9 mice (22%) had a two-fold tumor growth by day 21. The second population (78%) showed a rapid growth in the range of 2 to 6-fold growth over the first 21 days. All mice in the first population were able to survive past 21 days in contrast to only one mouse in the second population.

The mice treated with Doxil® (**Figure 2B**) showed a marked improvement over the PS101+US group with all mice surviving both treatment cycles. All mice showed either tumor growth stagnation or regression over the first 21 days. Once again, there was an inhomogeneous or bimodal distribution. One mouse (10%) showed complete regression/response by day 21; the remaining population (90%) showed tumor growth/recovery within 4 weeks after the last treatment (by day 49).

Treating mice using ACT with Doxil® showed a marked improvement over Doxil® alone (**Figure 2C**). Similar to both the PS101+US and Doxil® groups, there was an inhomogeneous population; in this instance three populations could be discerned. By day 21, three mice (38%; mice 4, 5, and 6 *c.f.*, **Supplemental Figure 3**) showed tumor regression. Two of the three mice (mice 4 and 5 *c.f.*, **Supplemental Figure 3**) stayed in complete remission until the end of the study (first population). Three mice (mice 6, 7, and 8 *c.f.*, **Supplemental Figure 3**) showed tumor re-growth after the second treatment cycle but presented a delayed response resulting in complete remission starting 70 ± 2 days after the last treatment cycle (*i.e.*, day 91) (second population). The third population (3 mice; 38%; mice 1, 2, and 3 *c.f.*, **Supplemental Figure 3**) showed continuous tumor re-growth and did not survive the entire study period.

Figure 3 compares the perfusion of the ACT with Doxil® tumors over the three sequential injections for both treatment days. The linear regression was not significantly different from zero for either of the treatment days indicating similar tumor perfusion in all three sequential injections.

Survival

Median Overall Survival

Figure 4 shows the survival curves for the animals in the three study groups. PS101+US resulted in a median overall survival of 21 days. Treating with Doxil® improved overall survival significantly to 67 days ($p = 0.04$ *vs.* PS101+US) while treating using ACT with Doxil® further improved survival ($p = 0.02$ *vs.* Doxil®, $p = 0.0004$ *vs.* PS101+US).

Complete Responders

Both the Doxil® and ACT with Doxil® group had complete responders, *i.e.,* mice that showed no signs of tumor burden and survived the complete study period of 175 days. There were no survivors for the PS101+US group. The Doxil® group had a

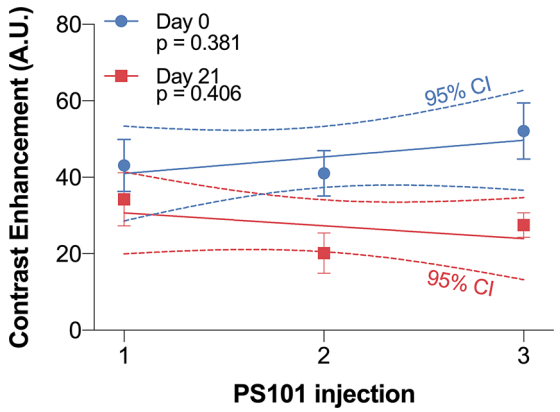

FIGURE 3 | Contrast enhancement difference 15 s post-PS101 injection for each of the three injections for day 0 (1st treatment) and day 21 (2nd treatment). The linear regression slope between the three sequential injections was not significantly different from zero on day 0 ($p = 0.381$) or day 21 ($p = 0.406$).

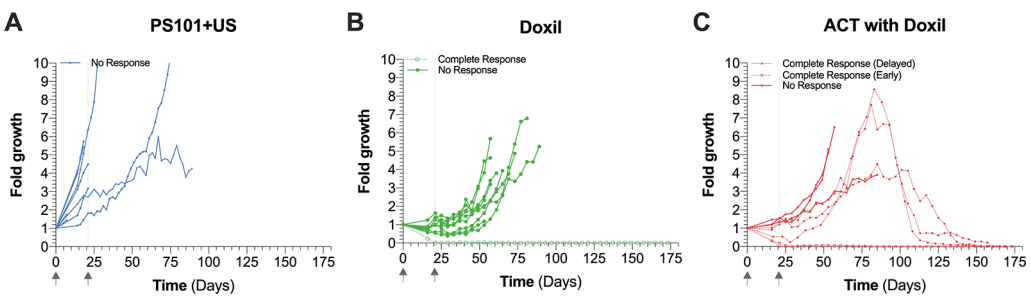

FIGURE 2 | Normalized tumor growth as a function of time. Each panel shows all the mice for the respective groups. Mice unable to survive the complete treatment period are considered non-responders. Gray arrows indicate the two treatment time points. Panel **(A)** shows the growth curves of the mice treated with PS101+US. Panel **(B)** shows the growth curves of the mice treated with Doxil®. Panel **(C)** shows the response of the mice treated with acoustic cluster therapy (ACT) with Doxil®.

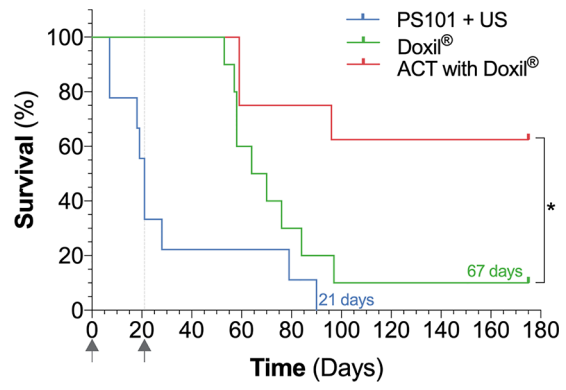

FIGURE 4 | Survival curves of the three groups evaluated in the study. *p = 0.02.

single complete responder (10%), while the ACT with Doxil® group had five complete responders (63%) clearly indicating the benefit of ACT; this difference was significant (p = 0.03).

Imaging Biomarkers of Therapeutic Response

Figure 5 shows the correlation between the imaging and therapy rankings. A significant positive correlation was observed (p = 0.0005, r = 0.96, Pearson r) indicating that non-linear contrast is a predictor of therapeutic outcome when using ACT with Doxil®. The therapy ranking of each mouse is shown in **Supplemental Table 2**.

Figure 6 shows example images of a low and a high imaging contrast ranked mouse from the ACT with Doxil® group. The sepia toned frames are example non-linear imaging mode frames that help visualize tumor perfusion. The last row (row 3), of images are subtractions of the pre-PS101 images (row 1) from the 15 s post-PS101 images (row 2). This subtraction removes the tissue harmonic component and emphasizes the Sonazoid component. In the two illustrated examples, pre-PS101 (**Figure 6**, first row), the tumors (red arrows) appear as a hypoechoic region in both B-mode and contrast-mode images and little difference can be seen between the two. The contrast observed is due to the tissue harmonic imaging. In the low imaging contrast ranked mouse (*Animal 2* in **Supplemental Figure 3** and **Supplemental Table 2**) very little enhancement can be seen when comparing pre-PS101 injection to 15 s post-PS101 injection, both in B-mode and non-linear contrast mode images, *i.e.,* the tumor remains hypoechoic (*c.f.,* **Figures 6A, B** *vs.* **Figures 6C, D**). This minimal change in image brightness can be clearly observed in the difference frames, both for contrast-mode and B-mode (**Figures 6E, F**). These frames only show the presence of microbubbles, as the tissue harmonic contrast component is removed *via* subtraction.

In the high imaging contrast ranked mouse (*Animal 7* in **Supplemental Figure 3** and **Supplemental Table 2**) 15 s post-PS101 injection a contrast enhancement can be observed in both B-mode and contrast-mode resulting in the tumor being visualized going from hypo-echoic to hyper echoic (*c.f.,* **Figures 6G, H** *vs.* **Figures 6I, L**). The difference frames (**Figures 6K, L**) clearly show the tumor noticeably bright in both the contrast-mode and B-mode indicating that this tumor is better perfused than the low imaging rank tumor.

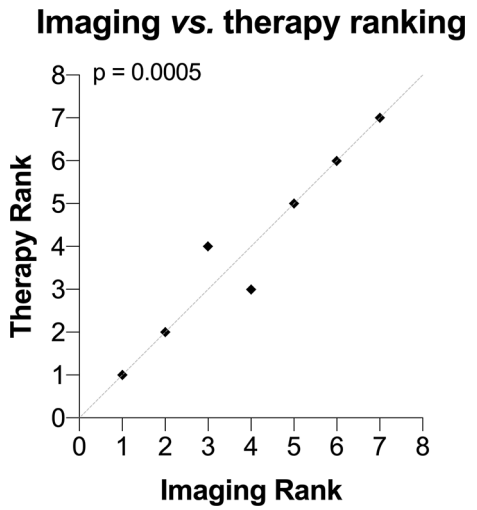

FIGURE 5 | Correlation between ultrasound imaging contrast rank and therapy rank. A significant correlation between the imaging and therapy rank was observed (p = 0.0005). The dashed gray line is the line of identity.

DISCUSSION

The use of ACT with Doxil® shows a significant improvement in therapeutic response *versus* Doxil® alone, indicating the potential of ACT to work synergistically with a liposomal nanoparticle drug formulation. This study shows that ACT with Doxil® can significantly improve the percentage of complete responders and extends overall survival. In addition, our results show that microbubble contrast enhancement of the tumor can be used as a therapeutic biomarker predicating the efficacy of ACT with Doxil, where more contrast enhancement indicates a potential for better treatment.

Tumor Model

All groups in this study showed an inhomogeneous tumor growth behavior in response to therapy, similar to that observed in clinical practice which is also given as a key factor behind the difficulty in successfully treating TNBC (Bianchini et al., 2016). In clinical disease progression, metastatic spread is also a significant reason for poor prognosis, Metastatic spread was, however, not evaluated in this study, the reason being that due to the high toxicity of treating with Doxil®, the addition of a whole body imaging step to detect metastasis (such as bioluminescence imagine) may have increased the stress on the mice, potentially introducing early dropouts. Metastatic spread should, however, be evaluated in future studies to determine if

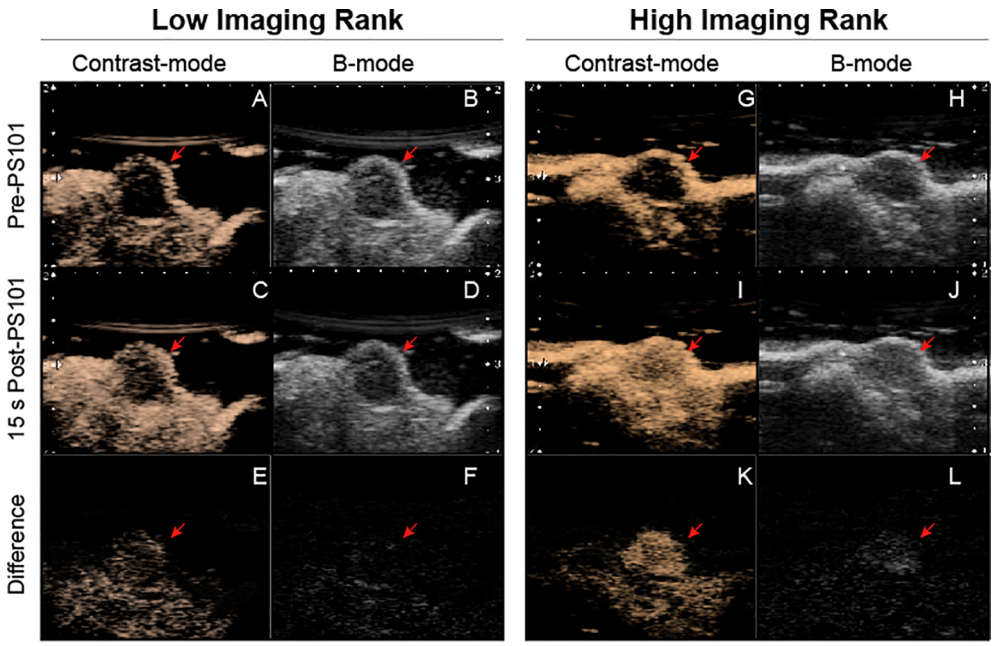

FIGURE 6 | Ultrasound images of two acoustic cluster therapy (ACT) with Doxil® mice just before and during the activation ultrasound procedure. The left panel (frames **A–F**) shows a low contrast image-ranked tumor and the right panel (frames **G–L**) shows a high contrast image-ranked tumor. The first row (frames **A**, **B**, **G**, and **H**) are prior to PS101 injection. The second row (frames **C**, **D**, **I**, and **J**) are 15 s post-PS101 injection, while activation ultrasound is being applied. The third row (frames **E**, **F**, **K**, and **L**) shows the difference between first and second row. A pronounced difference is observable between the low image-ranked tumor and high image-ranked tumor in both the contrast-mode and B-mode images.

there are correlations with overall survival and primary tumor size when treating using ACT with Doxil®.

Tumor Growth Inhibition and Survival

As expected, PS101+US showed the lowest overall survival indicating that PS101+US had little to no effect on tumor growth. To verify this an additional control group that received no treatment would have been ideal but was avoided to reduce the use of animals and unnecessary stress (Directive 2010/63/EU, 2010).

Doxil® showed a significant effect with the majority of animals having tumor regression, despite this, all but one mouse showed tumor re-growth after the two cycles of treatment. Transferring this to a clinical scenario, this would indicate that a patient may need many more treatment cycles or continuous therapy for an improved outcome.

When performing ACT with Doxil®, a synergistic effect was observed greatly improving the therapeutic efficacy of Doxil®. Some tumors showed rapid regression after a single treatment cycle. One of these mice (**Supplemental Figure 3**, mouse 6) showed re-growth once treatment was stopped. This single mouse showed a delayed response, and by the end of the treatment, no tumor could be detected. Furthermore, after a few weeks, the majority of mice (63%) had no observable tumors over 154 days after the last treatment. This indicated a significant improvement in response rate and therapeutic benefit, especially when compared to Doxil® alone. If such results could directly translate to the clinical response, this would indicate that patients would need fewer treatment cycles, resulting in less toxicity, with an improved therapeutic outcome.

When comparing the survival curves, ACT with Doxil® was significantly better than Doxil®. While the Doxil® group had a median overall survival of 67 days, due to the high curative efficacy of ACT with Doxil® it was not possible to calculate a representative median survival, further emphasizing the marked improvement over Doxil®.

PS101+US had no effect on tumor growth or survival by itself, whereas when performed with Doxil® a significant improvement was observed. This may imply that the mechanical action of PS101+US is able to enhance the efficacy of Doxil® by either increasing drug delivery or further sensitizing tissue; however, more research should be performed to determine the mechanisms of action behind the *in-vivo* synergy of ACT with therapeutic agents.

Imaging Biomarkers of Therapeutic Response

The correlation between the ultrasound image contrast and therapeutic outcome indicates that the more perfused a tumor is the better the treatment efficacy. This may indicate that higher perfusion allows more PS101 and/or more drugs to enter the tumor volume and may be a requisite for successful ACT based therapy. This indicates that tumor perfusion may be used as a therapeutic biomarker or predictor of efficacy. With the need for personalized

medicine being the next evolution of current treatment strategies this points toward ACT based therapies being an optimal choice for the next generation of therapeutics (Tran et al., 2018).

Comparing clinical findings for various breast cancer types, tumours of patients with TNBC show the largest amount of microbubble perfusion when using contrast enhanced ultrasound indicating the potential for ACT in treating patients with TNBC (Masumoto et al., 2016).

The primary limitations of this data set are the limited number of animals (n = 8), the limited proportion of the volume of each tumour (only a single imaging plane), that were studied. Future work should aim to determine the sensitivity and specificity of such imaging biomarkers using sufficient animals for adequately powered estimates, as well as characterize PS101 uptake in the entire tumor volume.

Limitations and Future Work

While this study provides strong evidence that ACT with Doxil® can enhance the therapeutic efficacy versus Doxil® alone, there are several limitations that should be addressed in future studies.

The underlying mechanisms of this enhanced therapeutic effect were not evaluated within this study. While it may be assumed that this is due to increased delivery of the chemotherapeutic agent or changing the release profile this has not been directly proven within this model. Nevertheless, previous work has demonstrated that ACT is able to enhance the deposition of large dyes molecules (2.5 nm diameter) into tissue *in vivo* (Van Wamel et al., 2016b) indicating that this may be a contributory mechanism. The mechanism underlying the delayed therapeutic response is, however, as yet not clearly understood.

In this study, three sequential injections of PS101 were performed, spaced only 6 min apart. As the *in-vivo* lifetime of PS101 can be longer than this time period, this allows the assumption that each subsequent injection may have residual un-activated PS101, increasing the attenuation with each injection. Consequently, further work should be performed to optimize the PS101 dose and acoustic conditions to account for this potential phenomenon.

Vascular shut down due to ultrasound and microbubble treatment has been reported at high mechanical indices [*e.g.*, MI 1.6 (Goertz et al., 2012)]. In our study here, no vascular shutdown was observed either after any of the three PS101 injections or on any of the treatment days. This indicates that vascular shut down may not be part of the mechanisms of action of ACT. This also supports the use of the three back-to-back injection of PS101 as the clusters will still be able to perfuse through the tumor.

To verify that the improved efficacy seen with ACT, over Doxil® alone, is due to the large activated ACT bubbles, not just the Sonazoid component, future work should include a Sonazoid control group.

Although the off-target toxicity/safety was not directly evaluated in this study it remains a key point of interest for such a targeted drug delivery mechanism. Extensive studies have been performed in several species and determined that there are minimal toxicities induced by ACT and, when they exist, they are transient and recoverable (Myhre et al., 2016; Bush et al., 2019).

While ultrasound and microbubbles have been used to enhance the treatment efficacy for TNBC (Bai et al., 2019; Jing et al., 2019; Song et al., 2019), this has not been previously explored with ACT and to our current knowledge, no other study has shown such a marked improvement in tumor regression, significantly improved survival and number of complete responders, and theranostic potential.

CONCLUSION

ACT significantly improves the response to treatment with Doxil® of human triple negative breast cancer in mice, as measured by tumor size and overall survival, with 63% of tumors entering complete regression with ACT versus 10% with Doxil® alone. ACT has potential theranostic attributes and ultrasound contrast enhancement during or before ACT treatment may be employed as a biomarker of therapeutic response and, potentially, for patient stratification in clinical management.

DATA AVAILABILITY STATEMENT

The datasets generated from this study can be found in the public repository hosted by "LabArchives" (https://mynotebook.labarchives.com/share_attachment/My%2520Notebook/MjMuNDAwMDAwMDAwMDAwMDAyfDQ5MDQxMS8xOC02L1RyZWVOb2RlLzMwMzgyMDMyMTV8NTkuNA==).

ETHICS STATEMENT

The animal study was reviewed and approved by The ICR Animal Welfare & Ethical Review Body.

AUTHOR CONTRIBUTIONS

NB, AH, AS, GB, VK, SE, PS, SvK, AW, CD, and JB contributed to the conception and design of the study. NB, AH, and GB performed the experiments. NB, AH, SpK, SvK, PS, and JB all co-wrote the manuscript. All authors contributed to the manuscript revision, read and approved the submitted manuscript.

FUNDING

This research was funded by Phoenix Solutions AS, partially through Research Council of Norway grant # 228604.

SUPPLEMENTARY MATERIAL

The Supplementary Material for this article can be found online at: https://www.frontiersin.org/articles/10.3389/fphar.2020.00075/full#supplementary-material

REFERENCES

Bai, M., Dong, Y., Huang, H., Fu, H., Duan, Y., Wang, Q., et al. (2019). Tumour targeted contrast enhanced ultrasound imaging dual-modal microbubbles for diagnosis and treatment of triple negative breast cancer. *RSC Adv.* 9, 5682–5691. doi: 10.1039/C8RA09737B

Bianchini, G., Balko, J. M., Mayer, I. A., Sanders, M. E., and Gianni, L. (2016). Triple-negative breast cancer: challenges and opportunities of a heterogeneous disease. *Nat. Rev. Clin. Oncol.* 13 (11), 674–690. doi: 10.1038/nrclinonc.2016.66

Bray, F., Ferlay, J., Soerjomataram, I., Siegel, R. L., Torre, L. A., and Jemal, A. (2018). Global cancer statistics 2018: GLOBOCAN estimates of incidence and mortality worldwide for 36 cancers in 185 countries. *CA. Cancer J. Clin.* 68, 394–424. doi: 10.3322/caac.21492

Bush, N. L., Healey, A., Shah, A., Box, G., Kirkin, V., Kotopoulis, S., et al. (2019). Therapeutic dose response of acoustic cluster therapy in combination with irinotecan for the treatment of human colon cancer in mice. *Front. Pharmacol.* 10, 1299. doi: 10.3389/FPHAR.2019.01299

Carpentier, A., Canney, M., Vignot, A., Reina, V., Beccaria, K., Horodyckid, C., et al. (2016). Clinical trial of blood-brain barrier disruption by pulsed ultrasound. *Sci. Transl. Med.* 8, 343re2. doi: 10.1126/scitranslmed.aaf6086

Devarajan, P. V., and Jain, S. (2015). Targeted drug delivery: concepts and design. Cham: Springer International Publishing. doi: 10.1007/978-3-319-11355-5

Dimcevski, G., Kotopoulis, S., Bjånes, T., Hoem, D., Schjøtt, J., Gjertsen, B. T., et al. (2016). A human clinical trial using ultrasound and microbubbles to enhance gemcitabine treatment of inoperable pancreatic cancer. *J. Control. Release* 243, 172–181. doi: 10.1016/j.jconrel.2016.10.007

Directive 2010/63/EU (2010). Directive 2010/63/EU of the European Parliament and of the Council of 22 September 2010 on the protection of animals used for scientific purposes. *Off. J. Eur. Union.* doi: 10.1002/9780470015902.a0024190

Foulkes, W. D., Smith, I. E., and Reis-Filho, J. S. (2010). Triple-negative breast Cancer. *N. Engl. J. Med.* 363, 1938–1948. doi: 10.1056/NEJMra1001389

Goertz, D., Todorova, M., and Mortazavi, O. (2012). Antitumor effects of combining docetaxel (taxotere) with the antivascular action of ultrasound stimulated microbubbles. *PloS One.* 7 (12), e52307. doi: 10.1371/journal.pone.0052307.

Gonçalves, H., Guerra, M. R., Duarte Cintra, J. R., Fayer, V. A., Brum, I. V., and Bustamante Teixeira, M. T. (2018). Survival study of triple-negative and non–triple-negative breast cancer in a Brazilian Cohort. *Clin. Med. Insights. Oncol.* 12, 117955491879056. doi: 10.1177/1179554918790563

Healey, A. J., Sontum, P. C., Kvåle, S., Eriksen, M., Bendiksen, R., Tornes, A., et al. (2016). Acoustic cluster therapy: in vitro and ex vivo measurement of activated bubble size distribution and temporal dynamics. *Ultrasound. Med. Biol.* 42, 1145–1166. doi: 10.1016/j.ultrasmedbio.2015.12.011

Jing, Y., Xiu-Juan, Z., Hong-Jiao, C., Zhi-Kui, C., Qing-Fu, Q., En-Sheng, X., et al. (2019). Ultrasound-targeted microbubble destruction improved the antiangiogenic effect of Endostar in triple-negative breast carcinoma xenografts. *J. Cancer Res. Clin. Oncol.* 145, 1191–1200. doi: 10.1007/s00432-019-02866-7

Jitariu, A.-A., Cîmpean, A. M., Ribatti, D., and Raica, M. (2017). Triple negative breast cancer: the kiss of death. *Oncotarget.* 8 (28), 46652–46662. doi: 10.18632/oncotarget.16938

Kooiman, K., Vos, H. J., Versluis, M., De Jong, N., Jong, N., and De Jong, N. (2014). Acoustic behavior of microbubbles and implications for drug delivery. *Adv. Drug Deliv. Rev.* 72, 28–48. doi: 10.1016/j.addr.2014.03.003

Kotopoulis, S., Stigen, E., Popa, M., Safont, M. M., Healey, A., Kvåle, S., et al. (2017). Sonoporation with Acoustic Cluster Therapy (ACT) induces transient tumour volume reduction in a subcutaneous xenograft model of pancreatic ductal adenocarcinoma. *J. Control. Release* 245, 70–80. doi: 10.1016/j.jconrel.2016.11.019

Lentacker, I., De Cock, I., Deckers, R., De Smedt, S. C., and Moonen, C. T. W. (2014). Understanding ultrasound induced sonoporation: Definitions and underlying mechanisms. *Adv. Drug Deliv. Rev.* 72, 49–64. doi: 10.1016/j.addr.2013.11.008

Maeda, H., Wu, J., Sawa, T., Matsumura, Y., and Hori, K. (2000). Tumor vascular permeability and the EPR effect in macromolecular therapeutics: A review. *J. Control. Release* 65, 271–284. doi: 10.1016/S0168-3659(99)00248-5

Martin, K. H., and Dayton, P. A. (2013). Current status and prospects for microbubbles in ultrasound theranostics. *Wiley Interdiscip. Rev. Nanomed. Nanobiotechnol.* 5, 329–345. doi: 10.1002/wnan.1219

Masumoto, N., Kadoya, T., Amioka, A., Kajitani, K., Shigematsu, H., Emi, A., et al. (2016). Evaluation of malignancy grade of breast cancer using perflubutane-enhanced ultrasonography. *Ultrasound. Med. Biol.* 42, 1049–1057. doi: 10.1016/J.ULTRASMEDBIO.2015.12.023

Miller, D. L., Averkiou, M. A., Brayman, A. A., Everbach, E. C., Holland, C. K., Wible, J. H., et al. (2008). Bioeffects considerations for diagnostic ultrasound contrast agents. *J. Ultrasound. In Med.* (4), 623–634. doi: 10.7863/jum.2008.27.4.611

Myhre, O., Bjørgan, M., Grant, D., Hustvedt, S. O., Sontum, P. C., and Dirven, H. (2016). Safety assessment in rats and dogs of acoustic cluster therapy, a novel concept for ultrasound mediated, targeted drug delivery. *Pharmacol. Res. Perspect.* 4 (6), e00274. doi: 10.1002/prp2.274

Nelson, T. R., Fowlkes, J. B., Abramowicz, J. S., and Church, C. C. (2009). Ultrasound biosafety considerations for the practicing sonographer and sonologist. *J. Ultrasound. Med.* 28, 139–150. doi: 10.7863/jum.2009.28.2.139

Nizzero, S., Ziemys, A., and Ferrari, M. (2018). Transport barriers and oncophysics in cancer treatment. *Trends In Cancer.* 4 (4), 277–228. doi: 10.1016/j.trecan.2018.02.008

O'Brien, M. E. R., Wigler, N., Inbar, M., Rosso, R., Grischke, E., Santoro, A., et al. (2004). Reduced cardiotoxicity and comparable efficacy in a phase III trial of pegylated liposomal doxorubicin HCl (CAELYX™/Doxil®) versus conventional doxorubicin for first-line treatment of metastatic breast cancer. *Ann. Oncol.* 15 (3), 440–449. doi: 10.1093/annonc/mdh097

Park, K. (2016). Acoustic cluster therapy for better treatment of solid tumors. *J. Control. Release.* 236, 117. doi: 10.1016/j.jconrel.2016.07.010

Song, K.-H., Trudeau, T., Kar, A., Borden, M. A., and Gutierrez-Hartmann, A. (2019). Ultrasound-mediated delivery of siESE complexed with microbubbles attenuates HER2+/- cell line proliferation and tumor growth in rodent models of breast cancer. *Nanotheranostics* 3, 212–222. doi: 10.7150/ntno.31827

Sontum, P., Kvåle, S., Healey, A. J., Skurtveit, R., Watanabe, R., Matsumura, M., et al. (2015). Acoustic Cluster Therapy (ACT)-a novel concept for ultrasound mediated, targeted drug delivery. *Int. J. Pharm.* 495, 1019–1027. doi: 10.1016/j.ijpharm.2015.09.047

Tran, W. T., Childs, C., Probst, H., Farhat, G., and Czarnota, G. J. (2018). Imaging biomarkers for precision medicine in locally advanced breast cancer. *J. Med. Imaging Radiat. Sci.* 49 (4), 342–351. doi: 10.1016/j.jmir.2017.09.006

Tsutsui, J. M., Xie, F., and Porter, R. T. (2004). The use of microbubbles to target drug delivery. *Cardiovasc. Ultrasound.* 2, 23. doi: 10.1186/1476-7120-2-23

Unga, J., and Hashida, M. (2014). Ultrasound induced cancer immunotherapy. *Adv. Drug Deliv. Rev.* 72, 144–153. doi: 10.1016/j.addr.2014.03.004

Van Wamel, A., Healey, A., Sontum, P. C., Kvåle, S., Bush, N., Bamber, J., et al. (2016a). Acoustic Cluster Therapy (ACT) - pre-clinical proof of principle for local drug delivery and enhanced uptake. *J. Control. Release* 224, 158–164. doi: 10.1016/j.jconrel.2016.01.023

Van Wamel, A., Healey, A., Sontum, P. C., Kvåle, S., Bush, N., Bamber, J., et al. (2016b). Acoustic Cluster Therapy (ACT) — pre-clinical proof of principle for local drug delivery and enhanced uptake. *J. Control. Release* 224, 158–164. doi: 10.1016/j.jconrel.2016.01.023

Van Wamel, A., Sontum, P. C., Healey, A., Kvåle, S., Bush, N., Bamber, J., et al. (2016c). Acoustic Cluster Therapy (ACT) enhances the therapeutic efficacy of paclitaxel and Abraxane® for treatment of human prostate adenocarcinoma in mice. *J. Control. Release* 236, 15–21. doi: 10.1016/j.jconrel.2016.06.018

Working, P. K., Newman, M. S., Huang, S. K., Mayhew, E., Vaage, J., and Lasic, D. D. (1994). Pharmacokinetics, biodistribution and therapeutic efficacy of doxorubicin encapsulated in stealth® liposomes (doxil®. *J. Liposome. Res.* 4 (1), 667–687. doi: 10.3109/08982109409037065

Workman, P., Aboagye, E. O., Balkwill, F., Balmain, A., Bruder, G., Chaplin, D. J., et al. (2010). Guidelines for the welfare and use of animals in cancer research. *Br. J. Cancer.* 102 (11), 1555–77. doi: 10.1038/sj.bjc.6605642

Conflict of Interest: AH, SpK, SvK, and PS were employed by the company Phoenix Solutions AS at the time of manuscript submission. NB, AH, SvK, PS, and AV are shareholders of Phoenix Solutions AS at the time of submission. The authors declare that this study received funding from Phoenix Solutions AS. The funder had the following involvement with the study: study design, data analysis, decision to publish and preparation of the manuscript.

The remaining authors declare that the research was conducted in the absence of any commercial or financial relationships that could be construed as a potential conflict of interest.

The two reviewers declared their involvement as co-editors in the Research Topic, and confirm the absence of any other collaboration.

frontiers in Pharmacology

ORIGINAL RESEARCH
published: 01 April 2020
doi: 10.3389/fphar.2020.00363

Nanobubble Mediated Gene Delivery in Conjunction With a Hand-Held Ultrasound Scanner

*Hiroshi Kida[1], Koyo Nishimura[2], Koki Ogawa[2], Akiko Watanabe[1], Loreto B. Feril[1], Yutaka Irie[1], Hitomi Endo[1], Shigeru Kawakami[2] and Katsuro Tachibana[1]**

[1] Department of Anatomy, Fukuoka University School of Medicine, Fukuoka, Japan, [2] Department of Pharmaceutical Informatics, Graduate School of Biomedical Sciences, Nagasaki University, Nagasaki, Japan

Recent research has revealed that nanobubbles (NBs) can be an effective tool for gene transfection in conjunction with therapeutic ultrasound (US). However, an approach to apply commercially available hand-held diagnostic US scanners for this purpose has not been evaluated as of now. In the present study, we first compared *in vitro*, the efficiency of gene transfer (pCMV-Luciferase) with lipid-based and albumin-based NBs irradiated by therapeutic US (1MHz, 5.0 W/cm^2) in oral squamous carcinoma cell line HSC-2. Secondly, we similarly examined if gene transfer in mice is possible using a clinical hand-held US scanner (2.3MHz, MI 1.0). Results showed that lipid-based NBs induced more gene transfection compared to albumin-based NBs, *in vitro*. Furthermore, significant gene transfer was also obtained in mice liver with lipid-based NBs. Sub-micro sized bubbles proved to be a powerful gene transfer reagent in combination with conventional hand-held ultrasonic diagnostic device.

Keywords: gene transfection, sonoporation, ultrasound, nanobubble, ultrasound diagnostic device

OPEN ACCESS

Edited by:
Marc Derieppe, Princess Maxima Center for Pediatric Oncology, Netherlands

Reviewed by:
Caterina Guiot, University of Turin, Italy
Anthony Clouet, Bracco, Switzerland

***Correspondence:**
Katsuro Tachibana
k-tachi@fukuoka-u.ac.jp

Specialty section:
This article was submitted to Translational Pharmacology, a section of the journal Frontiers in Pharmacology

Received: *18 November 2019*
Accepted: *10 March 2020*
Published: *01 April 2020*

Citation:
Kida H, Nishimura K, Ogawa K, Watanabe A, Feril LB, Irie Y, Endo H, Kawakami S and Tachibana K (2020) Nanobubble Mediated Gene Delivery in Conjunction With a Hand-Held Ultrasound Scanner. Front. Pharmacol. 11:363. doi: 10.3389/fphar.2020.00363

INTRODUCTION

For the past two decades, there has been much research on ultrasound (US)-mediated drug delivery. Microbubbles (MBs) are considered to play a major role in increasing permeabilization of various drugs through the cell membrane and into the cytoplasm (Tachibana et al., 1999). Recent experiments using high speed video cameras under optic microscopes have shown that oscillation of MBs during US irradiation actually disrupts the cell membrane to form transient pores (Kudo et al., 2009; Nejad et al., 2016; Song et al., 2019). This phenomenon, frequently referred as sonoporation (Lammertink et al., 2015), induces increase in cell uptake of administrated drugs, molecules, and in some cases plasmid DNA (Sennoga et al., 2017). Consequently, the combination of MB and US has been proposed as a novel therapeutic approach to deliver functional genetic molecules such as pDNA, siRNA, antisense oligonucleotides to cancer cells, normal tissues, and various organs for the purpose of preventing or treating diseases.

Previous studies have suggested that altering the MB shell compositions is of great importance for the purpose of increasing the efficacy of drug delivery (Dicker et al., 2013; Abenojar et al., 2019). MB shells that have targeting ligands are especially attractive from the viewpoint of concentrating functional genes to a specific site for gene therapy. Furthermore, such shell compositions as albumin and lipids can serve as a versatile carrier for various types of drugs (Paefgen et al., 2015). Drug

incorporated MBs can be destructed and payload released at the site of interest by externally applied therapeutic US (Cochran et al., 2011; Zhu et al., 2016). A considerable amount of gene therapy related literature exists detailing application of the above technique to treat various tissues and organs, including skeletal muscles (Taniyama et al., 2002a; Li et al., 2003), blood vessels (Taniyama et al., 2002b), cornea (Sonoda et al., 2006), and the brain (Negishi et al., 2015).

Generally, the MB used for drug delivery is between 1 and 10 μm in diameter. These sizes which are similar to red blood cells, limit MB extravasation from the bloodstream into the extravascular space in tumors and normal tissues. This becomes a major obstacle when taking into account the necessity to have the therapeutic gene and MB at close proximity to the target cell when irradiating US to a localized site. On the other hand, sub-micron sized NBs (recently officially termed as ultra-fine bubbles) have a potential advantage over MBs due to the fact that having a diameter in the nanoscale makes possible for them to extravasate through the vascular wall structure (Wu et al., 2013). Furthermore, NBs injected into the bloodstream can more easily accumulate in tumor vasculature due to the enhanced permeability and retention (EPR) effect.

Recent advances in acoustic technology have led to the miniaturization of diagnostic US devices to the size of laptop computers and mobile phones. These so called hand-held US scanners are used for bedside physical examination and have become a common place modality (Lapostolle et al., 2006). Although commercial US scanners are widely available for imaging and diagnosis in the clinical setting, to our knowledge, there has never been an approach on using the device for therapy in combination with NBs and genes. In this study, we first fabricated an albumin and lipid-based NBs and evaluated their effect on transfection efficiency *in vitro*. Secondly, a small clinically applicable US imaging device was applied to animals in conjunction with venous injection of genes and NBs. The final goal of the present study was to determine if the US intensities and acoustic parameters from small portable US scanners are adequate as to induce gene transfection in animals.

MATERIAL AND METHODS

Preparation of pDNA

pNL1.3CMV [secNluc/CMV] encoding secreted NanoLuc (secNluc) luciferase and pCMV-eGFP encoding the enhanced green fluorescent protein (eGFP) were purchased from Promega (Madison, WI, USA) and Nepagene (Chiba, JP), respectively. The firefly luciferase gene expression vector driven by a cytomegalovirus (CMV) promoter, pCMV-luciferase (Luc), was constructed as previously mentioned (Kawakami et al., 2002).

pDNA was amplified in Escherichia coli strain DH5α. After isolation, pDNA was purified using endotoxin-free plasmid purification kit. The pDNA was dissolved in Milli-Q water and stored at −20 °C prior to each experiment.

Preparation of Nanobubbles

The solutions of lipid based nanobubbles (L-NBs) and human serum albumin based nanobubbles (A-NBs) were prepared as follows. Firstly, L-NBs were extracted from commercially available US contrast agent, Sonazoid (Daiichi Sankyo, Tokyo, JP), perfluorobutane incapsulated with a phospholipid shell. The powder was dissolved and mixed following the manufacturer's instructions and utilized within 2 h after preparation, however, for *in vitro* experiments, the Sonazoid powder was directly dissolved with revised Eagle's Minimum Essential Media (opti-MEM: Thermo Fisher Scientific, Waltham, MA USA) instead of distilled water. The bubble including solution was then transferred to the 5 ml tube and centrifuged at 1,200 rpm for 10 min (MX-301; TOMY, Tokyo, JP) to separate the NB and MB component. The necessary amount of NBs within the transparent solution at the bottom of the tube was gently aspirated with a needle (18 G) into a 2.5 ml plastic disposable syringe (Terumo, Tokyo, JP). The 100% solution of NBs was diluted with equal amount of opti-MEM to 50 and 25%. For *in vivo* experiment, Sonazoid powder was reconstituted in 2 ml sterilized distilled water as recommended, and NBs were extracted in the same manner as in the *in vitro* experiments.

Secondly, human serum albumin based NBs were prepared according to a previous study reported elsewhere (Lafond et al., 2018). Briefly, the air in a plastic container tube (height, 30 mm, outer diameter, 25 mm) was replaced with 15 ml of perfluoropropane (C3F8; Takachiho Chemical Industrial, Tokyo, JP) gas using a 23-gauge needle inserted through a small opening in a custom made cap. Ten-ml sterile solution of 0.06% human serum albumin (fraction V, purity 96%; Aventis Behring L.L.C., IL, USA) in opti-MEM (Thermo Fisher Scientific, Waltham, MA, USA) was added in the gas filled container tube. The C3F8 gas and albumin solution in the container were tightly sealed to prevent gas leakage. The container tubes were then placed into a high-speed shaking-type tissue homogenizer device (Precellys Evolution; Bertin Instruments, France) and shaken four times at high speed under the following conditions: 6,500 rpm, 60 s duration, 5 min pause on ice between each shaking phase. After finishing all the shaking phases, the samples were incubated at room temperature for 1 h. To extract uniformly sized NBs from the agitated solution, centrifugation was carried out at 100 g for 10 min to separate all MBs and NBs. Similarly, 0.06% human serum albumin /distilled water NBs were prepared for *in vivo* experiment.

Characteristic Analysis of Nanobubbles

The physical character of L-NBs and A-NBs were measured as described previously (Watanabe et al., 2019). The particle size of NBs was measured by nanoparticle tracking analysis (NTA) device (NanoSight LM10; Malvern Instruments, Worcestershire, UK). The nanoparticle suspension was illuminated by a 638 nm wavelength red laser. The nanoparticle movement was visualized by light scattering and the Brownian motion recorded by a CCD camera (C11440-50B; Hamamatsu Photonics K.K., Shizuoka, JP). The above system automatically detects the center position of nanoparticles and tracks each particle motion in a two-

dimensional plane for later calculation of the average moving distance under Brownian motion. The image of particle movement with NTA was recorded for 60 s at room temperature. The range of particle size measurement of NTA method was adjusted from 10 to 1,000 nm. The particle size was estimated by the average moving distance to the Stokes-Einstein equation. The NBs suspension of 0.5 ml was injected into the sample measurement chamber of the Nanosight system with a 1.0 ml volume plastic syringe (Terumo, Tokyo, JP). Sample image capturing and data analysis were performed using the application software (NTA 3.2 Dev Build 3.2.16). All sample measurement experiments were performed independently for each sample. Particle size was presented as a mean and mode ± standard error of the average of three measurements.

The size and number of L-NBs and A-NBs were measured by a flow cytometer (CytoFLEX; Beckman Coulter, CA, USA). The flow cytometer was equipped with a 405 nm (violet) laser to detect the nanoparticles. The flow cytometer was set up to measure the Side Scatter (SS) from the violet laser for enhanced nanoparticle detection. The Violet-SS signal resolution limitation for particle detection was 200 nm. Superior resolution can be obtained with SS than the Forward Scatter (FS) signal and is suitable for measurement of small particles (e.g. nanoscale particles). In order to relate Violet-SS to a particle size, we calibrated the flow cytometer with beads of known size (Wisgrill et al., 2016; Zucker et al., 2016). The polystyrene standard beads (200, 350, and 800 nm; qNano Calibration Particles; Izon Science, Christchurch, New Zealand, 500 and 1000 nm; Archimedes Standard polystyrene beads; Malvern Instruments, Worcestershire, UK) was suspended in ultrapure water and measured beforehand with the flow cytometer. The acquired Violet-SS signals of lipid and albumin NBs were then analyzed by CytExpert analysis software version 2.0 (Beckman Coulter, CA, USA). A gate was created based on the size of standard beads in the range from 200 to 1,000 nm for determining the size of our fabricated NBs.

Cell Culture

Oral squamous carcinoma cell line HSC-2 was purchased from JCRB (Japanese Cancer Research Bank) cell bank and cultured in Minimum Essential Medium (MEM; Nacalai Tesque, Kyoto, JP) with 10% Fetal Bovine Serum (In Vitrogen, Tokyo, JP). Cells were maintained at 37.0 °C in humidified air with 5% CO_2. HSC-2 cells collected by trypsin–EDTA (Gibco, NY, USA). They were then washed and maintained in fresh medium immediately before each sonoporation experiments. On the day before the experiment, cells were collected and centrifuged at 100 g for 5 min. They were seeded by 4.5 x 10^3/well on 96 multi-well plate dish or Lab-Tek 16 well chamber slide (Thermo Fisher Scientific, Waltham, MA, USA). The cell line was free of viral pathogens with initial viability of more than 99% before use in the actual experiments.

In Vitro Sonoporation Method Using Cell Line on Multi-Wells Plate

pDNA encoding secNluc were respectively attenuated to 10 μg/ml with 25–100% L-NBs or A-NBs and used for *in vitro* sonoporation. The schematic representation of all steps of the experiments are depicted in **Figure 1**.

HSC2 cells were cultured on 96 multi-well plate, every second row and column, in order to prevent interaction of US irradiation to each other (**Figure 1G**). Five types of sonoporation medium; L-NBs of 25, 50, 100%, A-NBs and NBs-free opti-MEM as negative control were prepared for the

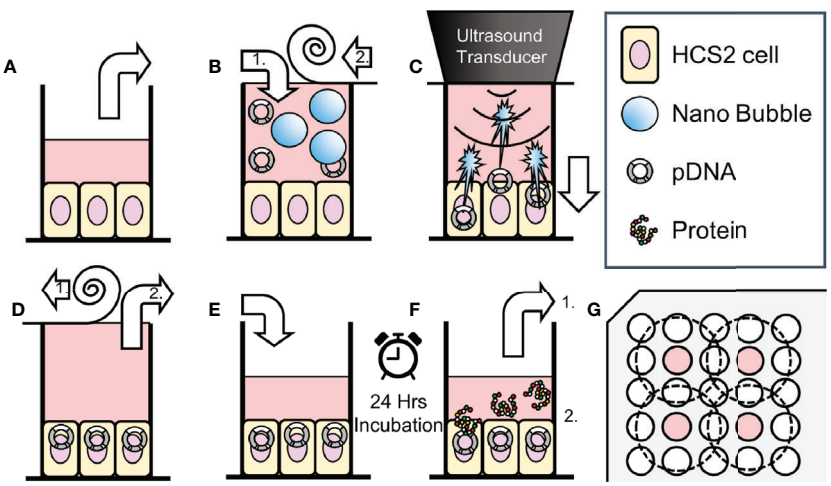

FIGURE 1 | Schematic representation of methods of sonoporation and analysis in 96-well plates. **(A)** Remove incubation medium from well of 96 multi well plate seeded HSC2 cells. **(B)** Fill wells with sonoporation medium, (B-1) and cover well with film (B-2). **(C)** Gene transfection by ultrasonic irradiation. **(D)** Film removal (D-1), and aspiration of battered medium (D-2). **(E)** Add new incubation medium. **(F)** After 24 h incubation, collect supernatant for reporter assay (F-1). Use cells for viability assay (use EGFP plasmid, fix and nuclear staining without collecting supernatant) (F-2). **(G)** Arrangement of wells seeded cells (indicated with color) and ultrasonic irradiation area (inside of dashed circle) on 96 multi-well plates.

experiments. Each cell culture wells were replaced and filled with 450 µl in all sonoporation samples pDNA incubated to the upper far edge of the wells followed by sealing the entire plate with acoustically transparent PCR film (Diversified Biotech, Dedham, MA, USA) (**Figures 1A, B**). Great attention was taken to avoid trapping of any gas or air bubbles within the wells. After this procedure, the plate with the PCR seal was placed below the surface of the US transducer via acoustic transmission gel (Aquasonic 100 gel; Parker lab, NJ, USA).

The cells were then exposed to US (**Figure 1C**). The US condition was at the driving frequency of 1 MHz, burst rate of 100 Hz, duty ratio of 50 % and intensity of 5.0 W/cm^2 and the US was emitted from the transducer (diameter 1.6 cm) (SONIDEL SP100, Sonidel Limited. Dublin, IRE). Each group was sonicated for 5 s in the first series of experiments. In order to clarify the relationship between ultrasonic irradiation time and gene transfer efficiency, the ultrasonic irradiation time was then varied at 0, 5, 10 s in the following experiments. After US irradiation treatment, the wells were emptied and the plate placed upside down on a paper towel to remove excess medium (**Figure 1D**). Then the same volume of medium before irradiation was re-filled to each culture well and incubated for another 24 h (**Figure 1E**). Reporter assay was later performed for measurement of luciferase activity.

eGFP pDNA was diluted to 100 µg/ml of L-NBs in the eGFP activity assay. Each well cultured with HSC2 cells of the 16 well chamber slide was replaced and filled with fresh 450 µl of 100% L-NB sonoporation medium. Then, the wells with secNluc were similarly sonicated (frequency; 1MHz, duty cycle; 50%, burst rate; 100 Hz, intensity; 5.0 W/cm^2). Sonoporation medium was replaced with new incubation medium in the wells after sonication.

Animals

Five-week-old male ddY mice were purchased from Kiwa Laboratory Animals (Wakayama, JP) and were housed in a cage in an air-conditioned room and maintained on a standard laboratory diet (CE-2, CLEA, Tokyo, JP) and water. All animal experiments were carried out in accordance with the guidelines for animal experimentation of Nagasaki University.

In Vivo Sonoporation Method

In vivo mice administrated with L-NBs or A-NBs with pDNA encording Luc was sonoporated with a clinical hand-held US imaging scanner under anesthesia. The schematic representation of all steps of the experiments is depicted in **Figure 2**.

Mice were anesthetized using an intraperitoneal injection that contained three types of mixed anesthetic agents (0.5 mg/kg of medetomidine, 4.0 mg/kg of midazolam, and 5.0 mg/kg of butorphanol), hold supine and removed abdominal hair (Kawai et al., 2011). The 300 µl solution consisting of 50 µg/150 µl pDNA in saline and 150 µl L-NBs or A-NBs was bolus injected manually from caudal vein. At 1 min after injection, US was transcutaneously irradiated toward the liver from center of abdomen with a Vscan Dual Probe (GE Healthcare, Waukesha, WI, USA) with Sector Probe (frequency, 2.3 MHz; mechanical index 1.0; thermal index 1.0, depth 6cm, duration 30 s). Mice were freed in the cage after awaking until sacrifice.

Evaluation of Luciferase Expression

In vitro luciferase activity was determined by bis-Coelenterazine (bis-CTZ) assay kit (JNC, Tokyo, JP) using Spark Multimode Microplate Reader (Tecan, Männedorf, Zürich, Switzerland). After 24 h incubation, 10 µl of incubation medium was retrieved on Costar 96-well white solid plate (Corning, NY, USA) each incubation well. Relative luminescence unit (RLU)

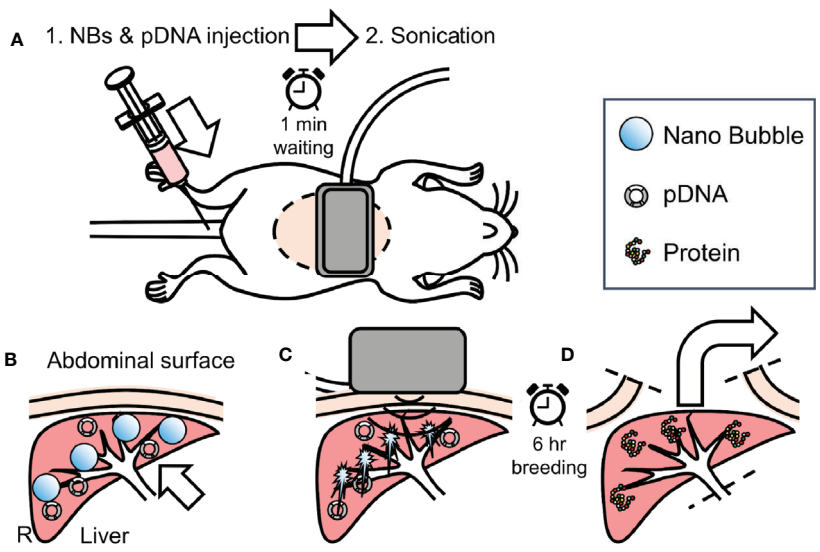

FIGURE 2 | Overview of *in vivo* sonoporation method. **(A)** intraoperative dorsal position. **(B)** accumulation NBs and pDNA into liver from caudal vein through venous and arterial system. **(C)** extracorporeal ultrasonic irradiation using clinical hand-held US imaging scanner. **(D)** 6 h after, sacrifice and harvest of organs for reporter assay.

value was plotted within 10 from 2 s after injection of 1 µg/100 µl bis-CTZ solution. Raw values were corrected with RLU value of blank wells with bis-CTZ solution only.

For evaluation of luciferase in the mice, the luciferase activity was measured as described previously (Fumoto et al., 2016). The liver was excised after 6 h from sonoporation. The extracted liver was homogenized with 5 times the cell lysate. The homogenized sample was centrifuged at 15,000 g for 5 min, at 4°C. Twenty microliters of tissue homogenate supernatant were mixed with 100 µl luciferase assay substrates (PicaGene, Toyo Ink Mfg, Tokyo, JP), The light produced was immediately measured using a luminometer (Lumat LB9507, Berthold Technologies, Bad Wildbad, Germany). Luciferase activity was inversely converted based on the amount of sample measured and the dilution factor with cell lysate, indicated as RLU/g of tissue.

Evaluation of eGFP Expression *In Vitro*

Cells were sonoporated with eGFP pDNA in 16well chamber slides and were fixed with 4% paraformaldehyde after 24 h of sonication. eGFP was immune-stained with an anti-GFP monoclonal antibody (Invitrogen, Carlsbad, CA, USA) at a dilution of 1:500, an Alexa488-conjugated secondary antibody (Abcam, Cambridge, MA, USA) and Hoechst 33342 (Dojindo Molecular Technologies, Kumamoto, JP) Fluorescence images of cells were analyzed using BZ-X710 digital microscopy (KEYENCE, Osaka, JP).

Statistical Analysis

Measurement data were displayed as mean ± standard error of the mean (s.e.m). Data was analyzed using unpaired t-test including Welch's correction. The statistically significant differences between various groups were analyzed using GraphPad Prism 8 software (GraphPad Software, La Jolla, CA, USA) and Microsoft Excel 2016 (Microsoft, Redmond, WA, USA). The probability value of p value < 0.05 was considered statistically significant.

RESULTS

Characterization of L-NBs and A-NBs

The size distribution data of the L-NBs and A-NBs obtained from NTA is shown in **Figures 3A, B**. The mean size of control sample of L-NBs and A-LB was 118.8±3.5 nm and 229.3±8.4 nm, respectively. The overlaid Violet-SS signal intensity histogram of L-NBs and A-NBs from FCM are shown in **Figures 3C, D**. The number of NBs having the same scattered Violet-SS signal intensity were correlated against standard known particles size ranging from 200 to 1,000 nm.

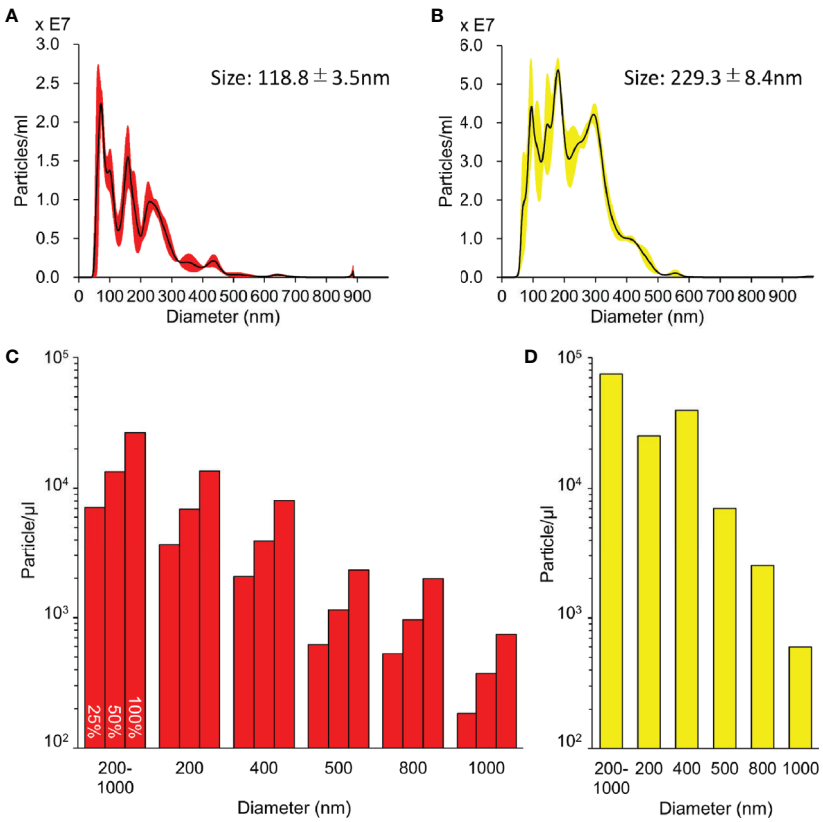

FIGURE 3 | Characterization of sonazoid and albumin NBs. **(A, B)** Detailed distribution and average size of L-NBs **(A)** and A-NBs **(B)** diluted in opti-MEM by NTA. **(C, D)** The concentrations and distribution of L-NBs **(C)** and A-NBs **(D)** based on Violet-SS signal resolution by FCM.

Both 100% L-NBs and A-NBs showed a unimodal distribution with peaks at 200 and 400 nm (modal diameter), respectively. The total number of A-NBs in the 200 to 1,000 nm size range was approximately 7.4 x 10^4 particles/μl, which was approximately three-fold compared with 0.26 x 10^4 particles/μl of 100% L-NBs. As expected, the concentration of L-NBs diluted to 25 and 50% was halved step by step while maintaining a 200 nm peak from 100% L-NBs.

In Vitro NBs and US Irradiation pDNA Transfection

Luciferase-expressing pDNA was introduced into HSC2 cells using various solution with or without NBs and 5 s sonication (**Figure 4A**). 24 h after ultrasonic irradiation, the expression level of luciferase increased in a concentration-dependent manner in L-NBs. The expression level of 100% L-NBs (RLU 15.03 ± 2.76 x10^5) was significantly increased, which was over 20-fold compared with sonicated opti-MEM without NB with pDNA as negative control (RLU 0.68 ± 0.16 x10^5). (p =0.0065).

Luciferase expression in A-NBs (RLU 1.81 ± 0.51 x10^5) increase to about three folds compared to negative control but was not statistically significant (p =0.1011).

The expression of luciferase was then examined when 25–100% of L-NBs was used by changing the ultrasonic irradiation time to 0 (no irradiation), 5 and 10 s (**Figure 4B**). The amount of expression markedly elevated when the irradiation time was increased to 5 or 10 from 0 s.

On immunohistological analysis of HCS2 after introducing pDNA encoding eGFP using 100% L-NBs and 5 s sonication, image of annularly distributed cells on culture well perforated in the center by bubble collapse energy was observed on low-power magnification field (**Figure 5A, C**). Strong eGFP protein expression was detected in cytoplasm on high-power magnification field (**Figure 5B, D**).

In Vivo Sonoporation Using Clinical Hand-Held US Imaging Scanner

In vivo gene transfection at the irradiated liver using L-NBs or A-NBs were evaluated after injection of solution consisting pDNA and NBs from caudal vein and transcutaneous ultrasonic irradiation for liver using a clinical hand-held US imaging scanner (**Figure 6**). In the luciferase activity assay group, a significant increase in expression was detected with the administration of L-NBs and ultrasonic irradiation. The combination of injection of NBs-free solution with pDNA and sonication, or the mixture consisting of pDNA and NBs injection without sonication alone did not result in increased luciferase expression. In the group with solution injected containing A-NBs groups, there was no difference in gene expression with or without ultrasonic irradiation, and was the same as negative control.

DISCUSSION

In recent years, US-mediated gene therapy has attracted much attention. Various type of MBs and acoustic parameters have been intensively investigated in order to increase gene transfection efficiency. Researchers have added modifications to the bubble shell with marker molecules that bind to targeted tissue sites, for example by coupling specific ligands (Paefgen et al., 2015). The shell can be composed from a variety of materials such as polymers, proteins, phospholipids, and surfactants. We previously compared several commercially available US contrast agents that have different MB shell characteristics and evaluated its gene transfection

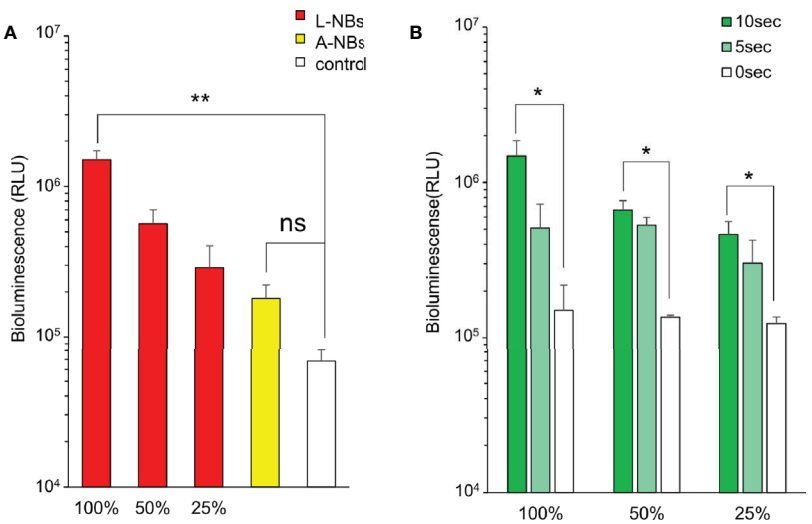

FIGURE 4 | Luciferase expression in HSC2 cells after pDNA administration by sonoporation with NBs. **(A)** Expression of luciferase protein in incubation medium by sonoporation using two types of NBs and concentrations. **(B)** L-NBs concentration and ultrasonic irradiation time dependent profile of luciferase expression. L-NBs, Lipid based nanobubble, A-NB, albumin-based NBs, control, NBs-free opti-MEM including pDNA. RLU, relative luminescence units. The data are presented as the mean ± standard error of the mean (s.e.m.). Statistical significance was assessed by unpaired t-test including Welch's correction. (*p < 0.05, **p < 0.01) (N=3), ns, not significant.

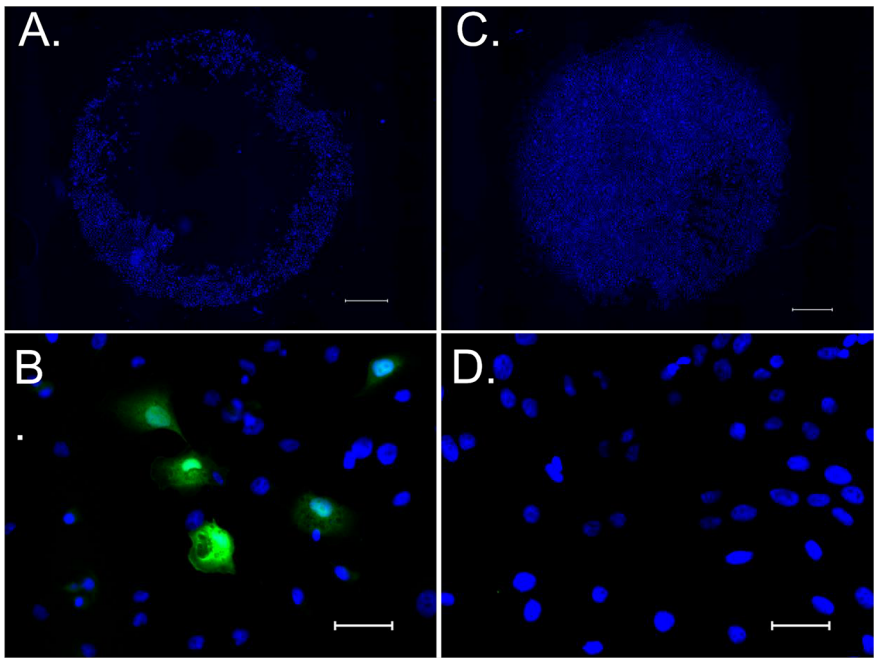

FIGURE 5 | eGFP expression in HSC2 cells after pDNA administration by sonoporation with NBs. **(A, C)** Low power magnified fluorescent microscopic image stained with hoechst 33342 taken 24 h after sonoporation. **(B, D)** High power magnified image stained with hoechst 33342 and anti-GFP antibody. **(A, B)** sonicated sample with pDNA encoding eGFP and L- NBs. **(C, D)** negative control without pDNA, NBs and sonication. Scale bars: 1,000 μm **(A**, **C)**, 50μm **(B**, **D)**.

efficiency in the skeletal muscles (Li et al., 2003). Results showed marked differences in transfection rate depending on shell material. Meanwhile, advancement of technology related to fabrication of smaller sub-micro sized bubbles (Alheshibri et al., 2016) and accurate bubble size measurement modalities (Hernandez et al., 2019) have led to great expectation of its application for gene therapy. Mainly for the reason that sub-micro sized bubbles or nanobubbles may potentially extravasate through the endothelial cell layer of the blood vessel, increased accumulation of NBs in normal tissue and tumor vasculature, can thus be expected. Several

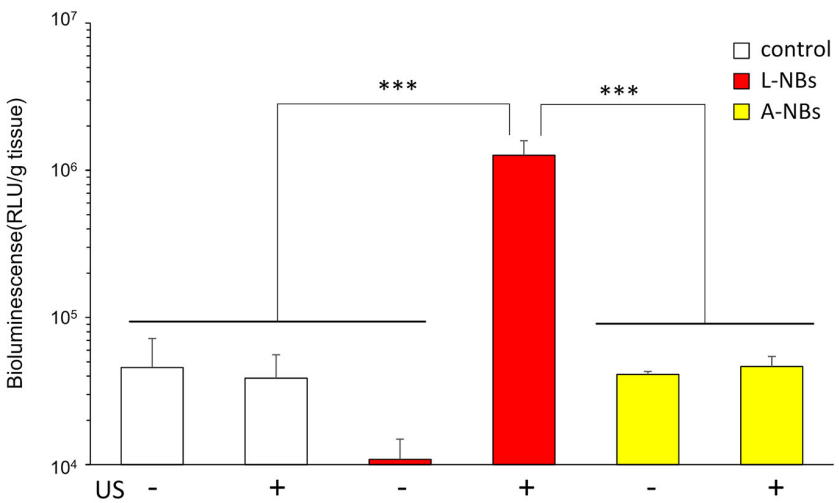

FIGURE 6 | Ultrasound irradiation by clinical hand-held US imaging scanner to the abdomen. Expression of luciferase protein extracted from sacrificed liver after sonoporation using two types of NBs. L-NBs; Lipid-based nanobubbles. A-NB; albumin-based nanobubbles. control, NBs-free saline including pDNA. US, US irradiation. pDNA, plasmid DNA encoding secreted NanoLuc. RLU, relative luminescence units. The data are presented as the mean ± standard error of the mean (s.e.m.). Statistical significance was assessed by Tukey's multiple comparison test. (***$p < 0.001$) (N=4).

researchers have investigated the acoustic character and pharmacokinetics of NBs, suggesting possible involvement of EPR effect (Tong et al., 2013; Wu et al., 2013; Cavalli et al., 2015; Du et al., 2018). Furthermore, it has recently been reported that the time-intensity-curve of extravasated NBs can be detected in tumors (Wu et al., 2019). Histologic analysis showed that NBs were retained in tumor tissue to a greater extent compared with MBs.

Lafond et al. (2018) recently demonstrated that their in-house fabricated albumin-based NBs, which is 100 to 250 nm in diameter were sensitive to specific acoustic pressures and could become efficient cavitation nuclei in the 3 to 5-MHz US frequency range. Acoustic passive cavitation detectors indicated that inertial cavitation threshold was lower than the commercially available MB US contrast agents. Watanabe et al. (2019) similarly conducted a detailed study of albumin-based NBs by 3 different nanoscale measurement modalities and characterized the bubble size distribution, gas/particle ratio, and concentration. Subsequently, superior contrast imaging and elevation of time signal intensity curve of the NBs were obtained in an *in vitro* flow vessel system driven at US frequencies of 40 MHz. They later went on to irradiate US to cultured cancer cells with therapeutic US (1 MHz) in the presence of NBs that functioned as cavitation nuclei thus potentiating acute cell disruption. In the present study, similar US conditions were irradiated to *in vitro* cultured cancer cells which resulted in induction of gene transfer. It is postulated that the NBs became cavitation nuclei to induce sonoporation at the cellular level, thus resulting in enhanced gene transfer. However, it is not clearly understood why lipid-based NBs resulted in significantly higher transfection rate compared to albumin-based NBs, in spite of the fact that both had similar size distribution and concentration. As this tendency was observed both in our *in vitro* and *in vivo* experiments, it is suggested that NB shell material may have attributed to this phenomenon but further verification is needed, as well as, considering the influence of bubble diameter which cannot be completely excluded from an acoustic stand point.

Nanobubbles have previously been applied for US mediated gene delivery in different anatomical locations. Nishimura et al. (2019) reported site-specific transgene expression locally at the defined area of the peritoneum with NB induced sonoporation. Naked pDNA and NBs were directly administered *in vivo* and multi-color deep imaging analysis revealed that the transgene expression can be in the peritoneal mesothelial cells. It was suggested that intraperitoneal gene delivery by sonoporation might be an effective therapeutic method for treatment of peritoneal fibrosis. Alternative drug delivery strategies have been reported by fabrication of US-sensitive siRNA-loaded polymeric micelles and liposome NBs for gliomas (Yin et al., 2013). Relatively low-frequency US was irradiation to induce release of siRNA micelles in tumor tissue from the siRNA loaded NBs and then effectively delivered into cancer cells. Furthermore, several promising data have been reported on liver gene therapy by combining various types of NBs and US (Wu et al., 2016; Zhang et al., 2018). Nevertheless, our animal sonoporation study also revealed induction of gene transfer in the liver after intravenous injection of lipid-based NBs. Our preliminary US irradiation (frequency 1.0 MHz, intensity 1.0 W/cm^2) experiments (**Supplementary Figure S1**) showed that NB/gene administrated mice had higher transfection rate in the liver compared to the spleen and kidney, however, the exact mechanism for these results is unclear. It is speculated that the acoustic parameters, especially the US intensity may greatly alter the rate of gene transfer. Dimcevski et al. (2016) conducted a human clinical trial using diagnostic US device and MBs to enhance gemcitabine treatment of inoperable pancreatic cancer. In their study, the echography scanner configuration was programmed to maximize the duty cycle, with short broadband linear pulse in order to excite as many MBs as possible. In our study, although US parameters were preset to supposedly maximum intensity, it was anticipated that sufficient acoustic peak pressure may not reach the target organ using such small low powered hand-held US scanners. Fortunately, gene transfer was detected at least in the most proximally located organ to the US scanner probe of this particular FDA approved device. In this respect, the present study provides limited information on the optimal acoustic conditions for NB induced sonoporation. It is speculated that a more acoustically customized US scanner can further improve the efficiency of gene transfer. It would thus be worthy to evaluate various parameters as well as the NB shell materials for future gene therapy experiments.

CONCLUSION

Ultrasound-mediated sonoporation induced gene transfection in both *in vitro* and *in vivo* in the presence of lipid-based NBs. Furthermore, we demonstrated that commercially available hand-held US scanners have sufficient acoustic pressure as to induce gene transfection in animal liver. Additional acoustic parameter studies should be carried out to investigate the applicability of this modality for gene therapy.

DATA AVAILABILITY STATEMENT

The raw data supporting the conclusions of this article will be made available by the authors, without undue reservation, to any qualified researcher.

ETHICS STATEMENT

The animal study was reviewed and approved by Regulations of the Animal Care and Use Committee, Nagasaki University.

AUTHOR CONTRIBUTIONS

KT, HK, LF, YI, and HE were involved in the design, analysis, data collection, and preparation of the manuscript. KN, KO, AW, and SK carried out the animal experiment, data analyses, and interpretation of the results. KT, HK, and AW contributed to the writing of the manuscript and revision of the text.

ACKNOWLEDGMENTS

The authors would like to thank Ms. Akino Akamine, Ms. Emi Nagamine, Ms. Shino Dehata for their assistance in bubble measurements and cell culture.

SUPPLEMENTARY MATERIAL

The Supplementary Material for this article can be found online at: https://www.frontiersin.org/articles/10.3389/fphar.2020.00363/full#supplementary-material

REFERENCES

Abenojar, E. C., Nittayacharn, P., de Leon, A. C., Perera, R., Wang, Y., Bederman, I., et al. (2019). Effect of Bubble Concentration on the in Vitro and in Vivo Performance of Highly Stable Lipid Shell-Stabilized Micro- and Nanoscale Ultrasound Contrast Agents. *Langmuir* 35, 10192–10202. doi: 10.1021/acs.langmuir.9b00462

Alheshibri, M., Qian, J., Jehannin, M., and Craig, V. S. (2016). A History of Nanobubbles. *Langmuir* 32, 11086–11100. doi: 10.1021/acs.langmuir.6b02489

Cavalli, R., Argenziano, M., Vigna, E., Giustetto, P., Torres, E., Aime, S., et al. (2015). Preparation and in vitro characterization of chitosan nanobubbles as theranostic agents. *Colloids Surf. B Biointerfaces* 129, 39–46. doi: 10.1016/j.colsurfb.2015.03.023

Cochran, M. C., Eisenbrey, J., Ouma, R. O., Soulen, M., and Wheatley, M. A. (2011). Doxorubicin and paclitaxel loaded microbubbles for ultrasound triggered drug delivery. *Int. J. Pharm.* 414, 161–170. doi: 10.1016/j.ijpharm.2011.05.030

Dicker, S., Mleczko, M., Siepmann, M., Wallace, N., Sunny, Y., Bawiec, C. R., et al. (2013). Influence of shell composition on the resonance frequency of microbubble contrast agents. *Ultrasound Med. Biol.* 39, 1292–1302. doi: 10.1016/j.ultrasmedbio.2013.02.462

Dimcevski, G., Kotopoulis, S., Bjanes, T., Hoem, D., Schjott, J., Gjertsen, B. T., et al. (2016). A human clinical trial using ultrasound and microbubbles to enhance gemcitabine treatment of inoperable pancreatic cancer. *J. Control. Release* 243, 172–181. doi: 10.1016/j.jconrel.2016.10.007

Du, J., Li, X. Y., Hu, H., Xu, L., Yang, S. P., and Li, F. H. (2018). Preparation and Imaging Investigation of Dual-targeted C3F8-filled PLGA Nanobubbles as a Novel Ultrasound Contrast Agent for Breast Cancer. *Sci. Rep.* 8, 3887. doi: 10.1038/s41598-018-21502-x

Fumoto, S., Nishimura, K., Nishida, K., and Kawakami, S. (2016). Three-Dimensional Imaging of the Intracellular Fate of Plasmid DNA and Transgene Expression: ZsGreen1 and Tissue Clearing Method CUBIC Are an Optimal Combination for Multicolor Deep Imaging in Murine Tissues. *PloS One* 11, e0148233. doi: 10.1371/journal.pone.0148233

Hernandez, C., Abenojar, E. C., Hadley, J., de Leon, A. C., Coyne, R., Perera, R., et al. (2019). Sink or float?Characterization of shell-stabilized bulk nanobubbles using a resonant mass measurement technique. *Nanoscale* 11, 851–855. doi: 10.1039/c8nr08763f

Kawai, S., Takagi, Y., Kaneko, S., and Kurosawa, T. (2011). Effect of three types of mixed anesthetic agents alternate to ketamine in mice. *Exp. Anim.* 60, 481–487. doi: 10.1538/expanim.60.481

Kawakami, S., Hirayama, R., Shoji, K., Kawanami, R., Nishida, K., Nakashima, M., et al. (2002). Liver- and lobe-selective gene transfection following the instillation of plasmid DNA to the liver surface in mice. *Biochem. Biophys. Res. Commun.* 294, 46–50. doi: 10.1016/s0006-291x(02)00432-1

Kudo, N., Okada, K., and Yamamoto, K. (2009). Sonoporation by single-shot pulsed ultrasound with microbubbles adjacent to cells. *Biophys. J.* 96, 4866–4876. doi: 10.1016/j.bpj.2009.02.072

Lafond, M., Watanabe, A., Yoshizawa, S., Umemura, S. I., and Tachibana, K. (2018). Cavitation-threshold Determination and Rheological-parameters Estimation of Albumin-stabilized Nanobubbles. *Sci. Rep.* 8, 7472. doi: 10.1038/s41598-018-25913-8

Lammertink, B. H., Bos, C., Deckers, R., Storm, G., Moonen, C. T., and Escoffre, J. M. (2015). Sonochemotherapy: from bench to bedside. *Front. Pharmacol.* 6, 138. doi: 10.3389/fphar.2015.00138

Lapostolle, F., Petrovic, T., Lenoir, G., Catineau, J., Galinski, M., Metzger, J., et al. (2006). Usefulness of hand-held ultrasound devices in out-of-hospital diagnosis performed by emergency physicians. *Am. J. Emerg Med.* 24, 237–242. doi: 10.1016/j.ajem.2005.07.010

Li, T., Tachibana, K., and Kuroki, M. (2003). Gene transfer with echo-enhanced contrast agents: comparison between Albunex, Optison, and Levovist in mice–initial results. *Radiology* 229, 423–428. doi: 10.1148/radiol.2292020500

Negishi, Y., Yamane, M., Kurihara, N., Endo-Takahashi, Y., Sashida, S., Takagi, N., et al. (2015). Enhancement of Blood-Brain Barrier Permeability and Delivery of Antisense Oligonucleotides or Plasmid DNA to the Brain by the Combination of Bubble Liposomes and High-Intensity Focused Ultrasound. *Pharmaceutics* 7, 344–362. doi: 10.3390/pharmaceutics7030344

Nejad, S. M., Hosseini, H., Akiyama, H., and Tachibana, K. (2016). Reparable Cell Sonoporation in Suspension: Theranostic Potential of Microbubble. *Theranostics* 6, 446–455. doi: 10.7150/thno.13518

Nishimura, K., Yonezawa, K., Fumoto, S., Miura, Y., Hagimori, M., Nishida, K., et al. (2019). Application of Direct Sonoporation from a Defined Surface Area of the Peritoneum: Evaluation of Transfection Characteristics in Mice. *Pharmaceutics* 11, 244. doi: 10.3390/pharmaceutics11050244

Paefgen, V., Doleschel, D., and Kiessling, F. (2015). Evolution of contrast agents for ultrasound imaging and ultrasound-mediated drug delivery. *Front. Pharmacol.* 6, 197. doi: 10.3389/fphar.2015.00197

Sennoga, C. A., Kanbar, E., Auboire, L., Dujardin, P. A., Fouan, D., Escoffre, J. M., et al. (2017). Microbubble-mediated ultrasound drug-delivery and therapeutic monitoring. *Expert Opin. Drug Deliv.* 14, 1031–1043. doi: 10.1080/17425247.2017.1266328

Song, J. H., Moldovan, A., and Prentice, P. (2019). Non-linear Acoustic Emissions from Therapeutically Driven Contrast Agent Microbubbles. *Ultrasound Med. Biol.* 45, 2188–2204. doi: 10.1016/j.ultrasmedbio.2019.04.005

Sonoda, S., Tachibana, K., Uchino, E., Okubo, A., Yamamoto, M., Sakoda, K., et al. (2006). Gene transfer to corneal epithelium and keratocytes mediated by ultrasound with microbubbles. *Invest. Ophthalmol. Vis. Sci.* 47, 558–564. doi: 10.1167/iovs.05-0889

Tachibana, K., Uchida, T., Ogawa, K., Yamashita, N., and Tamura, K. (1999). Induction of cell-membrane porosity by ultrasound. *Lancet* 353, 1409. doi: 10.1016/s0140-6736(99)01244-1

Taniyama, Y., Tachibana, K., Hiraoka, K., Aoki, M., Yamamoto, S., Matsumoto, K., et al. (2002a). Development of safe and efficient novel nonviral gene transfer using ultrasound: enhancement of transfection efficiency of naked plasmid DNA in skeletal muscle. *Gene Ther.* 9, 372–380. doi: 10.1038/sj.gt.3301678

Taniyama, Y., Tachibana, K., Hiraoka, K., Namba, T., Yamasaki, K., Hashiya, N., et al. (2002b). Local delivery of plasmid DNA into rat carotid artery using ultrasound. *Circulation* 105, 1233–1239. doi: 10.1161/hc1002.105228

Tong, H. P., Wang, L. F., Guo, Y. L., Li, L., Fan, X. Z., Ding, J., et al. (2013). Preparation of protamine cationic nanobubbles and experimental study of their physical properties and in vivo contrast enhancement. *Ultrasound Med. Biol.* 39, 2147–2157. doi: 10.1016/j.ultrasmedbio.2013.05.016

Watanabe, A., Sheng, H., Endo, H., Feril, L. B., Irie, Y., Ogawa, K., et al. (2019). Echographic and physical characterization of albumin-stabilized nanobubbles. *Heliyon* 5, e01907. doi: 10.1016/j.heliyon.2019.e01907

Wisgrill, L., Lamm, C., Hartmann, J., Preissing, F., Dragosits, K., Bee, A., et al. (2016). Peripheral blood microvesicles secretion is influenced by storage time, temperature, and anticoagulants. *Cytometry A.* 89, 663–672. doi: 10.1002/cyto.a.22892

Wu, H., Rognin, N. G., Krupka, T. M., Solorio, L., Yoshiara, H., Guenette, G., et al. (2013). Acoustic characterization and pharmacokinetic analyses of new nanobubble ultrasound contrast agents. *Ultrasound Med. Biol.* 39, 2137–2146. doi: 10.1016/j.ultrasmedbio.2013.05.007

Wu, B., Qiao, Q., Han, X., Jing, H., Zhang, H., Liang, H., et al. (2016). Targeted nanobubbles in low-frequency ultrasound-mediated gene transfection and

growth inhibition of hepatocellular carcinoma cells. *Tumour Biol.* 37, 12113–12121. doi: 10.1007/s13277-016-5082-2

Wu, H., Abenojar, E. C., Perera, R., De Leon, A. C., An, T., and Exner, A. A. (2019). Time-intensity-curve Analysis and Tumor Extravasation of Nanobubble Ultrasound Contrast Agents. *Ultrasound Med. Biol.* 45, 2502–2514. doi: 10.1016/j.ultrasmedbio.2019.05.025

Yin, T., Wang, P., Li, J., Zheng, R., Zheng, B., Cheng, D., et al. (2013). Ultrasound-sensitive siRNA-loaded nanobubbles formed by hetero-assembly of polymeric micelles and liposomes and their therapeutic effect in gliomas. *Biomaterials* 34, 4532–4543. doi: 10.1016/j.biomaterials.2013.02.067

Zhang, B., Chen, M., Zhang, Y., Chen, W., Zhang, L., and Chen, L. (2018). An ultrasonic nanobubble-mediated PNP/fludarabine suicide gene system: A new approach for the treatment of hepatocellular carcinoma. *PloS One* 13, e0196686. doi: 10.1371/journal.pone.0196686

Zhu, X., Guo, J., He, C., Geng, H., Yu, G., Li, J., et al. (2016). Ultrasound triggered image-guided drug delivery to inhibit vascular reconstruction via paclitaxel-loaded microbubbles. *Sci. Rep.* 6, 21683. doi: 10.1038/srep21683

Zucker, R. M., Ortenzio, J. N., and Boyes, W. K. (2016). Characterization, detection, and counting of metal nanoparticles using flow cytometry. *Cytometry A.* 89, 169–183. doi: 10.1002/cyto.a.22793

Conflict of Interest : KT owns stock in SonoCore Inc.

The remaining authors declare that the research was conducted in the absence of any commercial or financial relationships that could be construed as a potential conflict of interest.

frontiers in Pharmacology

ORIGINAL RESEARCH
published: 12 May 2020
doi: 10.3389/fphar.2020.00644

Increasing Doxorubicin Loading in Lipid-Shelled Perfluoropropane Nanobubbles *via* a Simple Deprotonation Strategy

*Pinunta Nittayacharn[1], Eric Abenojar[2], Al De Leon[2], Dana Wegierak[3] and Agata A. Exner[1,2]**

[1] Department of Biomedical Engineering, Case Western Reserve University, Cleveland, OH, United States, [2] Department of Radiology, Case Western Reserve University, Cleveland, OH, United States, [3] Department of Physics, Ryerson University, Toronto, ON, Canada

OPEN ACCESS

Edited by:
Marc Derieppe, Princess Maxima Center for Pediatric Oncology, Netherlands

Reviewed by:
Sudheer Kumar Ravuri, Steadman Philippon Research Institute, United States
William Raoul, Inserm U1069 Équipe Nutrition, Croissance et Cancer, France

***Correspondence:**
Agata A. Exner
agata.exner@case.edu

Specialty section:
This article was submitted to Translational Pharmacology, a section of the journal Frontiers in Pharmacology

Received: *21 November 2019*
Accepted: *22 April 2020*
Published: *12 May 2020*

Citation:
Nittayacharn P, Abenojar E, De Leon A, Wegierak D and Exner AA (2020) Increasing Doxorubicin Loading in Lipid-Shelled Perfluoropropane Nanobubbles via a Simple Deprotonation Strategy. Front. Pharmacol. 11:644. doi: 10.3389/fphar.2020.00644

Drug delivery to solid tumors using echogenic nanobubbles (NBs) and ultrasound (US) has recently gained significant interest. The approach combines attributes of nanomedicine and the enhanced permeation and retention (EPR) effect with the documented benefits of ultrasound to improve tumor drug distribution and treatment outcomes. However, optimized drug loading strategies, the drug-carrying capacity of NBs and their drug delivery efficiency have not been explored in depth and remain unclear. Here, we report for the first time on the development of a novel deprotonated hydrophobic doxorubicin-loaded C_3F_8 nanobubble (hDox-NB) for more effective US-mediated drug delivery. In this study, the size distribution and yield of hDox-NBs were measured *via* resonant mass measurement, while their drug-loading capacity was determined using a centrifugal filter technique. *In vitro* acoustic properties including contrast-imaging enhancement, initial echogenic signal, and decay were assessed and compared to doxorubicin hydrochloride loaded-NBs (Dox.HCl-NBs). In addition, *in vitro* therapeutic efficacy of hDox-NBs was evaluated by cytotoxicity assay in human ovarian cancer cells (OVCAR-3). The results showed that the hDox-NBs were small (300.7 ± 4.6 nm), and the drug loading content was significantly enhanced (2 fold higher) compared to Dox.HCl-NBs. Unexpectedly, the *in vitro* acoustic performance was also improved by inclusion of hDox into NBs. hDox-NB showed higher initial US signal and a reduced signal decay rate compared to Dox.HCl-NBs. Furthermore, hDox-NBs combined with higher intensity US exhibited an excellent therapeutic efficacy in human ovarian cancer cells as shown in a reduction in cell viability. These results suggest that hDox-NBs could be considered as a promising theranostic agent to achieve a more effective noninvasive US-mediated drug delivery for cancer treatment.

Keywords: nanobubbles, doxorubicin, drug-loading, ultrasound contrast agent, ovarian cancer

INTRODUCTION

Ovarian cancer (OC) is the fifth leading cause of cancer deaths among women in the United States. Because the cancer may be asymptomatic, many patients are diagnosed with metastatic disease (Xiao et al., 2009). Because tumor recurrence after surgical resection is common, most women are subsequently treated with systemic or regional chemotherapy. However, response rates are low, and fewer than 30% of these patients will survive beyond 5 years (Torre et al., 2018). To reduce the toxicity and multi-drug resistance of systemic chemotherapies, several nanoscale drug delivery platforms such as PEGylated liposomal doxorubicin (Doxil or Caelyx), micelles, and dendrimers have been developed for OC treatment and have shown more effective tumor accumulation and efficacy compared to free drug owing to the enhanced permeability and retention (EPR) effect (Sudimack and Lee, 2000; Xiao et al., 2009; Torre et al., 2018). Although passive delivery strategies can mediate some of the clinical systemic chemotherapy problems (such as severe cardiotoxicity associated with free doxorubicin), they nonetheless suffer from several limitations such as poor drug distribution and penetration resulting in an insufficient level of drug accumulation at the target tumor. This remains a big challenge in cancer drug delivery. To improve outcomes of systemic drug delivery to solid tumor, various active delivery approaches for triggering the release of drug from vehicles have been developed such as using temperature, ultraviolet (UV)/near-infrared (NIR) light, magnetic resonance (MR), and ultrasound (US) (Chilkoti et al., 2002; Derfus et al., 2007; Husseini and Pitt, 2008; Fomina et al., 2010; Manzoor et al., 2012). Among these, US is considered as an ideal modality for this purpose because it is widely available, relatively inexpensive, safe from hazardous ionizing radiation, and is a non-invasive module for simultaneous real-time imaging and triggering release from vehicle (Böhmer et al., 2009; Deckers and Moonen, 2010; Zhu et al., 2016). A variety of drug-loaded nanoparticles (NPs) such as liposomes or micelles in combination with therapeutic agents have been used in US-mediated drug delivery approach (Husseini et al., 2002; Pruitt and Pitt, 2002; Kim et al., 2013). However, the clinical application of NPs is limited due to their corresponding high resonant frequency which does not allow them to be easily be visible on clinical US. On the contrary, gas-filled microbubbles (MBs) provide great clinical US signal and have been widely used as US contrast agents (UCAs) (Villanueva et al., 2004; Ferrara et al., 2007; Hernot and Klibanov, 2008; Lee et al., 2017; Wang et al., 2017; de Leon et al., 2018). MBs can induce sonoporation of vasculature and cell membranes resulting in an increasing permeability, local drug release, and penetration (Martin and Dayton, 2013). However, their effectiveness *in vivo* is limited as a blood pool agent due to their large size (1–10 μm) which does not allow extravasation beyond the vasculature. Thus, they cannot take advantage of passive delivery *via* the EPR effect for increased tumor specific delivery and efficient intratumoral penetration, which requires particles with diameter in the range of 400-800 nm (Greish, 2010).

As an alternative, US-mediated smaller gas-filled UCAs such as nanobubbles (NBs) have been proposed to improve drug delivery to the tumor. NBs, with a size of 100–600 nm, allow extravasation outside of the vasculature, which can be facilitated *via* EPR effect resulting in higher accumulation in tumor tissue and potentially enhanced theranostic efficiency. Previously, we have developed a highly stable lipid shell-stabilized perfluoropropane (C_3F_8) gas NBs and shown that these NBs have minimal signal decay when insonated continuously *in vitro*, has a longer *in vivo* half-life, and has a delayed onset of *in vivo* signal decay (Abenojar et al., 2019; de Leon et al., 2019). We have expanded the application of the previous NB formulation by incorporating chemotherapeutic drug doxorubicin (Dox.HCl), an anthracycline topoisomerase inhibitor, into the NB shell (Nittayacharn et al., 2018). The Dox.HCl-NBs have been shown to improve drug loading efficiency without sacrificing acoustic properties compared to our first generation of US-mediated Dox.HCl-loaded interpenetrating polymer mesh stabilized NBs (Perera et al., 2017; Nittayacharn et al., 2019). However, there are two main limitations to current drug-loaded NBs: (1) the therapeutic efficiency of drug-loaded bubbles has been limited by the loading capacity of the shell which stabilizes the gas core; and (2) high drug loading can destabilize the bubbles, which can result in insufficient therapeutic effect. Accordingly, the objective of this work is to develop a more effective US-mediated drug delivery system that will serve as a theranostic agent for treatment of ovarian cancer. In this study, we aim to improve drug loading directly into the bubble shell by applying a drug-deprotonation strategy which has previously been used to improve micelle loading (Yoo and Park, 2004; Mohan and Rapoport, 2010; Zhang et al., 2016). To our knowledge, this is the first time the concept of deprotonation will be utilized in UCAs. We hypothesize that the loading efficiency of NB can be increased using deprotonated hydrophophobic Dox (hDox). Accordingly, hDox was prepared and loaded into NBs. Drug encapsulation efficiency, size, concentration, and *in vitro* acoustic properties were characterized and compared to commercially available doxorubicin-loaded NBs (Dox.HCl-NBs). In addition, the therapeutic efficacy of NBs was evaluated in cell culture model of human ovarian cancer cells (OVCAR-3).

MATERIALS AND METHODS

Materials

Lipids including DBPC (1,2-dibehenoyl-sn-glycero-3-phosphocholine), DPPA (1,2 dipalmitoyl-sn-Glycero-3-phosphate), and DPPE (1,2-dipalmitoyl-sn-glycero-3-phosphoethanolamine) were obtained from Avanti Polar Lipids (Pelham, AL), and mPEG-DSPE (1,2-distearoyl-sn-glycero-3-phosphoethanolamine-N-[methoxy(polyethylene glycol)-2000] (ammonium salt)) was obtained from Laysan Lipids (Arab, AL). Doxorubicin hydrochloride (Dox.HCl), triethylamine (TEA), tetrahydrofuran (THF), propylene glycol (PG), and the cell proliferation reagent WST-1 were purchased from Sigma

Aldrich (Milwaukee, WI). Glycerol was purchased from Acros Organics (Morris, NJ). Roswell Park Memorial Institute (RPMI) 1640 with 10% fetal bovine serum and 1% penicillin-streptomycin, trypsin-EDTA were purchased from Invitrogen (Grand Island, NY). OVCAR-3, human ovarian carcinoma cells were purchased from ATCC (Manassas, VA).

Preparation and Characterization of Hydrophobic Doxorubicin (hDox)

Commercial doxorubicin hydrochloride (Dox.HCl) was deprotonated to obtain hydrophobic Dox (hDox). Dox.HCl was dissolved in a mixture of chloroform and methanol (3:2, v/v) and incubated overnight with triethylamine (TEA) at 1:3 molar ratio of Dox to TEA which resulted in deprotonation of the sugar amino group (Shuai et al., 2004; Kim et al., 2008; Liu et al., 2012; Wei et al., 2015; Zhang et al., 2016). After solvent evaporation, the deprotonated Dox (hDox) powder was collected and kept in the freezer. The quality of hDox was evaluated by 1HNMR by comparing the main structure with Dox.HCl. The state of hDox was qualitatively determined by thin layer chromatography (TLC). The samples were dissolved in THF and spotted on silica gel TLC plate (TLC silica gel 60 F254, Merk, Darmstadt, Germany) by microcapillary. The plates were developed in the mobile phase consisting of dichloromethane, methanol, formic acid, and deionized water (82:24:2:1, v/v) and were examined under UV light. Testing was performed at least in triplicate.

Preparation and Purification of Drug-Loaded Nanobubbles

To formulate drug-loaded NBs, hDox was encapsulated in lipid-shell stabilized octafluoropropane (C_3F_8) bubbles, as described previously (de Leon et al., 2019). Briefly, lipids including DBPC, DPPA, DPPE, mPEG-DSPE, and 0.2 wt.% hDox were dissolved in propylene glycol (PG). A mixture of glycerol and phosphate buffer saline (PBS) was added then to the lipid solution, and the air inside a sealed 3 ml vial was replaced with C_3F_8. Finally, the vial was shaken on a ViralMix shaker (Bristol-Myers Squibb Medical Imaging, Inc., N. Billerica, MA) for 45 s to drive bubble self-assembly. NBs were isolated from the mixture by centrifugation at 50 rcf for 5 mins with the vial inverted. Equivalent NBs with regular doxorubicin (Dox.HCl-NBs) were formulated using the same method. The free drug was separated from the drug-loaded NBs by passing the mixture solution of drug-NBs and free drug over a Sephadex column (Sephadex G-25 in PD-10 desalting column, Sigma-Aldrich, UK). NBs were eluted through the column with PBS (pH 7.4) and the first 3 ml fraction containing NBs was collected for further experiments.

Drug Loading Content and Encapsulation Efficiency

Drug-loaded NB solution (n=3) was transferred into the ultrafiltration unit with a molecular weight cut-off of 50,000 Da (Vivaspin 20, Sartorious) and centrifuged at 4,000 rpm for 50 min to remove free drug (Nittayacharn et al., 2019). The obtained hDox-NBs solution was lyophilized, weighed and dissolved in mixed solution of PBS and THF (1:1, v/v). The fluorescence of hDox was measured by TECAN plate reader (Infinite M200, Tecan Group Ltd., Switzerland) at an excitation of 495 nm and an emission of 595 nm. Equivalent experiments with Dox.HCl-NBs (n=3) were done using the same methods. The encapsulated drug in NBs was calculated by calibration curve obtained with known amounts of drug dissolved in the same solvent solution. Drug content was expressed as the drug loading content (DLC), percentage of encapsulation efficiency (% EE), and the total amount of drug (μg) in bubbles as follows;

$$\mathrm{DLC} = \frac{\text{Amount of drug in particles}(\mu g)}{\text{Weight of lipids (mg)}} \quad (1)$$

$$\%\ \mathrm{EE} = \frac{\text{Amount of drug in particles } (\mu g)}{\text{Initial feeding drug } (\mu g)} \times 100 \quad (2)$$

$$\text{Total drug in bubbles} = \text{Encapsulated drug in particles } (\mu g) \times \text{Buoyant particle fraction} \quad (3)$$

Characterization of NB Morphology, Size, and Concentration

The size distribution, concentration and buoyant mass of NBs were measured using resonant mass measurement (RMM) (Archimedes, Malvern Pananalytical Inc., Westborough, MA, USA) using a calibrated nanosensor (100 nm–2 μm) (Hernandez et al., 2019). Sensors were pre-calibrated using NIST traceable 565 nm polystyrene bead standards (ThermoFisher 4010S, Waltham MA, USA). hDox-NBs were diluted 1:1,000 with phosphate buffered saline (PBS, pH 7.4). A total of 1,000 particles were measured for each trial (n=3). Equivalent experiments with Dox.HCl-NBs were done using the same methods. Bubble morphology was imaged with a transmission electron microscope (TEM; Tecnai™ G^2 Spirit BioTWIN, FEI Company) operated at 120 kV based on a previously reported method (Owen and Stride, 2015). 10 μl of a dilute suspension of the samples was placed in an inverted position for 1 min on a 400 mesh Formvar®-coated copper grid. The sample was then stained by placing it on top of a 20 μl droplet of 2% uranyl acetate for 30 s and the excess was removed. The TEM grid containing the bubble sample was allowed to dry for another 30 min. All the characterizations were carried out in triplicate.

Stability Under Ultrasound

NBs were diluted in PBS at 1:100 and poured into a tissue mimicking agarose phantom (Abenojar et al., 2019; de Leon et al., 2019) placed directly over an ultrasound transducer (PLT-1204BT). Nonlinear contrast images were continuously acquired using a clinical US scanner (AplioXG SSA-790A, Toshiba Medical Imaging Systems, Otawara-Shi, Japan) *via* contrast harmonic imaging (CHI, 12 MHz, mechanical index 0.1, focus depth of 1.5 cm, 2D gain of 70 dB, dynamic range of 65 dB) at 1 frame per second for 8 min. Raw echo power data was recorded and analyzed using built-in software. Initial signal enhancement, signal decay over time, and percent remaining signal at 8 min were determined from the data. The experiment was carried out in triplicate.

In Vitro Cell Viability

Cytoxicity of free drug against OVCAR-3 cells was evaluated by comparing the half maximal inhibitory concentration (IC_{50}) of free Dox.HCl and hDox prior to evaluating the *in vitro* efficiency of drug-loaded NBs. Cells were seeded in 96 well plates at $5x10^4$ cells/ml (200 µl/well) and incubated overnight. Then, cells were incubated with four concentrations of free drugs dissolved in a serum-free RPMI media with 1% DMSO (0.025, 0.25, 1.25, 2.5 µg/ml) for 3 h. After the 3-h incubation, the cells were washed with 100 µl PBS 3 times, and replaced with 200 µl of RPMI media with 10% FBS. Following an additional 72-h incubation, cell viability was determined using a proliferation reagent, WST-1, which is a colorimetric assay for the quantification of cell viability and proliferation based on mitochondrial dehydrogenases caused by the cleavage of the tetrazolium salt WST-1. Cells were incubated with WST-1 (1:10, v/v) for 1 h and the absorbance at 450 nm was measured using TECAN plate reader. To assess the *in vitro* efficiency of drug-loaded NBs, cells were prepared as above and were treated with the following treatment conditions: (1) hDox-NBs +US; (2) hDox-NBs; (3) plain NBs+US; (4) plain NBs, (5) free hDox+US; (6) free hDox; (7) free hDox+plain NBs +US; (8) free hDox+plain NBs. Cells were treated with serum-free RPMI medium only (with US and without US) as a control. The "plain NBs" were not loaded with drug. "Free hDox" refers to unencapsulated drug. hDox-NBs and plain NBs were purified with size exclusion gel chromatography as described in the previous section and further diluted with RPMI media at 1:10 dilution. The concentration of hDox and bubbles in each treatment group was control to be equal at 2 µg/ml of hDox and $8.75x10^8$ particles/ml of bubbles. Each well was filled with 400 µl of treatment solution and wrapped with sterile transparent film dressing (Tegaderm™). For the group with ultrasound (+US), cells were exposed to an unfocused US transducer with an effective radiating area of 2 cm^2 at 1 MHz, 1.7 W/cm^2, 100% duty cycle, for 1 min. After treatment and 3-h incubation, cells were washed with 100 µl PBS 3 times, replaced with complete RPMI media. Following a 72-h incubation, cell viability was determined using WST-1 as described above. All experiments regarding the cytotoxic activity were carried out in triplicate.

Statistical Analysis

In this study, all experiments were repeated in triplicate, and the results were presented as mean ± standard deviation (SD), unless otherwise noted. The results fit a normal distribution. Thus, a one-way analysis of variance (ANOVA) with the Tukey test were used to assess statistical significance between groups. All statistical analyses were performed using Origin. A p value of <0.05 was considered significant, unless otherwise noted.

RESULTS

NB Characterization

By using an excess amount of TEA, the protonated Dox.HCl was successfully deprotonated under the basic condition resulting in the formation of the hydrophobic Dox (hDox). To elucidate the state of Dox whether or not it is hydrophobic, polarity of the hDox was analyzed compared to Dox.HCl using TLC plate as shown in **Figure S1A**. The Dox.HCl or hydrophilic Dox presented one spot on the TLC plate with R_f of 0.63 while two spots with the larger R_f of 0.95 was found for the hDox. The ability of hDox to travel further on the TLC plate confirmed that it has less polarity on the other word it is more hydrophobicity. The 1HNMR spectrum also showed the main structure of hDox is similar to that of Dox.HCl which implied that the deprotonation doesn't change biological activity and the active part of Dox (**Figure S1B**).

The average diameter and concentration of the NBs before and after loading with Dox.HCl or hDox were determined by RMM. Results show consistent size of buoyant and non-buoyant particles in the range of 100–600 nm for both formulations, which is on par with the reported size range of nanobubbles as shown in **Figures 1A, B**. Plain NBs showed an average diameter of 280 ± 112 nm while 359 ± 95 and 296 ± 153 nm were observed in Dox.HCl-NBs and hDox-NBs, respectively. hDox loading significantly altered the size of NBs, resulting in 25% smaller size compared to Dox.HCl-NBs (**Figure 1D**). A 10% diameter increase was seen in both formulations after drug loading. Both formulations had a concentration on the order of 10^{11} particles/ml, but the buoyant fraction of hDox-NBs was 50% higher than the Dox.HCl-NBs. The difference was not significantly significant due to the high variability of yield of the Dox.HCl-NBs. The non-buoyant particles, which are likely a combination of micelles and lipid aggregates, were present in both formulations, but with a difference of bubble to micelle/lipid aggregate ratios. However, no significant differences were observed between formulations (**Figure 1C**).

The morphology of hDox-NBs was also evaluated by transmission electron microscopy (TEM) and compared to that of plain-NBs (**Figure 2**). The TEM image of hDox-NBs clearly showed spherical shape between 200 and 400 nm in diameter, consistent with the NB size distribution obtained from RMM. By Increasing the magnification, the discontinuities caused by folds in the shell was found at the surface of the NBs, which was similar to the phospholipid MB morphology reported in a previous study (Owen and Stride, 2015).

Dox Loading Content and Encapsulation Efficiency

hDox at initial feeding concentration of 2 mg/ml was considered as the optimal concentration as it presented the highest loading content and bubble yield compared to the others (**Figure S3**). The amount of hDox in particles (both bubbles and non-buoyant particles) of Dox.HCl-NBs and hDox-NBs was determined by centrifuge filtration and present as drug loading content (DLC), % EE, and amount of hDox in bubbles as previously described. High DLC and EE was obtained by hDox-NBs. The encapsulation efficiency of hDox-NBs and Dox.HCl-NBs was 18.7 ± 2.0% and 11.4 ± 4.5%, respectively. DLC in hDox-NBs (9.2 ± 3.5 µg) was two times higher than Dox.HCl-NBs (3.9 ± 0.6 µg) as shown in **Figure 3A**. hDox-NBs also had a significantly higher total amount of hDox in bubbles with 324.6 ± 9.2 µg compared to 179.7 ± 23.8 µg in Dox.HCl-NBs (**Figure 3B**).

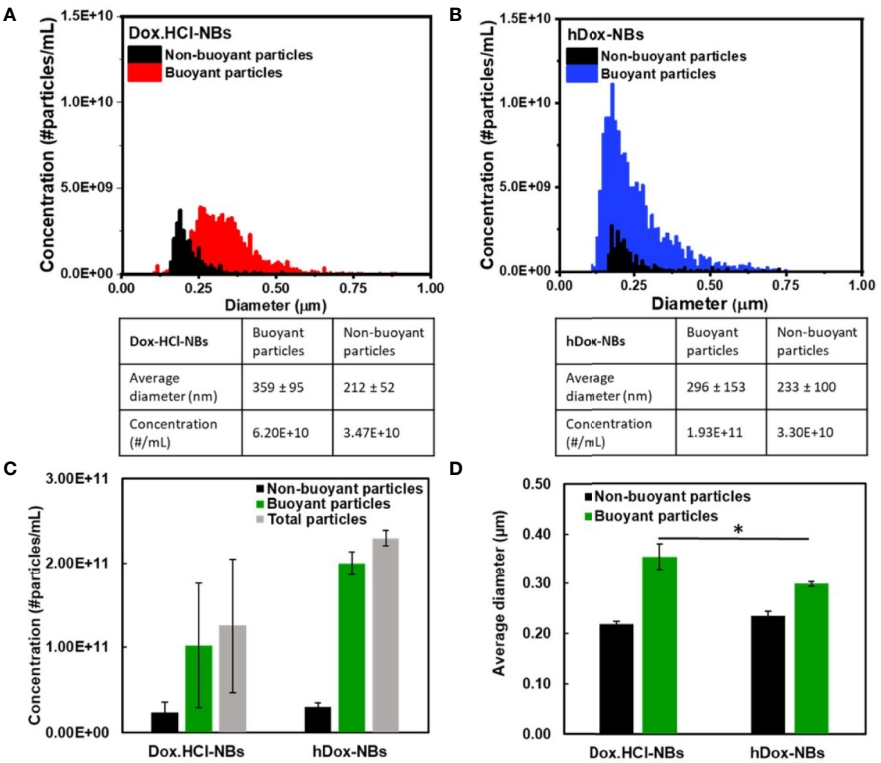

Dox-HCl-NBs	Buoyant particles	Non-buoyant particles
Average diameter (nm)	359 ± 95	212 ± 52
Concentration (#/mL)	6.20E+10	3.47E+10

hDox-NBs	Buoyant particles	Non-buoyant particles
Average diameter (nm)	296 ± 153	233 ± 100
Concentration (#/mL)	1.93E+11	3.30E+10

FIGURE 1 | Representative histograms showing the size distribution and concentration of **(A)** Dox.HCl-NBs (n=3) and **(B)** hDox-NBs (n=3), as measured by resonant mass measurement (RMM); The data is summarized to facilitate comparison between groups for both the **(C)** concentration and **(D)** size of buoyant and non-buoyant particles for the two different bubble formulations. Both bubble types were found to have similar concentrations of both buoyant (bubbles) and non-buoyant (solid lipids/aggregates), although the results from Dox.HCl-NBs were more variable and the concentration was on average 50% lower. The results were not statistically significant. The average bubble size of hDox was 25% smaller than Dox.HCl. Asterisk indicates significant difference at $p < 0.05$.

Echogenic Performance of hDox-NBs

The *in vitro* stability of hDox-NBs with continuous insonation was evaluated by using tissue-mimicking phantom made from agarose as shown in **Figure 4A** (Hernandez et al., 2019). The representative ultrasound contrast images of Dox-HCl and hDox-NBs showed enhanced nonlinear activity compared to plain NBs (**Figure 4B**). Interestingly, the signal decay rate of hDox-NBs was slower than plain NBs or Dox.HCl-NBs, as shown in **Figures 5A, B**. Although both Dox.HCl and hDox-NB formulations showed a higher initial signal intensity compared to plain NBs (**Figure 5C**), hDox-NBs showed less than 20% of signal loss after 8 min (**Figure 5D**).

Enhancement of an *In Vitro* Therapeutic Efficacy

The cytotoxicity of free Dox.HCl and hDox at various concentrations was evaluated in order to see the effect of deprotonation on the biological activity. We found that the IC_{50} corresponding to the concentration of the compound that shows 50% of cell viability of both Dox.HCl and hDox is 0.54 and 0.86 μg/ml, respectively (**Figure S6**). *In vitro* therapeutic efficacy of the hDox-NB construct was assessed using a human ovarian carcinoma cell line (OVCAR-3). The US delivery condition of 1 MHz and 1.7 W/cm^2 at 100% duty cycle with an exposure time of 1 min was used for cell experiments in this work. The cytotoxicity of plain NBs in combination with US at various bubble concentration was first determined as shown in **Figure S7**. At high NB concentration in the range of 86 to 430x10^8 particles/ml, there was no cytotoxicity. The treatment groups without NB (only cells) showed similar levels of cytotoxicity regardless of the US exposure. The high concentration of bubbles might attenuate the acoustic wave resulting in fewer cavitation events. When the concentration was reduced to 8.75 x10^8 particles/ml, which is equivalent to the concentration of hDox-NBs used in the following cell viability experiments, the cell viability was at 80%. However, cell viability was drastically reduced and the toxicity was noted again with bubble concentration of 35x10^8 particles/ml.

The therapeutic effect of hDox-NBs on OVCAR-3 cells is shown in **Figure 6A**. Without the application of US, free hDox alone shows the highest toxicity. In contrast, hDox-NBs without US showed a nearly 4-fold lower baseline toxicity, which implies that encapsulation of hDox in NBs could be safer to administer *in vivo* with compared to free hDox. When the US was applied, cell viability was decreased over 4-fold with

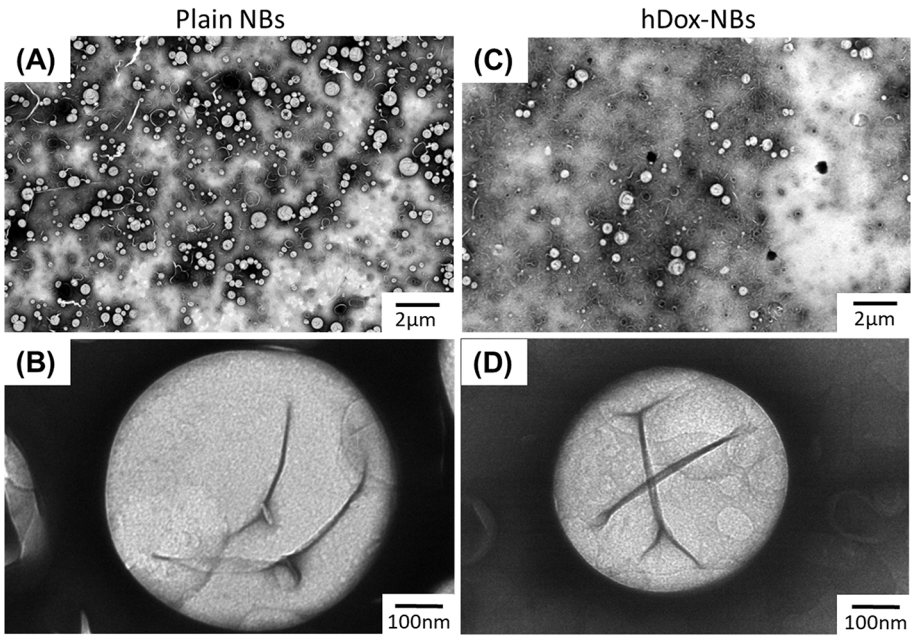

FIGURE 2 | Representative transmission electron microscope (TEM) images showing size and morphology of plain nanobubbles (NBs) or unloaded-NBs **(A**, **B)** and hDox-NBs **(C**, **D)** carried out using uranyl acetate staining. TEM studies were repeated in triplicate. The hDox-NBs show distinct patchy domains and increased ridges and buckles compared to bubbles without Dox.

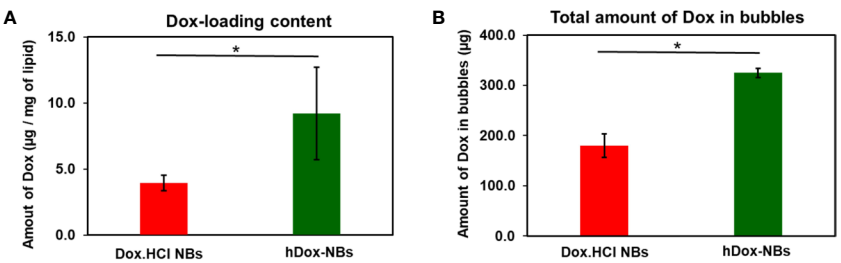

FIGURE 3 | Summary of drug loading into bubbles for hDox (n=3) and Dox.HCl (n=3). **(A)** hDox loading content per milligram of lipid; **(B)** Total hDox amount in bubbles (μg) calculated based on the buoyant particle concentration of both bubble types measured by resonant mass measurement (RMM). Dox in non-buoyant particle fraction was removed from this analysis. Significantly increased drug-loading of hDox can be seen in both test. Error bars represent standard deviation. Asterisk indicates significant difference at significant difference at $p < 0.05$.

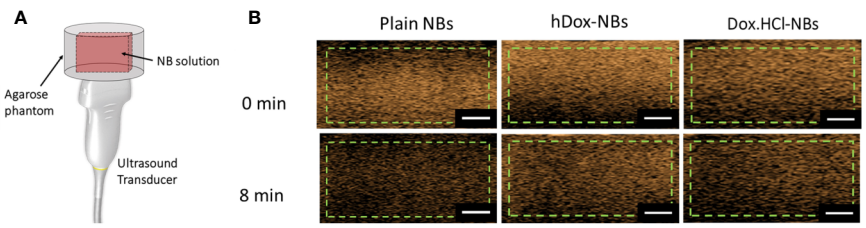

FIGURE 4 | (A) Schematic of the ultrasound transducer and agarose phantom with a thin channel (L × W × H = 22 × 1 × 10 mm^3) where is a sample location; As mentioned previously, the phantom design allows the entire bubble sample to be in the acoustic field, as the width of the slot is the same as the element array. This gives a more accurate measure of nanobubble (NB) stability in the acoustic field. **(B)** Representative ultrasound contrast images for each formulation with the analyzed region of interest (green dashed line). The scale bars are 0.5 cm.

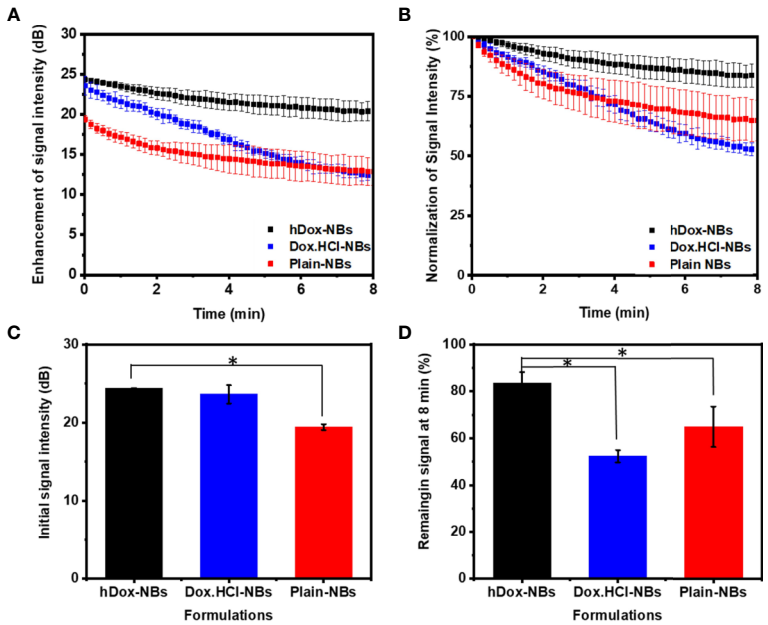

FIGURE 5 | Acoustic properties of hDox-NBs compared to unloaded nanobubbles (NBs) and NBs formulated with Dox.HCl (n=3 for each group). **(A)** Ultrasound signal decay of the three formulations over an 8-min exposure period. While both hDox and Dox.HCl increase the initial backscatter at t=0 compared to plain NBs, the signal decay is more rapid for Dox.HCl-NBs **(B)** Relative ultrasound signal decay rate illustrates the faster decay of Dox.HCl-NBs; Differences in initial ultrasound signal intensity **(C)** and remaining ultrasound signal at 8 min (% of signal at t=0) **(D)**. Error bars represent standard deviation. Asterisk indicates significant difference at $p < 0.05$.

hDox-NBs. In contrast, exposure to cells given free hDox (**Figure 6B**) does not offer additional benefit. Cell viability was also decreased when the US was applied to the plain NB together with free hDox. Free hDox and plain NB also showed significant decrease in cell viability compared to free hDox alone. This is likely the result of sonoporation which causes transient disruption of the cell membrane and increases free drug uptake (Fan et al., 2014; Abdalkader et al., 2017; Helfield et al., 2017; Wang et al., 2018).

DISCUSSION

We successfully loaded hDox into the shell of our bubbles where the co-localized hDox was observed by the microscopic image (**Figure S2**). Since most of NBs should be below the light diffraction limit, we used larger particles prior to separation of NB population in order to accurately visualize hDox loading on the bubble. The bubble morphology and dox localization in the bubble shell was clearly visualized and was similar to what was

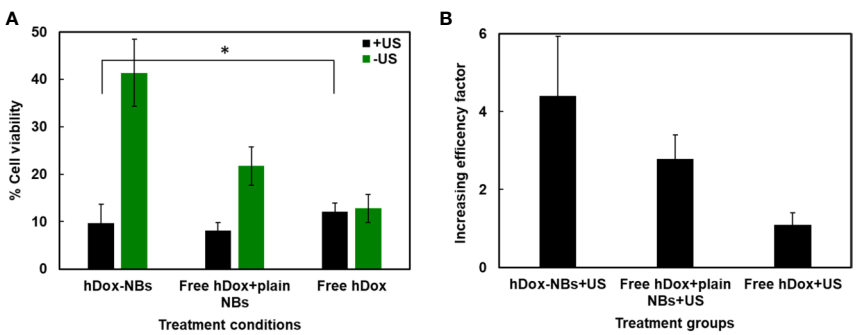

FIGURE 6 | Enhancement of Dox cytotoxicity in OVCAR-3 cells after treatment with hDox-NBs and ultrasound (+US). **(A)** Cell viability of OVCAR-3 cells for different treatments normalized to the untreated control; hDox-NBs have significantly lower toxicity compared to free hDox or free hDox with plain nanobubbles (NBs) when ultrasound is not present. With ultrasound application, the hDox-NBs lead to greater reduction in cell viability compared to free Dox and equivalent reduction compared to Dox co-injected with plain NBs. **(B)** An increasing efficacy factor for each treatment group compared to the group without ultrasound (-US). All experiments were carried out in triplicate. Error bars represent standard deviation. Asterisk indicates significant difference at $p < 0.05$.

previously observed. (Chen et al., 2017; Nittayacharn et al., 2019). To translate hDox-NBs to a clinical application in the future, it may be important to calculate the NB dose compared to typically used MB doses. We estimated the amount of hDox in one bubble to be 162.3 $x10^{-11}$ μg. Doxil, which is the liposomal formulation of doxorubicin hydrochloride (Dox.HCl) at a concentration of 2 mg/ml (per vial), is typically given intravenously at a dose of 50 mg/m^2 every 4 weeks until disease progression or unacceptable toxicity in ovarian cancer patients whose disease has progressed or recurred after platinum-based chemotherapy. This indicated dose corresponds to a dose of 100 mg for an adult of about 80 kg body weight. The standard clinical dose of DEFINITY® MBs (plain bubbles) is 10 μl/kg that makes 10^{10} MBs for a person of 80 kg (Shelton et al., 2017). To reach a 100 mg dose, about 6 x 10^{13} of hDox-NBs should be administered to the patient. However, because of the 10^3 decrease in bubble volume when bubble diameter is reduced by an order of magnitude, this NB dose can be achieved with the equivalent total material as needed for the MB dose. Moreover, research shows that DEFINITY® at 1,000 times higher than recommended dose does not produce adverse effects in non-human primates (Lentacker et al., 2010). It is thus likely that a therapeutic dose of drug loaded NBs is clinically feasible and experientially achievable. Furthermore, when considering high NB margination in flow due to lower particle density of NBs (Toy et al., 2011; Cooley et al., 2018), an increased tumor uptake and extravasation *via* concentration gradient will most likely allow us to reduce the clinical dose below 100 mg.

In vitro acoustic performance including contrast-imaging enhancement, initial echogenic signal, and decay was greatly improved by inclusion of hDox into NBs. These results suggest that incorporating hDox in the lipid shell stabilizes the NBs and significantly slows gas dissipation from NBs oscillating in the acoustic field. We hypothesize that hDox may represent a similar behavior as cholesterol by altering the flexibility of NB shell, resulting in more compressibility under insonation, less lipid shedding, and lower gas diffusion. The chemical structure of doxorubicin consists of active sites including sugar amino acid group, hydroxyl groups, and ketone groups and largely hydrophobic anthracycline backbone(Blum and Carter, 1974). This structure resembles with cholesterol, which can fill in the gaps between lipid membranes resulting in either an increase or decrease in membrane fluidity by disordering of gel-liquid crystalline phase (Hofsäß et al., 2003; Doxastakis et al., 2005). It is thus possible that, due to the high degree of hydrophobicity, hDox may incorporate more within the hydrocarbon chains of the lipid shell, thus preventing membrane lipids from packing close together. It is also possible that the microviscosity in the phospholipid head group is decreased by hDox (Alves et al., 2017). Accordingly, two interactions involved in hDox loading on NB shell including the hydrophobic interactions with the hydrocarbon chain of the phospholipid and the electrostatic interactions with the negative phosphate group. It is also possible that the degree of hydrophobicity of dox and it stability could influence on the interaction between the dox and lipid shell membrane. Deprotonation of Dox.HCl using TEA does not change this main structure but only removes the HCl at the sugar amino acid group. We found that hDox-NBs where Dox.HCl was deprotonated by TEA was more stable under insonation showing a slower decay rate than hDox-NBs where hydrophobic dox was deprotonated by sodium hydroxide (**Figure S4**).

We also found that the higher signal and slower signal decay were dependent on the amount of encapsulated hDox. An increasing enhancement of US signal was found only at 2 mg/ml of initial feeding hDox concentration (**Figure S5A**). This led us to also investigate the effect of shell composition on bubble surface tension using previously reported methods (Hernandez et al., 2018). One of the most common applications of the lipid solution is stabilization of the gas–water interface by lowering of interfacial tension. Pendant drop tensiometry was used to measure samples of the 0 mg, 0.1, 0.2, and 0.3 mg hDox solutions. In this technique, gravitational pull causes deformations in the shape of suspended droplets and the surface tension is determined from shape fitting of the droplet outline to the Young-Laplace model (Berry et al., 2015). In order to maximize the gravitational deformation of the droplets, samples were discharged from the needle to hold the largest possible, stable droplet (able to remain on the needle tip for a minimum of 15 s). Water was used to show accurate calibration of the system and measurements were collected at 22°C. 10 droplets of each hDox concentration were measured. The membrane surface tension was significantly reduced at only 2 mg/ml hDox loading (**Figure S5B**). This implies that hDox could act as a buffer, increasing the NB membrane fluidity and decreasing fluidity at a certain loading capacity. Together, this evidence is supportive of our hypothesis that the incorporation of hDox on the NB shell membrane may alter the compressibility of NB by adding more robustness to withstand applied US pressure. An in depth mechanism will be investigated in future work.

In vitro cytotoxicity of free hDox and hDox-NBs was assessed using a human ovarian carcinoma cell line (OVCAR-3). The biological activity of hDox was shown to be similar to that of Dox.HCl. The drug deprotonation strategy has previously been used to improve micelle loading and has been validated in other hormone-dependent cancers and other cancers including human squamous cell carcinoma (Yoo and Park, 2004); human ovarian cancer (A2780)(Mohan and Rapoport, 2010); and human liver cancer (HepG2)(Zhang et al., 2016). Our results show that the combination therapy of hDox-NBs in the presence of US lead to increased cytotoxicity in comparison to control groups including plain NBs, plain NBs+US, free hDox, free hDox+US, free hDox +plain NBs. Furthermore, the baseline cytotoxicity of hDox-NBs without sonication were lower than toxicity of free Dox with or without ultrasound. The cytotoxicity of plain NBs with and without US was also examined to assess baseline toxicity without drug. We found that at the selected NB concentration and sonication parameters, little to no toxicity was seen. Accordingly, it is likely that hDox-NBs in combination with US are responsible for the observed cytotoxic effects *in vitro*. It is also worth mentioning that perfluoropropane (C_3F_8) gas used in this formulation is also not likely to show toxic effects. The gas is used in several clinical applications including in commercially available microbubbles and in clinical vitreoretinal surgery (Kurt et al., 2009; Modi et al., 2017) with only rare adverse effects reported.

CONCLUSION

Overall, this work provides evidence that drug loading capacity, acoustic performance, and therapeutic efficacy can be enhanced by simple deprotonation of doxorubicin prior to its loading into lipid-stabilized NBs. These characteristics suggest that hDox-NBs may be a potential tool for more effective and tumor specific drug delivery when combined with molecular targeting in future work. Results from this study will lead to the development of US-mediated drug delivery system as a theranostic agent with the capability of diagnostic and treating metastatic cancer.

DATA AVAILABILITY STATEMENT

The raw data supporting the conclusions of this article will be made available by the authors, without undue reservation, to any qualified researcher.

AUTHOR CONTRIBUTIONS

PN conceptualized the idea, designed the study, completed the main experiments, analyzed the data and wrote the first draft of the paper. EA contributed to study design, nanobubble characterization and TEM imaging. AD participated in conceptualization of the idea and manuscript preparation. DW contributed to study design and carried out the surface tension experiments. AE conceptualized the idea, oversaw study design and implementation, data analysis and manuscript preparation. All authors have reviewed the final version of the manuscript and approved it for publication.

FUNDING

This work was supported by the National Institutes of Health (R01EB025741 and R01EB028144) and PN was supported by the Royal Thai Government, Thailand. Support was also provided through MITACS Globalink program.

SUPPLEMENTARY MATERIAL

The Supplementary Material for this article can be found online at: https://www.frontiersin.org/articles/10.3389/fphar.2020.00644/full#supplementary-material

REFERENCES

Abdalkader, R., Kawakami, S., Unga, J., Higuchi, Y., Suzuki, R., Maruyama, K., et al. (2017). The development of mechanically formed stable nanobubbles intended for sonoporation-mediated gene transfection. *Drug Deliv.* 24, 320–327. doi: 10.1080/10717544.2016.1250139

Abenojar, E. C., Nittayacharn, P., de Leon, A. C., Perera, R., Wang, Y., Bederman, I., et al. (2019). Effect of Bubble Concentration on the in Vitro and in Vivo Performance of Highly Stable Lipid Shell-Stabilized Micro- and Nanoscale Ultrasound Contrast Agents. *Langmuir* 35, 10192–10202. doi: 10.1021/acs.langmuir.9b00462

Alves, A. C., Magarkar, A., Horta, M., Lima, J. L. F. C., Bunker, A., Nunes, C., et al. (2017). Influence of doxorubicin on model cell membrane properties: Insights from in vitro and in silico studies. *Sci. Rep.* 7, 6343. doi: 10.1038/s41598-017-06445-z

Böhmer, M. R., Klibanov, A. L., Tiemann, K., Hall, C. S., Gruell, H., and Steinbach, O. C. (2009). Ultrasound triggered image-guided drug delivery. *Eur. J. Radiol.* 70, 242–253. doi: 10.1016/j.ejrad.2009.01.051

Berry, J. D., Neeson, M. J., Dagastine, R. R., Chan, D. Y. C., and Tabor, R. F. (2015). Measurement of surface and interfacial tension using pendant drop tensiometry. *J. Colloid Interface Sci.* 454, 226–237. doi: 10.1016/j.jcis.2015.05.012

Blum, R. H., and Carter, S. K. (1974). Adriamycin. A new anticancer drug with significant clinical activity. *Ann. Intern. Med.* 80, 249–259. doi: 10.7326/0003-4819-80-2-249

Chen, P.-Y., Yeh, C.-K., Hsu, P.-H., Lin, C.-Y., Huang, C.-Y., Wei, K.-C., et al. (2017). Drug-carrying microbubbles as a theranostic tool in convection-enhanced delivery for brain tumor therapy. *Oncotarget* 8, 42359–42371. doi: 10.18632/oncotarget.16218

Chilkoti, A., Dreher, M. R., Meyer, D. E., and Raucher, D. (2002). Targeted drug delivery by thermally responsive polymers. *Adv. Drug Deliv. Rev.* 54, 613–630. doi: 10.1016/S0169-409X(02)00041-8

Cooley, M., Sarode, A., Hoore, M., Fedosov, D. A., Mitragotri, S., and Sen Gupta, A. (2018). Influence of particle size and shape on their margination and wall-adhesion: implications in drug delivery vehicle design across nano-to-micro scale. *Nanoscale* 10, 15350–15364. doi: 10.1039/c8nr04042g

de Leon, A., Perera, R., Nittayacharn, P., Cooley, M., Jung, O., and Exner, A. A. (2018). Ultrasound Contrast Agents and Delivery Systems in Cancer Detection and Therapy. *Adv. Cancer Res.* 139, 57–84. doi: 10.1016/bs.acr.2018.04.002

de Leon, A., Perera, R., Hernandez, C., Cooley, M., Jung, O., Jeganathan, S., et al. (2019). Contrast enhanced ultrasound imaging by nature-inspired ultrastable echogenic nanobubbles. *Nanoscale* 11, 15647–15658. doi: 10.1039/c9nr04828f

Deckers, R., and Moonen, C. T. W. (2010). Ultrasound triggered, image guided, local drug delivery. *J. Control. Release* 148, 25–33. doi: 10.1016/j.jconrel.2010.07.117

Derfus, A. M., Von Maltzahn, G., Harris, T. J., Duza, T., Vecchio, K. S., Ruoslahti, E., et al. (2007). Remotely triggered release from magnetic nanoparticles. *Adv. Mater.* 19, 3932–3936. doi: 10.1002/adma.200700091

Doxastakis, M., Sum, A. K., and de Pablo, J. J. (2005). Modulating membrane properties: the effect of trehalose and cholesterol on a phospholipid bilayer. *J. Phys. Chem. B* 109, 24173–24181. doi: 10.1021/jp054843u

Fan, Z., Kumon, R. E., and Deng, C. X. (2014). Mechanisms of microbubble-facilitated sonoporation for drug and gene delivery. *Ther. Deliv.* 5, 467–486. doi: 10.4155/tde.14.10

Ferrara, K., Pollard, R., and Borden, M. (2007). Ultrasound Microbubble Contrast Agents: Fundamentals and Application to Gene and Drug Delivery. *Annu. Rev. Biomed. Eng.* 9, 415–447. doi: 10.1146/annurev.bioeng.8.061505.095852

Fomina, N., McFearin, C., Sermsakdi, M., Edigin, O., and Almutairi, A. (2010). UV and near-IR triggered release from polymeric nanoparticles. *J. Am. Chem. Soc* 132, 9540–9542. doi: 10.1021/ja102595j

Greish, K. (2010). Enhanced permeability and retention (EPR) effect for anticancer nanomedicine drug targeting. *Methods Mol. Biol.* 624, 25–37. doi: 10.1007/978-1-60761-609-2_3

Helfield, B. L., Chen, X., Qin, B., Watkins, S. C., and Villanueva, F. S. (2017). Mechanistic Insight into Sonoporation with Ultrasound-Stimulated Polymer Microbubbles. *Ultrasound Med. Biol.* 43, 2678–2689. doi: 10.1016/j.ultrasmedbio.2017.07.017

Hernandez, C., Nieves, L., de Leon, A. C., Advincula, R., and Exner, A. A. (2018). Role of Surface Tension in Gas Nanobubble Stability Under Ultrasound. *ACS Appl. Mater. Interfaces* 10, 9949–9956. doi: 10.1021/acsami.7b19755

Hernandez, C., Abenojar, E. C., Hadley, J., De Leon, A. C., Coyne, R., Perera, R., et al (2019). Sink or float? Characterization of shell-stabilized bulk nanobubbles using a resonant mass measurement technique. *Nanoscale* 11, 851–855. doi: 10.1039/c8nr08763f

Hernot, S., and Klibanov, A. L. (2008). Microbubbles in ultrasound-triggered drug and gene delivery. *Adv. Drug Deliv. Rev.* 60, 1153–1166. doi: 10.1016/j.addr.2008.03.005

Hofsäß, C., Lindahl, E., and Edholm, O. (2003). Molecular dynamics simulations of phospholipid bilayers with cholesterol. *Biophys. J.* 84, 2192–2206. doi: 10.1016/S0006-3495(03)75025-5

Husseini, G. A., and Pitt, W. G. (2008). Micelles and nanoparticles for ultrasonic drug and gene delivery. *Adv. Drug Deliv. Rev.* 60, 1137–1152. doi: 10.1016/j.addr.2008.03.008

Husseini, G. A., Christensen, D. A., Rapoport, N. Y., and Pitt, W. G. (2002). Ultrasonic release of doxorubicin from Pluronic P105 micelles stabilized with an interpenetrating network of N,N-diethylacrylamide. *J. Control. Release* 83, 303–305. doi: 10.1016/S0168-3659(02)00203-1

Kim, D., Lee, E. S., Oh, K. T., Gao, Z., and Bae, Y. H. (2008). Doxorubicin-loaded polymeric micelle overcomes multidrug resistance of cancer by double-targeting folate receptor and early endosomal pH. *Small* 4, 2043–2050. doi: 10.1002/smll.200701275

Kim, H., Britton, G. L., Peng, T., Holland, C. K., McPherson, D. D., and Huang, S. L. (2013). Nitric oxide-loaded echogenic liposomes for treatment of vasospasm following subarachnoid hemorrhage. *Int. J. Nanomed.* 9, 155–165. doi: 10.2147/IJN.S48856

Kurt, M., Shaikh, K. A., Peterson, L., Kurrelmeyer, K. M., Shah, G., Nagueh, S. F., et al. (2009). Impact of Contrast Echocardiography on Evaluation of Ventricular Function and Clinical Management in a Large Prospective Cohort. *J. Am. Coll. Cardiol.* 53, 802–810. doi: 10.1016/j.jacc.2009.01.005

Lee, H., Kim, H., Han, H., Lee, M., Lee, S., Yoo, H., et al. (2017). Microbubbles used for contrast enhanced ultrasound and theragnosis: a review of principles to applications. *Biomed. Eng. Lett.* 7, 59–69. doi: 10.1007/s13534-017-0016-5

Lentacker, I., Geers, B., Demeester, J., De Smedt, S. C., and Sanders, N. N. (2010). Design and evaluation of doxorubicin-containing microbubbles for ultrasound-triggered doxorubicin delivery: cytotoxicity and mechanisms involved. *Mol. Ther.* 18, 101–108. doi: 10.1038/mt.2009.160

Liu, R., He, B., Li, D., Lai, Y., Chang, J., Tang, J. Z., et al. (2012). Effects of pH-sensitive chain length on release of doxorubicin from mPEG-b-PH-b-PLLA nanoparticles. *Int. J. Nanomed.* 7, 4433–4446. doi: 10.2147/IJN.S32053

Manzoor, A. A., Lindner, L. H., Landon, C. D., Park, J. Y., Simnick, A. J., Dreher, M. R., et al. (2012). Overcoming limitations in nanoparticle drug delivery: Triggered, intravascular release to improve drug penetration into tumors. *Cancer Res.* 72, 5566–5575. doi: 10.1158/0008-5472.CAN-12-1683

Martin, K. H., and Dayton, P. A. (2013). Current status and prospects for microbubbles in ultrasound theranostics. *Wiley Interdiscip. Rev. Nanomed. Nanobiotechnol.* 5, 329–345. doi: 10.1002/wnan.1219

Modi, A., Giridhar, A., and Gopalakrishnan, M. (2017). Sulfurhexafluoride (SF6) versus perfluoropropane (C3F8) gas as tamponade in macular hole surgery. *Retina* 37, 283–290. doi: 10.1097/IAE.0000000000001124

Mohan, P., and Rapoport, N. (2010). Doxorubicin as a molecular nanotheranostic agent: effect of doxorubicin encapsulation in micelles or nanoemulsions on the ultrasound-mediated intracellular delivery and nuclear trafficking. *Mol. Pharm.* 7, 1959–1973. doi: 10.1021/mp100269f

Nittayacharn, P., De Leon, A., Abenojar, E. C., and Exner, A. A. (2018). "The Effect of Lipid Solubilization on the Performance of Doxorubicin-Loaded Nanobubbles," in *IEEE International Ultrasonics Symposium, IUS* (Kobe: IEEE Computer Society). 1-4. doi: 10.1109/ULTSYM.2018.8579716

Nittayacharn, P., Yuan, H.-X., Hernandez, C., Bielecki, P., Zhou, H., and Exner, A. A. (2019). Enhancing Tumor Drug Distribution With Ultrasound-Triggered Nanobubbles. *J. Pharm. Sci.* 108, 3091–3098. doi: 10.1016/j.xphs.2019.05.004

Owen, J., and Stride, E. (2015). Technique for the Characterization of Phospholipid Microbubbles Coatings by Transmission Electron Microscopy. *Ultrasound Med. Biol.* 41, 3253–3258. doi: 10.1016/j.ultrasmedbio.2015.07.024

Perera, R. H., Wu, H., Peiris, P., Hernandez, C., Burke, A., Zhang, H., et al. (2017). Improving performance of nanoscale ultrasound contrast agents using N,N-diethylacrylamide stabilization. *Nanomed. Nanotechnol Biol. Med.* 13, 59–67. doi: 10.1016/j.nano.2016.08.020

Pruitt, J. D., and Pitt, W. G. (2002). Sequestration and ultrasound-induced release of doxorubicin from stabilized Pluronic P105 micelles. *Drug Deliv. J. Deliv. Targeting Ther. Agents* 9, 253–258. doi: 10.1080/10717540260397873

Shelton, S. E., Lindsey, B. D., Dayton, P. A., and Lee, Y. Z. (2017). First-in-Human Study of Acoustic Angiography in the Breast and Peripheral Vasculature. *Ultrasound Med. Biol.* 43, 2939–2946. doi: 10.1016/j.ultrasmedbio.2017.08.1881

Shuai, X., Ai, H., Nasongkla, N., Kim, S., and Gao, J. (2004). Micellar carriers based on block copolymers of poly(ε-caprolactone) and poly(ethylene glycol) for doxorubicin delivery. *J. Control. Release* 98, 415–426. doi: 10.1016/j.jconrel.2004.06.003

Sudimack, J., and Lee, R. J. (2000). Targeted drug delivery via the folate receptor. *Adv. Drug Deliv. Rev.* 41, 147–162. doi: 10.1016/S0169-409X(99)00062-9

Torre, L. A., Trabert, B., DeSantis, C. E., Miller, K. D., Samimi, G., Runowicz, C. D., et al. (2018). Ovarian cancer statistics 2018. *CA. Cancer J. Clin.* 68, 284–296. doi: 10.3322/caac.21456

Toy, R., Hayden, E., Shoup, C., Baskaran, H., and Karathanasis, E. (2011). The effects of particle size, density and shape on margination of nanoparticles in microcirculation. *Nanotechnology* 22 (11), 115101. doi: 10.1088/0957-4484/22/11/115101

Villanueva, F. S., Wagner, W. R., Vannan, M. A., and Narula, J. (2004). Targeted ultrasound imaging using microbubbles. *Cardiol. Clin.* 22, 283–298. doi: 10.1016/j.ccl.2004.02.008

Wang, J., Qin, B., Chen, X., Wagner, W. R., and Villanueva, F. S. (2017). Ultrasound Molecular Imaging of Angiogenesis Using Vascular Endothelial Growth Factor-Conjugated Microbubbles. *Mol. Pharm.* 14, 781–790. doi: 10.1021/acs.molpharmaceut.6b01033

Wang, M., Zhang, Y., Cai, C., Tu, J., Guo, X., and Zhang, D. (2018). Sonoporation-induced cell membrane permeabilization and cytoskeleton disassembly at varied acoustic and microbubble-cell parameters. *Sci. Rep.* 8, 3885. doi: 10.1038/s41598-018-22056-8

Wei, T., Chen, C., Liu, J., Liu, C., Posocco, P., Liu, X., et al. (2015). Anticancer drug nanomicelles formed by self-assembling amphiphilic dendrimer to combat cancer drug resistance. *Proc. Natl. Acad. Sci. U. S. A.* 112, 2978–2983. doi: 10.1073/pnas.1418494112

Xiao, K., Luo, J., Fowler, W. L., Li, Y., Lee, J. S., Xing, L., et al. (2009). A self-assembling nanoparticle for paclitaxel delivery in ovarian cancer. *Biomaterials* 30, 6006–6016. doi: 10.1016/j.biomaterials.2009.07.015

Yoo, H. S., and Park, T. G. (2004). Folate receptor targeted biodegradable polymeric doxorubicin micelles. *J. Control. Release* 96, 273–283. doi: 10.1016/j.jconrel.2004.02.003

Zhang, Y., Yang, C., Wang, W., Liu, J., Liu, Q., Huang, F., et al. (2016). Co-delivery of doxorubicin and curcumin by pH-sensitive prodrug nanoparticle for combination therapy of cancer. *Sci. Rep.* 6, 21225. doi: 10.1038/srep21225

Zhu, X., Guo, J., He, C., Geng, H., Yu, G., Li, J., et al. (2016). Ultrasound triggered image-guided drug delivery to inhibit vascular reconstruction via paclitaxel-loaded microbubbles. *Sci. Rep.* 6, 21683. doi: 10.1038/srep21683

Conflict of Interest: The authors declare that the research was conducted in the absence of any commercial or financial relationships that could be construed as a potential conflict of interest.

Advantages of publishing in Frontiers

OPEN ACCESS
Articles are free to read for greatest visibility and readership

FAST PUBLICATION
Around 90 days from submission to decision

HIGH QUALITY PEER-REVIEW
Rigorous, collaborative, and constructive peer-review

TRANSPARENT PEER-REVIEW
Editors and reviewers acknowledged by name on published articles

Frontiers
Avenue du Tribunal-Fédéral 34
1005 Lausanne | Switzerland

Visit us: www.frontiersin.org
Contact us: info@frontiersin.org | +41 21 510 17 00

REPRODUCIBILITY OF RESEARCH
Support open data and methods to enhance research reproducibility

DIGITAL PUBLISHING
Articles designed for optimal readership across devices

FOLLOW US
@frontiersin

IMPACT METRICS
Advanced article metrics track visibility across digital media

EXTENSIVE PROMOTION
Marketing and promotion of impactful research

LOOP RESEARCH NETWORK
Our network increases your article's readership